الجامعة الإسلامية بالمدينة المنورة
ISLAMIC UNIVERSITY OF MADINAH

The Islamic University Journal of Applied Sciences (IUJAS)

Refereed periodical scientific journal

An Open Access Journal

Print ISSN: 1658-7936
Online ISSN: 1658-7944

Special Issue – February 2026

بسم الله الرحمن الرحيم

Islamic University Journal of Applied Sciences (IUJAS)

The Islamic University Journal of Applied Sciences (IUJAS)

Issued By

Islamic University of Madinah, Madinah, Saudi Arabia

Special issue

The 1st National Conference of Advanced Electrical and Electronics Engineering

NCAEEE'25

held at the Institute of Electrical and Electronic Engineering,
University M'Hamed Bougara of Boumerdes, Algeria,
November 30th, 2025.

Paper version

Filed at the King Fahd National Library No. 8742/1439 on 17/09/1439 AHInternational serial number of periodicals (ISSN) 1658-7936

Online version

Filed at the King Fahd National Library No. 8742/1439 on 17/09/1439 AHInternational Serial Number of Periodicals (e-ISSN) 1658-7944

The Journal's Website

https://journals.iu.edu.sa/jesc

Publication Rules at the Journal (*)

❖ General rules:

- Report original scientific research (the main results and conclusions must not have beenpublished or submitted elsewhere).
- Fit with the topics of the journal.
- Report novel results, innovative work and show a new scientific contribution.
- Not to bear similarity of more than 25% of a previously published work of the sameauthor(s).
- Follow the rules, regulation and authentic research methodologies.
- Fulfill the required items and the format of the journal provided in appendix below relatedto the guide for author.
- Opinions expressed in published articles commit the authors themselves only and notnecessarily the opinion of the journal.

❖ For all articles:

- The exclusive right to publish and distribute and article, and to grant rights to others,including commercial purposes.
- For open access articles, IU will apply the relevant third-party user license where IUpublishes the article on its online platforms.
- The right to provide the article in all forms and media so the article can be used on thelatest technology even after publication.
- The authority to enforce the rights in the article, on behalf of an author, against thirdparties, for example in the case of plagiarism or copyright infringement.

(*) These general rules are explained in details along with other rules for Author's guide in the journal's website: https://journals.iu.edu.sa/jesc

Editorial Board

Editorial Board Members

	**Mussa. A. Said** Professor, Chemistry, Islamic University of Madinah, Saudi Arabia. **Orcid:** https://orcid.org/0000-0003-3073-5449
	**Fazal Noor** Professor, Computer science and engineering, Islamic University of Madinah. Saudi Arabia **Orcid:** https://orcid.org/0000-0002-0096-3435
	**Basem Rashid Alamri** Associate Professor, Electrical Engineering, Taif University, Saudi Arabia https://orcid.org/0000-0002-8667-0042
	**Saad Talal Alharbi** Professor in Computer Science, � Human Computer Interaction, Faculty of Computers, Taibah University, Saudi Arabia https://orcid.org/0000-0003-0913-8631
	**Yazed Alsaawy** Associate Professor, Computer and information systems, Islamic University of Madinah. Saudi Arabia **Orcid:** https://orcid.org/0000-0001-5031-3388

	**Abdul Qadir Bhatti** Professor, Civil Engineering, Faculty of Engineering, Islamic University of Madinah. Saudi Arabia ORCID Link https://orcid.org/0000-0001-5433-7803
	**Shamsuddin Ahmed** Professor, Industrial Engineering, The Faculty of Computer and Information Systems Islamic University of Madinah, Saudi Arabia. https://orcid.org/ orcid.org/

Editorial Secertary

	**Ahmad Ziad Al-Zuhaily** Assistant Editor, Computer science, Engineer, Islamic University of Madinah. Saudi Arabia
	**Abdulrahman Saeed Odeh** Assistant Editor, Computer science, Engineer, Islamic University of Madinah. Saudi Arabia

Table of Contents

Islamic University Journal of Applied Sciences (IUJAS)
https://journals.iu.edu.sa/jesc
Special Issue, February 2026, Pages 01-06
https://igee.univ-boumerdes.dz/ncaeee25/

An Ultra-Wide-Band non-Conventional two Element MIMO Antenna

Khelil FERTAS [1,*], Fouad FERTAS [1]

[1] Institute of Electrical and Electronic Engineering, University M'Hamed Bougara of Boumerdes, Boumerdes, Algeria,

* Corresponding author (Khelil Fertas), Email address: k.fertas@gmail.com

Abstract

This paper describes a planar Multiple-Input-Multiple-Output (MIMO) antenna designed for Ultra-Wide-Band (UWB) applications. The configuration consists of two identical non-conventional parallel pieces. Each element is optimized using Genetic Algorithm code created in the CST microwave studio's visual basic scripting (VBS) environment. T-shaped is appropriate for parallel and. The suggested MIMO antenna attains operating band of over 171.4% on (2 - 26 GHz), ECC less than 0.01 and Diversity Gain (DG) more than 9.98 were obtained. The proposed structure is designed on the Rogers RT6002 substrate with a dielectric constant of 2.94, a height of 1.52mm, and a loss tangent of 0.0012. The simulated isolation between ports is better than -20 dB in most bandwidth. The proposed antenna is well-suited for UWB MIMO applications.

Keywords: MIMO, Ultra-Wide-Band, diversity gain, ECC, isolation enhancement, non-conventional antenna.

---

https://doi.org/10.63070/jesc.2026.001
Received 30 November 2025; Revised 12 January 2026; Accepted 24 January 2026.

Published by Islamic University of Madinah on behalf of *Islamic University Journal of Applied Sciences*.

1. Introduction

Wireless communications continue to progress strongly, requiring new technologies to offer improved performance, coverage, quality of service, and capacity. Printed antennas are necessary in mobile terminals due to their low weight, cost, and flexibility.

However, conventional printed antennas are faced with challenges like electromagnetic coupling between MIMO systems, leading to interference and degradation of signals. MIMO diversity and UWB technology offer remedies, but new designs are always in need.

Antennas enable wireless communication by converting electrical energy to electromagnetic energy and vice versa. They radiate signals during transmission and capture signals during reception, operating in both modes [1]. A microstrip antenna consists of a conducting patch on a dielectric substrate, with the opposite side covered by a large metallic ground plane. It is created through photoetching, printing, or similar methods [2]. Microstrip antenna patches come in various shapes, such as rectangular, circular, and triangular, chosen based on size, radiation pattern, gain, and bandwidth requirements. Operating modes depend on patch dimensions, substrate properties, and feeding configuration. Various dielectric materials are used as substrates [3]. Single-input, single-output (SISO) antennas are not suitable with high channel capacity demands and data rates in wireless systems. Printed multiple-input, multiple-output (MIMO) antennas have proven to be the right selection for high-speed communication technologies [5-6].

Individual feeding systems are utilized by MIMO antenna structures to transmit and receive information on different radiating elements. Port coupling diminishes performance, yet with the employment of other methodologies, isolation is strengthened. An efficient solution [7-8] is to design MIMO structures based on metamaterial. A periodic electrically coupled square split-ring resonator (SRR) metasurface is used over the antenna array to improve decoupling [9]. A split ring with an inductive line electrically coupled with a capacitive gap electrically coupled enables magnetic and electric coupling, forming the decoupling structure [10]. Orthogonal MIMO antenna structure yields high isolation [11]. Massive MIMO systems reduce latency in MIMO [12]. A rectangular strip decoupling structure improves isolation [13]. High terminal isolation in a MIMO system is required for the system to give high accuracy [14].

This paper emphasizes the design of a MIMO UWB patch antenna for WiMAX communication systems with the aim of attaining high data rates, a reliable transmission, compactness, and electromagnetic compatibility.

2. Antenna design and configuration

The fundamental antenna is an ultra-wideband (UWB) patch antenna which is used to construct a two-element MIMO antenna then simulated, with efforts to reduce coupling between elements. The design procedure, parametric study, and improvement in performance are performed using CST Microwave Studio (MWS).

Two parallel element MIMO antenna (fig.1) is tested using three distance parameters with reference to $\lambda/2$ ($\lambda = 62$ mm). Simulation experiments show that wider spacing (D) between the elements reduces mutual coupling (S21), lessening inter-antenna interference and improving spatial selectivity, Excessive inter-element spacing between MIMO antennas can impair spatial coherence and diversity, affecting performance. To reduce this, the research seeks to reduce the distance ($D < \lambda/2$) and coupling effects using a T-shaped parasitic structure. After optimization of the T-shaped element and the resizing of the ground plane, decoupling of the antenna elements is reduced.

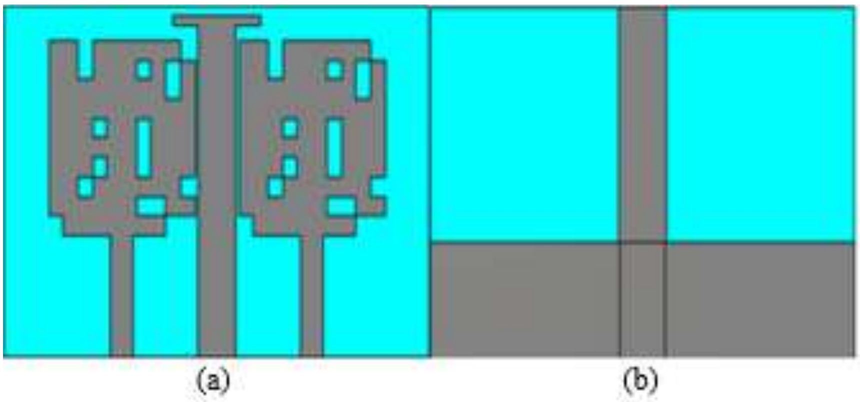

Figure 1. MIMO antenna with T-shaped structure: (a) Front view, (b) Back view.

3. Simulated results

The simulated MIMO antenna's return loss and mutual coupling are represented by figures 2 and 3. S11 and S22 parameters confirm the ultra-wideband characteristics of the antenna.

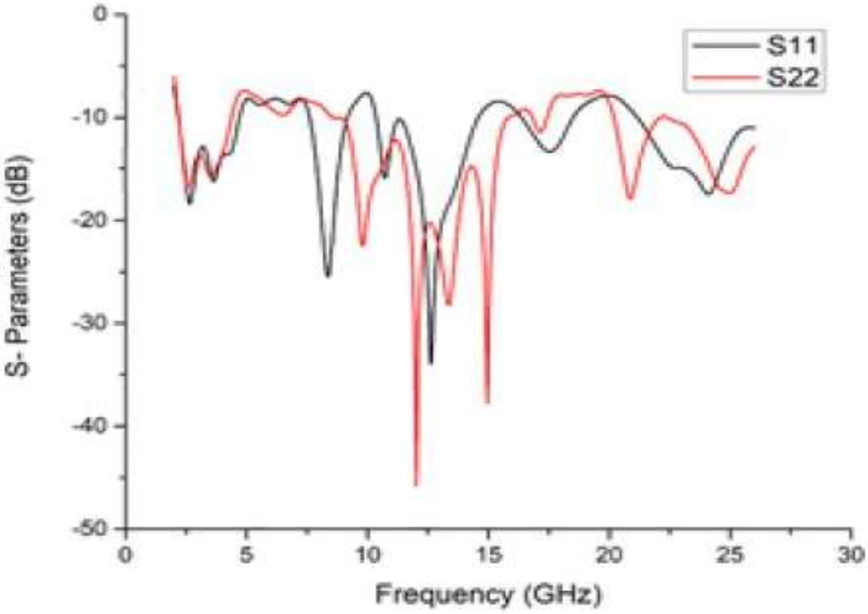

Figure 2. Simulated S11 and S22 parameters.

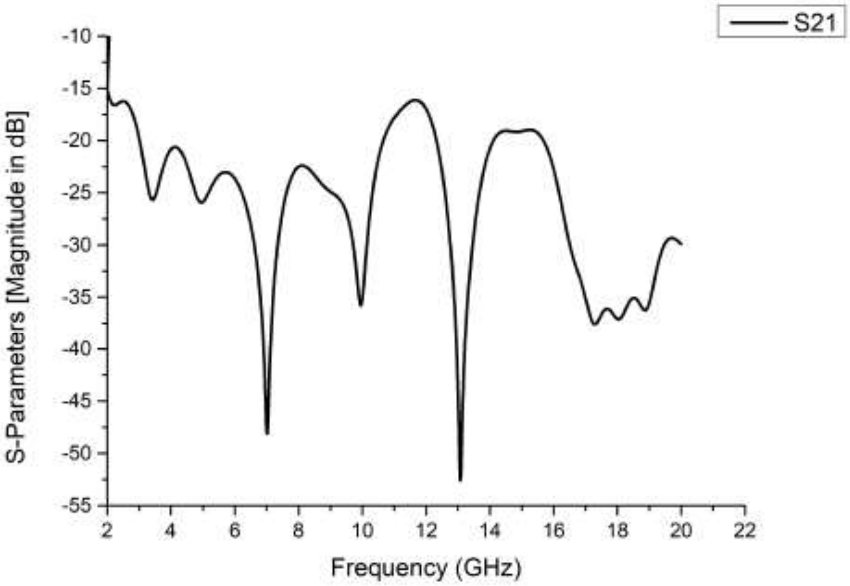

Figure 3. Simulated mutual coupling.

Envelope correlation coefficient (ECC) and diversity gain of the proposed design are shown in figures 4 and 5, respectively.

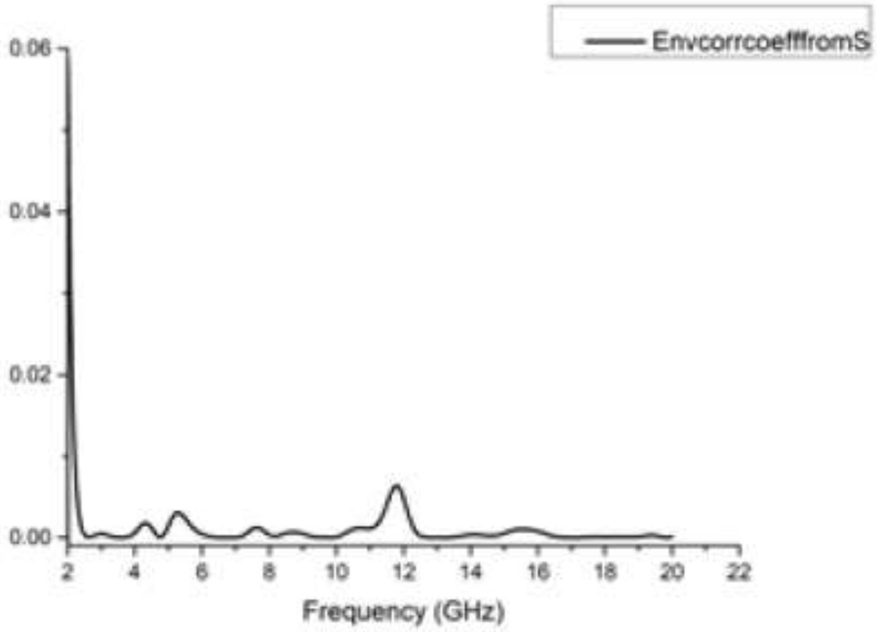

Figure 4. ECC simulated of MIMO antenna.

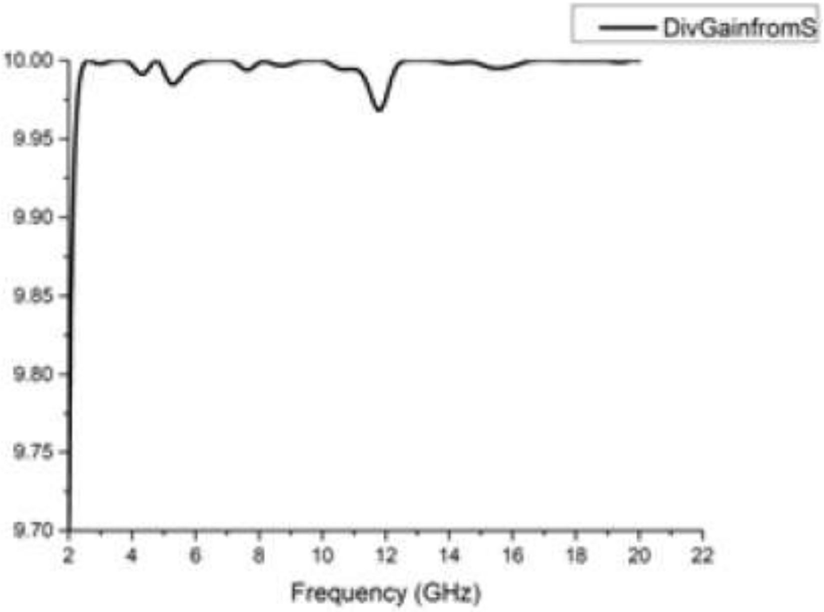

Figure 5. Diversity gain (DG) simulated of MIMO antenna.

We can see from fig.4-5 that both of the two MIMO performance metrics are well within the acceptable limit. The ECC should be at least 0.05 (our ECC value < 0.009), which is well acceptable.

4. Conclusion

The work presents design and simulation of an ultra-wideband MIMO antenna for WiMAX and other wireless communication systems through CST software and Rogers substrate. The size of proposed antenna is 58 x 36 mm² having two parallel elements and T-shaped structure, ECC = 0.0089 the simulation data gives a good performance. The paper bridges the theoretical research gap to practical implementation gap in MIMO antenna technology to pave the future for innovations in wireless communications.

References

[1] R. Karli and H. Ammor, A simple and original design of multi-band microstrip patch antenna for wireless communication, International Journal of Microwaves Applications, 2013.
[2] K. Fertas, F. Fertas, M. Challal, and T. A. Denidni, A novel miniaturized V-shaped monopole antenna for GSM/WiMAX/WLAN applications, Frequenz, vol. 77, pp. 155-162, 2023.
[3] F. Fertas, M. Challal, and K. Fertas, Miniaturized quintuple band antenna for multiband applications, Progress In Electromagnetics Research M, vol. 89, pp. 83-92, 2020.
[4] Tao, J.; Feng, Q. Compact ultra-wideband MIMO antenna with half-slot structure, IEEE Antennas Wirel. Propag. Lett. , 16, pp. 792–795, 2016.
[5] Xu, Y.; Dong, Y.; Wen, S.; Wang, H. Vertically polarized quasi-Yagi MIMO antenna for 5G N78 band application, IEEE Access , 9, pp. 7836–7844, 2021.
[6] Sakli, H.; Abdelhamid, C.; Essid, C.; Sakli, N. Metamaterial-based antenna performance enhancement for MIMO system applications, IEEE Access, 9, pp. 38546–38556, 2021.
[7] Garg, P.; Jain, P. Isolation improvement of MIMO antenna using a novel flower shaped metamaterial absorber at 5.5GHz WiMAX band, IEEE Trans. Circuits Syst. Vol. 67, pp. 675–679, 2020.
[8] Wang, Z.; Zhao, L.; Cai, Y.; Zheng, S.; Yin, Y. A meta-surface antenna array decoupling (MAAD) method for mutual coupling reduction in a MIMO antenna system, Sci. Rep. vol. 8, pp. pp. 3152–3159, 2018.
[9] Xue, C.D.; Zhang, X.Y.; Cao, Y.F.; Hou, Z.; Ding, C.F. MIMO antenna using hybrid electric and magnetic coupling for isolation enhancement, IEEE Trans. Antennas Propag. , vol. 65, pp. 5162–5170, 2017.
[10] Yang, C.; Kim, J.; Kim, H.; Wee, J.; Kim, B.; Jung, C. Quad-band antenna with high isolation MIMO and broadband SCS for broadcasting and telecommunication services, IEEE Antennas Wirel. Propag. Lett. Vol. 9, pp. 584–587, 2010.
[11] Bhattacharya, A.; Roy, B. Investigations on an extremely compact MIMO antenna with enhanced isolation and bandwidth, Microw. Opt. Technol. Lett. , vol. 62, pp. 845–851, 2020.
[12] Pei, T.; Zhu, L.; Wang, J.; Wu, W. A low-profile decoupling structure for mutual coupling suppression in MIMO patch antenna, IEEE Trans. Antennas Propag. , vol. 69, pp. 6145–6153, 2021.
[13] Pan, B.C.; Cui, T.J. Broadband decoupling network for dual-band microstrip patch antennas, IEEE Trans. Antennas Propag. , vol. 65, pp. 5595–5598, 2017.
[14] Khalid, M.; Iffat Naqvi, S.; Hussain, N.; Rahman, M.; Mirjavadi, S.S.; Khan, M.J.; Amin, Y. 4-port MIMO antenna with defected ground structure for 5G millimeter wave applications, Electronics , vol.9, 71, 2020.

Islamic University Journal of Applied Sciences (IUJAS)
https://journals.iu.edu.sa/jesc
Special Issue, February 2026, Pages 07-19
https://igee.univ-boumerdes.dz/ncaeee25/

Simulation Study of Robust Backstepping Control for Five-Phase PMSM under Load Variations and Open Fault Phase

Haithem Boughezala Hamad [1,*], Toumi Djaafar [2], Boughezala Mohammed Salah [2]
[1] Ziane Achour University of Djelfa Algeria, haithem.boughezala@univ-djelfa.dz
[2] Chahid Hamma Lakhdhar university of El-oued. Algeria. BM.salah@gmail.com;
Toumi.djaafar@gmail.com
*Corresponding author (Haithem Boughezala), *Email Address*: haithem.boughezala@univ-djelfa.dz

Abstract

This study investigates the behavior of a Five-Phase Permanent Magnet Synchronous Motor (5P-PMSM) when an open-phase fault occurs. It applies a sensorless control approach that combines backstepping control with a Model Reference Adaptive System (MRAS) observer. Using measurable electrical quantities, including stator currents and voltages, the proposed method accurately estimates both rotor position and speed. The design of the backstepping controller follows a structured procedure to achieve global or semi-global stability, making it suitable for applications that demand reliable operation under changing conditions. Lyapunov theory is used to analyze and verify the stability of the combined observer and controller. The main objective of the research is to maintain motor performance and stable operation in the presence of an open-phase fault. Simulations conducted in MATLAB/Simulink compare normal motor performance with performance during the fault to evaluate the effectiveness of the control strategy. The findings show that the backstepping controller, supported by the MRAS observer, enhances fault tolerance and reduces the adverse effects. The simulation results confirm that the proposed approach sustains motor operation with minimal decline in performance, offering a dependable solution for industrial systems requiring resilience to faults.

Keywords: 5-phase permanent magnet synchronous motor; Backstepping control; Sensorless control Fault open phase; Fault tolerant; Model reference adaptative system (MRAS) Observer.

---

https://doi.org/10.63070/jesc.2026.002
Received 30 November 2025; Revised 15 January 2026; Accepted 25 January 2026.

Published by Islamic University of Madinah on behalf of *Islamic University Journal of Applied Sciences*.

1. Introduction

The growing use of Five-Phase Permanent Magnet Synchronous Motors (5P-PMSMs) in both industrial and automotive sectors highlight the importance of developing dependable and efficient control strategies. Ensuring high performance and operational safety requires effective fault detection and diagnosis methods, especially for faults that can compromise system functionality, such as open-phase faults. Among various electrical faults, the open-phase fault is considered one of the most frequent occurrences. [1], where one or more phases of the motor become disconnected or lose functionality, can severely degrade motor performance and its associated drive system.

This paper focuses on advanced techniques for identifying and evaluating open-phase faults in Five-Phase Permanent Magnet Synchronous Motors (5P-PMSMs). These machines are attracting significant attention due to their inherent fault-tolerant characteristics. Unlike traditional three-phase motors, a five-phase PMSM can maintain operation even if one or more phases become disconnected, though with reduced performance. This increased phase redundancy enhances system reliability and makes the motor suitable for safety-critical applications such as electric vehicles, aerospace actuators, and industrial automation. Accurately detecting an open-phase fault is essential to ensure continued operation, prevent further damage, and maintain acceptable torque and speed performance. Therefore, developing robust detection and control methods plays an important role in improving the resilience and efficiency of five-phase PMSM drive systems [2], focusing on sensorless control strategies. Conventional fault detection techniques frequently depend on physical sensors, which increase system cost and complexity and may themselves be susceptible to malfunction. To overcome these limitations, the study examines sensorless fault diagnosis methods based on backstepping control and a Model Reference Adaptive System (MRAS). Although many studies have explored sensorless observers for multiphase motors, the MRAS approach remains attractive for five-phase PMSM drives due to its relatively simple structure and ease of implementation. [3].

Backstepping control is widely recognized for its strong performance when dealing with nonlinear systems. Unlike classical control approaches such as linearization-based feedback and conventional PI controllers, which often rely on simplified or linearized models, backstepping is designed to handle system nonlinearities directly within the control structure. This allows it to provide better stability, more accurate tracking, and stronger robustness against disturbances and parameter uncertainties. Due to these advantages, backstepping control is considered a more suitable choice in applications where dynamic behavior is complex and system parameters may vary[4], the recursive structure of the backstepping control method provides strong robustness and flexibility when dealing with nonlinear dynamics and parameter uncertainties, which makes it a promising choice for use in fault detection and control applications. Meanwhile, the Model Reference Adaptive System (MRAS) approach relies on adaptive estimation to monitor the motor’s operating states and identify deviations from expected performance.

By combining backstepping control with MRAS-based estimation, this research aims to improve the precision and reliability of fault detection, while also removing the dependence on additional physical sensors. This integrated approach supports stable motor operation even when faults occur and contributes to higher system efficiency and fault tolerance.

This paper begins by presenting a detailed discussion of the theoretical principles underlying backstepping control and the Model Reference Adaptive System (MRAS) when applied to five-phase PMSM drives. After establishing this foundation, the work describes the formulation of a fault detection strategy that integrates both techniques, explaining each design step and its role in enhancing system robustness. The proposed approach is then validated through simulation studies, where its performance is assessed under both normal and faulted operating conditions. The results demonstrate the effectiveness of the combined method in improving fault tolerance and operational stability. Overall, the contributions of this research support the development of more reliable PMSM drive systems, offering practical benefits such as increased motor durability, reduced downtime, and lower maintenance costs in real industrial environments.

This paper is structured to guide the reader through both the theoretical development of the proposed control approach. Section 2 introduces the system configuration and presents the mathematical model of the five-phase PMSM, forming the foundation for subsequent controller design. Section 3 describes the implementation of the backstepping control strategy tailored for the 5P-PMSM drive. Section 4 focuses on the rotor position estimation method based on the Model Reference Adaptive System (MRAS), providing a detailed explanation of its structure and operation. Section 5 presents the simulation results obtained using MATLAB/Simulink, along with a thorough analysis of the motor's performance under different operating conditions. The final section summarizes the main conclusions of the study and highlights key contributions as well as potential directions for future research.

2. Mathematical Modelling of Five-Phase PMSM

In natural base, the following electrical equation describe model of Five-PMSM:

$$[\mathrm{V}_s]=[\mathrm{R}_s][\mathrm{I}_s]+\frac{\mathrm{d}[\varphi_s]}{\mathrm{dt}} \qquad (1)$$

[Vs], [Is]: are the voltage and current of input system.

[Rs]: is the stator resistance per phase.

[Øs]:is the global flux linkage

The dynamic behavior of a Five-Phase Permanent Magnet Synchronous Motor (5P-PMSM) is first described using a set of coupled differential equations that relate stator currents, voltages, and electromagnetic torque. However, the inherent coupling between phases introduces complexity in controller design and analysis. To overcome this challenge, a fifth-order Park transformation is applied. This mathematical transformation converts the original five-phase variables from the stationary reference frame into multiple orthogonal rotating reference frames. As a result, the system dynamics are reformulated into partially or fully decoupled equations, which significantly simplifies control development, facilitates independent current regulation, and improves computational efficiency. This decoupling is essential for implementing advanced control strategies and fault-tolerant algorithms in 5P-PMSM drive systems.[6]

And, the matrix of Park transformation which defined as follow:

$$[M]=\sqrt{\frac{2}{5}}\begin{bmatrix} \cos\theta & \cos(\theta-\frac{2\pi}{5}) & \cos(\theta-\frac{4\pi}{5}) & \cos(\theta+\frac{4\pi}{5}) & \cos(\theta+\frac{2\pi}{5}) \\ \sin\theta & \sin(\theta-\frac{2\pi}{5}) & \sin(\theta-\frac{4\pi}{5}) & \sin(\theta+\frac{4\pi}{5}) & \sin(\theta+\frac{2\pi}{5}) \\ \cos\theta & \cos(\theta+\frac{4\pi}{5}) & \cos(\theta-\frac{2\pi}{5}) & \cos(\theta+\frac{2\pi}{5}) & \cos(\theta-\frac{4\pi}{5}) \\ \sin\theta & \sin(\theta+\frac{4\pi}{5}) & \sin(\theta-\frac{2\pi}{5}) & \sin(\theta+\frac{2\pi}{5}) & \sin(\theta-\frac{4\pi}{5}) \\ \frac{1}{\sqrt{2}} & \frac{1}{\sqrt{2}} & \frac{1}{\sqrt{2}} & \frac{1}{\sqrt{2}} & \frac{1}{\sqrt{2}} \end{bmatrix} \quad (2)$$

The general model of the five-phase PMSM in the reference frame (d1- q1- d2– q2-o) continent the electrical equation can be written in the following form:

$$\begin{cases} V_{d1}=R_sI_{d1}+L_{d1}\dfrac{dI_{d1}}{dt}+wL_{q1}I_{q1} \\ V_{q1}=R_sI_{q1}+L_{q1}\dfrac{dI_{q1}}{dt}+wL_{d1}I_{d1}+w\varphi_m \\ V_{d2}=R_sI_{d2}+L_{d2}\dfrac{dI_{d2}}{dt} \\ V_{q2}=R_sI_{q2}+L_{q2}\dfrac{dI_{q2}}{dt} \end{cases} \quad (3)$$

And the mechanical equation in the following formule:

$$\begin{cases} J\dfrac{d\Omega}{dt}=T_{em}-T_L-F\Omega \\ T_{em}=\dfrac{5}{2}P(\varphi_mI_{q1}+(L_{d1}-L_{q1})I_{q1}I_{d1}) \end{cases} \quad (4)$$

where, θ is the electrical angle, φm is the permanent magnet flux ,W and Ω are the electrical and mechanical angular velocity respectively, J is the inertia moment, ,Tl is the load torque, Tem the electromagnetic torque and F denotes the friction coefficient.

3. Backstepping Control Design

In this section, the fundamental principle of the backstepping control approach is introduced. The method constructs the closed-loop control system by sequentially stabilizing first-order subsystems, using Lyapunov-based design at each step. This recursive framework guarantees robustness and ensures global asymptotic stability of the overall system [7]. The development of the proposed backstepping controller is carried out in two main stages:

3.1. Calculation of the desired current references

To guarantee that the speed controller accurately tracks the desired reference trajectory, the speed tracking error and its time derivative are defined as follows:

$$\begin{cases} e_1 = \omega^* - \hat{\omega} \\ \dot{e}_1 = \dot{\omega}^* - \dot{\hat{\omega}} \end{cases} \tag{5}$$

To assess how effectively the actual speed follows the reference speed, a Lyapunov candidate function is introduced based on the defined speed tracking error. This function serves as a measure of system stability and tracking performance, the first Lyapunov function associated with the speed error is defined as follows:

$$V_1 = \frac{1}{2} e_1^2 \tag{6}$$

According the stability condition of Lyapunov can be write the following expression:

$$\dot{e}_1 = \dot{\omega}^* - \dot{\hat{\omega}} = -k_1 e_1 \tag{7}$$

The reference current expressions are then obtained as shown in equation (8). In this formulation, the Iq1component is responsible for generating the electromagnetic torque, while the remaining current components are set to zero since they do not contribute to torque production.

$$\begin{cases} i_{d1}^* = 0 \\ i_{q1}^* = \left(\dot{\omega}^* + \frac{T_L}{J} + \frac{f\,\hat{\omega}}{J} + k_1 e_1 \right) / \left(\frac{K\,\varphi_m P}{J} \right) \\ i_{d2}^* = 0 \\ i_{q2}^* = 0 \end{cases} \tag{8}$$

3.2. Calculation of the desired voltages references

Figure 1 presents the overall backstepping control structure implemented for the five-phase PMSM drive. In this scheme, the backstepping controller operating in the d−q reference frame takes the speed tracking error e_Ω as its input and generates the corresponding Iq_1 reference current.

Based on this current reference, the required stator voltage components are then computed according to Equation (8). To determine these voltages, the current tracking errors are formulated, which allows the control law to compute the appropriate reference voltage signals as follows :

$$\begin{cases} e_2 = i_{d1}^* - i_{d1} \\ e_3 = i_{q1}^* - i_{q1} \\ e_4 = i_{d2}^* - i_{d2} \\ e_5 = i_{q2}^* - i_{q2} \end{cases} \tag{9}$$

By Setting (3) in the previous equation, one obtains:

$$\begin{cases} e_2 = -i_{d1} \\ e_3 = \left(\dot{\omega}^* + \dfrac{T_L}{J} + \dfrac{f\hat{\omega}_r}{J} + k_1 e_1 \right) / \left(\dfrac{K\varphi_m P}{J} \right) - i_{q1} \\ e_4 = -i_{d2} \\ e_5 = -i_{q2} \end{cases} \tag{10}$$

To verify the overall stability of the proposed control strategy [8], a second Lyapunov candidate function is formulated. This function builds upon the previous stability analysis and accounts for the additional control terms introduced during the backstepping design process. It is expressed as follows:

$$V_2 = \frac{e_1^2 + e_2^2 + e_3^2 + e_4^2 + e_5^2}{2} \tag{11}$$

By imposing the Lyapunov stability condition on the previously defined function and expressing the tracking errors accordingly, the reference voltage signals can be derived. These expressions ensure that the control inputs drive the system states toward their desired values. The obtained reference voltages are given as follows:

$$\begin{cases} V_{d1}^* = L_s \left(k_2 e_2 + \dot{i}_{d1}^* + \dfrac{R_s}{L_s} i_{d1} - \omega\, i_{q1} \right) \\ V_{q1}^* = L_s \left(k_3 e_3 + k\,\varphi_m P e_1 + \dot{i}_{q1}^* + \dfrac{R_s}{L_s} i_{q1} + \omega\, i_{d1} + \dfrac{\varphi_m}{L_s} \omega \right) \\ V_{d2}^* = L_{ls} \left(k_4 e_4 + \dot{i}_{d2}^* + \dfrac{R_s}{L_{ls}} i_{d2} - 3\omega\, i_{q2} \right) \\ V_{q2}^* = L_{ls} \left(k_4 e_5 + \dot{i}_{q2}^* + \dfrac{R_s}{L_{ls}} i_{q2} + 3\omega\, i_{d2} \right) \end{cases} \tag{12}$$

Where P is the pole number, Ls and Lls are the primer end secondary stator inductances of the five-phase PMSM in the reference frame (d1- q1- d2– q2-o).

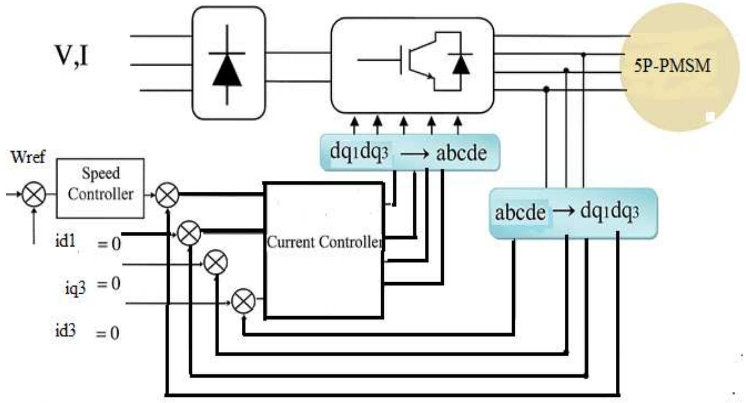

Fig 1. The Backstepping control structure of five-phase PMSM drive

4. DESIGN OF MRAS OBSERVER

To estimate both the rotor position and speed, a Model Reference Adaptive System (MRAS) is employed. The primary objective of using MRAS in the control of a five-phase PMSM is to reduce torque and speed fluctuations that may arise under variable load conditions. In this work, a sensorless control strategy based on the MRAS structure is introduced specifically for the FPMSM. The MRAS approach operates by comparing the outputs of a reference model and an adaptive model. The difference between these two outputs is processed through an adaptation mechanism, commonly implemented using a PI controller, which provides the rotor speed estimate. This concept is illustrated schematically in Figure 2

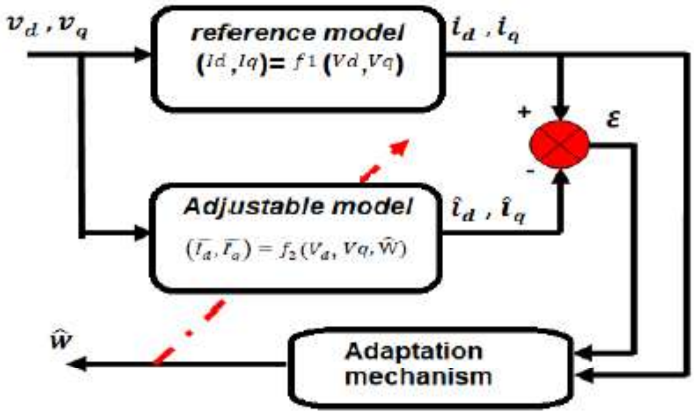

Fig 2. Structure of model reference adaptative system (MRAS)

The reference model used in the MRAS scheme is derived directly from the state-space representation of the five-phase PMSM. This model describes the expected dynamic behavior of the motor under ideal conditions, without parameter uncertainties or disturbances. It serves as the benchmark model in the adaptation process. The mathematical formulation of the reference model can therefore be expressed as follows:

$$\begin{cases} [\dot{X}] = [A][X] + [B][V] + [C] \\ [Y] = [I][X] \end{cases} \quad (13)$$

With:

The MRAS observer input is $[\mathrm{V}] = \left[\mathrm{V}_{\mathrm{d}1}, \mathrm{V}_{\mathrm{q}1}, \mathrm{V}_{\mathrm{d}2}, \mathrm{V}_{\mathrm{q}2}\right]^{\mathrm{T}}$,the output variable of system is $[\mathrm{X}] = \left[\mathrm{I}_{\mathrm{d}1}, \mathrm{I}_{\mathrm{q}1}, \mathrm{I}_{\mathrm{d}2}, \mathrm{I}_{\mathrm{q}2}\right]^{\mathrm{T}}$, and [I] the unitary matrix. Then the state-space matrices of model defined as:

$$[A] = \left\{\begin{matrix} -\frac{R_s}{\mathrm{L}_{d1}} & \frac{\mathrm{L}_{q1}\mathrm{W}}{\mathrm{L}_{d1}} & 0 & 0 \\ -\frac{\mathrm{L}_{d1}\mathrm{W}}{\mathrm{L}_{q1}} & -\frac{R_s}{\mathrm{L}_{q1}} & 0 & 0 \\ 0 & 0 & -\frac{R_s}{\mathrm{L}_{d2}} & 0 \\ 0 & 0 & 0 & -\frac{R_s}{\mathrm{L}_{q2}} \end{matrix}\right\} [B] = \left\{\begin{matrix} \frac{1}{\mathrm{L}_{d1}} & 0 & 0 & 0 \\ 0 & \frac{1}{\mathrm{L}_{q1}} & 0 & 0 \\ 0 & 0 & \frac{1}{\mathrm{L}_{d2}} & 0 \\ 0 & 0 & 0 & \frac{1}{\mathrm{L}_{q2}} \end{matrix}\right\} and [C] = \left\{\begin{matrix} 0 \\ -\frac{\varphi_m W}{L_{q1}} \\ 0 \\ 0 \end{matrix}\right\}$$

Similarly, the adaptive (or adjustable) model is obtained from the mathematical representation of the five-phase PMSM, but it incorporates the estimated parameters rather than the actual ones. This model produces output signals that depend on the estimated rotor speed, which allows the MRAS algorithm to adjust and refine the estimation. The adjustable model can therefore be expressed in the following form:

$$\begin{cases} \hat{X} = [\hat{A}][\hat{X}] + [B][V] + [\hat{C}] \\ [\hat{Y}] = [I][\hat{X}] \end{cases} \quad (14)$$

Where $[\hat{\mathrm{X}}] = \left[\hat{\mathrm{I}}_{\mathrm{d}}, \hat{\mathrm{I}}_{\mathrm{q}}, \hat{\mathrm{I}}_{\mathrm{x}}, \hat{\mathrm{I}}_{\mathrm{y}}\right]^{\mathrm{T}}$is the estimated state vector, so the state-space matrices of adjustable model written in the form :

$$[\hat{A}] = \left\{\begin{matrix} -\frac{R_s}{\mathrm{L}_{d1}} & \frac{\mathrm{L}_q\widehat{W}}{\mathrm{L}_{d1}} & 0 & 0 \\ -\frac{\mathrm{L}_d\widehat{W}}{\mathrm{L}_{q1}} & -\frac{R_s}{\mathrm{L}_{q1}} & 0 & 0 \\ 0 & 0 & -\frac{R_s}{\mathrm{L}_{d2}} & 0 \\ 0 & 0 & 0 & -\frac{R_s}{\mathrm{L}_{q2}} \end{matrix}\right\} [\hat{\mathrm{C}}] = \left\{\begin{matrix} 0 \\ -\frac{\varphi_{\mathrm{m}}\widehat{\mathrm{W}}}{\mathrm{L}_{\mathrm{q}1}} \\ 0 \\ 0 \end{matrix}\right\} (15)$$

In this configuration, the outputs correspond to the measured stator currents and their estimated counterparts generated by the adaptive model. The purpose of the identification process is to minimize the discrepancy between these two sets of outputs, that is, to reduce the modeling error. Consequently, the error signal can be expressed as follows:

$$[\varepsilon] = \begin{cases} \varepsilon_d = I_{d1} - \widehat{I_{d1}} \\ \varepsilon_q = I_{q1} - \widehat{I_{q1}} \\ \varepsilon_x = I_{d2} - \widehat{I_{d2}} \\ \varepsilon_y = I_{q2} - \widehat{I_{q2}} \end{cases} \qquad (16)$$

Once the reference and adjustable models have been formulated, a PI adaptation mechanism is incorporated to perform the parameter adjustment within the MRAS framework. The adaptive law continuously updates the estimated rotor speed by driving the model error toward zero. To ensure stable convergence of the estimation process, the speed adaptation law is derived based on the Popov stability criterion. The resulting expression for the estimated speed can be written as follows:

$$\widehat{W} = \left(K_P + \frac{K_i}{\rho}\right)\left(\frac{L_{q1}}{L_{d1}}\varepsilon_{d1} I_{q1} - \frac{L_{d}1}{L_{q1}}\varepsilon_{q1} I_{d1} - \frac{\varphi_m}{L_{q}1}\varepsilon_{q1}\right) \qquad (17)$$

5. DISCUSSIONS OF SIMULINK RESULTS

In this section, MATLAB/Simulink simulations are carried out to evaluate the performance of the five-phase PMSM drive using the proposed backstepping control combined with the MRAS observer. The motor is operated with a reference speed of 150 rad/s, and a load torque of 0.4 N·m is applied at t=0.2 s to assess dynamic response. The simulation sampling period is set to 0.5 s. In addition, a fault scenario is introduced at t=0.3 s to examine the behavior of the drive under open-phase fault conditions while maintaining the same sampling period. This allows a direct comparison between load variation and faulty operating modes. The 5P-PMSM (Five-Phase Permanent Magnet Synchronous Motor) was subjected to two different tests: one under load variation operating mode and another with a fault in the open phase. Simulations results have been carried out in MATLAB Simulink power environment to check whether the suggested control strategy works.

5.1. Simulink Results of load variation operating conditions

In this initial test, the five-phase PMSM drive is evaluated under normal operating conditions with load variation using the proposed Backstepping controller together and the MRAS-based observer, without introducing parameter uncertainties or faults. The reference speed is maintained at 150 rad/s, while the load torque is varied from 0 N·m up to 4 N·m. As shown in Fig. 3(a), the estimated speed closely follows the actual rotor speed. The corresponding speed estimation error displayed in Fig. 3(b) remains very small, within the range of approximately 0.11 to 0.3 rad/s at steady state, which is considered acceptable and aligns well with results reported in [9] and [10]. Similarly, Fig. 3(c) illustrates that the estimated load torque accurately tracks the applied reference torque, indicating that the five-phase PMSM maintains stable and efficient performance under changing load conditions. These results confirm that the MRAS-based observer provides reliable speed and torque estimation during normal operation and under load variations when integrated with the Backstepping control strategy.

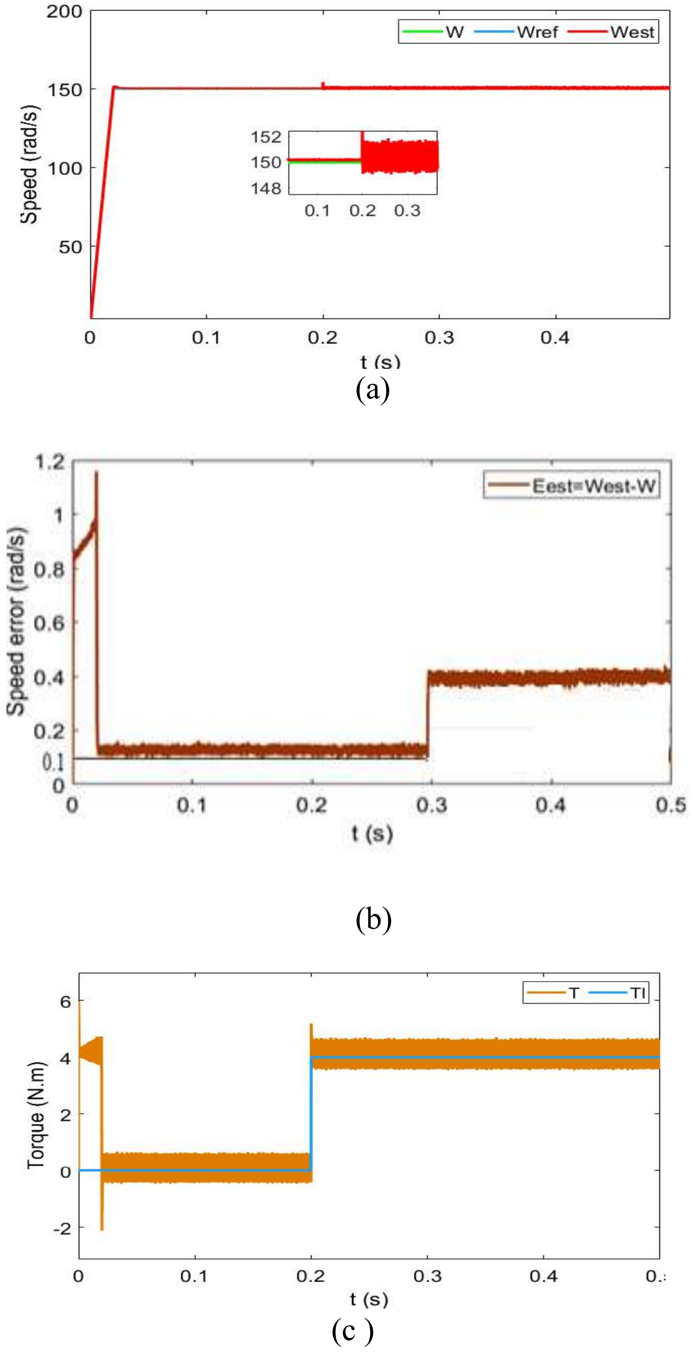

(a)

(b)

(c)

Fig 3. Result of Sensorless backstepping control of 5P-PMSM using MRAS under load torque variation in normal condition

5.2. Simulink results of 5P-PMSM fault open phase

In the second test, an open-phase fault is deliberately introduced in the five-phase PMSM to assess the fault-tolerant capability of the proposed control scheme. The operating conditions are kept identical to the normal-mode test: the reference speed is set to 150 rad/s and a load torque of 4 N·m is applied at t=0.2 s. The open-phase fault is triggered at t=0.3 s, as illustrated in Fig. 4(a).

The corresponding speed response in Fig. 4(b) demonstrates that the estimated speed continues to track the actual rotor speed, although small fluctuations appear due to the fault condition. The associated speed estimation error, shown in Fig. 4(c), remains limited within approximately 0.1 to 0.3 rad/s, which is considered acceptable. A similar oscillatory behavior is also observed in the electromagnetic torque response, as presented in Fig. 4(d).

When compared to the outcomes reported in [5] and [11], the obtained results indicate an improved level of fault tolerance for the five-phase PMSM. These results further confirm the effectiveness of the Backstepping control combined with the MRAS observer, even when external disturbances such as load variations or phase faults occur.

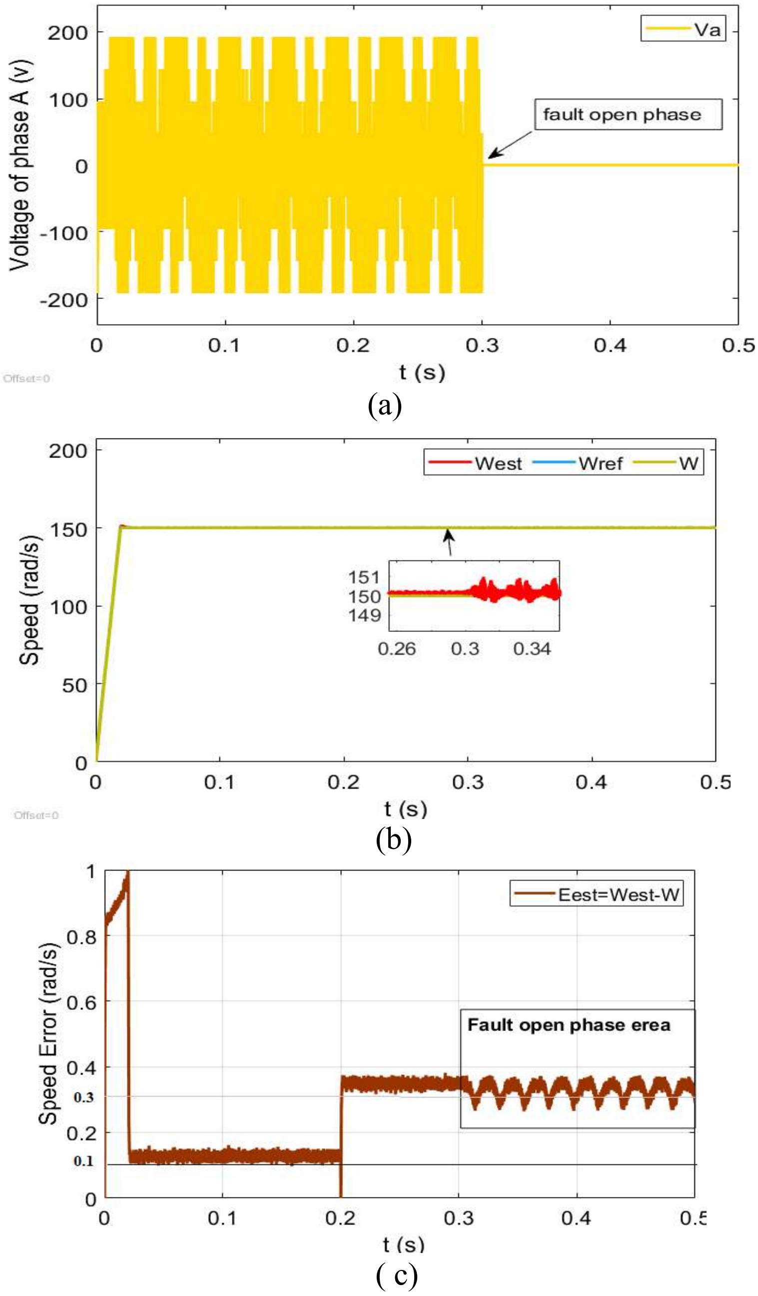

(a)

(b)

(c)

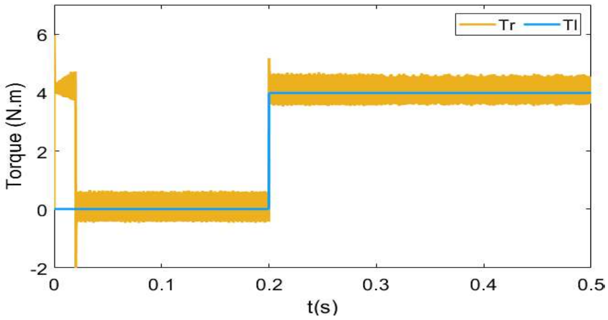

(d)

Fig 4. Result of Sensorless backstepping control of 5P-PMSM using MRAS under fault open phase operating mode

6. CONCLUSION

The study conducted on open-phase fault analysis in a Five-Phase Permanent Magnet Synchronous Motor (5P-PMSM) using a backstepping controller combined with a Model Reference Adaptive System (MRAS) observer confirms the effectiveness of this control strategy in preserving drive performance under fault conditions. Due to its multi-phase structure, the 5P-PMSM inherently provides higher efficiency and natural fault tolerance, allowing the motor to continue operating even when one or more phases become open-circuited. This characteristic significantly enhances operational reliability.The simulation results further show that the integration of the MRAS observer with the backstepping controller enables accurate estimation of motor states during the fault, allowing the controller to properly adjust the control signals and mitigate performance degradation. As a result, the motor maintains stable speed and torque responses with only minor deviations when the fault occurs. Overall, the combination of backstepping control and MRAS estimation forms a robust fault-tolerant control approach, improving the resilience and reliability of 5P-PMSM drives in industrial environments where continuous and safe operation is essential.

The parameters of tested 5P-PMSM are listed in flowing Table.

Table 1:parametres of 5P-PMSM drive

P	L_s	L_{ls}	R_s	φm	J
2	2.1 mH	0.13 mH	0.18 Ω	0.163 T	0.0011Kg.m2

References

[1] H. Eldeeb, A. Berzoy, and A. Emadi, “Fault-tolerant control of five-phase permanent-magnet motors: A review,” *IEEE Transactions on Transportation Electrification*, vol. 4, no. 1, pp. 86–102, Mar. 2018. J.

[2] J. Zhao, X. Gao, B. Li, X. Liu, and X. Guan, “Open-phase fault tolerance techniques of five-phase dual-rotor permanent magnet synchronous motor,” *Energies*, vol. 8, no. 11, pp. 12810–12838, Nov. 2015..

[3] I. S. Jacobs and C. P. Bean, “Fine particles, thin films and exchange anisotropy,” in Magnetism, vol. III, G. T. Rado and H. Suhl, Eds. New York: Academic, 1963, pp. 271–350.

[4] M. Jamma Mustapha et al., “Comparative study of PI and backstepping with integral action for three-phase PWM rectifier,” *International Journal of Electrical and Electronics Engineering (IJEEE)*, vol. 9, no. 2, 2017..

[5] R. Nicole, “Title of paper with only first word capitalized,” J. Name Stand. Abbrev., in press.

[6] Y. Yorozu, M. Hirano, K. Oka, and Y. Tagawa, “Electron spectroscopy studies on magneto-optical media and plastic substrate interface,” IEEE Transl. J. Magn. Japan, vol. 2, pp. 740–741, August 1987 [Digests 9th Annual Conf. Magnetics Japan, p. 301, 1982].

[7] M. Young, The Technical Writer’s Handbook. Mill Valley, CA: University Science, 1989.

[8] K. A. Hosseynia, R. Trabelsi, A. Iqbal, and M. F. Mimouni, “Backstepping control for a five-phase permanent magnet synchronous motor drive,” *International Journal* of *Power Electronics and Drive Systems (IJPEDS)*, vol. 6, no. 2, pp. 851–862, Jun. 2015.

[9] D. P. *Kingma and M. Welling, “Auto-encoding variational Bayes,” 2013, arXiv:1312.6114. [Online]. Available: https://arxiv.org/abs/1312.6114*

[10] S. Liu, “Wi-Fi Energy Detection Testbed (12MTC),” 2023, gitHub repository. [Online]. Available: https://github.com/liustone99/Wi-Fi-Energy-Detection-Testbed-12MTC

[11] “Treatment episode data set: discharges (TEDS-D): concatenated, 2006 to 2009.” U.S. Department of Health and Human Services, Substance Abuse and Mental Health Services Administration, Office of Applied Studies, August, 2013, DOI:10.3886/ICPSR30122.v2

Islamic University Journal of Applied Sciences (IUJAS)
https://journals.iu.edu.sa/jesc
Special Issue, February 2026, Pages 20-32
https://igee.univ-boumerdes.dz/ncaeee25/

Rapid Control Prototyping Platform for Real-Time Implementation of IM Speed Controllers

Mansour Bechar [1*], Mohamed Habbab [1], Younes Safi [1]

[1] Laboratory of CAOSEE, University of Tahri Mohammed
Bechar, Algeria, bechar.mensour@univ-bechar.dz

*Corresponding author: (Mansour Bechar), *Email Address*: bechar.mensour@univ-bechar.dz

Abstract

In this paper, a rapid control prototyping platform for Real-Time implementation of IM speed controllers is made. The sliding mode controller, the nonlinear PI controller and the classical PI controller are applied to control an induction motor. All controllers were successfully implemented in real-time using rapid control prototyping techniques based on the digital simulator OP5600 that simulate the vector control of induction motor technique with the real speed sensor. The model first developed under Matlab/Simulink on RT-LAB software then loaded on the target via network connections TCP/IP protocol. Each response is analyzed and explained by graphics considering the performance at different speeds and the response to compensate changes in load. Experimental results demonstrate the high precision and the robustness of the sliding mode controller compared with the vector controller PI and NPI mainly in case of speed sense reverse and load changes.

Keywords: Rapid Control Prototyping; Induction Motor; PI Controller; Nonlinear PI Controller; Sliding Mode Controller; Digital Simulator (OP5600).

---

https://doi.org/10.63070/jesc.2026.003
Received 30 November 2025; Revised 19 January 2026; Accepted 26 January 2026.

Published by Islamic University of Madinah on behalf of *Islamic University Journal of Applied Sciences*.

1. Introduction

Induction Motor (IM) drives are used in several industrial applications due to their advantages of simple construction, less maintenance and reliability. The main advantage is that IM does not require any mechanical commutator, because of this they are maintenance free motors. These machines are highly non-linear and it requires complex speed control techniques. Different methods of speed control are developed and it can be classified into scalar and vector control methods. Scalar current control may be adequate for a simple low-performance drive system, but for high performance drive system it is not preferred. Vector control method is a well-known control technique, which uses the principle of stator current control of IM to get desired speed control. The torque and flux are controlled separately in the vector controlled induction motor drives [1].

A lot of speed controllers for induction motor have been proposed in the last few years. In our case we focused on three main control strategies:

First one, proportional integral (PI) controller [2]. PI controller can be easily implemented for second order system using analytic approach. In fact3-phase induction motor system is accurately modelled as third order system without approximation [3, 4]. It is difficult to use the PI controller alone for third or higher order plant as the order of the plant is greater than the number of zeros provided by the PI controller [5, 6]. PI controller has the ability to control the speed of induction motor and also provide stability but, it does not come up with wide overshoot and large settling time.

Second one, a nonlinear PI (NPI) controller for speed sensorless control of the IM. While, the improvement of NPI controller is achieved by the use of nonlinear gains [7], the combination of nonlinear terms can provide additional degrees of freedom to achieve a much improved system performance. The NPI controller can adjusts its gains in real time according to the speed error and it is able to reject the effect of time-varying and nonlinear behaviors in the process [8].

Third one, the sliding mode is an effective control strategy for nonlinear systems with uncertainties [9]. Its principle is based on the definition of a surface called sliding surface depending on system states so that it is attractive. The synthesized global control consists of two terms: the first allows the state trajectory to approach this surface and the second maintaining and sliding along it towards the origin of the phase plane [10]. It is characterized by good robustness, fast response time and disturbance ejection. However, the one of the drawback of this controller is the chattering phenomenon caused from the discontinue control action.

In our paper, we present a comparative study between the cited controllers using a rapid control prototyping techniques (RCP). The sliding mode and the PI and nonlinear PI controllers are proposed.

This paper begins with the introduction of the speed control of an induction motor drive system with different types of control strategies. The following section explains the operation of the proposed field-oriented control techniques. The proposed techniques are implemented using (OP5600) RTDS, and the analysis of experimental results is discussed in section VI. The conclusion of this project is discussed in the last section.

2. Model of Induction Machine

The dynamic model of induction motor in two-phase stationary frame with assuming that the stator current and the flux as state variables. It is described as follows [11-12]:

$$
\left\{
\begin{array}{l}
\dfrac{di_{s\alpha}}{dt} = -\dfrac{1}{\sigma.L_s}\left(R_s + \left(\dfrac{M_{sr}}{L_r}\right)^2 .R_r\right).i_{s\alpha} + \dfrac{M_{sr}.R_r}{\sigma.L_s L_r^2}\varphi_{r\alpha} \\
+\dfrac{M_{sr}}{\sigma.L_s L_r} w_r.\varphi_{r\beta} + \dfrac{1}{\sigma L_s} V_{s\alpha} \\
\dfrac{di_{s\beta}}{dt} = -\dfrac{1}{\sigma.L_s}\left(R_s + \left(\dfrac{M_{sr}}{L_r}\right)^2 .R_r\right) i_{s\beta} - \dfrac{M_{sr}}{\sigma.L_s L_r} w_r.\varphi_{r\alpha} \\
+\dfrac{M_{sr}.R_r}{\sigma.L_s L_r^2}\varphi_{r\beta} + \dfrac{1}{\sigma.L_s} V_{s\beta} \\
\dfrac{d\varphi_{r\alpha}}{dt} = \dfrac{M_{sr}.R_r}{L_r} i_{s\alpha} - \dfrac{R_r}{L_r}\varphi_{r\alpha} - w_r.\varphi_{r\beta} \\
\dfrac{d\varphi_{r\beta}}{dt} = \dfrac{M_{sr}.R_r}{L_r} i_{s\beta} + w_r.\varphi_{r\alpha} - \dfrac{R_r}{L_r}\varphi_{r\beta}
\end{array}
\right. \tag{1}
$$

Where

$i_{s\alpha}$, $i_{s\beta}$ are stator current vector components in [α, β] stator coordinate system.

$V_{s\alpha}$, $V_{s\beta}$ are stator voltage vector components in [α, β] stator coordinate system.

$\varphi_{r\alpha}$, $\varphi_{r\beta}$ are rotor magnetic flux in [α, β] stator coordinate system.

M_{sr} Magnetizing inductance; Lr Rotor inductance; Ls Stator inductance; Rr Rotor resistance; Rs Stator resistance; wr Rotor angular speed; σ leakage coefficient $\sigma = 1 - \frac{M_{sr}^2}{Lr.Ls}$; P poles number; $Tr = \frac{Lr}{Rr}$ the rotor time constant $\sigma = 1 - \frac{M_{sr}^2}{Lr.Ls}$.

The electromagnetic torque can be expressed by:

$$T_e = \frac{3.\mathrm{P}.\mathrm{M}_{\mathrm{sr}}}{2.\mathrm{L}_{\mathrm{r}}}.(\varphi_{r\alpha}.i_{s\beta} - \varphi_{r\beta}.i_{s\alpha})$$

3. Field Oriented Control of IM

The FOC has been developed to allow varying IM speed over a wide range. It separates the stator currents of IM into flux and torque components in the (d, q) coordinate reference frame. The model equation (1) is a heavily coupled, multivariable and nonlinear system. These properties complicate the control design of the IM. The rotor flux-oriented coordinate is applied in order to simplify the model of the IM, where the rotor flux is aligned to the direct axis (d) and the electromagnetic torque is aligned to the quadratic axis (q). In this coordinate system the rotor flux is assumed as [13]:

$$\begin{cases} \varphi_{rd} = \varphi_r \\ \varphi_{rq} = 0 \end{cases} \tag{2}$$

The electromagnetic torque expression becomes:

$$T_e = n_p \frac{M_{sr}}{L_r} \varphi_{rd} i_{qs} = K_t.\varphi_{rd}.i_{qs} \tag{3}$$

Where:

$$k_t = n_p \frac{M_{sr}}{L_r}$$

The new model motor dynamics is described by the following space vector differential equations:

$$\begin{cases} \frac{\mathrm{d}i_{ds}}{\mathrm{dt}} = \frac{V_{ds}}{\sigma L_{sc}} - \eta_1 i_{ds} + n_p \omega i_{qs} - \left(\eta_2 i_{ds} + \alpha_1 \beta_1 \varphi_{rd} + \alpha_1 M_{sr} \frac{{i_{qs}}^2}{\varphi_{rd}} \right) \\ \frac{\mathrm{d}i_{qs}}{\mathrm{dt}} = \frac{V_{qs}}{\sigma L_{sc}} - \eta_1 i_{qs} - n_p \omega i_{ds} - \beta_1 n_p \omega \varphi_{rd} - R_r \left(\eta_2 i_{qs} + \alpha_1 M_{sr} \frac{i_{qs} i_{ds}}{\varphi_{rd}} \right) \\ \frac{\mathrm{d}\omega}{\mathrm{dt}} = \mu \varphi_{rd} i_{qs} - \frac{T_l}{J} \\ \frac{\mathrm{d}\varphi_{rd}}{\mathrm{dt}} = \alpha_1 M_{sr} R_r i_{ds} - \alpha_1 R_r \varphi_{rd} \end{cases} \tag{4}$$

as:

$$\mu = \frac{2n_p M_{sr}}{2JL_r};\eta_1 = \frac{R_s}{\sigma L_r};\eta_2 = \frac{M_{sr}^{\ 2}}{\sigma L_s L_r^{\ 2}};\alpha_1 = \frac{1}{L_r};\beta_1 = \frac{M_{sr}}{\sigma L_s L_r}$$

Fig. 1, is shown the block diagram of field oriented control of IM with PI speed controller.

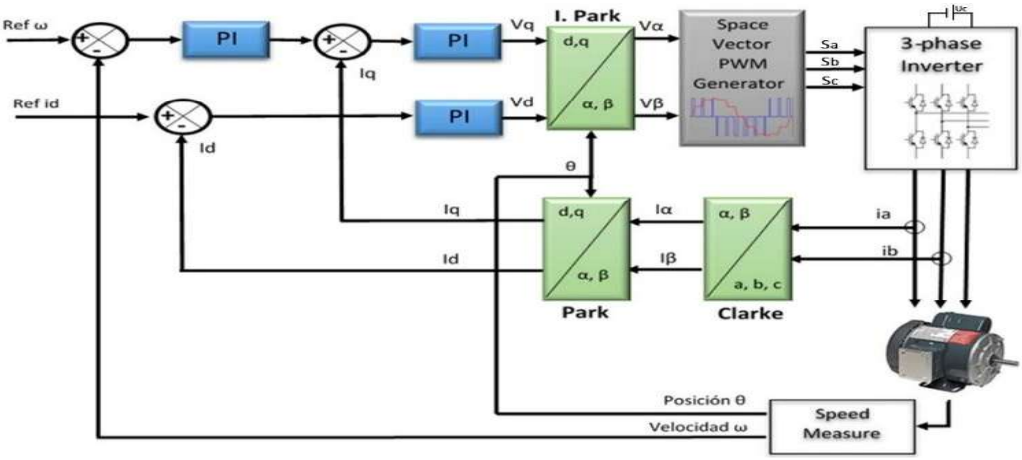

Figure 1. IM field oriented control.

4. Controller Synthesis

In this section, three types of controllers are examined and presented to regulate the speed of the IM.

4.1 Proportional integral (PI) controller

The conventional Proportional plus Integral controller (PI) is a simple speed controller in industrial applications. Under the load condition, the PI controllers try to modify the motor speed to attain the desired system speed. The output of the PI controller is a function of the speed error and the integral of error [14]:

$$u(t) = K_p\, e(t) + K_i \int e(t)\, d(t) \qquad (5)$$

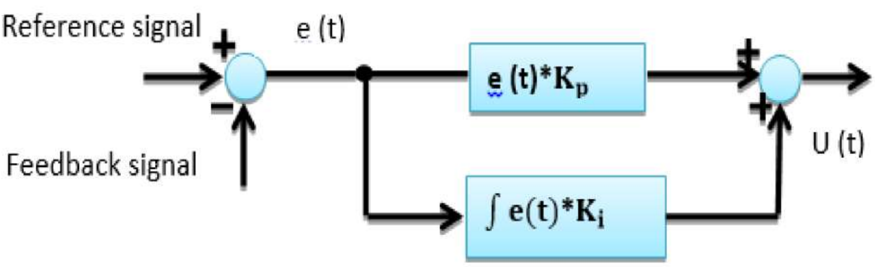

Figure 2. The block diagram of the used PI speed controller.

4.2 Non Linear (PI) Controller

In order to improve the control quality, a nonlinear PI (NPI) induction motor speed controller can be constructed as shown in Fig. 3, The combination of a nonlinear terms can provide additional degrees of freedom to achieve a much improved system performance. The nonlinear PI controller action is given by [15].

$$T_e^* = K_p.fal\left(e,\alpha_p,\delta_p\right) + K_i.fal\left(\int e,\alpha_i,\delta_i\right) \qquad (6)$$

$$fal\left(x,\alpha,\delta\right) = \begin{cases} |x|^{\alpha}\ sign(x) & |x| > \delta, \delta > 0 \\ \dfrac{x}{\delta^{1-\alpha}} & |x| \le \delta \end{cases} \qquad (7)$$

Where

$fal\left(x,\alpha,\delta\right)$ is nonlinear function represented in Fig. 4,

x is a variable which can be e or $\int e\,.\,dt$,

e is the error between the speed reference and real speed of the induction motor $e = \omega_r^* - \omega_r$.

K_p and K_i are respectively proportional and integral gains of the PI controller.

T_e^* is the referential torque (the control signal), the parameters α_p and α_i are constant, empirically chosen in the range 0 to 1. When $\alpha_p = \alpha_i = 1$, the controller becomes a linear PI controller, δ is a constant, which can be set empirically to a small value.

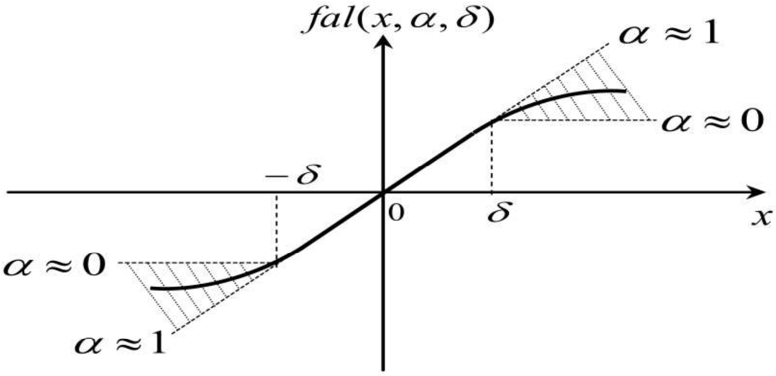

Figure 3. Function characteristics.

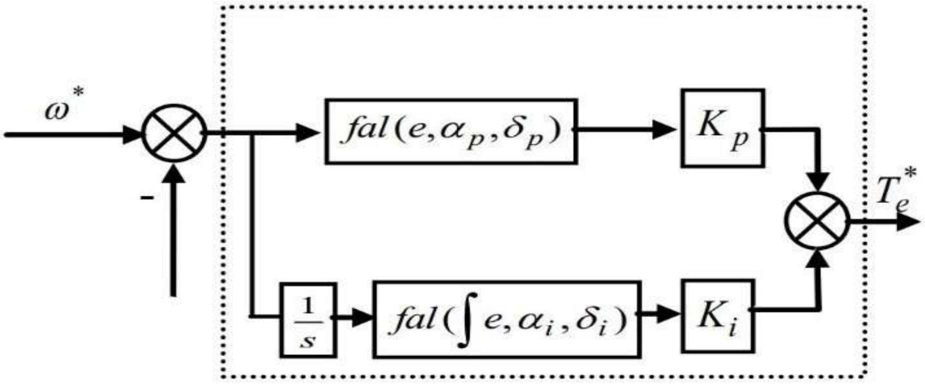

Figure. 4. Nonlinear PI controller.

4.3 Sliding Mode Controller Design

Based on complete indirect field orientation, sliding mode control with integral sliding surface is discussed in this section. Under the complete field oriented control, the mechanical equation can be equivalently described as:

$$J\frac{d\omega}{dt}+B\omega+T_l=T_e \tag{8}$$

The electromechanical equation can be modified as

$$\dot{\omega}+a\omega+d=bT_e \tag{9}$$

Where $a=\frac{B}{J}, b=\frac{1}{J}$ and $d=\frac{T_l}{J}$

By considering (9) with uncertainties as

$$\dot{\omega}=-(a+\Delta a)\omega-(d+\Delta d)+(b+\Delta b)\,T_e \tag{10}$$

$\Delta a, \Delta b$ and Δd represents the uncertainties of the terms a, b and d introduced by system parameters J and B. Now let us define the tracking speed error further as

$$e(t)=\omega(t)-\omega^*(t) \tag{11}$$

Where ω^* is the rotor reference speed command in angularfrequency.

Taking derivative of (11) with respect to time yields

$$\dot{e}(t)=\dot{\omega}(t)-\dot{\omega}^*(t)=-ae(t)+f(t)+x(t) \tag{12}$$

Where the following terms have been collected in the signal $f(t)$,

$$f(t)=bT_e\,(t)-a\omega^*\;-d(t)-\dot{\omega}(t) \tag{13}$$

And the $x(t)$, lumped uncertainty, defined as

$$x(t) = -\Delta a\,\omega(t) - \Delta d(t) + \Delta b T_e(t) \qquad (14)$$

Now, the sliding variable with integral component, is defined as

$$S(t) = e(t) - \int_0^t (h-a)e(\tau)d\tau \qquad (15)$$

where h is a constant gain. Also in order to obtain the speed trajectory tracking, the following assumptions are made [16].

Assumtion-1: The h must be chosen so that the term $(h-a)$ is strictly negative and hence $h<0$.

Then the sliding surface is defined as follows:

$$S(t) = e(t) - \int_0^t (h-a)e(\tau)d\tau = 0 \qquad (16)$$

Based on the developed switching surface, a switching control that guarantees the existence of sliding mode, a speed controller is defined as

$$f(t) = h\,e(t) - \beta sgn(S(t)) \qquad (17)$$

where β is the switching gain, $S(t)$ is the sliding variable

defined by (15) and $sgn(.)$ is the sign function defined as

$$sgn(S(t)) = \begin{cases} +1, & if\ S(t) > 0 \\ -1, & if\ S(t) < 0 \end{cases} \qquad (18)$$

Assumtion-2: The β must be chosen so that

$\beta \geq |x(t)|$ for all time. When the sliding mode occurs on the sliding surface (16), then, $S(t) = \dot{S}(t) = 0$ and the tracking error $e(t)$ converges to zero exponentially. Finally, the reference torque command T_e^* can be obtained by substituting (17) in (13) as follows.

$$T_e^*(t) = \frac{1}{b}\left[(h.e) - \beta sgn(S) + a\omega^* + \dot{\omega}^* + d\right] \qquad (19)$$

5. Experimental Results

Rapid control prototyping platform for validation of the proposed study between different controllers is shown in Fig. 5, this platform was built using RT-LAB as a real-time platform, and it contains OP-5600 OPAL-RT real-time simulator used as a core of the hardware prototype system. Currently, CAOSEE laboratory at Bechar university is equipped with one OP5600 OPAL-RT simulator and one drivelab OPAL-RT board [17]. The vector control algorithm is created in Matlab/Simulink software on the RT-LAB host computer with two subsystems SM and SC, the SM subsystem is converted into ‘C’ source code using Mathworks code generator Real-Time-Workshop (RTW) and compiled using RT-LAB. This code is then uploaded into the OP5600 target via network connections TCP/IP protocol.

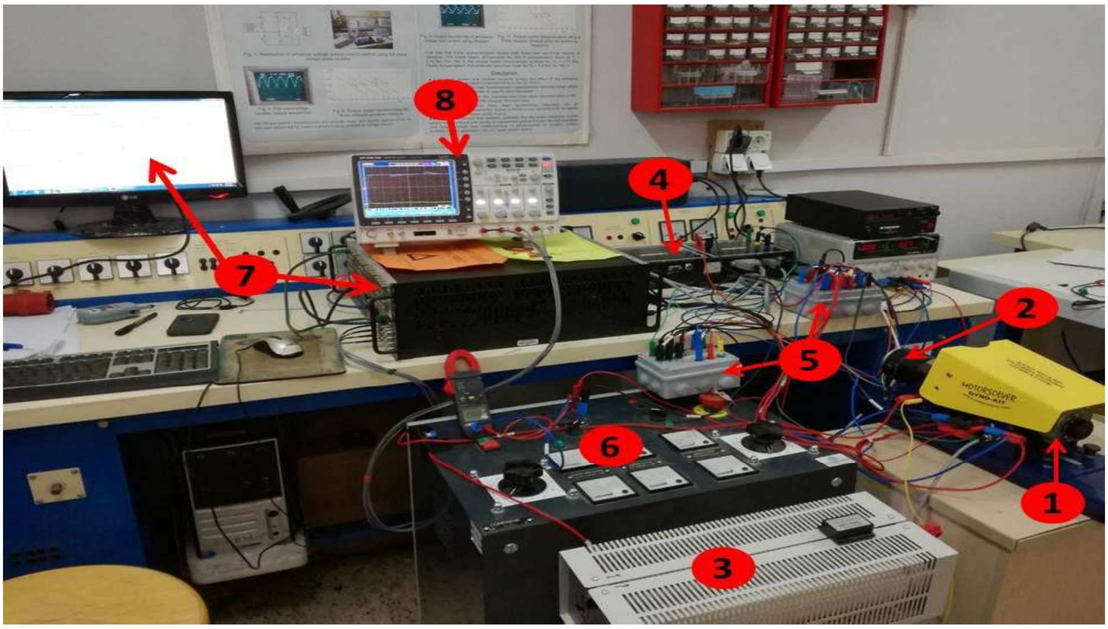

Figure 5. Rapid control prototyping system: real view of bench.

The test bench of RCP is shown in Fig. 5, that is composed of:

(1) Squirrel cage induction motor with the following characteristics: Δconnected, four poles, 125 W, 4000 rpm, 30 V, 133 Hz with the 1024 points integrated incremental coder,
(2) DC generator motor,
(3) Resistive load,
(4) Inverter Drivelab Board,
(5) Hall type current sensors, voltage sensors,
(6) Auto transformer (0-450 V),
(7) OP5600 real-time digital simulator with Host computer equipped by RT-LAB software,
(8) Numerical oscilloscope.

The different waveforms below show the experimental validation of field-oriented control in different operation modes such as transient and steady state, load application, reverse speed test, for the PI, NPI, and SMC controllers.

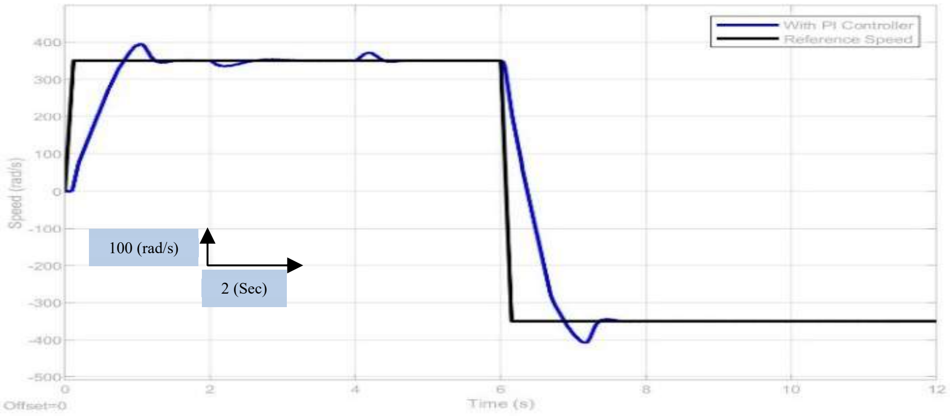

Figure 6. Rotor speed with PI controller.

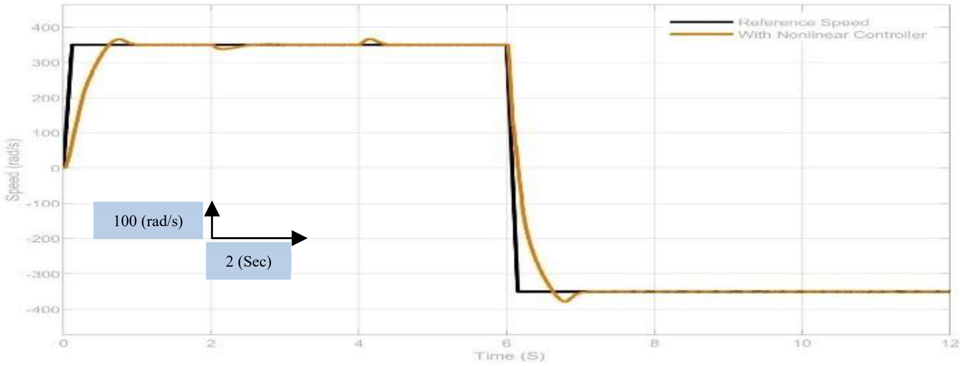

Figure 7. Rotor speed with nonlinear PI controller.

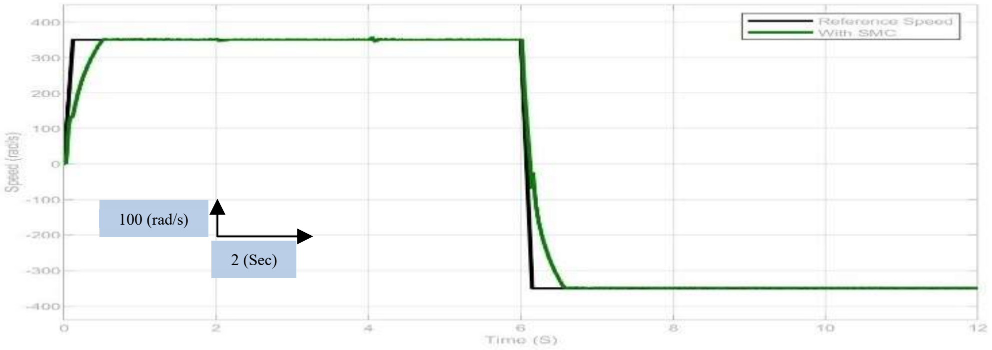

Figure 8. Rotor speed with SMC.

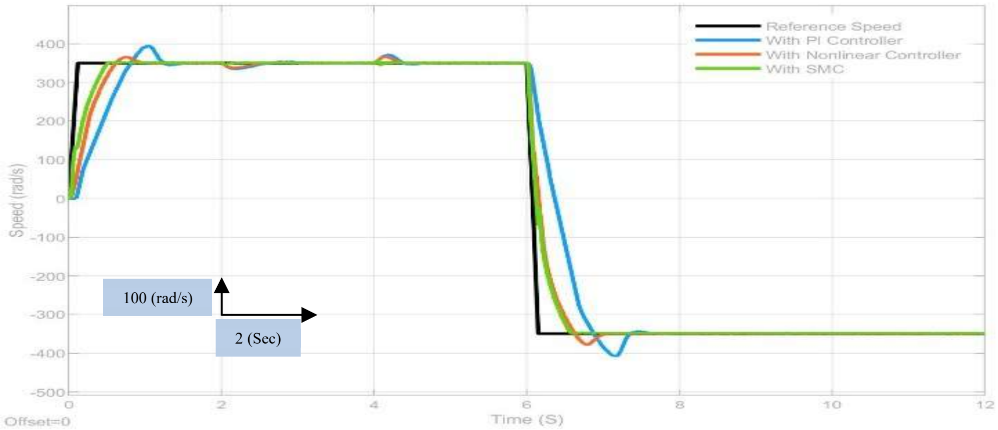

Figure 9. Rotor speeds with different controllers.

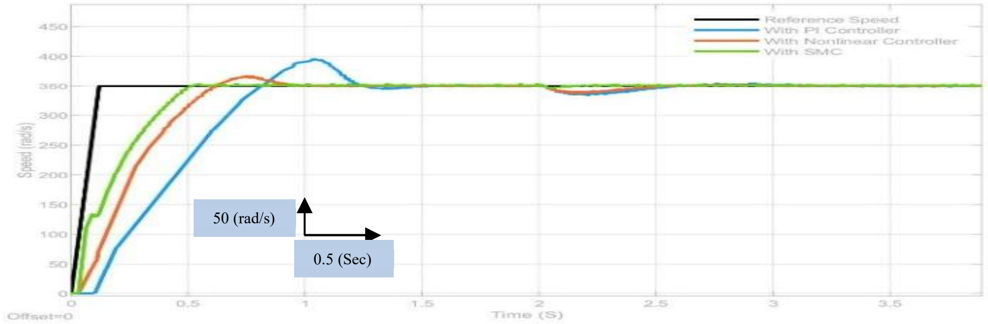

Figure 10. Zoom of rotor speeds.

First, the motor is started under no load with a nominal speed of 350rad/sec, and after 2 sec, a rated load is applied, in 4 sec the motor is unloaded again, at t=6 sec the speed sense reverses (350rad/sec, -350rad/sec).

Fig. 6 shows the behavior of an induction motor at nominal speed with a disturbance load application. The reference speed is set to 350rad/sec. It is clear that the PI controller exhibits good performances at steady state, but in the dynamic regime, when the motor starts up, the PI controller exceeds the saturation value and generates inadequate performances for the system as a large overshoot and a long settling time, as shown in Fig. 6.

In Fig.7, the nonlinear PI controller rejects the load disturbance very rapidly compared with the PI controller, Fig.7, rotor speed sense reversing (350rad/sec, -350rad/sec) the nonlinear PI provides perfect superposition and better tracking than PI by reducing the overshoot and settling time.

Fig. 8, shows the speed response of the SMC. The speed response of SMC has a small overshot, and it is clear that the load change does not extend the proposed control performance. The system maintains robustness against the effects of the load change.

Based on comparative results obtained in Fig.9, it can be seen that the SMC can provide robust performance. It has been shown that the proposed control scheme performs reasonably well in practice, and that the speed tracking objective is achieved under speed step variations and load disturbances. The result for Fig.10, shows the zoomed performance of the rotor speed.

6. Conclusion

This work presents a comparative study between different controllers using a rapid control prototyping technique: the proportional integral (PI) controller, nonlinear PI controller and sliding mode controller. Controller tests were performed in order to make a comparison in Induction Machine speed performances.

Two different control strategies have been implemented. To obtain better performances than the PI classical speed controller, according to our real-time implementation, the sliding mode controller rejects perfectly the disturbances and the nonlinear PI controller is characterized by a small response time. Through the experimental results, the sliding mode and the nonlinear PI controllers present the high performances in speed tracking and disturbance rejection.

References

[1] R. Krishnan, “ELECTRIC MOTOR DRIVES Modelling, Analysis and control”, 1st Edition, Prentice-Hall, 2001.
[2] S. Jung, and R.C. Dorf, “Novel analytic technique for PID and PIDA controller design”, in Proc. 13th IFAC World Congress, San Francisco, USA, 1996.
[3] R.C. Dorf and R.H. Bishop, “Modern Control System”, 7th edition, Addison Wesley, 1995.
[4] K. Ogata, “Modern Control Engineering”, 2nd edition, Prentice Hall, 1990.
[5] S. Jung and R.C. Dorf, “Analytic PIDA Controller Design Technique for a Third Order System”, Proceedings of the 35th IEEE Conference on Decision and Control, Kobe, pp. 2513-2518, 11-13 December 1996.
[6] R .C. Dorf and D. R. Miller, “A method for enhanced PID controller design”, Journal of Robotics and Automation, vol.6, pp, 41 47, 1991.
[7] Cruz, M. A. Gallegos, R. Alvarez, and F. Pazos, “Comparison of several nonlinear controllers for induction motors”, IEEE Int'l. Power Electronics Congress (CIEP), 2004, pp. 134 –139.
[8] Y.X. Su, Dong Sun, B.Y. Duan, “Design of an Enhanced Nonlinear PID Controller”, Mechatronics 15 (2005) pp. 1005–1024.
[9] Zhifeng Zhang, Jianguang Zhu, Renyuan Tang, BaodongBai, and Hongyang Zhang, “Second order sliding mode control of flux and torque for induction motor”, Power and Energy Engineering Conference (APPEEC), 2010 Asia-Pacific. IEEE, pp. 1-4, 2010.
[10] M. Moutchou, A. Abbou, and H. Mahmoudi, “Induction machine speed and flux control using vector-sliding mode control with rotor resistance adaptation”, International Review of Automatic Control, (Theory and Application) (IREACO), Vol. 5 (n. 6), 2012.

[11] G. Tarchala, T. Orlowska-Kowalska, “Sliding mode speed observer for the induction motor drive with different sign function approximation forms and gain adaptation”, Przeglad. Elektrotechniczny., vol.89, 2013, 1-6.

[12] I. Bendaas, F. Naceri, “A new method to minimize the chattering phenomenon in sliding mode control based on intelligent control for induction motor drives”, Serb. J. Electr. Eng., vol. 10, June. 2013, 231-246.

[13] T. Ameid, A. Menacer, H. Talhaoui, and I. Harzelli, “Broken rotor bar fault diagnosis using fast Fourier transform applied to field-oriented control induction machine: simulation and experimental study”, Int. J. Adv. Manuf. Technol., 2017.

[14] Menghal, P. M., Laxmi, A. J., & Anusha, D. (2014), “Speed control of induction motor using fuzzy logic controller”, i-Manager's Journal on Electrical Engineering, 8(2), 21.

[15] F. Mokhtari, P. Sicard and A. Hazzab, “Cascade Decentralized Nonlinear PI Control Continuous Production Process”, ELECTRIMACS, Québec, Canada, Jun. 2008, CD-ROM.

[16] O. Barambones, P. Alkorta, A. J. Garrido et al. , “An Adaptive Sliding Mode Control Scheme for Induction Motor Drives”, International Journal of Circuit, System and Signal Processing, vol. 1, no. 1, pp. 73-78, 2007.

[17] M. Bechar, A. Hazzab, M. Habbab, “Real-Time Scalar Control of Induction Motor using RT-Lab Software”, The 5th International Conference on Electrical Engineering (ICEE-B), October. 2017.

Islamic University Journal of Applied Sciences (IUJAS)
https://journals.iu.edu.sa/jesc
Special Issue, February 2026, Pages 33-45
https://igee.univ-boumerdes.dz/ncaeee25/

Kernel Vertices PCA: A Novel Interval-Valued PCA Approach for Fault Detection in Nonlinear Complex Systems

Abdelhalim Louifi [1,*], Abdesamia Azizi [2], Abdelmalek Kouadri [2], Abderazak Bensmail [2], Mohamed Faouzi Harkat [3]

[1] National polytechnic school Oran, Algeria,
[2] *Institute of Electrical and Electronics Engineering, M'Hamed Bougara University, Boumerdes, Algeria.*
[3] *Electronics Department, Faculty of Engineering, Badji Mokhtar University of Annaba,* 23000 Annaba, Algeria.

*Corresponding author: (Abdelhalim Louifi), *Email Address*: ab.louifi!@gmail.com

Abstract

Interval-valued data techniques are widely utilized in fault detection to enhance robustness against uncertainty. Among these, Vertices Principal Component Analysis (VPCA) is one of the most commonly applied methods. Constructing a VPCA model involves transforming the interval data matrix into a vertices matrix. This study introduces a novel data-driven approach for fault detection in uncertain nonlinear processes called Kernel VPCA (K-VPCA), which extends the VPCA method to handle nonlinear interval data. Specifically, the data are mapped into a high-dimensional kernel feature space before applying VPCA, allowing nonlinear relationships to be effectively modeled. The K-VPCA approach maintains robustness against false alarms without compromising fault detection performance. The proposed method is validated using data from a cement rotary kiln, confirming its effectiveness in fault detection.

Keywords: Fault Detection, Interval-Valued data, KPCA, Vertices Principal Component Analysis, Cement rotary kiln.

---

https://doi.org/10.63070/jesc.2026.004
Received 20 November 2025; Revised 15 January 2026; Accepted 24 January 2026.

Published by Islamic University of Madinah on behalf of *Islamic University Journal of Applied Sciences*.

1. Introduction

Principal Component Analysis (PCA) is a widely utilized data-driven method for monitoring and diagnosing complex systems [1]–[3]. Despite its success, PCA's performance in monitoring industrial systems with nonlinear dynamics is often limited due to its inherently linear nature, which prevents it from effectively modeling the nonlinear relationships present in such data [4], [5]. To overcome these limitations, various nonlinear extensions of PCA have been developed, with Kernel Principal Component Analysis (KPCA) being one of the most prominent approaches [6]. Originally introduced by Scholkopf ̈ [7], KPCA uses a nonlinear transformation to map the data into a higher-dimensional feature space, where linear PCA is then applied. This allows KPCA to capture the nonlinear characteristics of real-world processes, making it a robust tool for fault detection and diagnosis (FDD) [8]. As a result, KPCA has gained considerable attention for its ability to monitor and analyze nonlinear systems with higher precision [9]. However, a key limitation of KPCA lies in its assumption that sensor data is accurate and free from uncertainty, an assumption often violated in real-world applications where data is influenced by noise and approximations [10]. To overcome the challenges posed by uncertainty and nonlinearity in fault detection, researchers have developed algorithms tailored for interval-valued data [8], [11]. Examples of such methods include PCA vertices (VPCA), center PCA (CPCA), midpoint-radii PCA (MRPCA), and complete information PCA (CIPCA) [12]. Although these approaches show promise, their effectiveness is largely constrained to linear systems, limiting their applicability to nonlinear processes [13]. To address this limitation, recent research has focused on combining interval analysis with techniques capable of handling nonlinear systems [11]. This study introduces a new method, kernel vertices Principal Component Analysis (K-VPCA), which extends the VPCA framework by incorporating a nonlinear mapping that transforms the data into a higher-dimensional feature space. Within this space, interval-valued VPCA is applied, enabling K-VPCA to handle data uncertainties while effectively modeling nonlinear relationships. As a result, K-VPCA provides a robust and reliable solution for fault detection in complex, uncertain, and nonlinear processes. The effectiveness of the K-VPCA technique is validated using data from a rotary cement kiln, a complex industrial system characterized by significant non-linear behavior [14]. The results demonstrate that K-VPCA excels in minimizing false detections while maintaining high accuracy, without compromising detection speed or sensitivity to deviations. This establishes K-VPCA as a robust and dependable tool for fault detection in nonlinear systems, offering significant improvements over traditional PCA and other interval-based methods.

Additionally, the proposed method enhances fault detection reliability and provides a more comprehensive and precise diagnosis, contributing to improved process monitoring and control.

The structure of the paper is organized as follows: Section 2 outlines the theoretical foundations of the VPCA method as an interval-valued approach for process monitoring. Section 3 introduces the proposed K-VPCA method. In Section 4, the interval-based control chart for Hotelling's T^2, the squared predictive error Q, and the combined index Φ statistics is presented. Section 5 describes the cement plant setup, the application of the proposed method, and the resulting findings. Finally, Section 6 concludes with key remarks and future directions.

2. VERTICES PRINCIPAL COMPONENT ANALYSIS (VPCA)

VPCA is a two-step analysis that begins with numerical coding of a box's vertices and ends with a standard PCA on the coded data [13], [15]. Each observation in *Rm* can be represented as a hyperrectangle with 2*m* vertices and the total number of vertices is $n \times 2m$. Therefore, from the interval data:

$$[X] = \begin{pmatrix} \begin{bmatrix} \underline{x_1(1)} & \cdots & \underline{x_m(1)} \\ \vdots & \ddots & \vdots \\ \overline{x_1(1)} & \cdots & \overline{x_m(1)} \end{bmatrix} \\ \vdots \\ \begin{bmatrix} \underline{x_1(n)} & \cdots & \underline{x_m(n)} \\ \vdots & \ddots & \vdots \\ \overline{x_1(n)} & \cdots & \overline{x_m(n)} \end{bmatrix} \end{pmatrix} \tag{1}$$

VPCA does not directly summarize the interval-valued data matrix *X*, it is replaced by a single-valued data matrix obtained as follows. Each interval-valued row is transformed into the numerical matrix X_i as follows:

$$[X] = \left(\begin{bmatrix} \underline{x_1}(k) & \underline{x_2}(k) & \underline{x_3}(k) & \cdots & \underline{x_{m-1}}(k) & \underline{x_m}(k) \\ \overline{x_1}(k) & \underline{x_2}(k) & \underline{x_3}(k) & \cdots & \underline{x_{m-1}}(k) & \underline{x_m}(k) \\ \underline{x_1}(k) & \overline{x_2}(k) & \underline{x_3}(k) & \cdots & \underline{x_{m-1}}(k) & \underline{x_m}(k) \\ \overline{x_1}(k) & \overline{x_2}(k) & \underline{x_3}(k) & \cdots & \underline{x_{m-1}}(k) & \underline{x_m}(k) \\ \vdots & \vdots & \vdots & \cdots & \vdots & \vdots \\ \overline{x_1}(k) & \overline{x_2}(k) & \overline{x_3}(k) & \cdots & \overline{x_{m-1}}(k) & \overline{x_m}(k) \end{bmatrix}\right) \tag{2}$$

By stacking below, each other all the matrices *Xi's*, *i* = 1, ..., *n*, we get the new data matrix X_{VPCA} with $nx2^m$ rows and *m* columns:

$$X_{VPCA} = \begin{pmatrix} X_1 \\ X_2 \\ \vdots \\ X_m \end{pmatrix} \tag{3}$$

VPCA entails performing PCA on 3. As with standard PCA, it is best to pre-process the data to avoid unwanted differences between variables. The matrix in 3 can be pre-processed in the same way that the standard single-valued case is. The application of PCA to the matrix X_{VPCA} will give $\hat{X}_{VPCA}= T_{VPCA}\ P^T$, and if *B* is chosen to be column-wise orthonormal, we have $X_{VPCA} = T_{VPCA}\ P^T$. To facilitate the interpretation of the solution, for each observation unit, for each component, the segment containing all component scores for vertices associated with this observation unit. Specifically, with respect to the k^{th} component, *k* = 1, ..., *p*, if n_i denotes the set of all the vertices for the i^{th} observation unit, *i* = 1, ..., *n*. The dimension of matrix X_{VPCA} is huge which will make the PCA of a such matrix practically impossible. This computational problem can be overcome by considering a special property of PCA. Specifically, it is well known that the columns of the component loadings matrix are the eigenvectors obtained from the eigen-decomposition of the cross-products matrix. Note that the eigenvectors are arranged in such a way that the first ones are associated with the highest eigenvalues [16]. Dealing with the cross products matrix $\Sigma_V= X_{VPCA}^T X_{VPCA}$, after simplification the covariance matrix Σ_V can be written as in equ. 4.

$$\Sigma_V= 2^{m-2}\begin{pmatrix} 2\sum_{k=1}^{n}\left(\overline{x}_1^2(k) + \underline{x}_1^2(k)\right) & \sum_{k=1}^{n}((\overline{x}_1(k) + \underline{x}_1(k))(\overline{x}_2(k) + \underline{x}_2(k))) & \cdots & \sum_{k=1}^{n}((\overline{x}_1(k) + \underline{x}_1(k))(\overline{x}_m(k) + \underline{x}_m(k))) \\ \sum_{k=1}^{n}((\overline{x}_2(k) + \underline{x}_2(k))(\overline{x}_1(k) + \underline{x}_1(k))) & 2\sum_{k=1}^{n}\left(\overline{x}_2^2(k) + \underline{x}_2^2(k)\right) & \cdots & \sum_{k=1}^{n}((\overline{x}_2(k) + \underline{x}_2(k))(\overline{x}_m(k) + \underline{x}_m(k))) \\ \vdots & \vdots & \ddots & \vdots \\ \sum_{k=1}^{n}((\overline{x}_m(k) + \underline{x}_m(k))(\overline{x}_1(k) + \underline{x}_1(k))) & \sum_{k=1}^{n}((\overline{x}_m(k) + \underline{x}_m(k))(\overline{x}_2(k) + \underline{x}_2(k))) & \cdots & 2\sum_{k=1}^{n}\left(\overline{x}_m^2(k) + \underline{x}_m^2(k)\right) \end{pmatrix} \tag{4}$$

Then, the components can be extracted by performing the eigen-decomposition on Σ_V , indeed the obtained loading matrix *P* is column-wise orthonormal. However, this would require that we nevertheless use the huge matrix X_{VPCA}, we use a shortcut to define what we may call the positive and negative component loadings matrices, respectively, $P^+$and P^- with generic elements

$$p_{jk}^{+} = \begin{cases} p_{jk}, & if\ \ p_{jk} \geq 0 \\ 0, & otherwise \end{cases} \tag{5}$$

$$p_{jk}^{-} = \begin{cases} p_{jk}, \ if \ p_{jk} \leq 0 \\ 0, \ otherwise \end{cases} \qquad (6).$$

Where p_{jk} gives the loading of variable j on component k. In matrix notation, the bounds of the component scores matrix are given by:

$$\begin{cases} \underline{t}(k) = \overline{X}(k)P^{-} + \underline{X}(k)P^{+} \\ \overline{t}(k) = \overline{X}(k)P^{+} + \underline{X}(k)P^{-} \end{cases} \qquad (7)$$

Thus, it can be seen that score matrices were computed without explicitly having to compute all the component scores for all the vertices. It follows that this computational approach to VPCA finds the same component loadings and the same segments for the observation units, as the original computational approach to VPCA. We only lose the component scores of all individual vertices, but not of the segments that enclose them. Estimates of interval measurements are also computed as mentioned before

$$\hat{X}_{VPCA} = T_{VPCA} \, P^{T} \qquad (8)$$

The estimated interval-valued measurements for the principal components are then computed as:

$$\begin{cases} \underline{\hat{x}}_j(k) = \underline{t}(k)P^{-} \\ \overline{\hat{x}}_j(k) = \overline{t}(k)P^{+} \end{cases} \qquad (9)$$

3. THE PROPOSED METHOD KERNEL VERTICES PCA (K-VPCA)

Let X *be* a training data matrix of n samples (or observations) and m variables (or features). That is $X \in R^{nxm}$, where

$$X = [X_1, X_2, \ldots, X_n]^T \qquad (10).$$

These data points are mapped to a higher-dimensional feature space

$$\Phi : \ X_i \in \mathcal{R}^m \rightarrow \Phi\,(X_i) = \ \Phi_i \in \mathcal{F} \qquad (11)$$

Note that the feature space F has an arbitrarily large, possibly infinite, dimensionality equal to $\mathcal{H}$ [7]. An essential property of the feature space is the dot product of two vectors, $\Phi\ (x_i)$ and $\Phi\ (x_i)$, i, j = 1, . . . n. It is calculated as follows:

$$\phi(x_i)^T.\phi(x_j) = \mathbf{k}(x_i,\ x_J) \qquad (12)$$

where **k** is the kernel function. In the literature, several core functions have been presented, the most common of which is the radial basis function (RBF), which is provided by the following:

$$k(x_i,\ x_J) = exp[\frac{-|x_i - x_J|}{2\sigma^2}] \qquad (13)$$

where σ is the width of a Gaussian function that controls the flexibility of the kernel. A common choice for σ is the average minimum distance (d) between two points in the training data set.

The suggested method’s fundamental idea is to map data into a feature space via a nonlinear mapping, and then execute a linear interval-valued VPCA in feature space. The flow chart of Fig. 1 explains the procedure of the work.

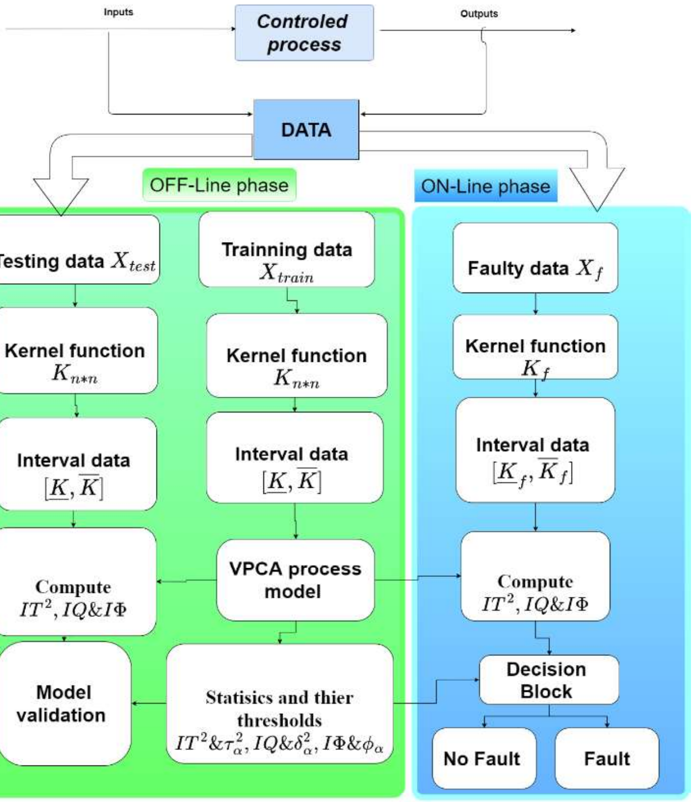

Figure 1. K-VPCA flowchart.

4. FAULT DETECTION USING K-VPCA METHOD

In this part, we present numerous fault detection indices based on K-VPCA for interval-valued data approaches to obtain the highest degree of robustness against uncertainty. In multivariate fault detection using a KPCA model, many statistics that quantify variances in distinct projection subspaces are utilized. The most often used fault indicators are T^2 and SPE (Q-statistic).

4.1. Interval-valued indices

The interval $[T^2]$ statistic is computed for the first interval principal components using a combination of interval eigenvalues and interval principal components as follows:

$$\begin{cases} \underline{T^2}(k) = \hat{\underline{t}}^T(k)\Delta_l^{-1}\hat{\underline{t}}(k) \\ \overline{T}^2(k) = \hat{\overline{t}}^T(k)\Delta_l^{-1}\hat{\overline{t}}(k) \end{cases} \tag{14}$$

For the interval-valued case, the Q statistic is computed as in the classical case, providing an interval [SPE] ($[Q]$) with upper and lower limits that correspond to the upper and lower bounds of the estimated residuals, as follows:

$$\begin{cases} \underline{Q} = \|\underline{e}(k)\|^2 = \underline{e}^T(k)\underline{e}(k) \\ \overline{Q} = \|\overline{e}(k)\|^2 = \overline{e}^T(k)\overline{e}(k) \end{cases} \tag{15}$$

Given that $\underline{e}(k) = [\underline{e}_1(k), \ldots, \underline{e}_m(k)]$, $\overline{e}(k) = [\overline{e}_1(k), \ldots, \overline{e}_m(k)]$.

4.2 The interval fault detection index

The interval fault detection index was developed owing to the ambiguity in fault detection decisions due to the interval structure of statistics presented above. When each bound draws a different conclusion about the appearance of faults [13]. The interval fault detection index presented here is denoted by the interval square prediction error (IQ), which is defined as:

$$IQ(k) = ||[e(k)]||^2 = \sum_{j=1}^{m}\|[e_j(k)]\|^2 \tag{16}$$

Where

$$||[e(k)]||^2 = \underline{e}_j^2(k) + \underline{e}_j(k)\overline{e}_j\ (k) + \overline{e}_j^2(k)) \quad (17).$$

Similarly, the interval Hotelling T^2 statistic (IT^2) is computed as follows:

$$IT^2\ (k) = \left\| \frac{[\hat{t}(k)]}{[\Delta_l]^{\frac{1}{2}}} \right\| \qquad (18)$$

The combined index, Φ, is evaluated as a combination of the principal subspace indicator, T^2, and the residual subspace indicator, SPE (Q). For interval data, the interval Φ depends on both T^2 and $[Q]$ as described by the following equation:

$$\begin{cases} \underline{\phi} = \frac{\underline{T}^2}{\overline{\tau}_\alpha^2} + \frac{\underline{Q}}{\overline{\delta}_\alpha^2} \\ \overline{\phi} = \frac{\overline{T}^2}{\underline{\tau}_\alpha^2} + \frac{\overline{Q}}{\underline{\delta}_\alpha^2} \end{cases} \qquad (19)$$

The new interval statistic $I\Phi$ also based on the combined interval fault detection indices IT^2 & IQ could be calculated as follows:

$$I\Phi = \frac{IT^2(k)}{\tau_\alpha^2} + \frac{IQ(k)}{\delta_\alpha^2} \qquad (20)$$

where τ_α^2 and δ_α^2 are the threshold of $IT^2\ (k)$ and $IQ\ (k)$ respectively.

5. APPLICATION ON CEMENT ROTARY KILN

This section provides an overview of the cement plant process and describes the signals employed for fault detection. Additionally, it details the fault detection methodology by specifying the types and sizes of datasets collected for the development and evaluation of the monitoring methods' performance

5.1 *Process description*

The rotary kiln plays a pivotal role in cement production and comprises several key components, including the head-sealing device, tail-sealing device, and hood. During normal operation, the kiln is driven by a primary motor through a reducer, which powers a large gear ring attached to the cylinder near the kiln tail via a spring plate. Raw materials are fed into the kiln from the top and transported through the rotating chamber to the opposite end, where they undergo high-temperature decomposition. In indirect-fired rotary kilns, heat is supplied by an external burner, whereas in indirect-fired kilns, the heat source is located within the chamber, maintaining the integrity of the raw materials. The rotation speed and temperature of the cylinder are adjusted to accommodate different materials and operational requirements. After calcination, the clinker undergoes initial cooling within the chamber before being transferred to the cooler for further cooling. Detailed descriptions of the various process variables can be found in [4].

5.2 Application of the Proposed Monitoring Scheme

The proposed K-VPCA technique is applied to monitor industrial cement production in this part. 44 sensors are used to monitor the process. These variables were picked from a pool of 55 to build a strong monitoring strategy and evaluate its detection capacity based on data from process computers in real time. Because standard PCA and its interval variants are already noise separation techniques, preprocessing or filtering the data is unnecessary.

The software used in the simulation was MATLAB. The data utilized in this article are of two types:

1) A healthy dataset which are divided into training (11000 samples), and testing (768 samples) data.
2) A faulty dataset that contains an actual involuntary process fault. It consists of 2084 samples.

The flowchart in fig 1 explains the steps that have been done.

After transforming the interval data into single-valued data, the PCA model is constructed based on the Cumulative Percentage of Variance (CPV) rule. The performance of the proposed technique is evaluated using several metrics:

- False Alarm Rate (FAR): This metric is calculated as:

$$FAR = 100 \times \frac{N_{h,f}}{N_h}\%.$$

where $N_{h,f}$ represents the number of samples exceeding the threshold while the system is healthy, and N_h is the total number of healthy samples.

- Missed Detection Rate (MDR): This metric is calculated as:

$$MDR = 100 \times \frac{N_{f,f}}{N_f}\%.$$

where $N_{f,f}$ is the number of samples below the threshold while the system is faulty, and N_f is the total number of faulty samples.

- Fault Detection Time Delay (DTD):

$$\mathrm{DTD} = t_d - t_o.$$

DTD is the number of samples while the system is faulty before it exceeds its threshold, t_d and t_o are the detection time and occurrence time of a fault, respectively.

Table 1 compares the False Alarm Rate (FAR) for T^2, Q and Φ statistics across PCA, VPCA, and K-VPCA methods for training and testing datasets. In the training set, PCA exhibits a FAR of 10% for all metrics, whereas VPCA and K-VPCA consistently achieve a lower FAR of 5%, indicating greater reliability in handling training data. For the testing set, PCA shows significant variability, with a low FAR for T^2, (5.07%) but much higher values for Q (18.7%) and Φ (12.5%), highlighting its sensitivity to uncertainty. In contrast, VPCA demonstrates consistent and reduced FAR values (T^2 = 6.07%, Q = 6.00%, Φ = 6.04%), showcasing improved robustness. K-VPCA further enhances performance, achieving the lowest FAR across all metrics (T^2= 5.55%, Q = 6.00%, Φ = 5.33%), particularly reducing false alarms in Φ. Overall, the results establish K-VPCA as the most robust and reliable method for fault detection in uncertain nonlinear systems.

Table 1. FAR % contributed by T 2, Q and Φ statistics, for the training and testing sets.

Data Set	Training Set			Testing Set		
Statistics	T^2	Q	Φ	T^2	Q	Φ
PCA [12]	10.0	10.0	10.0	5.07	18.7	12.5
VPCA [12]	5.00	5.00	5.00	6.07	6.00	6.04
K-VPCA	5.00	5.00	5.00	5.55	6.00	5.33

5.2 Real process fault detection

Table II presents the False Alarm Rate (FAR), Missed Detection Rate (MDR), and Detection Time Delay (DTD) for the faulty dataset based on three statistical indices (T 2, Q, and Φ) across PCA, VPCA, and K-VPCA methods. PCA shows a high FAR, particularly for Q (94.8%) and Φ (98.4%), with T^2 also contributing significantly (30%), indicating frequent false alarms. Additionally, PCA has an MDR and DTD of zero across all indices, suggesting it fails to detect faults effectively. VPCA reduces FAR substantially, with T^2 and Φ achieving zero, but exhibits an MDR of 61.2% for Q and a high DTD for Q (115) and T^2 (15), indicating delayed and missed fault detections in some cases.

Table 2. FAR, MDR & DTD of the faulty dataset contributed by the three statistic indices.

Data Set	FAR			MDR			DTD		
Statistics	T^2	Q	Φ	T^2	Q	Φ	T^2	Q	Φ
PCA [12]	30.0	94.8	98.4	0.00	0.00	0.00	0.00	**0.00**	**0.00**
VPCA [12]	0.00	6.22	0.00	1.40	61.2	0.00	15.0	**115**	20.0
K-VPCA	5.00	5.00	5.00	5.55	6.00	5.33	0.00	**26.0**	**0.00**

K-VPCA achieves the best balance, with minimal FAR (Q = 0.00%), reduced MDR (Q = 2.14%), and significantly lower DTD compared to VPCA, particularly for Q (26). Overall, K-VPCA demonstrates superior fault detection performance with fewer false alarms, improved detection accuracy, and faster response times, making it the most robust method among the three. Concerning the data of the real fault, Fig. 2, shows the result of the proposed interval approach K-VPCA method where the first 450 samples are healthy; the remaining ones are related to the real fault.

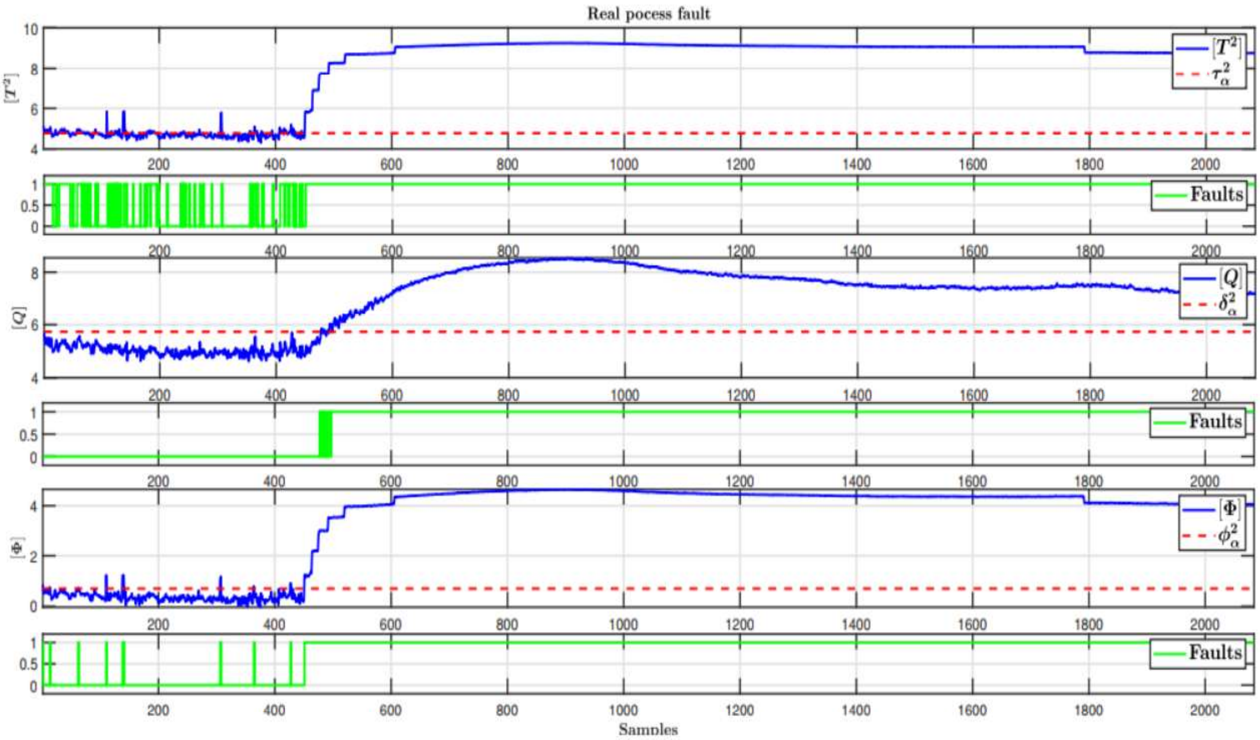

Figure 2. $\boldsymbol{T}^2$, Q, and Φ monitoring results of the faulty process operation, using the proposed K-VPCA method.

4. Conclusion

The interval nature of the projections ensures that approximation errors are eliminated during the fault identification and isolation process. This study introduces a novel data-driven approach for detecting faults in uncertain nonlinear processes. By incorporating sensor data and uncertainties through interval representation, interval-valued methods provide a robust strategy for fault detection and isolation (FDI). The objective was to evaluate the applicability and reliability of VPCA for

fault identification in nonlinear systems, utilizing data from a cement rotary kiln. The results demonstrated the effectiveness of the proposed K-VPCA technique compared to interval VPCA and traditional PCA approaches. This research aims to establish an efficient interval diagnosis methodology that addresses the limitations of existing interval-based methods.

References

[1] F. Palumbo and C. N. Lauro, “A pca for interval-valued data based on midpoints and radii,” in New Developments in Psychometrics: Proceedings of the International Meeting of the Psychometric Society IMPS2001. Osaka, Japan, July 15–19, 2001, 2003, pp. 641–648.

[2] M.-F. Harkat, G. Mourot, and J. Ragot, “An improved pca scheme for sensor fdi: Application to an air quality monitoring network,” Journal of Process Control, vol. 16, no. 6, pp. 625–634, 2006.

[3] S. J. Qin, “Data-driven fault detection and diagnosis for complex industrial processes,” IFAC Proceedings Volumes, vol. 42, no. 8, pp. 1115–1125, 2009.

[4] F. Bencheikh, M. Harkat, A. Kouadri, and A. Bensmail, “New reduced kernel pca for fault detection and diagnosis in cement rotary kiln,” Chemometrics and Intelligent Laboratory Systems, vol. 204, p. 104091, 2020.

[5] L. Rouani, M. F. Harkat, A. Kouadri, and S. Mekhilef, “Shading fault detection in a grid-connected pv system using vertices principal component analysis,” Renewable Energy, vol. 164, pp. 1527–1539, 2021.

[6] M. T. H. Kaib, A. Kouadri, M. F. Harkat, A. Bensmail, and M. Mansouri, “Improving kernel pca-based algorithm for fault detection in nonlinear industrial process through fractal dimension,” Process Safety and Environmental Protection, vol. 179, pp. 525–536, 2023.

[7] B. Scholkopf, A. Smola, and K.-R. M ¨ uller, “Nonlinear component ¨ analysis as a kernel eigenvalue problem,” Neural computation, vol. 10, no. 5, pp. 1299–1319, 1998.

[8] I. Hamrouni, H. Lahdhiri, K. b. Abdellafou, and O. Taouali, “Fault detection of uncertain nonlinear process using reduced interval kernel principal component analysis (rikpca),” The International Journal of Advanced Manufacturing Technology, vol. 106, no. 9, pp. 4567–4576, 2020.

[9] I. Hamrouni, H. Lahdhiri, K. Ben Abdellafou, A. Aljuhani, O. Taouali, and K. Bouzrara, “Anomaly detection and localization for process security based on the multivariate statistical method,” Mathematical Problems in Engineering, vol. 2022, 2022.

[10] K. Dhibi, R. Fezai, M. Mansouri, A. Kouadri, M.-F. Harkat, K. Bouzara, H. Nounou, and M. Nounou, “A hybrid approach for process monitoring: improving data-driven methodologies with dataset size reduction and interval-valued representation,” IEEE Sensors Journal, vol. 20, no. 17, pp. 10 228–10 239, 2020.

[11] M.-F. Harkat, M. Mansouri, M. Nounou, and H. Nounou, “Faultdetection of uncertain nonlinear process using interval-valued datadriven approach,” Chemical Engineering Science, vol. 205, pp. 36–45, 2019.

[12] A. Louifi, S. E. Louhab, A. Kouadri, L. Rouani, A. Bensmail, and M. F. Harkat, “Interval valued pca-based approach for fault detection in complex systems,” in 19th International Multi-Conference on Systems, Signals & Devices, SSD 2022, Setif, Algeria, May 6-10, 2022. IEEE, 2022, pp. 184–189.

[13] T. Ait-Izem, M.-F. Harkat, M. Djeghaba, and F. Kratz, “On the application of interval pca to process monitoring: A robust strategy for sensor fdi with new efficient control statistics,” Journal of Process Control, vol. 63, pp. 29–46, 2018.

[14] M. T. H. Kaib, A. Kouadri, M. F. Harkat, and A. Bensmail, “Rkpcabased approach for fault detection in large scale systems using variogram method,” Chemometrics and Intelligent Laboratory Systems, vol. 225, p. 104558, 2022.

[15] P. Cazes, A. Chouakria, E. Diday, and Y. Schektman, “Extension de l’analyse en composantes principales a des donn ` ees de type intervalle,” ´ Revue de Statistique appliquee ´ , vol. 45, no. 3, pp. 5–24, 1997.

[16] A. Tarek, W. Bougheloum, M. F. HARKAT, and M. Djeghaba, “Fault detection and isolation using interval principal component analysis methods,” IFAC-PapersOnLine, vol. 48, no. 21, pp. 1402–1407, 2015.

Islamic University Journal of Applied Sciences (IUJAS)
https://journals.iu.edu.sa/jesc
Special Issue, February 2026, Pages 46-59
https://igee.univ-boumerdes.dz/ncaeee25/

Experimental Evaluation of Bicopter Stabilization Using PID Control

Fadhila Lachekhab [1,*], Messaouda Benzaoui [2], Acheli Dalila [3], Achite lotfi[4], Ferroudj Tedj Eddine[4], Sidahmed Hadjouti[4]

[1] Applied Automatics Laboratory, Faculty of hydrocarbons and chemistry,University of M'hamed Bougara, Boumerdes, Algeria, f.lachekhab@univ-boumerdes.dz

[2] Applied Automatics Laboratory, Inst electrical & electronic engineering, University of M'hamed Bougara, Boumerdes, Algeria, m.benzaoui@univ-boumerdes.dz

[3] Acheli Dalila, Applied Automatics Laboratory, Faculty of technology, University of M'hamed Bougara, Boumerdes, Algeria, d.acheli@univ-boumerdes.dz

[4] Faculty of hydrocarbons and chemistry,University of M'hamed Bougara, Boumerdes, Algeria
achite.lotfi@gmail.com, tadjouferroudj@gmail.com, s.hadjouti@univ-boumerdes.dz

*Corresponding author: Fadhila Lachekhab, f.lachekhab@univ-boumerdes.dz

Abstract

This paper presents an experimental study on the stabilization and control of a bicopter system using classical control techniques. The bicopter consists of two motors driven by electronic speed controllers (ESCs) and equipped with an MPU6050 inertial measurement unit to measure angular variations around the pitch axis. A series of real-time tests were conducted using proportional (P), proportional–derivative (PD), and proportional–integral–derivative (PID) controllers to evaluate their performance in achieving system stability. The results show that the proportional controller alone was insufficient to stabilize the bicopter, leading to strong oscillations. The addition of a derivative term improved damping and reduced oscillations, while the inclusion of an integral term further eliminated steady-state error when properly tuned. The optimized PID parameters ($K_p = 3$, $K_i = 0.001$, $K_d = 0.8$) provided stable performance with minimal error and acceptable response time. The findings confirm the effectiveness of the PID controller for maintaining balance and stability in bicopter systems, providing a foundation for future improvements such as adaptive and intelligent control methods.

Keyword: Bicopter; PID Control; Stability; UAV; Arduino; Flight Control

---

https://doi.org/10.63070/jesc.2026.005
Received 25 November 2025; Revised 18 January 2026; Accepted 26 January 2026.
Available online 31 January 2026.
Published by Islamic University of Madinah on behalf of *Islamic University Journal of Applied Sciences*.

1. Introduction

Unmanned Aerial Vehicles (UAVs) have become an essential part of modern engineering applications due to their increasing use in surveillance, mapping, environmental monitoring, and transportation systems [1][2]. Among the various UAV configurations, the bicopter stands out for its mechanical simplicity and reduced energy consumption, using only two rotors for lift and control. However, due to its underactuated and nonlinear dynamics, the bicopter remains one of the most challenging aerial vehicles to stabilize and control effectively [3][6].

Stabilization and attitude control of UAVs have been extensively studied through both classical and modern control techniques. Traditional controllers, such as Proportional (P), Proportional–Derivative (PD), and Proportional–Integral–Derivative (PID), remain widely used because of their simplicity and robustness for real-time implementation [6][15]. Despite the rise of more advanced approaches—such as LQR, adaptive, and intelligent control strategies [9][10][13]—PID controllers continue to provide reliable performance for small-scale UAVs when properly tuned.

In this work, an experimental bicopter platform was developed and tested using an Arduino-based control system. The setup includes two brushless motors with Electronic Speed Controllers (ESCs) and an MPU6050 sensor for real-time attitude measurement. A series of experimental tests were conducted to analyze the behavior of the bicopter under P, PD, and PID controllers, and to determine the optimal set of parameters ensuring stability and minimal steady-state error.

The study aims to highlight the effect of each control action (proportional, derivative, and integral) on system performance and to validate the PID controller's ability to stabilize the bicopter. The results obtained serve as a foundation for future developments, including adaptive and active disturbance rejection control methods [16][19][21].

2. Methodology & discussion

The experimental study focuses on the stabilization of a bicopter using classical control techniques implemented on an Arduino-based platform. The developed prototype consists of a single rigid arm equipped with two brushless DC motors, each controlled by an Electronic Speed Controller (ESC), allowing independent speed regulation. This minimal configuration represents an underactuated aerial vehicle, which poses significant challenges in attitude stabilization due to its nonlinear dynamics [3][6]. An MPU6050 Inertial Measurement Unit (IMU) was installed at the center of the arm to measure angular variations around the pitch axis (Y-axis).

The measured angle θ serves as the primary feedback signal for the control loop. The control algorithm was implemented on an Arduino microcontroller, which computes the control signal according to the chosen control law and transmits the command to both ESCs to adjust the motor speeds and maintain equilibrium.

The bicopter's control was tested using three classical approaches:

2.1 Proportional (P) control

The proportional controller generates a control signal directly proportional to the error between the desired and measured angles. Its main objective was to observe the system's natural response and assess the impact of the proportional gain Kp on stability [15].

2.2 Proportional derivative (PD) control

To improve transient response and reduce oscillations, a derivative term was added to anticipate system behavior. This approach is widely used in aerial vehicle stabilization due to its ability to provide additional damping [6][9].

2.3 Proportional integral derivative (PID) control

The final configuration included the integral term to eliminate steady-state error and improve overall precision. Several combinations of gains were tested, with the most stable response achieved for Kp = 3, Ki = 0.001, and Kd = 0.8, which provided minimal overshoot and a fast-setting time. Each test recorded the angle θ and motor speeds over time. The data were analyzed to compare the stability, oscillation amplitude, and error behavior across the three control strategies.

The experimental workflow consisted of:

- Bicopter construction and sensor calibration
- Control algorithm development in Arduino IDE.
- Parameter tuning for P, PD, and PID controllers
- Real-time testing and data acquisition

This experimental methodology follows the common approach used in UAV control research [6][8][9], providing a practical validation of classical control strategies on an underactuated bicopter platform.

3. System modelling and control design

3.1 Bicopter mathematical modelling

The bicopter can be represented as a rigid body rotating around its pitch axis. The rotational motion follows Euler's rotational equation:

$$Jy\ddot{\theta}=\tau 1-\tau 2 \tag{1}$$

where:

- Jy is the moment of inertia around the pitch axis,
- $\tau 1$ and $\tau 2$ are the torques generated by the left and right motors, respectively,
- θ represents the pitch angle.

Each motor produces a thrust force proportional to the square of its angular speed:

$$Fi=Kt\omega i^{2} \tag{2}$$

Where Kt is the thrust coefficient and ωi is the rotational speed of the motor i.

The corresponding torque around the pitch axis is:

$$\tau i=FiL=kTL\omega i2$$

with L being the distance between each motor and the center of rotation.

Substituting these expressions into the rotational equation gives:

$$\ddot{\theta}=\frac{ktL}{Jy(\omega 1^{2}-\omega 2^{2})} \tag{3}$$

This equation represents the nonlinear pitch dynamics of the bicopter. For small deviations around the hover condition

($\omega 1\approx\omega 2\approx\omega 0$), the system can be linearized and expressed as:

$$\ddot{\theta}=KuU \tag{4}$$

where:

$U=\omega 1^{2}-\omega 2^{2}$ is the control input and $Ku=\frac{ktL}{Jy}$

Taking the Laplace transform yields the linear transfer function:

$$G(s)=\frac{\theta(s)}{u(s)}-\frac{1}{JyS^{2}} \tag{5}$$

This model shows that the bicopter behaves as a second-order unstable system requiring active feedback control for stabilization.

3.2 Control architecture

The bicopter attitude control system is implemented as a closed feedback loop. The MPU6050 inertial measurement unit measures the pitch angle θ θ, which is compared to the desired reference angle θ ref θ ref to compute the tracking error:

$$e\ (t) = \theta \text{ ref } (t) - \theta\ (t) \tag{6}$$

This error is processed by the PID controller, which generates a control signal u(t) used to adjust the speeds of the left and right motors. The variation in motor speeds produces the necessary aerodynamic torque to correct the pitch deviation.

This structure ensures continuous correction of deviations and allows the bicopter to remain balanced even in the presence of disturbances or reference changes.

3.3 PID control implementation

The controller used in this work is based on the classical proportional–integral–derivative (PID) law, widely applied in UAV stabilization due to its simplicity and real-time applicability. The continuous-time expression of the control law is:

$$u(t)=Kpe(t)+Ki\int e(\tau)d\tau+kd*\frac{de(t)}{dt} \tag{7}$$

where:

- Kp is the proportional gain,
- Ki is the integral gain,
- Kd is the derivative gain.

Because the control is computed on an Arduino microcontroller, the PID law is implemented in discrete form with sampling period Ts.

$$u[k]=Kpe[k]+KiTsi \sum_{i=0}^{k} ke[i]\ Kd* \frac{e[k]-e[k-1]}{Ts} \tag{8}$$

The generated control signal modifies the motor speeds as:

$$\omega 1=\omega 0+u[k], \quad \omega 2=\omega 0-u[k]$$

where ω0 is the nominal motor speed at hover.This allocation causes opposite motor variations, generating corrective torque to stabilize the aircraft

3.4 Controller parameter tuning

The selection of the controller gains Kp, Ki, and Kd was performed experimentally according to a structured procedure:

- Proportional gain adjustment

Kp was increased until the system exhibited sustained oscillations. This value defines the proportional stability limit and provides a fast but oscillatory response.

- Derivative gain introduction

A derivative term Kd was then added to introduce artificial damping. Increasing Kd reduces overshoot and oscillations by compensating for rapid variations in the error signal.

- Integral gain refinement

An integral gain Ki was finally introduced to eliminate the small steady-state error remaining after PD control. A very small Ki was chosen to prevent integral wind-up, which would otherwise destabilize the system.

Following these steps, the optimal gains were determined experimentally as:

$$Kp=3,\ Ki=0.001,\ Kd=0.8$$

These values ensured a minimal overshoot, fast settling time, and near-zero steady-state error.

3.5 Model-based interpretation

The mathematical model derived earlier shows that the bicopter behaves as a second-order system with no intrinsic damping. This theoretical property explains the behaviors observed in the experiments:

- **Proportional control only**

  With Kp alone, the closed loop resembles a lightly-damped oscillator. This leads to strong oscillations with no convergence, consistent with experimental observations.

- **Addition of derivative action**

  The derivative term adds effective damping to the system. Increasing Kd reduces oscillations and improves the transient response, explaining the improved performance observed in the PD tests.

- **Effect of the integral term**

  The integral action compensates for the small offset remaining with PD control. However, excessive integral gain accumulates error too quickly and can destabilize the system, as observed when Ki=0.01. Reducing Ki significantly improve the steady-state precision without compromising stability.

- **Final PID configuration**

  With the optimized gains, the system achieved a negligible steady-state error, reduced oscillations, and settling time of approximately 3 seconds and stable tracking of reference changes.

  These observations confirm strong agreement between theoretical expectations and experimental behavior.

4. Results and discussion

A series of experimental tests were conducted on the bicopter prototype to evaluate the performance of different control strategies Proportional (P), Proportional Derivative (PD), and Proportional Integral Derivative (PID) controllers. The goal of each test was to determine the controller parameters that ensure system stability, reduce oscillations, and minimize steady-state error.

4.1 Test with proportional (P) controller

The first test aimed to evaluate the response of the bicopter under a proportional controller with a gain of Kp = 5. The functional diagram of the bicopter using the proportional control law is shown by the figure bellow:

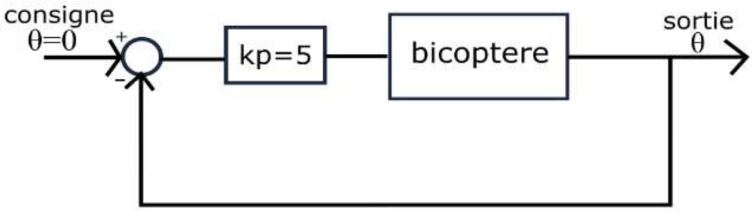

Figure 1. The bicopter functional diagram with proportional control.

The time response of the pitch angle θ under this configuration is presented in figure 2 The results reveal that the system exhibits strong and rapid oscillations, indicating that the proportional action alone is insufficient to stabilize the bicopter. The absence of derivative or integral terms causes the controller to react proportionally to the instantaneous error, which leads to continuous oscillatory motion.

The speed of both motors fluctuates between approximately 1270 and 1330 rpm, further confirming the system's instability.

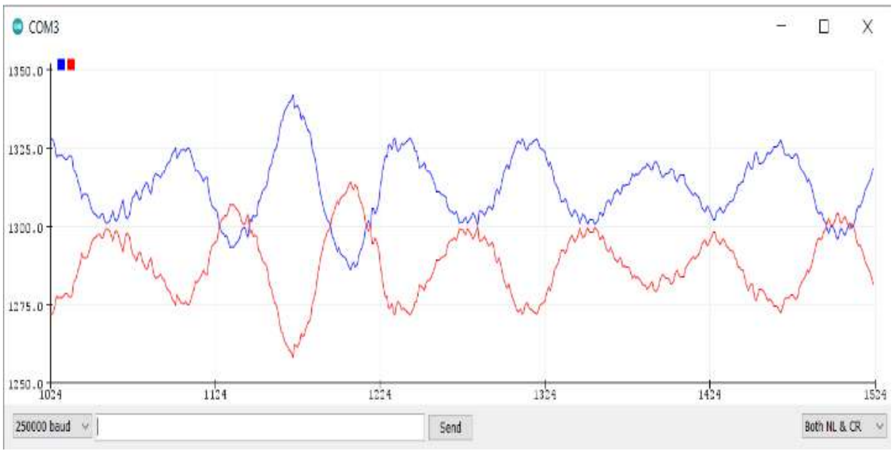

Figure 2. The time response of the pitch angle θ.

4.2 Test with proportional derivative (PD) controller

In the second test, a derivative term was introduced to improve damping and reduce oscillations. The control parameters were set to Kp = 5 and Kd = 0.001 are shown by:

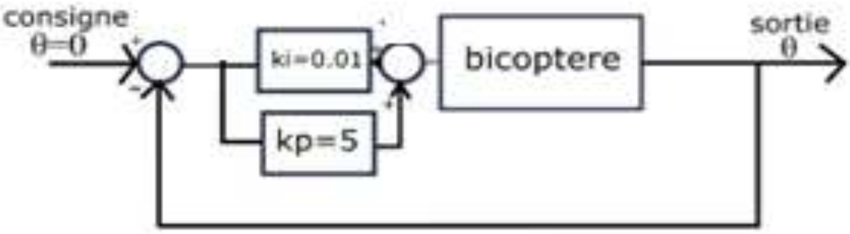

Figure 3. The bicopter functional diagram with proportional derivative control

The angular response of the system with these parameters is shown in figure 4.

Although the oscillations decreased slightly, the response remained unstable, indicating that the derivative gain was too small to have a significant stabilizing effect.

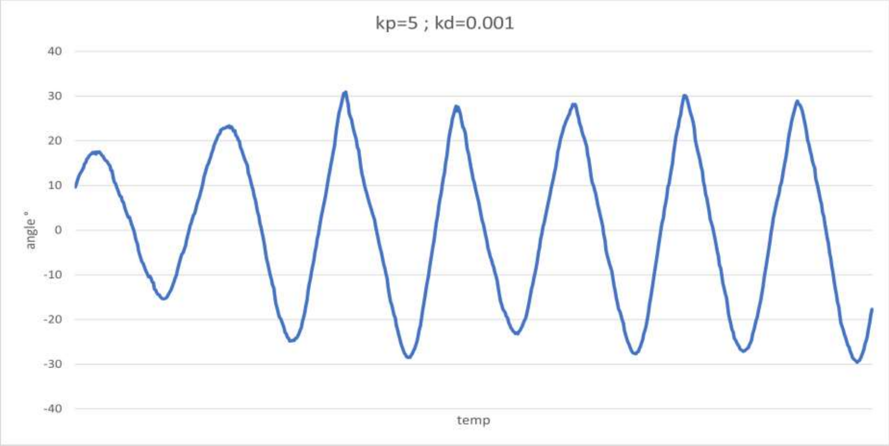

Figure 4. The time response of the pitch angle θ.

When Kd was increased to 0.01, the response improved notably

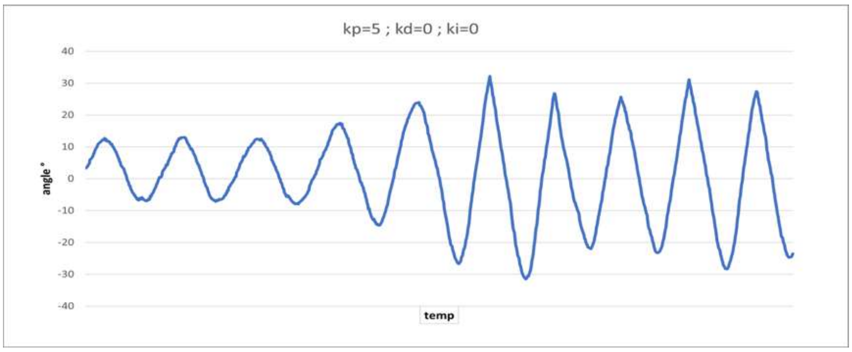

Figure 5. The time response of the pitch angle θ.

The oscillations were considerably reduced, and the system reached a quasi-stable state with a steady-state error of approximately 3°, oscillating within the range [2°, 4°].

The corresponding motor speed curves show that the speeds of both motors stabilize with small variations, confirming an improvement in the dynamic response. These findings align with prior studies that demonstrate how derivative action enhances damping and reduces overshoot in multirotor control systems [6][9][15].

4.3 Test with proportional integral–Derivative (PID) Controller

To eliminate steady-state error, an integral term was added, resulting in a full PID controller. The initial test used Kp = 5, Ki = 0.01, Kd = 0.010.

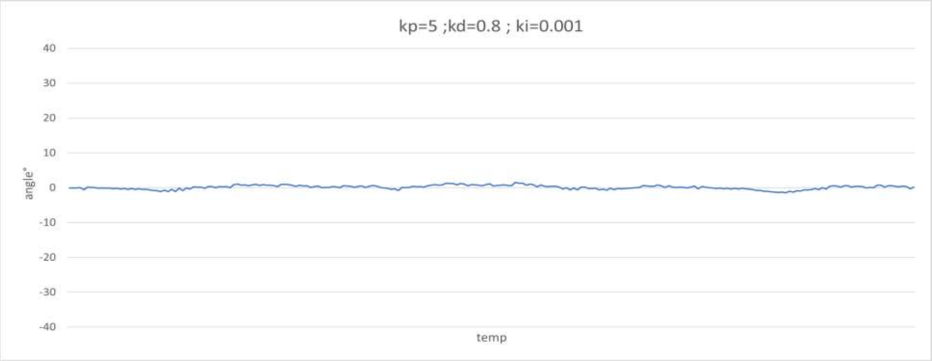

Figure 6. The bicopter functional diagram with PID control.

The corresponding angular response is shown in the figure bellow

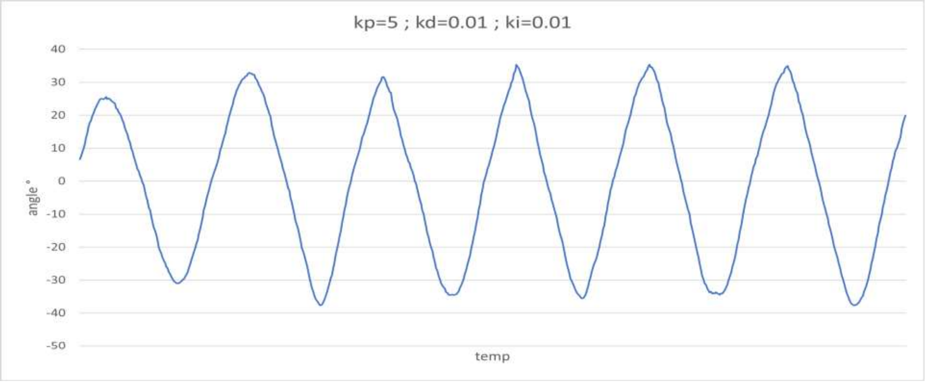

Figure 7. The time response of the pitch angle θ.

At this tuning, the system became unstable again, with oscillations ranging from −38° to +38°. This was attributed to an excessively large integral gain Ki, which caused the accumulation of error and overshoot. To optimize performance, the parameters were adjusted to Kp = 3, Ki = 0.001, and Kd = 0.8.

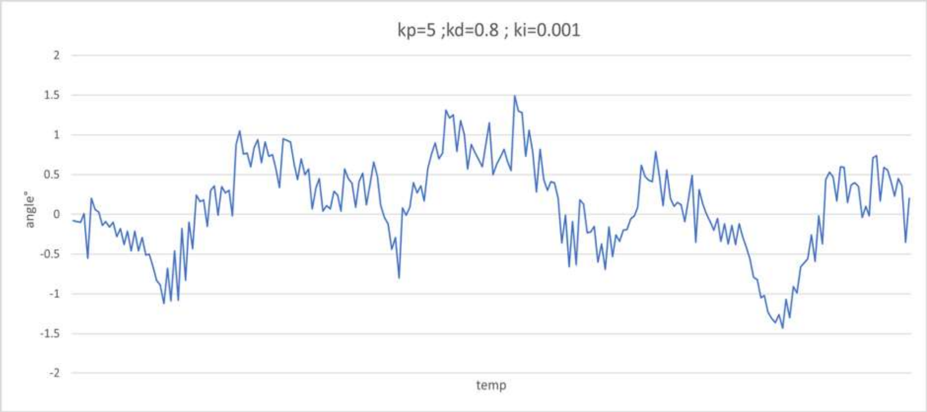

Figure 8. The time response of the pitch angle θ.

The resulting response demonstrated significant improvement in system stability and accuracy.

The steady-state error was nearly zero, the settling time was approximately 3 seconds, and the oscillations were limited within the range [−1.4°, +1.5°] with a maximum overshoot of 30°.

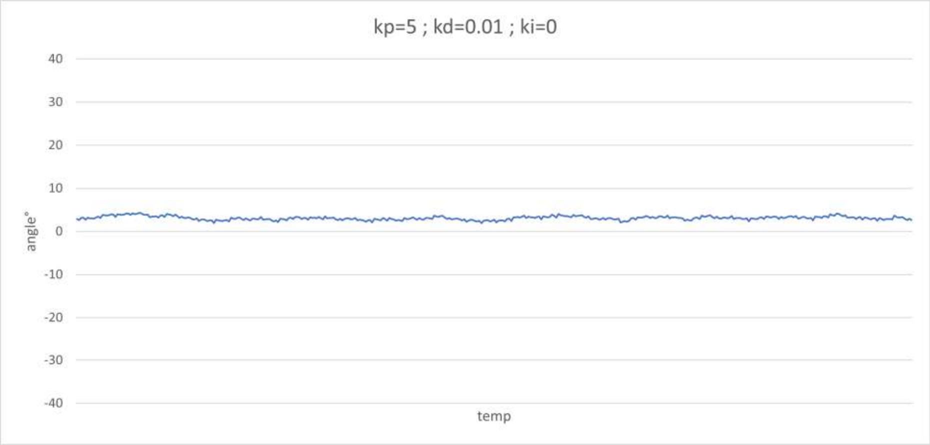

Figure 9. The time response of the pitch angle θ.

A detailed zoom of the stabilized part of the curve is presented in these results validate the effectiveness of the PID controller for bicopter stabilization, consistent with previous findings on quadrotor control systems using classical PID approaches [6][8].

4.4 Test with PID controller and reference change

Finally, the robustness of the optimized PID controller was evaluated under a change of the reference. Initially, the bicopter maintained equilibrium at 0° for 5 seconds, then tilted to −20°, before returning to 0°. The response of the pitch angle followed the reference trajectory accurately with an acceptable transient

The corresponding motor speeds showed symmetrical adjustments around the equilibrium value of 1200 rpm, confirming the controller’s ability to handle setpoint changes while maintaining stability.

Overall, the PID configuration provided the best performance among the three tested strategies, ensuring fast convergence, reduced oscillations, and minimal steady-state error.

5. Conclusion

In this work, an experimental study was conducted on the stabilization and control of a bicopter using classical control strategies. The system was developed on an Arduino-based platform, incorporating an MPU6050 inertial measurement unit to measure the pitch angle and two brushless motors controlled through electronic speed controllers. Different control configurations—Proportional (P), Proportional–

Derivative (PD), and Proportional–Integral–Derivative (PID)—were implemented and tested to evaluate their effect on system stability and performance.

The experimental results demonstrated that the proportional controller alone was unable to stabilize the bicopter, as it produced strong oscillations and a significant steady-state error. The addition of a derivative term improved damping characteristics, reducing oscillations and enhancing the transient response. The introduction of an integral component, when properly tuned, eliminated steady-state error and yielded a stable response with minimal overshoot and acceptable settling time. The optimal tuning parameters were determined as Kp = 3, Ki = 0.001, and Kd = 0.8, which provided a fast and stable system response with negligible steady-state error.

These results confirm the effectiveness of the PID controller in stabilizing underactuated aerial vehicles such as bicopters, aligning with existing research on multirotor control systems. the future work will focus on enhancing the performance of the control system through the implementation of adaptive or intelligent control techniques, such as Active Disturbance Rejection Control (ADRC) [19][21] or fuzzy logic control, to improve robustness under external disturbances. Moreover, integration with MATLAB/Simulink and digital twin environments will allow real-time monitoring, advanced tuning, and virtual validation of control strategies before experimental deployment.

References

[1] González-Jorge, H., Martínez-Sánchez, J. and Bueno, M.,”Unmanned aerial systems for civil applications: A review”, Drones, 1(1), p.2, 2017.

[2] Nascimento, T.P. and Saska, M., ”Position and attitude control of multi-rotor aerial vehicles: A survey”. Annual Reviews in Control, *48*, pp.129-146*,* 2019.

[3] Emran, B.J. and Najjaran, H.,”A review of quadrotor: An underactuated mechanical system”. Annual Reviews in Control, *46*, pp.165-180, 2018.

[4] Molnár, A.,”Surveying Archaeological Sites and Architectural Monuments with Aerial Drone Photos”, Acta Polytechnica Hungarica, 16(7), 2019.

[5] Giernacki, W., Kozierski, P., Michalski, J., Retinger, M., Madonski, R., Campoy, P., Bebop 2, ” Quadrotor As a Platform for Research and Education in Robotics and Control Engineering”, In 2020 International Conference on Unmanned Aircraft Systems (ICUAS) (pp.1724-1732), IEEE, 2020.

[6] Argentim, L.M., Rezende, W.C., Santos, P.E. and Aguiar, R.A.,”PID, LQR and LQR-PID on a quadcopter platform”. In 2013 International Conference on Informatics, Electronics and Vision (ICIEV) (pp. 1-6). IEEE. May 2013.

[7] Chen, X., Zhang, G., Lu, C. and Cheng, J.,"Quadrotor aircraft attitude control algorithm based on improved UKF". In IOP Conference Series: Earth and Environmental Science (Vol. 233, No. 4, p. 042037), 2019.

[8] Barbosa, F.D.S., "4DOF Quadcopter: development, modeling and control" (Doctoral dissertation, Universidade de São Paulo, Advisor: Prof. Dr. Bruno Augusto Angélico), 2017.

[9] Greatwood, C. and Richards, A.G., " Reinforcement learning and model predictive control for robust embedded quadrotor guidance and control". Autonomous Robots, 43(7), pp.1681-1693, 2019.

[10] Santos, M.C.P., Rosales, C.D., Sarapura, J.A., Sarcinelli-Filho, M. and Carelli, R.,"An adaptive dynamic controller for quadrotor to perform trajectory tracking tasks". Journal of Intelligent & Robotic Systems, 93(1-2), pp.5-16, 2019.

[11] Pérez-Alcocer, R. and Moreno-Valenzuela, J., "Adaptive control for quadrotor trajectory tracking with accurate parametrization", IEEE Access, 7, pp.53236-53247, 2019.

[12] Fethalla, N., Saad, M., Michalska, H. and Ghommam, J., "*Robust observer-based backstepping controller for a quadrotor UAV*". In *2017* IEEE 30th Canadian Conference on Electrical and Computer Engineering (CCECE) (pp. 1-4), 2017.

[13] Kayacan, E. and Maslim, R., "Type-2 fuzzy logic trajectory tracking control of quadrotor VTOL aircraft with elliptic membership functions". IEEE/ASME Transactions on Mechatronics, 22(1), pp. 339-348, 2016.

[14] Guo, Y., Jiang, B. and Zhang, Y., "A novel robust attitude control for quadrotor aircraft subject to actuator faults and wind gusts". IEEE/CAA Journal of Automatica sinica, 5(1), pp. 292-300, 2017.

[15] Han, J., "From PID to active disturbance rejection control", IEEE Transactions on Industrial Electronics, 56(3), pp. 900-906, 2009.

[16] Gao, Z., "On the centrality of disturbance rejection in automatic control". ISA transactions, 53(4), pp. 850-857, 2014.

[17] Chen, S., Bai, W., Hu, Y., Huang, Y. and Gao, Z., "On the conceptualization of total disturbance and its profound implications". Science China Information Sciences, 63(2), p.129201, 2020.

[18] Chen, S. and Chen, Z., "On Active Disturbance Rejection Control for a Class of Uncertain Systems with Measurement Uncertainty". IEEE Transactions on Industrial Electronics, 2020.

[19] Huang, Y. and Xue, W., "Active disturbance rejection control: methodology and theoretical analysis". ISA transactions, 53(4), pp.963-976, 2014.

[20] Xue, W. and Huang, Y., "Performance analysis of 2-DOF tracking control for a class of nonlinear uncertain systems with discontinuous disturbances". International Journal of Robust and Nonlinear Control, 28(4), pp.1456-1473, 2018.

[21] Guo, B.Z. and Zhao, Z.L., ”Active disturbance rejection control for nonlinear systems: An introduction”. John Wiley & Sons, 2016.

[22] Chen, S., Xue, W. and Huang, Y.,"Analytical design of active disturbance rejection control for nonlinear uncertain systems with delay”. Control Engineering Practice, 84, pp.323-336, 2019.

[23] Wu, Z.H. and Guo, B.Z., ”Extended state observer for MIMO nonlinear systems with stochastic uncertainties”. International Journal of Control, 93(3), pp.424-436, 2020.

[24] Lakomy, K., Patelski, R., & Pazderski, D., ”ESO architectures in the trajectory tracking ADR controller for a mechanical system: a comparison”, In Advanced, Contemporary Control (pp. 1323-1335). Springer, Cham, 2020.

[25] Sira-Ramírez, H., Luviano-Juárez, A., Ramírez-Neria, M. and Zurita-Bustamante, E.W., ”Active disturbance rejection control of dynamic systems: a flatness based approach”. Butterworth-Heineman, 2018.

[26] Stanković, M.R., Naumovic, M., Manojlovic, S. and Simic, S., ”Optimized pure hardware FPGA-based implementation of active disturbance rejection control”. Electrical Engineering, 100(1), pp.111-121. 2018.

[27] Zhang, Y., Chen, Z., Zhang, X., Sun, Q. and Sun, M., ”A novel control scheme for quadrotor UAV based upon active disturbance rejection control”. Aerospace Science and Technology, 79, pp.601-609, 2018.

[28] Stanković, M.R., Manojlović, S.M., Simić, S.M., Mitrović, S.T. and Naumović, M.B.,”FPGA system-level based design of multi-axis ADRC controller”. Mechatronics, 40, pp.146-155. 2016.

[29] Michałek, M.M., ”Robust trajectory following without availability of the reference time-derivatives in the control scheme with active disturbance rejection”. In 2016 American Control Conference (ACC) (pp. 1536-1541). IEEE. 2016, July.

[30] Madonski, R., Shao, S., Zhang, H., Gao, Z., Yang, J. and Li, S.,”General error-based active disturbance rejection control for swift industrial implementations”. Control Engineering Practice, 84, pp.218-229. 2019.

[31] Michałek, M. M., Łakomy, K., and Adamski, W., ”Robust output-feedback cascaded tracking controller for spatial motion of anisotropically-actuated vehicles”. Aerospace Science and Technology, 92, pp.915-929. 2019

Islamic University Journal of Applied Sciences (IUJAS)
https://journals.iu.edu.sa/jesc
Special Issue, February 2026, Pages 60-77
https://igee.univ-boumerdes.dz/ncaeee25/

Implementation and Evaluation of a Conjugate Gradient (CG) Detector for 5G/6G-Like MIMO Scenarios Using Sionna

Amina Saoudi[1], Tahir Imene[2], Nessrine Smaili[3], Ahmed Ouameur Messoud[4]

Department of Electroncis, IGEE , University of Boumerdes, Algeria
aminasaoudi2003@gmail.com, imenetahir03@gmail.com, nessrinesmaili3@gmail.com, Messaoud.Ahmed.Ouaneur@uqtr.ca

*Corresponding author (Amina Saoudi), Email: aminasaoudi2003@gmail.com

Abstract

Massive multiple-input multiple-output (MIMO) systems are a cornerstone of 5G and emerging 6G wireless networks due to their ability to provide high spectral efficiency and improved reliability. However, signal detection in large-scale MIMO systems remains a major challenge because of the high computational complexity associated with conventional linear detectors. In this paper, we investigate the Conjugate Gradient (CG) algorithm as a low-complexity iterative detection technique for massive MIMO systems. The MIMO detection problem is formulated as a system of linear equations and solved using the CG method implemented within the Sionna simulation framework. The convergence behavior and bit error rate (BER) performance of the proposed detector are analyzed under different signal-to-noise ratio (SNR) levels and spatial correlation scenarios. Simulation results show that the CG-based detector achieves near-optimal BER performance while significantly reducing computational complexity compared to classical linear detectors such as the linear minimum mean square error (LMMSE) detector. These results demonstrate that CG-based detection is a promising and efficient solution for practical large-scale MIMO deployments.

Keywords: Massive MIMO; Conjugate Gradient; Signal Detection; 5G and 6G; Bit Error Rate.

---

https://doi.org/10.63070/jesc.2026.006
Received 30 November 2025; Revised 18 January 2026; Accepted 26 January 2026.

Published by Islamic University of Madinah on behalf of *Islamic University Journal of Applied Sciences*.

1. Introduction

The growth of data-intensive applications, IoT, and autonomous systems demands higher throughput and lower latency in wireless communications. Massive MIMO enhances spectral efficiency, robustness, and spatial multiplexing but makes signal detection challenging under interference and spatial correlation. Conventional detectors like ZF and LMMSE are reliable but computationally expensive. The Conjugate Gradient (CG) algorithm offers a low-complexity iterative alternative, approximating LMMSE performance efficiently. In this paper, we implement CG-based MIMO detection using Sionna and analyze its BER, convergence, and computational complexity under various SNR and channel conditions.

2. Related Work

Several linear detection techniques have been proposed for MIMO systems to address the challenges of high-dimensional signal detection. Among the most common are the Zero-Forcing (ZF) and Linear Minimum Mean Square Error (LMMSE) detectors. The ZF detector aims to completely eliminate interference by inverting the channel matrix. Although it provides interference-free estimation, it amplifies noise, especially in ill-conditioned channels [1, 3]. The LMMSE detector improves performance in noisy environments by introducing a regularization term to balance noise enhancement and interference suppression, but this comes at the cost of higher computational complexity [1, 3].

To reduce the complexity of linear detection, iterative methods have been proposed. In particular, the Conjugate Gradient (CG) algorithm has gained attention as a low-complexity alternative that approximates LMMSE performance without directly inverting the channel matrix [4–6].

CG-based detectors have been shown to achieve near-optimal performance while significantly reducing computational overhead, making them suitable for large-scale and massive MIMO systems [4–6].

Recent works have also focused on realistic implementation and evaluation of CG-based detection. Frameworks such as Sionna facilitate accurate simulations of massive MIMO systems, including channel effects, spatial correlation, and varying SNR conditions [7, 9, 10]. These platforms allow researchers to evaluate the convergence behavior, bit error rate (BER), and computational complexity of CG-based detectors in scenarios that closely resemble practical 5G and 6G deployments.

3. System Model

3.1 MIMO Signal Model

Multiple-Input Multiple-Output (MIMO) systems form a core component of modern wireless communication standards such as LTE, 5G NR, and future 6G networks. The fundamen- tal narrowband MIMO signal model is expressed as

$$\mathbf{y} = \mathbf{H}\mathbf{x} + \mathbf{n}, \tag{1}$$

where $\mathbf{y} \in \mathbb{C}^{N_r \times 1}$ is the received signal vector, $\mathbf{H} \in \mathbb{C}^{N_r \times N_t}$ is the channel matrix, $\mathbf{x} \in \mathbb{C}^{N_t \times 1}$ is the transmitted symbol vector, and $\mathbf{n} \in \mathbb{C}^{N_r \times 1}$ represents additive white Gaussian noise (AWGN) with zero mean and variance σ^2. Each transmitted symbol is drawn from a modulation constellation such as QAM.

3.2 Transceiver Operation

In a typical MIMO transceiver, input data bits are first encoded for error correction, then mapped to complex symbols and transmitted simultaneously across multiple antennas. At the receiver, the received signal is processed through channel estimation, equalization, and signal detection to recover the transmitted symbols. Finally, demodulation and decoding reconstruct the original bitstream. This architecture enables spatial multiplexing and diversity gains, improving spectral efficiency and link reliability [1–3].

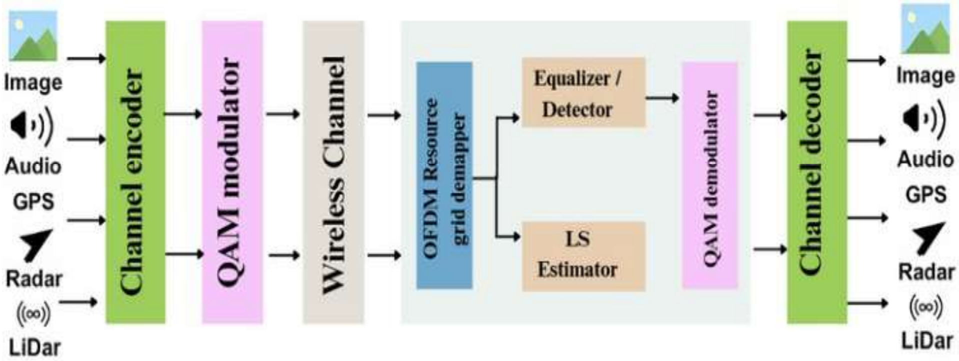

Figure 1: MIMO System Transmit-Receive Block Diagram

4. System Model

4.1 Channel Model Overview

In this work, we evaluate the performance of the Conjugate Gradient (CG) detector under various channel conditions in a basic MIMO system. Specifically, we consider both uncorrelated and spatially correlated channels to study how antenna correlation affects detection performance and convergence speed.

Uncorrelated channels serve as a baseline scenario, where each transmit-receive antenna pair experiences independent Rayleigh fading. In contrast, spatially correlated channels arise in practical deployments due to limited antenna spacing or environmental scattering, which introduces statistical dependencies between antenna elements. Understanding CG performance in both scenarios is critical for assessing its suitability in realistic 5G and 6G MIMO systems. For correlated channels, we adopt the Kronecker correlation model [10] with exponential correlation matrices for both transmitter and receiver sides. By varying the correlation coefficient and the number of CG iterations, we investigate the trade-off between computational complexity and detection accuracy, providing a comprehensive view of CG performance across different channel conditions.

4.2 Flat Fading Assumption

For simplicity, we assume flat-fading channels, where each transmit-receive antenna pair experiences a single complex gain that remains constant over the symbol period. This simplification allows us to focus on evaluating the CG detector without additional complications from frequency-selective fading, making it suitable for our basic MIMO simulations.

4.3 Correlated Channel Model (Kronecker)

In practical MIMO systems, the signals received at multiple antennas are often spatially correlated due to limited scattering or insufficient antenna spacing. To model this effect, we adopt the Kronecker correlation model [10]:

$$\mathbf{H}_{\text{corr}} = \mathbf{R}_{\text{rx}}^{1/2}\mathbf{H}_{\text{iid}}\mathbf{R}_{\text{tx}}^{1/2}, \tag{2}$$

where:

- $\mathbf{H}_{\text{iid}} \in \mathbb{C}^{N_r \times N_t}$ contains i.i.d. complex Gaussian entries $\mathcal{CN}(0, 1)$ representing an uncorrelated Rayleigh fading channel.
- $\mathbf{R}_{\text{rx}} \in \mathbb{C}^{N_r \times N_r}$ is the receive correlation matrix.
- $\mathbf{R}_{\text{tx}} \in \mathbb{C}^{N_t \times N_t}$ is the transmit correlation matrix.

We adopt the exponential correlation model, where each matrix entry is defined as:

$$[\mathbf{R}]_{i,j} = \rho^{|i-j|}, \quad 0 \leq \rho \leq 1, \tag{3}$$

with ρ being the spatial correlation coefficient.
In our simulations, we set $\rho_{\text{tx}} = 0.4$ for the transmit antennas and $\rho_{\text{rx}} = 0.7$ for the receive antennas. This setup corresponds to moderate correlation at the transmitter and higher correlation at the receiver. The Kronecker model is implemented in Sionna to fully define the correlated channel and ensure reproducibility of our results.

4.4 SNR Range Selection and Noise Power

The performance of the Conjugate Gradient (CG) detector is evaluated over a range of signal-to-noise ratio (SNR) values to study its robustness under different channel conditions. In our simulations, we consider SNR values from −10 dB to −1 dB, which represent challenging uplink scenarios commonly encountered in massive MIMO systems with many users or limited transmit power.
For a normalized transmitted signal vector with unit average power ($E[|x|^2] = 1$), the noise vector **n** is modeled as additive white Gaussian noise (AWGN) with variance:

$$\sigma^2 = \frac{N_t}{10^{\text{SNR}_{\text{dB}}/10}} \tag{4}$$

where N_t is the number of transmit antennas. This ensures that the SNR per receive antenna matches the desired simulation value. The following Table 4.4 shows the corresponding noise variance for selected SNR values.

Table 1 . Noise Variance Corresponding to SNR Values (for $N_t = 16$)

SNR (dB)	Linear SNR	Noise Variance σ^2
-10	0.1	10
-5	0.316	3.16
-1	0.794	1.26

Reason for chosen range At very low SNR (e.g., −10 dB), the noise dominates the received signal, making detection extremely challenging. This allows us to observe CG divergence behavior when the number of iterations is insufficient. At higher SNR (e.g., −1 dB), the signal power is comparable to noise, and the CG detector converges faster, showing near-LMMSE performance with fewer iterations. This SNR range also provides insight into numerical stability, since low SNR increases the relative magnitude of rounding errors in iterative methods.

5. Conjugate Gradient Detection

Conventional LMMSE detection involves inverting the matrix $(\mathbf{H}^H\mathbf{H} + \sigma^2\mathbf{I})$, which becomes computationally prohibitive in massive MIMO. Iterative methods such as the Conjugate Gradient (CG) algorithm approximate the LMMSE solution through successive iterations without explicitly computing the matrix inverse, achieving comparable detection performance at significantly reduced computational cost [4–6].

5.1 CG Algorithm

Table 1 summarizes the iterative steps of the CG detector used in this study.

Algorithm 1 CG Detector (based on [8])

```
Require: $\mathbf{A}$ and $\mathbf{b}$
Ensure: Estimated transmit signal vector $\hat{\mathbf{s}}$
Initialize $\hat{\mathbf{s}}^{(0)} = 0, \hat{\mathbf{r}}^{(0)} = \mathbf{b}, \hat{\mathbf{d}}^{(0)} = \hat{\mathbf{r}}^{(0)}$
while $\|\hat{\mathbf{r}}^{(i)}\| > \varepsilon$ do
    Compute step size: $\alpha^{(i)} = \frac{\langle \hat{\mathbf{r}}^{(i)}, \hat{\mathbf{r}}^{(i)} \rangle}{\langle \hat{\mathbf{d}}^{(i)}, \mathbf{A}\hat{\mathbf{d}}^{(i)} \rangle}$
    Update estimate: $\hat{\mathbf{s}}^{(i+1)} = \hat{\mathbf{s}}^{(i)} + \alpha^{(i)}\hat{\mathbf{d}}^{(i)}$
    Update residual: $\hat{\mathbf{r}}^{(i+1)} = \hat{\mathbf{r}}^{(i)} - \alpha^{(i)}\mathbf{A}\hat{\mathbf{d}}^{(i)}$
    Compute direction factor: $\beta^{(i)} = \frac{\langle \hat{\mathbf{r}}^{(i+1)}, \hat{\mathbf{r}}^{(i+1)} \rangle}{\langle \hat{\mathbf{r}}^{(i)}, \hat{\mathbf{r}}^{(i)} \rangle}$
    Update search direction: $\hat{\mathbf{d}}^{(i+1)} = \hat{\mathbf{r}}^{(i+1)} + \beta^{(i)}\hat{\mathbf{d}}^{(i)}$
    $i = i + 1$
end while
return $\hat{\mathbf{s}} = \hat{\mathbf{s}}^{(i)}$
```

Here, $\alpha^{(i)}$ controls the update magnitude, $\beta^{(i)}$ refines the conjugate search direction, $\hat{\mathbf{r}}^{(i)}$ is the residual vector, and $\hat{\mathbf{d}}^{(i)}$ is the search direction. Iterations continue until the residual norm $\|\hat{\mathbf{r}}^{(i)}\|$ is sufficiently small.

CG Divergence and Iteration Trade-Off. The CG algorithm is an iterative solver that approximates the LMMSE solution without directly inverting the channel matrix. For very few iterations, the residual vector may remain large, causing the detector to diverge or produce high BER, especially at low SNR where noise dominates. As the number of iterations increases, the residual decreases, and the BER approaches the LMMSE benchmark. This trade-off between number of iterations and detection accuracy is central to evaluating CG for massive MIMO systems.

5.2 Computational Complexity

After introducing the Conjugate Gradient (CG) algorithm, analyzing its computational complexity is crucial to assess efficiency against other detectors. This reveals the operations per iteration and overall cost relative to system dimensions, helping balance performance and load. Compared to direct methods like LMMSE, it guides the choice of iteration numbers for practical massive MIMO systems. Table 1 compares the computational complexity of LMMSE and CG detectors.

The LMMSE detector provides an exact solution but scales cubically with N_t, which is impractical for massive MIMO. The CG detector iteratively approximates the LMMSE solution

Table 1: Computational Complexity of LMMSE and CG Detectors

Detector	LMMSE	CG
Matrix inversion	$O(8N_t^3)$	–
Matrix-vector multiplication	$O(4N_t^2)$	$O(4N_t^2 + 4N_t + 4)$
Residual update	–	$O(4N_t^2 + 2N_t)$
Search direction update	–	$O(2N_t)$
Total complexity	$O(8N_t^3 + 4N_t^2)$	$O(L(8N_t^2 + 14N_t + 8))$

with per-iteration complexity $O(N_t^2)$. When the number of iterations $L \ll N_t$, CG achieves near-LMMSE performance with significantly lower computational cost, making it suitable for large-scale 5G and 6G systems.

6. Simulation Setup

6.1 Simulation Parameters

This setup, shown in Table 2, provides a scalable and reproducible test environment for analyzing detector behavior under realistic massive MIMO configurations. While the current evaluation focuses on the flat-fading MIMO case, the same CG-based detection process can be applied independently to each subcarrier in wideband MIMO systems, forming the foundation for future 6G experiments.

Table 2: Simulation Parameters and Configurations

Parameter	**5G Configuration**	**6G Configuration**
MIMO Setup	16×64	16×128
Modulation Scheme	16-QAM	128-QAM
Coding	5G LDPC (rate = 1/2)	5G LDPC (rate = 1/2)
Detector	CG vs LMMSE	CG vs LMMSE
Iterations	2, 5, 10, 16	2, 5, 10, 16
Metrics	BER, Residual Norm	BER, Residual Norm
Channel Type	Flat-Fading MIMO	Flat-Fading MIMO
Spatial Correlation	$\rho_{\mathrm{tx}} = 0.4, \rho_{\mathrm{rx}} = 0.7$	$\rho_{\mathrm{tx}} = 0.4, \rho_{\mathrm{rx}} = 0.7$
Tolerance	10^{-12}	10^{-12}

7. Results and Discussion

7.1 Effect of Spatial Correlation on 5G-BER

To evaluate the impact of spatial correlation on massive MIMO detection, we simulated a 16 × 64 5G MIMO system using the CG detector with multiple iteration counts. Two channel scenarios were considered: uncorrelated (i.i.d.) and correlated channels modeled using the Kronecker model with exponential correlation coefficients $\rho_{\text{tx}} = 0.4$ and $\rho_{\text{rx}} = 0.7$.

These Figures presents the BER performance over SNR values from −10 dB to −1 dB for both scenarios.

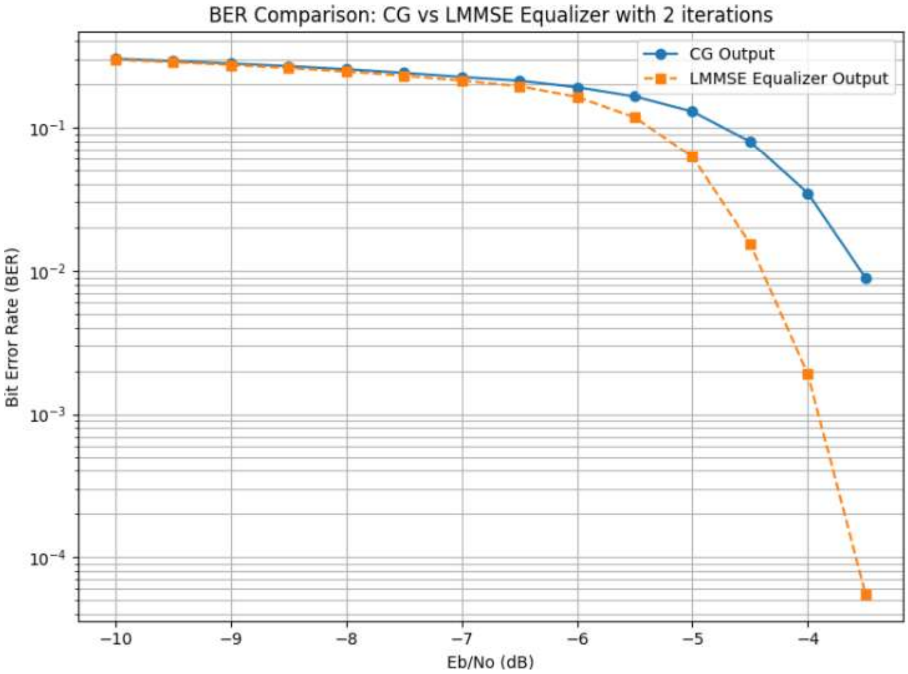

Figure 2: BER vs SNR for uncorrelated channel with 2 iterations.

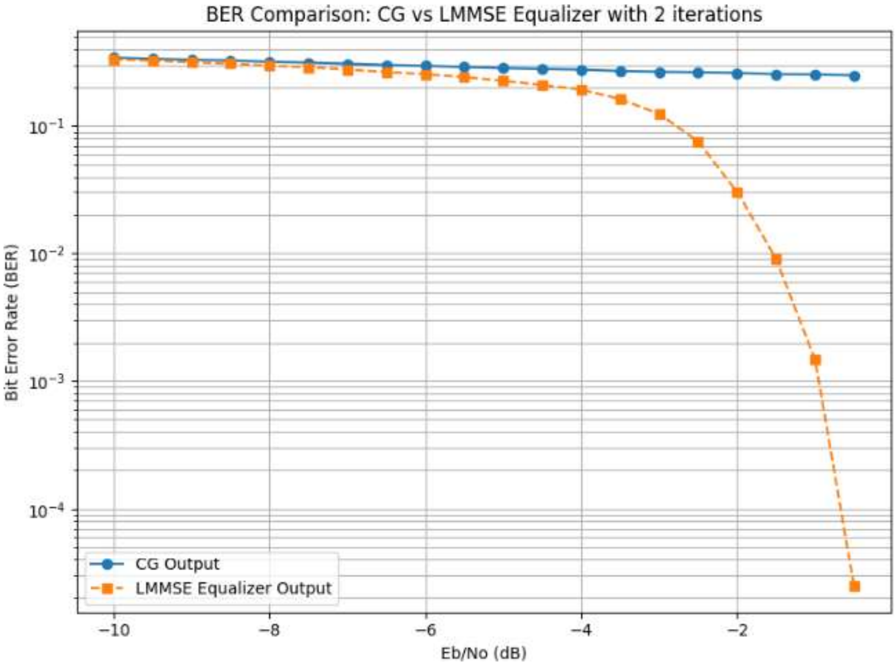

Figure 3: BER vs SNR for correlated channel with 2 iterations in 5G.

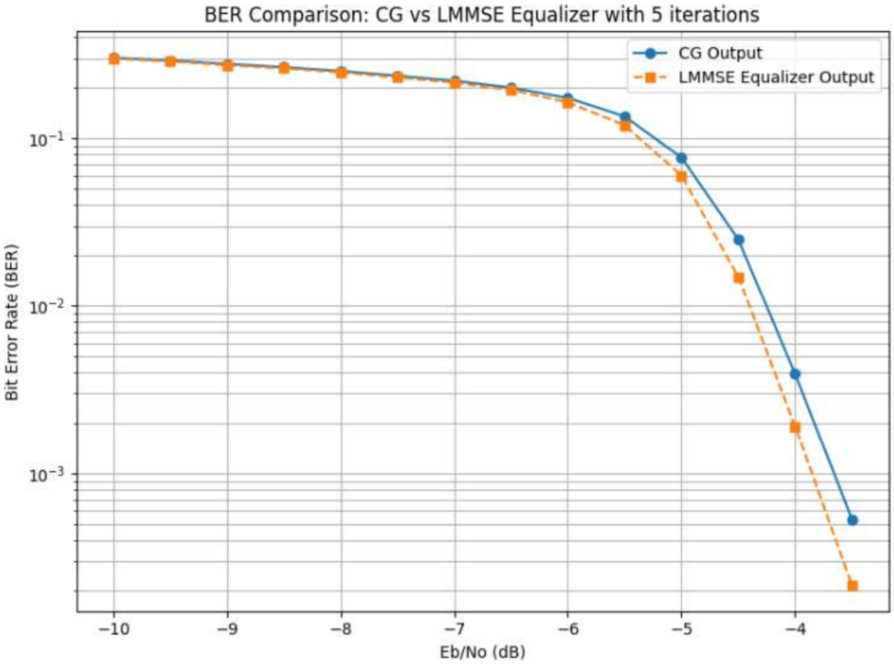

Figure 4: BER vs SNR for uncorrelated channel with 5 iterations in 5G.

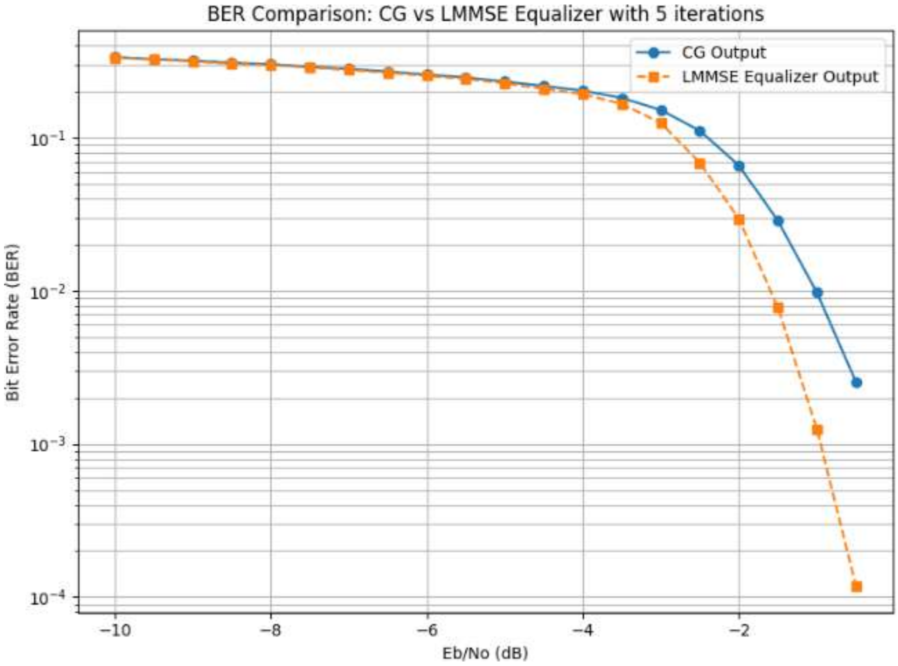

Figure 5: BER vs SNR for correlated channel with 5 iterations in 5G.

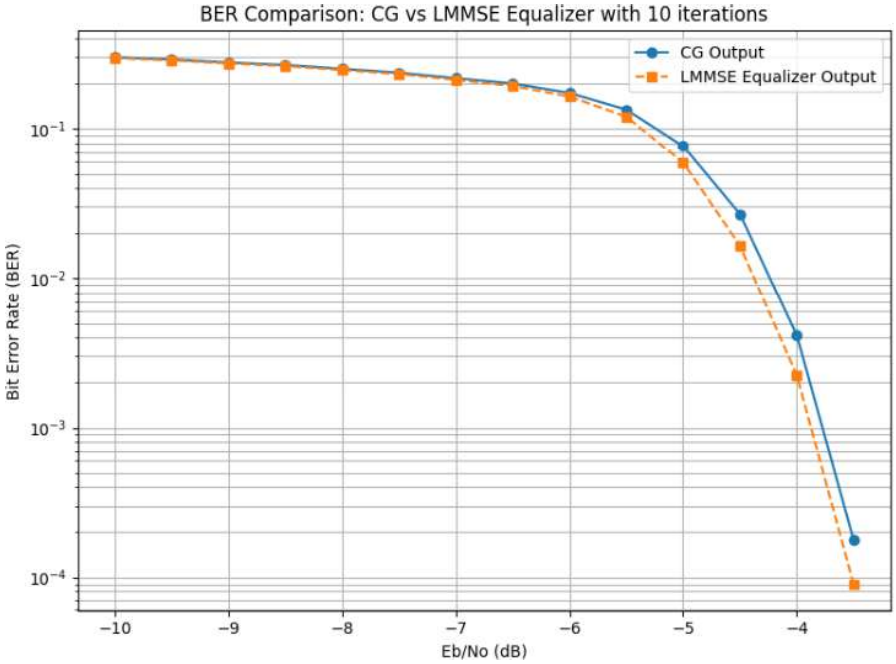

Figure 6: BER vs SNR for uncorrelated channel with 10 iterations in 5G.

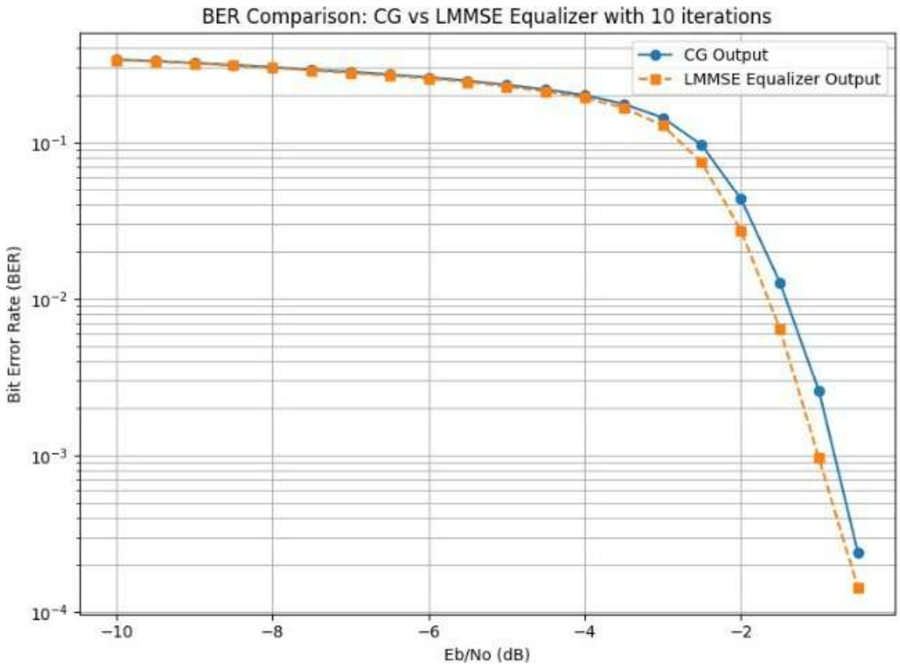

Figure 7: BER vs SNR for correlated channel with 10 iterations in 5G.

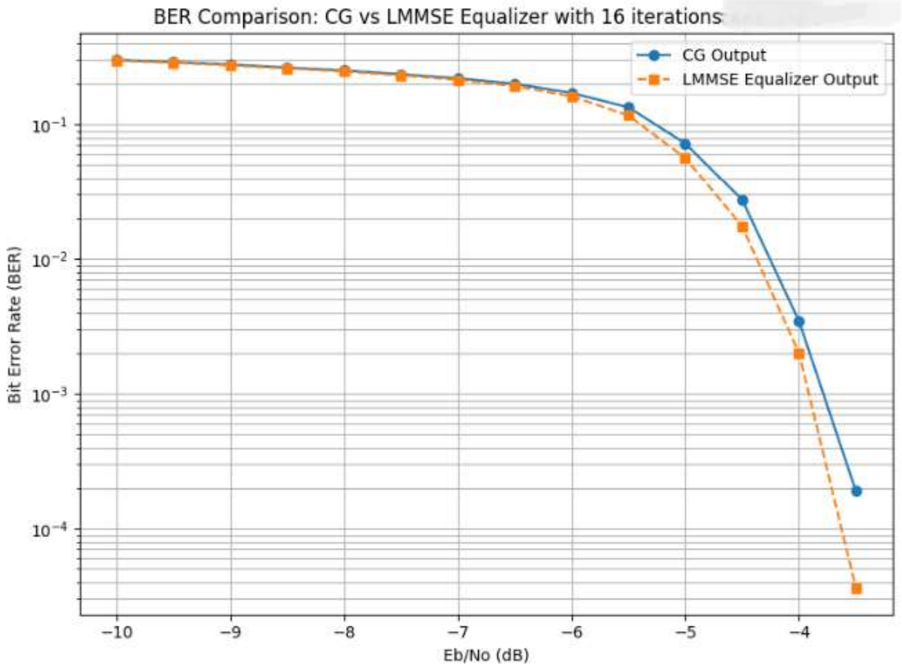

Figure 8: BER vs SNR for uncorrelated channel with 16 iterations in 5G.

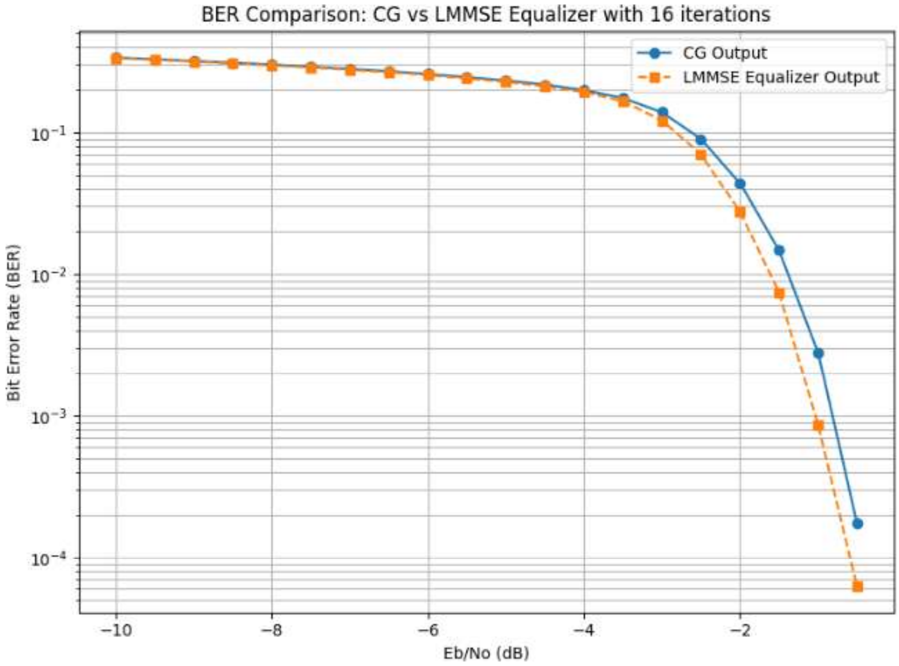

Figure 9: BER vs SNR for correlated channel with 16 iterations in 5G.

The results demonstrate that spatial correlation slightly increases BER compared to the uncorrelated case. This occurs because correlation reduces the effective rank of the channel matrix, which increases interference among transmitted streams and slows convergence of the CG detector. The effect is more pronounced at low SNR values where noise dominates the signal, highlighting that correlated channels are inherently more challenging for iterative detection.

These observations confirm that spatial correlation must be considered when evaluating the performance of CG-based detection algorithms in massive MIMO systems. Additionally, they illustrate the trade-off between channel conditions and detector performance: while CG approximates LMMSE effectively, its convergence and resulting BER are sensitive to the underlying channel correlation structure.

7.2 Performance of CG in Correlated 5G vs 6G Channels

Building upon the 5G results presented in the previous Section, we now evaluate the CG detector performance in correlated 5G and 6G MIMO channels. The goal is to investigate how the detector scales with increasing system size and higher-order modulation while maintaining near-LMMSE performance.

For this analysis, we focus on two representative iteration numbers, 5 and 10, to illustrate the trade-off between convergence speed and system dimensions.

As observed previously, spatial correlation affects BER in 5G; here we examine whether the same trend holds for larger 6G configurations and how additional iterations impact performance in both systems. These results demonstrate the scalability and robustness of the CG detector in massive MIMO systems under realistic correlated channels.

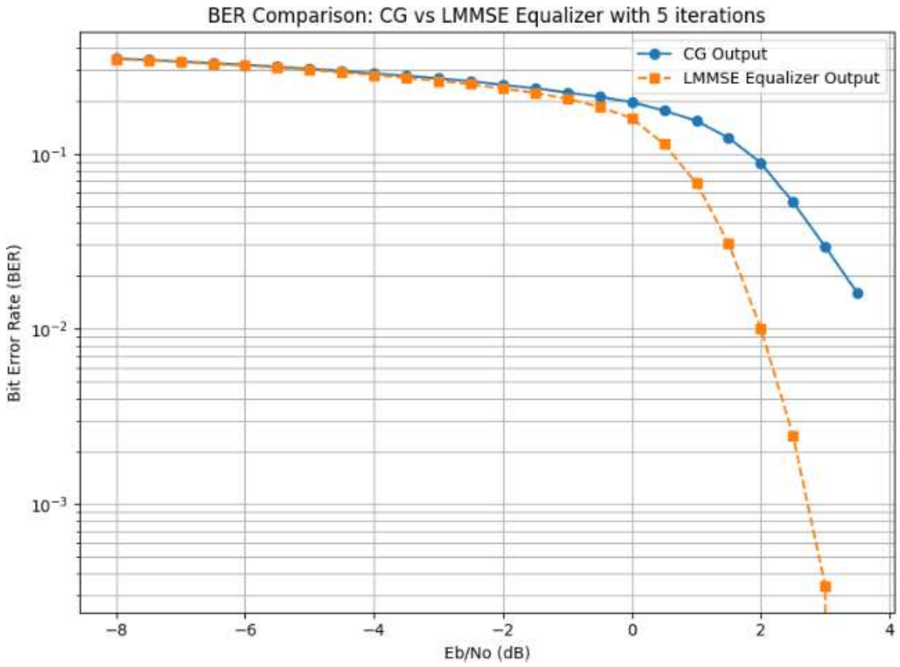

Figure 10: BER vs SNR for correlated channel with 5 iterations in 6G.

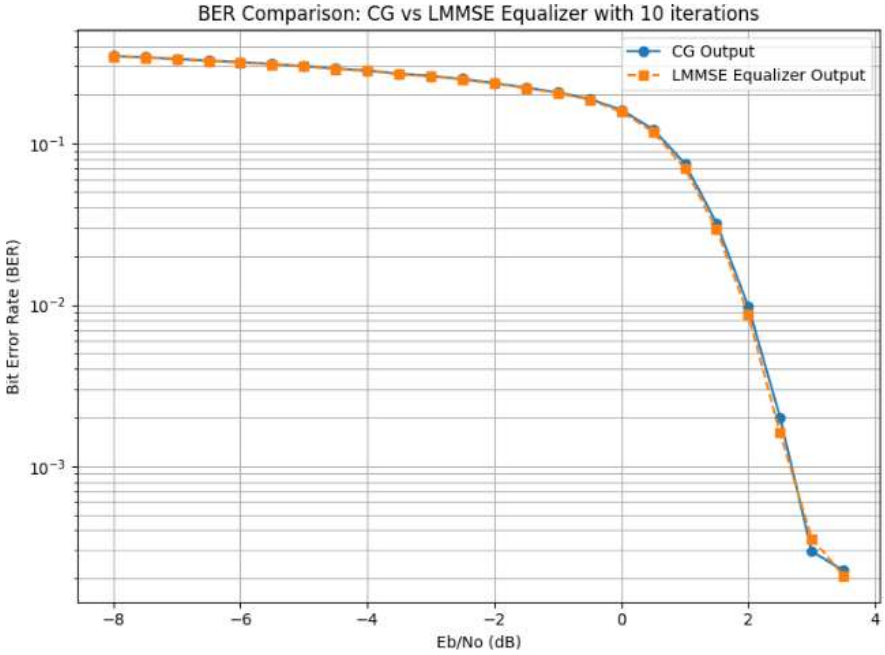

Figure 11: BER vs SNR for correlated channel with 10 iterations in 6G. We can clearly observe that:

- For 5 iterations, the 5G system achieves slightly lower BER than 6G. This is due to the smaller channel dimension and lower-order modulation, which allow faster residual convergence in fewer iterations.
- For 10 iterations, the 6G system achieves better BER performance. With additional iterations, the larger 6G channel matrix benefits more from iterative refinement, allowing the CG detector to approach LMMSE-level performance and slightly surpass 5G in these settings.
- This demonstrates that CG's effectiveness depends not only on SNR and correlation but also on the number of iterations relative to system size and modulation order.

Overall, these results confirm that CG detection scales well with system dimensions and can achieve near-optimal performance in 6G massive MIMO with a reasonable number of iterations.

7.3 Residual Convergence Analysis

The residual norm $\|\mathbf{r}^{(i)}\|$ provides insight into the convergence of the CG detector. Fig. 12 shows the residual evolution for correlated 5G channels, while Fig. 13 shows the residuals for correlated 6G channels.

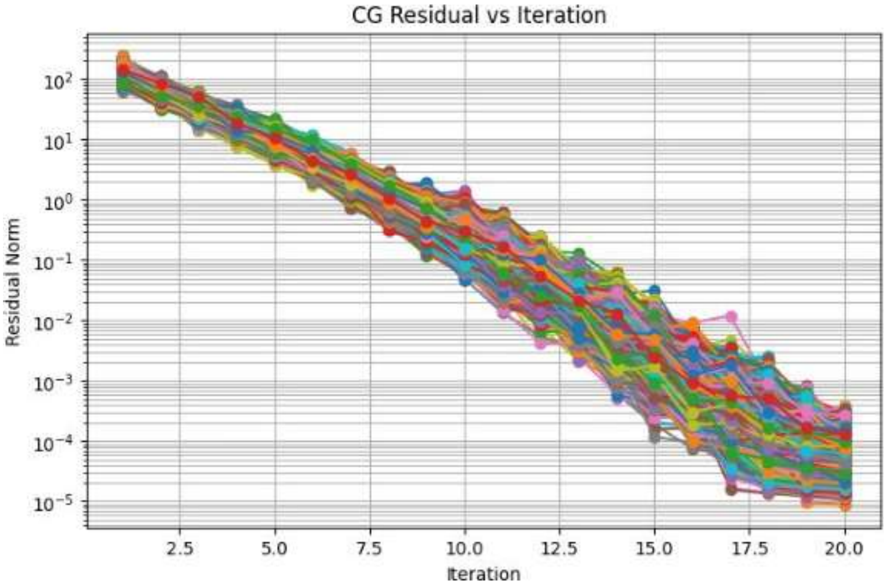

Figure 12: BER performance of the CG detector for 5G correlated and uncorrelated channels.

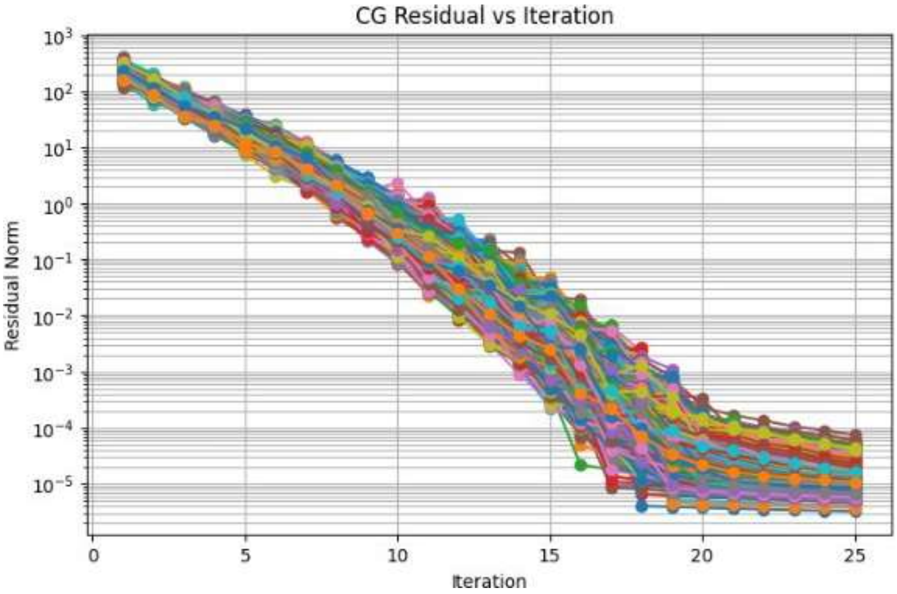

Figure 13: BER performance of the CG detector for 6G correlated and uncorrelated channels.

For 5G, the residual decreases rapidly with iteration count, and after 15 iterations, it is sufficiently small to ensure near-LMMSE detection accuracy. For 6G, the initial residual is higher due to the larger system size and higher modulation order, but it also converges with sufficient iterations. These residual trends explain the BER behavior observed:

At low iteration counts, residuals remain large, resulting in higher BER, especially for correlated channels.

As iterations increase, residuals reduce and BER approaches the LMMSE benchmark.

The comparison between 5G and 6G shows that CG scales well, achieving similar convergence and performance with a reasonable number of iterations.

The results show that CG converges more slowly in larger MIMO systems due to the increased number of unknowns, while channel correlation slightly slows convergence by increasing the condition number. A convergence threshold of 10^{-12} ensures near-LMMSE accuracy without unnecessary computation. Overall, the residual analysis confirms that CG closely approximates the LMMSE solution and indicates how many iterations are needed for different system sizes and channel conditions.

7.4 Computational Complexity

The computational complexity of the Conjugate Gradient (CG) detector, measured in memory cost (bits), depends strongly on the number of iterations. With 10 iterations, CG requires 22,820 bits, which is lower than the 33,792 bits needed by the LMMSE detector. However, increasing the number of iterations to 20 raises CG’s memory usage to 45,640 bits, surpassing LMMSE. This behavior is consistent in both 5G and dense 6G configurations with $N_t = 16$ transmit antennas. It highlights an important trade-off: CG is more efficient when the number of iterations is smaller than the number of transmit antennas, but becomes more resource-intensive if this threshold is exceeded, which is a key consideration in massive MIMO system design.

8. Conclusion

In this paper, we investigated the Conjugate Gradient (CG) detector as a low-complexity alternative to LMMSE for massive MIMO systems in 5G and 6G scenarios. We analyzed its performance over both uncorrelated and correlated flat-fading channels and evaluated the impact of iteration numbers on BER and residual convergence. Simulation results demonstrated that CG achieves near-LMMSE detection accuracy while significantly reducing computational complexity for a moderate number of iterations. Furthermore, spatial correlation slight degrades performance, but CG remains robust, and its efficiency scales well with system dimensions.

These findings confirm that CG-based detection is a practical and scalable solution for real-time massive MIMO deployments, providing an effective trade-off between performance and complexity in next-generation wireless networks.

References

[1] D. Tse and P. Viswanath, Fundamentals of Wireless Communication, Cambridge University Press, 2005.

[2] 3GPP TR 38.901, "Study on channel model for frequencies from 0.5 to 100 GHz," 3rd Generation Partnership Project, 2020.

[3] A. Goldsmith, Wireless Communications, Cambridge University Press, 2005.

[4] C. Jeon, J. Lee, and Y. Sung, "An Efficient Conjugate Gradient-Based Detector for Massive MIMO Systems," IEEE Transactions on Communications, vol. 64, no. 5, pp. 2108–2119, 2016.

[5] B. Yin, M. Wu, C. Studer, J. R. Cavallaro, and J. E. Kneckt, "Conjugate Gradient-Based Soft-Output Detection and Precoding in Massive MIMO Systems," IEEE GLOBECOM, 2014.

[6] A. Liu and V. K. N. Lau, "Low-Complexity Iterative Linear Detection for Large-Scale MIMO Systems via Conjugate Gradient," IEEE Signal Processing Letters, vol. 24, no. 3, pp. 293–297, 2017.

[7] A. Bennatan, M. Stark, H. Wymeersch, and E. Nachmani, "Sionna: An Open-Source Library for Next-Generation Physical Layer Research," arXiv preprint arXiv:2203.11854, 2022.

[8] Y. Wei, M.-M. Zhao, M. Hong, M.-J. Zhao, and M. Lei, "Learned Conjugate Gradient Descent Network for Massive MIMO Detection," in Proc. IEEE Int. Conf. Commun. (ICC), Dublin, Ireland, Jun. 2020, pp. 1–6, doi: 10.1109/ICC40277.2020.9149227.

[9] NVIDIA, "Realistic Multiuser MIMO Simulations — Sionna Documentation," NVIDIA Developer, 2023. [Online]. Available: https://nvlabs.github.io/sionna/phy/tutorials/Realistic_Multiuser_MIMO_Simulations.html

[10] NVIDIA, "Simple MIMO Simulation — Sionna Documentation," NVIDIA Developer, 2023. [Online]. Available: https://nvlabs.github.io/sionna/phy/tutorials/Simple_MIMO_Simulation.html

Islamic University Journal of Applied Sciences (IUJAS)
https://journals.iu.edu.sa/jesc
Special Issue, February 2026, Pages 78-86
https://igee.univ-boumerdes.dz/ncaeee25/

Energy-Aware, PV-Driven Smart Irrigation: A Stepwise Implementation and Field Validation in Biskra

Mohamed Laaouad[1*], Aicha Guergazi[2]

[1]Department of Electrical Engineering, LGEB Laboratory, University of Biskra, Algeria;
Email: Mohamed.laaouad@univ-biskra.dz
[2]Department of Electrical Engineering, LI3CUB Laboratory, University of Biskra, Algeria;
Email: a.guergazi@univ-biskra.dz

[*]Corresponding author:(Mohamed Laaouad) Email: Mohamed.laaouad@univ-biskra.dz

Abstract

This paper presents a reproducible, stepwise implementation and field validation of a photovoltaic (PV)-driven smart irrigation controller that tightly couples soil moisture feedback, low-cost sens-ing to improve energy and water efficiency in semi-arid agriculture. We document hardware selec-tion, laboratory calibration of FC-28 sensors against volumetric water content (VWC) reference samples (including regression statistics), controller design (bounded proportional law and safety interlocks), and an energy accounting inline power measurement. A field deployment in Biskra (March conditions) demonstrates soil moisture regulation within target bounds while reducing pump electrical consumption by approximately 18 % relative to a fixed speed benchmark. We dis-cuss limitations, sensor drift mitigation, and extensions—predictive scheduling using short term irradiance forecasts and distributed sensing for larger fields.

Keywords: Photovoltaic, Arduino, Solar irrigation, Variable drive, FC-28, Efficiency.

---

https://doi.org/10.63070/jesc.2026.007
Received 28 November 2025; Revised 15 January 2026; Accepted 25 January 2026.

Published by Islamic University of Madinah on behalf of *Islamic University Journal of Applied Sciences*.

1. Introduction

Water and energy are tightly coupled resources in arid and semi-arid regions, where irrigation is the principal consumer of scarce freshwater and a growing share of rural electricity demand [1, 2]. Conventional irrigation systems typically operate pumps at fixed speed or on simple timed schedules, decoupling water delivery from instantaneous crop needs and from renewable energy availability [3]. This mismatch leads to avoidable water loss, elevated energy consumption, and dimin-ished resilience to supply variability [4,5]. Recent advances in distributed photovoltaic generation, power electronics, and embedded sensing enable active coupling of irrigation dynamics to both plant water demand and instantaneous renewable supply, opening a path to more efficient, resilient irrigation [6, 7].

This paper contributes a reproducible, field validated methodology that integrates a PV array, Arduino based controller, calibrated low-cost moisture sensing (FC-28), and a DC pump. Our work addresses three gaps in the literature: (1) a lack of reproducible stepwise implementation for re-source constrained contexts where PV and pumping hardware are constrained; (2) underreported calibration and drift characteristics of low-cost resistive moisture probes in field conditions, which impede reliable closed loop control; and (3) scarce empirical studies that jointly quantify agro-nomic performance (moisture regulation) and energy performance (pump energy aligned to PV generation) for variable irrigation.

We present the complete pipeline from component selection through laboratory calibration, control design, bench validation, and field deployment in Biskra, Algeria. Key contributions are: (i) a stepwise implementation framework with concrete calibration and control parameters to enable reproducibility; (ii) an empirical evaluation linking moisture regulation fidelity to measured electrical energy savings and PV utilisation; and (iii) an analysis of practical limitations and recommended extensions such as forecast driven scheduling and distributed telemetry.

The remainder of the paper is organised stepwise. Section 2 details the experimental methodology and calibration procedures. Section 3 reports field measurements linking moisture dynamics and energy consumption. Section 4 discusses implications and future directions. Section 5 conclusion.

2. Methodology: Stepwise Implementation

We organised the methodology into discrete, sequential steps to facilitate reproducibility and systematic validation. Each step is designed to be self-contained, clearly specifying implementation procedures, instrumentation configurations, and operational parameters. Quantitative acceptance criteria are defined to assess performance and ensure consistency across experimental trials.

This structured approach enables transparent evaluation and straightforward replication of the proposed system.

2.1. Step 1 — Component Selection and Sizing

Component choices were driven by resource constrained deployment objectives (low-cost, local availability) while meeting agronomic and hydraulic needs.

PV array: A commercial 20 W module (XD20-12P) was used for prototyping. Key parameters nameplat (Table 1):

Table 1: Photovoltaic module parameters

Parameter	Value	Unit
Maximum Power $P_{\max}$	20	W
Voltage at $P_{\max}$ V_{mp}	17.5 V	V
Current at $P_{\max}$ I_{mp}	1.14	A
Open-Circuit Voltage V_{oc}	21.24 V	V
Short-Circuit Current I_{sc}	1.28	A
Power tolerance	±0.6	%

Pump and motor: A small centrifugal pump driven by a 24 DC voltage motor was selected to deliver the observed irrigation requirement L/h. The pump was controlled via boost converter of receiving an PWM input from the Arduino.

Control and sensing hardware: The embedded controller is an Arduino (ATmega328P platform). Soil moisture sensing used FC-28 resistive probes. A LM393 comparator provided a hardware pressure interlock interface; inline current transducer (Hall effect) and a power meter were used for electrical energy measurement. All instrumentation was logged with timestamps to an SD card on the Arduino and backed up via a laptop during field tests.

Acceptance criteria (Step 1). Each component must interface electrically and mechanically; boost converter accepts controller input and responds within nominal latency (¡200 ms); power metering operational.

2.2. Step 2 — FC-28 Sensor Calibration

Low-cost FC-28 probes exhibit non-linear and soil-dependent behavior, which has been observed in several studies [9, 10]. We performed laboratory calibration against volumetric water content (VWC) reference samples prepared with locally sourced soil.

Procedure.

1. Prepare soil samples at target VWC setpoints: 10, 15, 20, 25, 30, 35, 40 % (gravimetric method converted to VWC using bulk density).
2. Insert FC-28 probes into each sample and record ADC output voltage (10-bit ADC, 0–5 V reference) ADC output voltage after stabilisation (60 s) for 10 repeated readings.
3. Fit regression models mapping ADC voltage V_{out} to VWC using ordinary least squares.

Model selection. Over the 10–40 % range the response was well approximated by a single linear model:

$$\mathrm{VWC} \approx aV_{\mathrm{out}} + b,$$

with coefficients obtained by least squares: $a = -11.24$ %/V, $b = 42.8$ % (example values from our calibration run). Regression statistics: $R^2 = 0.987$, RMSE $= 1.12$ percentage points, $n = 70$ observations (7 setpoints × 10 readings). The negative slope reflects the typical resistive probe response where higher moisture reduces resistance and thus changes voltage reading direction depending on the conditioning circuit.

Uncertainty and drift. Short term repeatability (within a single calibration session) produced standard deviation $\sigma \approx 0.6$ % VWC. Field drift was observed over weeks; we recommend periodic recalibration every 4–8 weeks or use of a two-point field recalibration.

Acceptance criteria (Step 2). The linear model RMSE was RMSE ¡ 1.5% VWC across the oper-ational range 10–40%, which meets the standard performance requirements for low-cost moisture sensors in agricultural applications [8].

2.3. Step 3 — Control Law, Set points, and Safety Interlocks

Control is implemented on the Arduino and issues an analogue 0–5 V command to boost converter mapped to motor speed.

Notation. Let $\mathrm{VWC}_{\mathrm{meas}}$ denote measured volumetric water content (%), and $\mathrm{VWC}_{\mathrm{target}}$ the desired set point. Let ω_{min} and ω_{max} denote minimum and maximum motor speeds (normalised to Boost converter input), and K_p the proportional gain (normalised to produce compatible command units).

Activation/deactivation thresholds.

- Activation threshold: $\mathrm{VWC}_{\mathrm{act}} = 10\,\%$ (below this the controller enables irrigation).
- Deactivation (target): $\mathrm{VWC}_{\mathrm{target}} = 35\,\%$ (irrigation stops when this is reached).

Proportional control law with saturation.

$$\omega_{\mathrm{cmd}} = \omega_{\mathrm{min}} + K_p \cdot (\mathrm{VWC}_{\mathrm{target}} - \mathrm{VWC}_{\mathrm{meas}})$$

saturated to $\omega_{\mathrm{min}} \leq \omega_{\mathrm{cmd}} \leq \omega_{\mathrm{max}}$.

In implementation, the proportional control law with saturation is expressed as:

$$\omega_{\mathrm{cmd}} = \min(\omega_{\mathrm{max}}, \max(\omega_{\mathrm{min}}, \omega_{\mathrm{min}} + K_p\,(VWC_{\mathrm{target}} - VWC_{\mathrm{meas}}))),$$

ensuring that the commanded motor speed remains within the allowable range:

$$\omega_{\min} \leq \omega_{\text{cmd}} \leq \omega_{\max}.$$

Example tuning used $\omega_{\min} = 0.25$ (25 % normalised speed), $\omega_{\max} = 1.0$, $K_p = 0.018$ (per percent-age point VWC) yielding stable convergence without oscillation in field trials.

Safety interlocks.

- Minimum PV voltage check: if PV array voltage $V_{\text{pv}} < 12.5\,\text{V}$, the controller ramps to $\omega_{\min}$ and inhibits further speed increases to avoid boost converter faulting.
- Pressure interlock (LM393): if pressure below safe threshold (pump cavitation risk) or above maximum (blocked discharge), controller disables pump.
- Watchdog and fault states: Arduino watchdog resets controller on software freeze

Acceptance criteria (Step 3). Controller must maintain moisture within hysteresis band [VWC_{act}, $\text{VWC}_{\text{target}}$] during steady conditions and respect safety interlocks.

2.4. Step 4 — Integration, Bench Validation, and Logging

Bench tests. Hardware integration verified in controlled bench tests Figure 1: closed loop response to step changes in simulated soil moisture (potentiometer emulating probe output), boost converter command response time (trs <200 ms), and power draw characterisation at multiple speeds using inline power meter (Fluke class instrument).

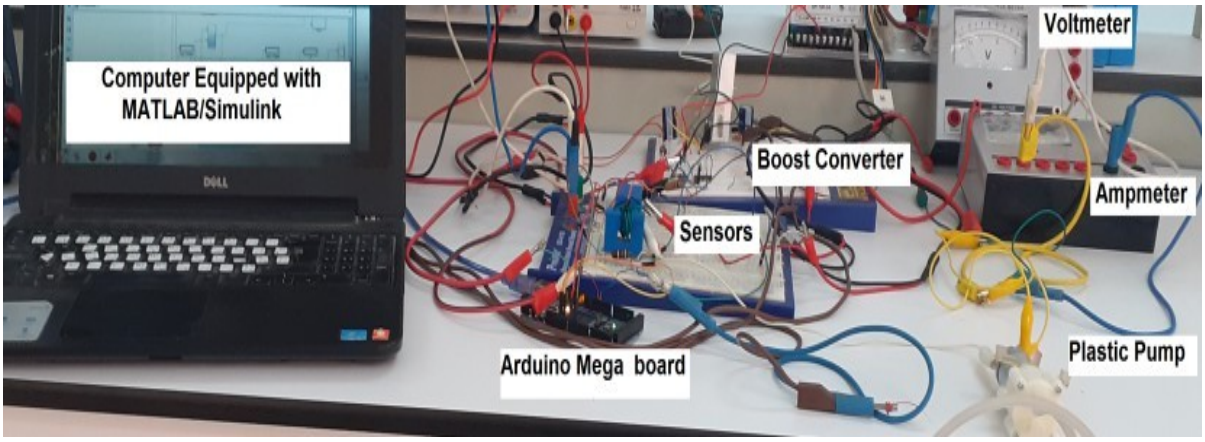

Figure 1: The Tests Bench

Logging. The Arduino logs at 1 Hz: timestamp, VWC (calibrated), boost converter command (normalised), PV voltage, PV current, pump current, and pressure sensor. Data were backed up to a laptop during field sessions.

Field deployment layout. The Biskra site was divided into three monitored zones with an FC-28 probe per zone and pressure gauges at pump discharge and in-field laterals to capture spatial vari-ability.

Acceptance criteria (Step 4). All logs consistent, no persistent boost converter faults during trials, and sensors return physically plausible values.

3. Field Results and Analysis

We summarise representative results obtained from the March field deployment as ordered performance derived from continuous system operation. The analysis focuses on irrigation efficiency, photovoltaic energy utilisation, and adaptive control stability under real environmental conditions, these outcomes are as following points.

3.1. Climatic context and PV availability

Climate on March figure 2 clear sky showed peak global horizontal irradiance to approximate 1100 Wm^{-2} at midday, sunrise around 06:15 and sunset to approximate 18:00 local time. Under clear skies direct irradiance dominated near noon (estimated direct fraction 85-90 %), producing PV output sufficient to operate the pump near rated power during a midday window.

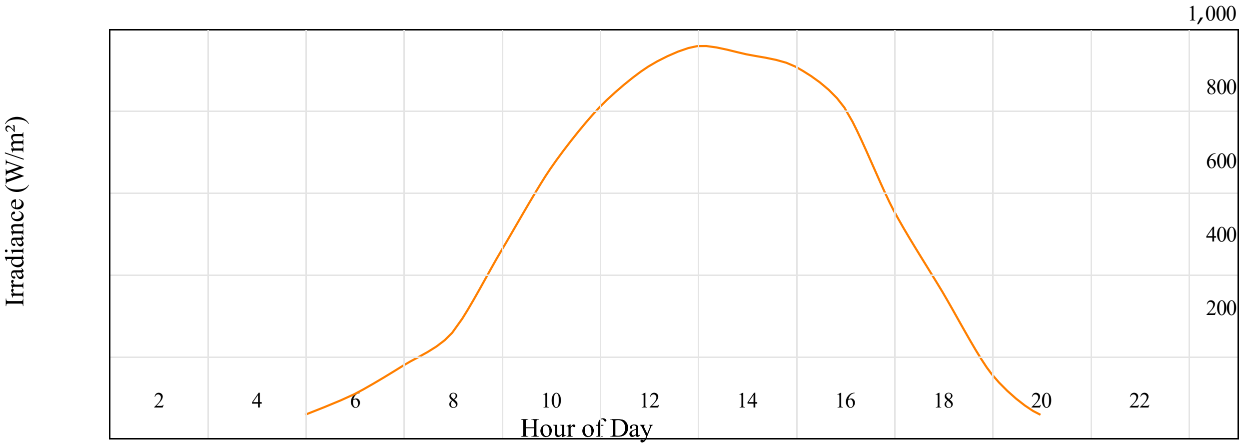

Figure 2: Solar Irradiance in Biskra on a Typical Day (March 2025)

3.2. Soil moisture regulation

Figure 3 shows a representative moisture trace across a diurnal irrigation event for one monitored zone. The controller activated near 10 % VWC, modulated pump speed to raise moisture towards 35 %, and then allowed depletion until the next activation cycle. Measured moisture remained within the specified hysteresis band with peak overshoot below 2 % on average across experiments.

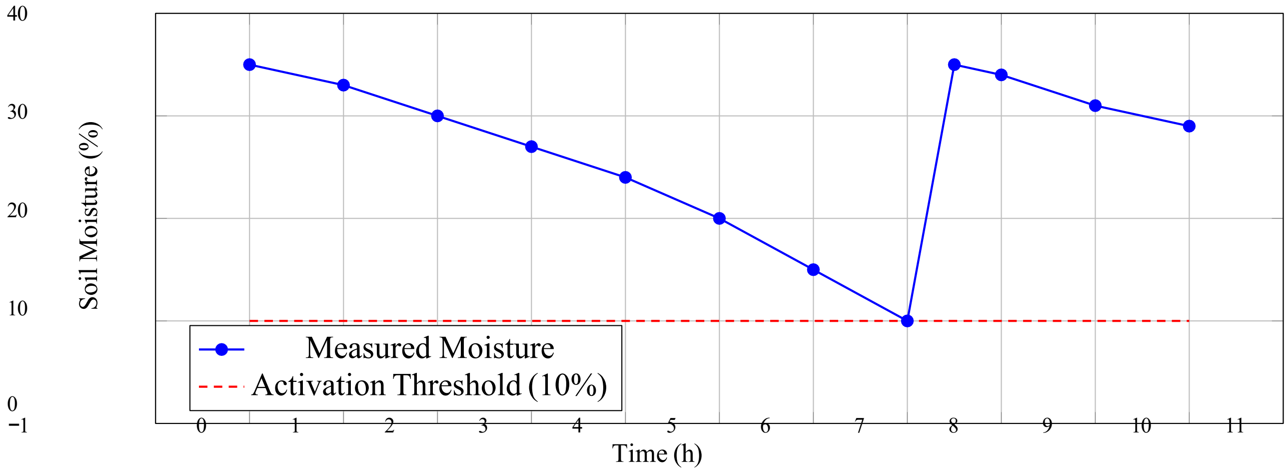

Figure 3: Soil moisture response during a representative irrigation cycle

3.3. Energy accounting and comparison to fixed-speed baseline

Energy consumption was measured with an inline power meter and cross-checked against boost converter internal energy counters. We compared two control modes over identical irrigation demands:

3.3.1. Variable-speed (our PV aware proportional controller).

3.3.2. Fixed-speed (baseline): pump runs at constant 100 % normalized speed until target moisture is reached; pump operation scheduled identically when PV available.

Over multiple irrigation cycles across 10 experimental days, variable speed operation reduced electrical energy consumption by an average of 18 % relative to the fixed speed benchmark while maintaining target moisture levels and comparable irrigation volumes. Energy savings arise from reduced hydraulic losses at lower speeds (pump affinity laws) and improved synchronisation with PV peak output, which reduces reliance on stored/grid power.

3.4. Sensor reliability and operational observations

After field deployment the FC-28 probes retained acceptable accuracy but exhibited slow drift: a mean bias of +0.9 % VWC after four weeks relative to initial calibration. We therefore recommend scheduled recalibration (monthly in harsh soils) or use of two point field recalibration anchored to a gravimetric sample.

4. Discussion

The experimental results demonstrate that proportional modulation of pump speed under PV constraints yields measurable energy savings without compromising moisture regulation. Low-cost FC-28 probes are operationally useful after laboratory calibration; however, drift and site dependence limit unattended deployments without periodic recalibration.

Research opportunities and practical extensions include:

- **Predictive scheduling.** Integrating short term irradiance forecasts (e.g., persistence or satel-lite nowcasts) to shift irrigation to forecasted high PV windows can increase renewable util-isation and further cut grid reliance.
- **Distributed sensing and optimisation.** Scaling to larger fields requires distributed probes, wireless telemetry, and multi zone optimisation to minimise moisture variance across zones.
- **Sensor fusion for robustness.** Combining low-cost resistive probes with time domain re-flectometry (TDR) spot checks or root zone tensiometers can increase confidence in closed loop control.
- **Economic and lifecycle analysis.** Long term studies should quantify maintenance, sensor replacement frequency, and cost benefit tradeoffs under realistic farmer operation models.

5. Conclusion

We presented a stepwise, reproducible implementation of a PV-driven, DC-modulated smart irrigation system integrating Arduino based control and calibrated FC-28 soil-moisture probes. Laboratory calibration, conservative control tuning, and embedded safety interlocks ensured stable field operation in Biskra's semi-arid climate, characterised by high solar irradiance and variable soil moisture response. Experimental validation confirmed that the system achieved an average energy reduction of approximately 18 %compared to a conventional fixed-speed pumping configuration, while maintaining acceptable soil-moisture regulation within the agronomic tolerance range.

Beyond the quantitative savings, the developed platform demonstrated that low-cost, open-source hardware combined with renewable-energy integration can significantly enhance water-use effi-ciency and reduce dependence on fossil-powered pumping infrastructure. The modular system architecture allows scalable adaptation to different crop types, soil textures, and photovoltaic ca-pacities, enabling broader deployment in resource-constrained agricultural in arid and semi-arid regions.

Acknowledgments

The authors thank the University of Biskra field team for assistance with site preparation and data acquisition.

References

[1] J. A. Allan, "Irrigation in the Middle East: A review of the potential for sustainable management," *Water Resour. Dev.*, vol. 19, no. 3, pp. 415–437, 2003.

[2] B. A. Lankford, "Rural energy and irrigation in developing regions," *Int. J. Water Resour. Dev.*, vol. 28, no. 4, pp. 453–466, 2012.

[3] D. Lohmann and X. Zeng, "Smart irrigation systems: Challenges and opportunities," *Renew. Sustain. Energy Rev.*, vol. 68, pp. 688–702, 2017.

[4] S. Geerts and D. Raes, "Deficit irrigation as an on-farm strategy to maximize crop water productivity in dry areas," *Agric. Water Manag.*, vol. 96, no. 9, pp. 1287–1294, 2009.

[5] Z. Zeng et al., "Water-Energy Nexus in Agricultural Irrigation: A Case Study of the United States," *Nat. Sustain.*, vol. 1, no. 10, pp. 495–502, 2018.

[6] J. Zhao et al., "Advances in Photovoltaic Irrigation Systems: Challenges and Prospects," *Energy Rep.*, vol. 5, pp. 370–379, 2019.

[7] J. He et al., "Integration of renewable energy in irrigation systems: Photovoltaic water pump-ing in China," *Renew. Energy*, vol. 118, pp. 143–150, 2018.

[8] A. Verma *et al.*, "Renewable energy driven irrigation systems for small-scale agriculture: A review," *Energy Convers. Manag.*, vol. 213, p. 112810, 2020.

[9] M. M. Kharita *et al.*, "Field calibration of soil moisture sensors in semi-arid regions," *Soil Tillage Res.*, vol. 150, pp. 107–114, 2015.

[10] A. H. Reinders *et al.*, "Performance of low-cost moisture sensors in soil," *Sensors*, vol. 19, no. 14, p. 3199, 2019.

Islamic University Journal of Applied Sciences (IUJAS)
https://journals.iu.edu.sa/jesc
Special Issue, February 2026, Pages 87-95
https://igee.univ-boumerdes.dz/ncaeee25/

Magnetothermal Analysis of Gold Melting in Crucible-Based Induction Furnaces Using Finite Volume Method

Zine Rezgui [1*], Sid-Ahmed Touil [2], Ammar Tibouche [1], Nabil Ikhlef [1]

[1]*Department of Electrical Engineering, Laboratory of electrical engineering and industrial electronics L2EI* University of Jijel*,* ALGERIA rezguizine73@gmail.com, tibouche_ammar@yahoo.fr, ikhlefnabil@yahoo.fr

[2]Institute of Electrical and Electronic Engineering, University of M'hamed BOUGARA - Boumerdes, ALGERIA s.touil@univ-boumerdes.dz

*Corresponding author: (Zine Rezgui), *Email Address*: rezguizine73@gmail.com

Abstract

This study examines the thermal and electromagnetic behavior of pure gold during induction heating, an area that has received limited research attention despite the widespread industrial use of induction technology for melting various metals. The research employs a finite volume computational method to analyze a 50 Hz crucible-based induction furnace [1], diverging from the finite element techniques typically used in previous investigations. The analysis focuses on determining the time and energy requirements needed to bring gold to its melting point of 1337.33 K, tracking the coupled magnetic and thermal processes throughout the heating cycle. The study presents theoretical foundations of electromagnetic and heat transfer principles. However, the modeling approach does not capture the actual melting transition or the coexistence of solid-liquid phases, as incorporating these phenomena would require advanced phase-change modeling and fluid dynamics calculations beyond the current scope.

Keywords: Induction heating, Gold, Magnetic process, Thermal process, Phase-change modeling,

---

https://doi.org/10.63070/jesc.2026.008
Received 25 November 2025; Revised 18 January 2026; Accepted 24 January 2026.

Published by Islamic University of Madinah on behalf of *Islamic University Journal of Applied Sciences*.

1. Introduction

Induction heating represents a widely adopted industrial technology for metal processing, yet the specific thermal and electromagnetic characteristics of pure gold during induction melting have received comparatively limited research attention. This study addresses this gap by investigating the coupled magneto-thermal behavior of gold subjected to 50 Hz crucible-based induction heating, employing a finite volume computational approach that differs from the finite element methods predominantly used in the literature.

The research focuses on characterizing the time-dependent electromagnetic and thermal processes that occur as gold progresses from ambient conditions to its melting point of 1337.33 K. Understanding these coupled phenomena is essential for optimizing industrial induction melting operations, where energy efficiency and process control directly impact manufacturing economics and product quality.

Induction heating operates through electromagnetic induction, where alternating current flowing through a coil generates time-varying magnetic fields that induce eddy currents within electrically conductive workpieces. These induced currents encounter electrical resistance, generating volumetric heat through Joule heating. The process exhibits inherent complexity due to the interdependence of electromagnetic and thermal fields: material electrical conductivity varies with temperature, which in turn affects current distribution and heat generation patterns.

This investigation employs sequential coupling methodology to solve the governing electromagnetic and heat transfer equations using finite volume discretization. The approach tracks the evolution of magnetic vector potential distributions, induced current patterns, volumetric power dissipation, and temperature fields throughout the heating cycle [1]. Particular attention is given to the skin effect phenomenon, the tendency of alternating currents to concentrate near conductor surfaces which produces characteristic thermal gradients in the gold specimen.

The study provides theoretical foundations of the electromagnetic and heat transfer principles governing induction heating, presents the mathematical framework and numerical solution techniques, and analyzes the spatiotemporal behavior of key physical quantities during the heating process. While the current modeling approach does not incorporate phase-change phenomena or fluid dynamics associated with actual melting, it successfully predicts the energy requirements and temporal characteristics needed to bring gold to its fusion temperature, offering valuable insights for industrial furnace design and operation.

2. Mathematical Framework

Electromagnetic Theory

The mathematical modeling of induction heating can be simplified by neglecting charge distribution effects [2] and expressing the electromagnetic behavior solely through magnetic vector potential. For non-magnetic materials experiencing sinusoidal electromagnetic variations, the governing equation reduces to a more manageable form shown in Eq. (1),

$$Rot\left(Rot(\vec{A})\right) + j\omega\sigma(T)\mu\vec{A} = \mu J_{ex} \tag{1}$$

Where A represents the circumferential magnetic vector potential component (measured in *T.m*), *j* denotes the imaginary unit, ω indicates angular frequency (*rad/s*), σ represents electrical conductivity (*S/m*), and μ signifies magnetic permeability (*H/m*). The workpiece's electrical conductivity changes with temperature according to established relationships in references [3, 4], while the crucible is modeled with air-equivalent properties and the coil region excludes induced current effects by removing transient terms.

Heat Transfer Formulation

The thermal behavior during heating is captured through a transient diffusion equation (Eq. 2) that accounts for temperature-dependent material properties.

$$\rho(T)\,C(T)\,\frac{\partial T}{\partial t} = \nabla\cdot(k(T)\,\nabla T) + Q(T) \tag{2}$$

With: $\boldsymbol{Q(T) = \frac{1}{2}\sigma(T)\omega^2 AA^*}$.

In this formulation, *T* denotes temperature (*K*), ρ represents density (*kg/m³*), *C* indicates specific heat capacity (*J/(kg.K)*), *k* signifies thermal conductivity (*W/(m.K)*), and *Q* represents internal heat generation (*W/m³*) derived from the electromagnetic solution through the complex conjugate of the magnetic vector potential A^*. Both the crucible and gold workpiece exhibit temperature-dependent variations in their thermal properties ρC and k [3, 5-7].

Henceforth, for notational convenience, we omit the temperature dependence term and simply write instead σ of $\sigma(T)$, with similar notation for ρC and k and Q.

Coupled Magnetothermal Numerical Technique

Electromagnetic Modeling

The magneto-dynamic equation for axisymmetric geometries in cylindrical coordinates takes the form shown in Eq. (3). The finite volume method divides the computational domain into discrete cells [1].

$$-\frac{\partial^2 A}{\partial z^2}+\frac{A}{r^2}-\frac{1}{r}\frac{\partial}{\partial r}\left(r\frac{\partial A}{\partial r}\right)+j\omega\sigma\mu A=\mu J_{ex} \qquad (3)$$

The spatial derivatives are converted to algebraic differences between nodal values through standard integration procedures. Assuming uniform grid spacing and applying appropriate algebraic operations, the continuous differential equation reduces to a discrete five-point formula given by Eq. (4),

$$a'_p A_p = a'_e A_E + a'_w A_W + a'_n A_N + a'_s A_S + b'_p \qquad (4)$$

Where:

$$a'_e=\frac{r_e\Delta z}{\Delta r},\ a'_w=\frac{r_w\Delta z}{\Delta r},\ a'_n=\frac{r_p\Delta r}{\Delta z},\ a'_s=\frac{r_p\Delta r}{\Delta z},$$

$$a'_p=a'_e+a'_w+a'_n+a'_s+j\omega\sigma_p\mu r_p\Delta r\Delta z+\ln\left(\frac{r_e}{r_w}\right)\Delta z \ \text{ and } b'_p=\mu J_{ex} r_p\Delta r\Delta z$$

Here, in represents the natural logarithm function.

Where coefficients $\boldsymbol{a'_e, a'_w, a'_n, a'_s,}$ ***and*** $\boldsymbol{b'_p}$ are defined in terms of mesh dimensions, material properties, and excitation current density.

Heat Transfer Modeling

For axisymmetric problems where temperature varies only with radial and axial coordinates, the thermal diffusion equation simplifies to Eq. (5).

$$\rho C\frac{\partial T}{\partial t}=\frac{1}{r}\frac{\partial}{\partial r}\left(rk\frac{\partial T}{\partial r}\right)+\frac{\partial}{\partial z}\left(k\frac{\partial T}{\partial z}\right)+Q \qquad (5)$$

Although electromagnetic calculations encompass the entire domain including the coil, thermal analysis is restricted to the workpiece and crucible regions based on physical relevance [1, 2]. The discretization strategy follows the finite volume approach [1, 8, 9], integrating Eq. (5) over both the control volume and time interval to produce Eq. (6).

$$\int_t^{t+\Delta t}\int_s^n\int_w^e \rho C\frac{\partial T}{\partial t}2\pi r dr dz\, dt = \int_t^{t+\Delta t}\int_s^n\int_w^e \frac{1}{r}\frac{\partial}{\partial r}\left(rk\frac{\partial T}{\partial r}\right)2\pi r dr dz dt +$$
$$\int_t^{t+\Delta t}\int_s^n\int_w^e \frac{\partial}{\partial z}\left(k\frac{\partial T}{\partial z}\right)2\pi r dr dz\, dt + \int_t^{t+\Delta t}\int_s^n\int_w^e Q 2\pi r dr dz\, dt$$

(6)

An implicit time-marching scheme is employed to ensure computational stability and accuracy. Under uniform mesh spacing assumptions, these manipulations culminate in the discrete five-point stencil formula shown in Eq. (7), with coefficients $\boldsymbol{a'_e, a'_w, a'_n, a'_s,}$ ***and*** $\boldsymbol{b'_p}$ defined based on thermal properties, mesh parameters, and time step size.

$$a_p T_p^{n+1} = a_e T_E^{n+1} + a_w T_W^{n+1} + a_n T_N^{n+1} + a_s T_S^{n+1} + b_p \qquad (7)$$

Where: $a_e = \frac{r_e k_e \Delta z}{\Delta r}$, $a_w = \frac{r_w k_w \Delta z}{\Delta r}$, $a_n = \frac{r_p k_n \Delta r}{\Delta z}$, $a_s = \frac{r_p k_s \Delta r}{\Delta z}$, $a_p = a_e + a_w + a_n + a_s + \frac{\rho C_p r_p \Delta r \Delta z}{\Delta t}$, and $b_p = Q_p r_p \Delta r \Delta z + \frac{\rho C_p r_p \Delta r \Delta z}{\Delta t} T_p^n$

The Gauss-Seidel iterative technique is applied to solve both electromagnetic and thermal algebraic equation systems.

Coupling Strategies for Electromagnetic-Thermal Analysis

This section examines two primary methodologies for simulating systems involving electromagnetic and thermal interactions. The direct approach integrates both phenomena into a unified solution framework, while the sequential method treats them as separate but interconnected processes solved iteratively. Although direct coupling provides comprehensive simultaneous solutions, it demands extensive computational resources requiring five simultaneous variables per discretized element. Given these resource constraints, direct methods warrant application only when physical conditions strictly require such treatment. This work adopts the sequential approach, offering an effective compromise between numerical efficiency and accurate physical representation of coupled phenomena.

System Configuration and Operating Parameters for Gold Induction Melting

This investigation focuses on an induction heating system designed to melt pure gold contained within an alumina crucible. The experimental setup utilizes a cylindrical ceramic vessel with 100 mm internal diameter, 100 mm height, and 10 mm thick walls, loaded with gold measuring 100 mm in diameter and 90 mm in height. A single-turn copper conductor with rectangular profile serves as the heating coil, positioned 5 mm from the crucible surface. The system operates at standard power frequency (50 Hz) with a coil current density of 6.17×10^8 A/m², generating electromagnetic fields sufficient to raise the gold temperature to its liquefaction point of 1337.33 K. The computational model extends 100 mm beyond the coil's outer boundary to capture the complete electromagnetic field distribution.

The physical configuration examined and the imposed boundary specifications appear in Fig. 1.

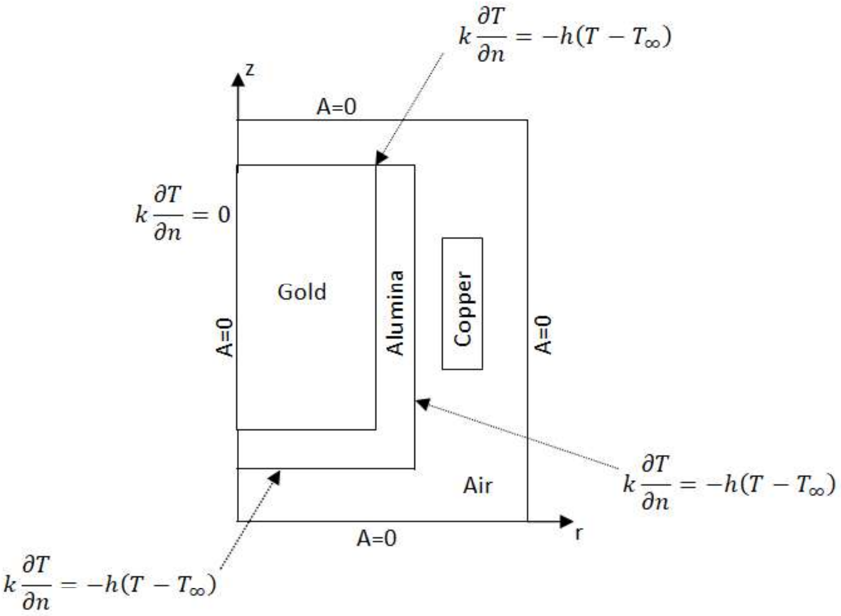

Fig. 1. Physical configuration and boundary specifications.

3. Results and Discussion

3.1. Study of Temperature Distributions

This analysis investigates how thermal fields develop over time throughout the induction heating cycle [1]. During the initial 60-second phase, electromagnetic power concentrates primarily at the gold specimen's exterior surface, creating steep radial thermal gradients Fig. 2. The outer regions experience accelerated temperature rise while interior zones remain comparatively cold, a consequence of electromagnetic skin depth limitations in conductive materials. Beyond one minute of operation, heat diffusion becomes the dominant transport mechanism. Gold's superior thermal transport coefficient (approximately 317 W/m.K at room temperature) enables effective radial heat migration from hot exterior surfaces toward cooler central regions, progressively equalizing the temperature distribution throughout the specimen volume.

This two-stage behavior, initial surface heating followed by conductive redistribution, characterizes the temporal dynamics of electromagnetic induction melting processes.

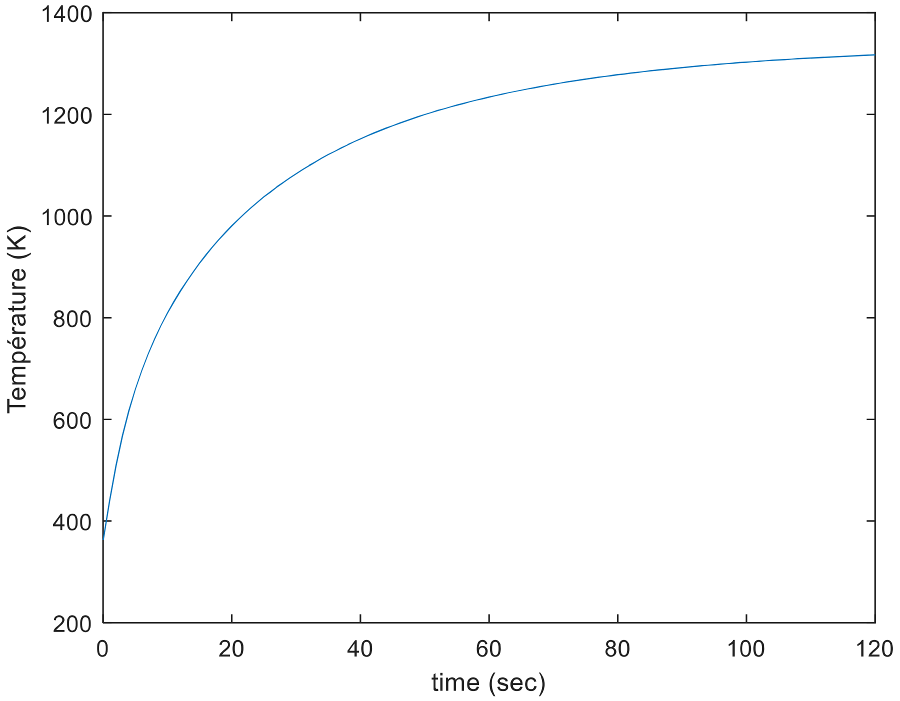

Fig. 2. Temperature evolution with time at the mid-point of the load.

3.2. Spatiotemporal Behavior of the magnetic vector potential A

This section examines the magnetic vector potential A, which serves as the fundamental electromagnetic quantity from which electric and magnetic fields are derived. The vector potential maintains remarkable spatiotemporal consistency throughout the heating process. Its spatial distribution exhibits a bell-shaped axial profile concentrated in the primary coupling region Fig. 3, accompanied by an exponential decay pattern in the radial direction Fig. 4. Temporal variations prove minimal, with fluctuations on the order of 10^{-6} in the axial direction and 10^{-4} to 10^{-5} radially, representing the most stable parameter among all measured quantities. This near-constant behavior contrasts sharply with its derivatives (induced currents and volumetric power dissipation), which demonstrate significant time-dependent changes. The phenomenon reveals a fundamental characteristic of induction systems: the primary electromagnetic driver remains essentially invariant while generating substantial variations in secondary electromagnetic effects [1].

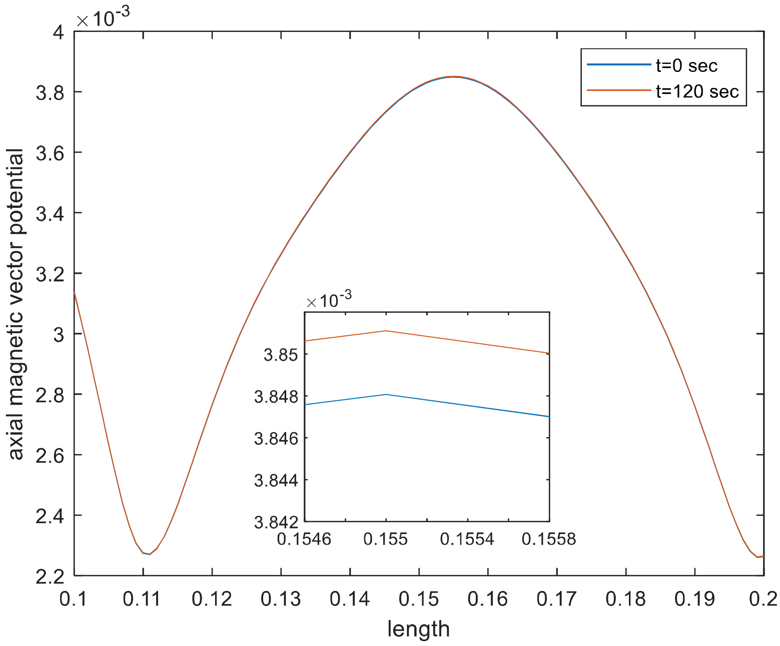

Fig. 3. Magnetic vector potential in the axial direction.

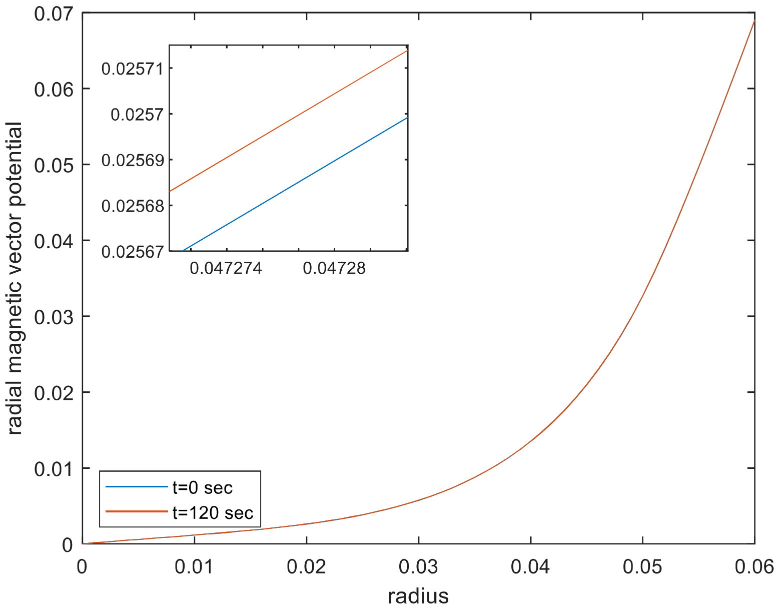

Fig. 4. Magnetic vector potential in the radial direction.

4. Conclusion

This research presents a finite volume numerical framework for analyzing coupled electromagnetic and thermal physics in 50 Hz induction melting of gold. Results demonstrate that skin effect produces steep radial thermal gradients, with outer surfaces heating considerably faster than interior regions [1]. Despite gold's excellent heat conduction properties (thermal conductivity near 317 W/m•K), complete thermal uniformity remains unattainable due to persistent electromagnetic heating at the surface. The sequential coupling methodology delivers computational efficiency while accurately predicting temporal and energy requirements for reaching gold's fusion temperature (1337.33 K). A striking contrast emerges between electromagnetic field behavior where electric field, magnetic field, and vector potential display spatial consistency with negligible temporal drift and thermal response, which evolves dynamically throughout the process. These findings illuminate the intricate relationship between quasi-steady electromagnetic forcing and time-dependent thermal response mechanisms inherent to induction heating technology.

References

[1] Rezgui, Z., Tibouche, A., & Ikhlef, N. (2025). Numerical investigation of gold melting in an induction crucible furnace: a parametric study of electromagnetic and thermal characteristics using finite volume method. *Gold Bulletin*, *58*(1), 11.

[2] Rudnev, V., & Totten, G. E. (Eds.). (2014). Induction heating and heat treatment. ASM international.

[3] Auerkari, P. (1996). Mechanical and physical properties of engineering alumina ceramics (Vol. 23). Espoo, Finland: Technical Research Centre of Finland.

[4] Rudnev, V., Loveless, D., & Cook, R. L. (2017). Handbook of induction heating. CRC press.

[5] VUILLERMOZ, P. L., & LAURENT, M. (1993). *Conductivité thermique des solides*. Ed. Techniques Ingénieur.

[6] Khvan, A. V., Uspenskaya, I. A., Aristova, N. M., Chen, Q., Trimarchi, G., Konstantinova, N. M., & Dinsdale, A. T. (2020). Description of the thermodynamic properties of pure gold in the solid and liquid states from 0 K. Calphad, 68, 101724.

[7] Arblaster, J. W. (2016). Thermodynamic properties of gold. *Journal of Phase Equilibria and Diffusion*, *37*(2), 229-245.

[8] Mazumder, S. (2015). Numerical methods for partial differential equations: finite difference and finite volume methods. Academic Press.

[9] Murthy, J. Y., & Mathur, S. R. (2002). Numerical methods in heat, mass, and momentum transfer. School of Mechanical Engineering Purdue University.

Islamic University Journal of Applied Sciences (IUJAS)
https://journals.iu.edu.sa/jesc
Special Issue, February 2026, Pages 96-110
https://igee.univ-boumerdes.dz/ncaeee25/

5G New Radio OFDM Multi-Numerology Interference Mitigation

Aicha. BENDAIMI[1], Zehor LAHLAH[2], Mouloud. CHALLAL[1]

[1] Institute of Electrical and Electronic Engineering, University M'Hamed BOUGARA of Boumerdes, Boumerdes, ALGERIA
Bendaimi.aicha1@gmail.com, lahlahzehor@gmail.com, mchallal@univ-boumerdes.dz
*Corresponding author: (Aicha BENDAIMI), *Email Address*: Bendaimi.aicha1@gmail.com

Abstract

This work examines the importance of inter-numerology interference mitigation in fifth-generation (5G) NR orthogonal frequency-division multiplexing (OFDM) based systems. The impact of multi-numerology on coexistence issues, latency, and performance is highlighted in this work. The proposed work is a hybrid mitigation approach that combines time domain mitigation by zero padding WOLA filtering and frequency domain mitigation using a fixed guard-band. The work discusses each case separately, then combines them and studies the overall improvements and the possible trade-off. The hybrid ZP WOLA mitigation approach reached 78% - 91% BER reduction percentage in the ideal case (under AWGN) and 37% - 72% BER reduction percentage under moderate fading (flat Rayleigh fading).

Keywords: 5G, Multi-Numerology, OFDM, Interference Mitigation, Wireless Communications.

---

https://doi.org/10.63070/jesc.2026.009
Received 28 November 2025; Revised 24 January 2026; Accepted 27 January 2026.

Published by Islamic University of Madinah on behalf of *Islamic University Journal of Applied Sciences*.

1. Introduction

As the demand for higher data rates continues to increase, the shift to more advanced technologies that support more services is essential. The fifth generation (5G) wireless networks, which is based on the adoption of multi-numerology OFDM systems, addresses this need, offering different services and maintaining excellent quality of service (QoS) [1]. However, multi-numerologies results in the emergence of inter-numerology interference (INI), a fundamental challenge that affects signal integrity.

INI arises due to spectral leakage and imperfect orthogonality between adjacent numerologies, leading to mutual interference that distorts received signals. Several techniques have been implemented to reduce the effect of this issue, such as filtering, equalization, and machine learning, each has its own advantages and disadvantages. In this paper, a hybrid INI mitigation model is proposed based on guard band and filtering technique, specifically, ZP-WOLA under AWGN channel and flat Rayleigh fading channel for both QPSK and 16-QAM schemes. This method is followed by a comparative analysis of the BER performance.

2. OFDM in 5G Networks

OFDM, short for Orthogonal Frequency Division Multiplexing, is a digital modulation and multiplexing technique used in wireless communication systems like 5G networks. It is widely recognized for its ability to minimize inter-symbol interference (ISI) and maximize spectral efficiency. By dividing bandwidth into orthogonal subcarriers, OFDM enables parallel data transmission, reducing multi-path fading and enhancing robustness in frequency- selective environments [2]. In 5G, OFDM has evolved into multi numerology OFDM, allowing flexible subcarrier spacing to support diverse use cases like eMBB, URLLC and mMTC [3]. In 5G, OFDM's flexibility is further enhanced through the introduction of multiple numerologies. Each numerology is characterized by a unique set of parameters, including subcarrier spacing, cyclic prefix (CP) duration, and symbol length. The relationship between these parameters is given by [2]:

$$T_s = \frac{1}{\Delta f} + \mathrm{T_{cp}} \qquad \textbf{(1)}$$

Where Ts represents the total symbol duration, Δf denotes the subcarrier spacing, and Tcp is the cyclic prefix duration. Different numerologies can be designed to meet specific service requirements, optimizing the balance between latency, reliability, and spectral efficiency [1].

2.1 Mathematical Foundations of OFDM

OFDM relies on the Inverse Fast Fourier Transform (IFFT) and Fast Fourier Transform (FFT). At the transmitter, the IFFT converts parallel data symbols into a time-domain OFDM signal, while at the receiver, the FFT transforms the signal back to the frequency domain for demodulation.[3]. The orthogonality of subcarriers is maintained by ensuring that the subcarrier spacing is equal to the inverse of the symbol duration. As a result, OFDM can be implemented effectively in both hardware and software since subcarrier bands overlap without interfering. Mathematically, the OFDM signal in the time domain can be expressed as [3]:

$$s(t)=\sum_{k=0}^{N-1} X_k \,.\, e^{j2\pi k\Delta f t},\ 0\leq t\leq T_s \qquad \textbf{(2)}$$

Where:

1. N is the total number of subcarriers.
2. X_k is the complex modulation symbol (e.g, QAM or PSK) assigned to the k-th subcarrier.
3. Δf is the subcarrier spacing.
4. T_s is the symbol duration.

The orthogonality condition is satisfied when the subcarrier spacing Δf is chosen such that [3]:

$$\Delta f=\frac{1}{T_S} \qquad \textbf{(3)}$$

This ensures that the integral of the product of any two subcarriers over the symbol duration *Ts* is zero, i.e.,

$$\int_0^{T_s} e^{j2\pi k\Delta f t} . e^{-j2\pi m\Delta f t}\, dt = T_s\ , If\ k = m \qquad \textbf{(4)}$$

$$\int_0^{T_s} e^{j2\pi k\Delta f t} . e^{-j2\pi m\Delta f t}\, dt=0\ \ , If\, k\neq m \qquad \textbf{(5)}$$

where *k* and *m* are indices of different subcarriers. This orthogonality allows for efficient spectrum utilization and simplifies the receiver design, as the subcarriers can be separated using a Fast Fourier Transform (FFT) without requiring complex filtering [3], [4].

2.2 Cyclic Prefix in OFDM

One of the key challenges in wireless communication is mitigating the effects of multipath propagation, which causes ISI and inter-carrier interference (ICI). To address this, OFDM employs a cyclic prefix (CP), which is a guard interval inserted at the beginning of each OFDM symbol. The CP is a copy of the last portion of the symbol appended to its start, ensuring that the linear convolution of the channel is transformed into a circular convolution. Mathematically, the CP length T_{cp} is chosen to be longer than the maximum delay spread τ_{max} of the channel [3]:

$$T_{cp} \geq \tau_{max} \quad \textbf{(6)}$$

The inclusion of the CP eliminates ISI and ICI, as long as the delay spread does not exceed the CP duration. However, the CP introduces an overhead that reduces the spectral efficiency, as the effective symbol duration becomes ($T_S + T_{cp}$). In 5G, the CP length is dynamically adjusted based on the channel conditions and the numerology configuration, balancing the trade-off between robustness and efficiency [1].

3. Inter numerology Interference

In 5G networks, INI happens when many numerologies with various subcarrier spacings (SCS) and symbol durations share a frequency band. The introduction of non-orthogonality between subcarriers of different numerologies causes energy leakage and performance deterioration, even if this flexibility facilitates a variety of applications. INI results from time-domain misalignment (various symbol lengths) and frequency-domain misalignment (different SCS values), which are exacerbated by Doppler effects in high-mobility situations [4]. This interference lowers dependability, spectral efficiency, and signal quality, especially for applications that are latency-sensitive [5].

A developing technology called orthogonal frequency division multiplexing with index modulation (OFDM-IM) improves spectral efficiency by modifying information in subcarriers' activation patterns in addition to their amplitude and phase. However, there are particular difficulties with INI when several numerologies coexist in OFDM-IM systems. Dogan-Tusha et al. [6] showed that because mixed numerologies are non-orthogonal, the subcarrier activation patterns in OFDM-IM systems worsen INI. Their research emphasizes the necessity of sophisticated interference mitigation strategies designed for OFDM-IM systems, especially in situations with high mobility and fluctuating channel conditions.

Optimizing resource allocation, maintaining accurate synchronization, minimizing interference through sophisticated signal processing, and addressing scalability as numerologies grow are some of the main obstacles. It's crucial to strike a balance between flexibility and performance trade-offs and to instantly adjust to changing network conditions [7],[8],[9].

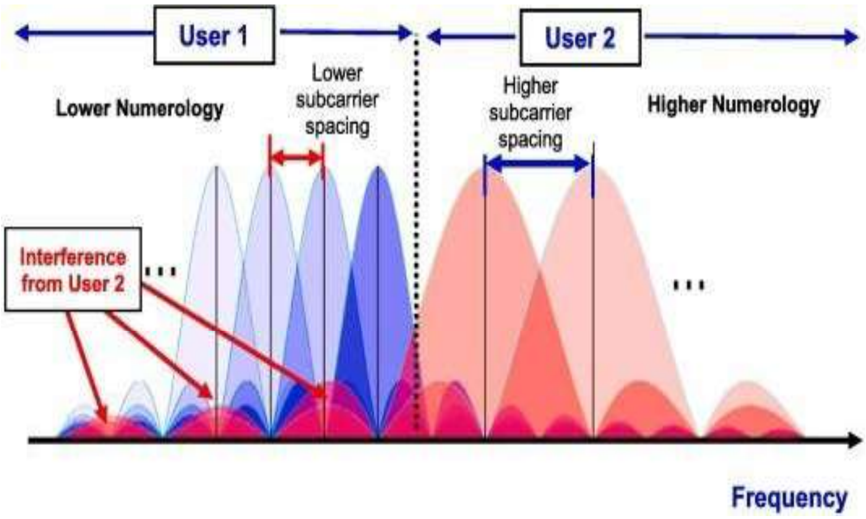

Figure 1. Coexistence of two numerologies in OFDM systems [4]

4. Related work

This section reviews the primary methodologies used to mitigate INI in multi-numerology OFDM systems. Each approach is examined in terms of its underlying principles, simulation results, and practical limitations.

Table 1 highlights the advantages, limitations, and performance gains of each method, offering a comprehensive overview of their applicability in different scenarios.

Table 1. Comparison of INI Mitigation Techniques

Technique	Advantages	Limitations	Performance Gain
Frequency- Domain Filtering [10]	Simple implementation; effective in static channels	Increased latency; less adaptive	3-5 dB SINR
Pre- Equalization [11]	Compensates interference pre-transmission	Requires accurate channel estimation; sensitive to	Notable gains in controlled scenarios

		mobility	
Adaptive Guard Allocation [12],[13]	Dynamic; preserves spectral efficiency	Complex integration with scheduling	Balances throughput and interference
Machine Learning-Based [14], [15]	Adaptive and predictive	High computational overhead; training data requirements	Early-stage promising results

5. Proposed work

Frequency-domain filtering aims to suppress out-of-band emissions that cause interference. This is achieved by designing digital filters that attenuate the energy of subcarriers outside the desired bandwidth. A key study by Ouazziz et al. [10] demonstrated that designing low-pass filters for individual numerologies can reduce INI by up to 5 dB in Signal-to-Interference-plus-Noise (SINR) under static conditions. However, it requires a high level of trade-off consideration. The increased length of filters alongside additional computation requirements results in higher processing delays and energy demands.

To reduce this effect, an initial hybrid experiment with a gard band and a Finite Impulse Response filter (FIR) was simulated, indicating minimal interference mitigation resulting in a high BER=0.47. Consequently, a more advanced filtering technique was required to reduce out-of-band emission (OOBE). The Weighted Overlap and Add (WOLA) filtering was adopted.

5.1 Weighted Overlap and Add (WOLA) filtering

WOLA is a time-domain windowing algorithm specifically selected to reduce spectral leakage and soften signal transitions at the subband edges. It employs a raised cosine window on overlapping segments of OFDM signals, therefore reducing Out-of-Band Emissions (OOBE) and lowering the abrupt discontinuities that cause Inter-Numerology Interference (INI). After incorporating WOLA into our simulation cycle, we observed remarkable improvements in the BER traces compared to the FIR-based filtering approach. The improvements verified that WOLA was better aligned with the structural and spectral demands of multi-numerology systems. However, despite the result appearing more logical and promising on-screen, as shown in figure , some drawbacks still persisted.

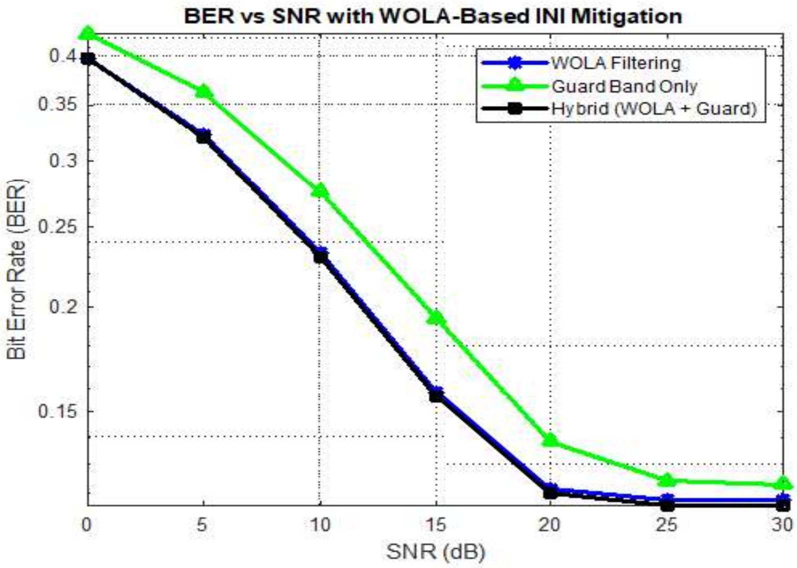

Figure 2. BER of WOLA filtering, Gard band and Hybrid mitigation

Figure 2 shows that the BER remained excessively high at moderate and high SNR values. This means that, despite increased smoothing, WOLA by itself was not able to completely prevent interference between adjacent numerologies. A big contributor to this was the subcarrier spacing and allocation, which offered too little guard bands between numerologies. This made it possible, even with WOLA, for overlapping FFT windows to pick up partially unwanted energy from nearby numerologies, especially in aggressive spectral packing scenarios. To correct this, we turned to a more sophisticated hybrid solution: hybridizing WOLA filtering with fixed guard band insertion and time-domain zero padding. Although guard bands provided spectral isolation, padding ensured that the WOLA-filtered signal avoided spilling over into the FFT window of the adjacent numerology, specifically Numerology-1 that uses a longer symbol duration. The motivation for padding was not simply temporal aliasing, but to relocate the energy of WOLA's roll-off tails outside the sensitive FFT processing window of the co-communicating numerology. This was important since even with a best-case shaped filter, if overlap bleeds into the FFT window, interference is still unavoidable. Padding and delaying the WOLA-filtered signal before combination allowed us to limit its interference footprint more effectively.

5.2 Padded WOLA filtering

As we observed from WOLA performance that it was not optimal under all conditions, we applied a modification: zero-padded WOLA, in which the zero-valued samples are filled in between each OFDM symbol before applying the WOLA window.

As Fig 3 illustrates, this padding achieves better isolation between adjacent numerologies by stretching the overlapping ends of the windowed waveform beyond the adjacent numerologies' FFT window for both QPSK and 16 QAM.

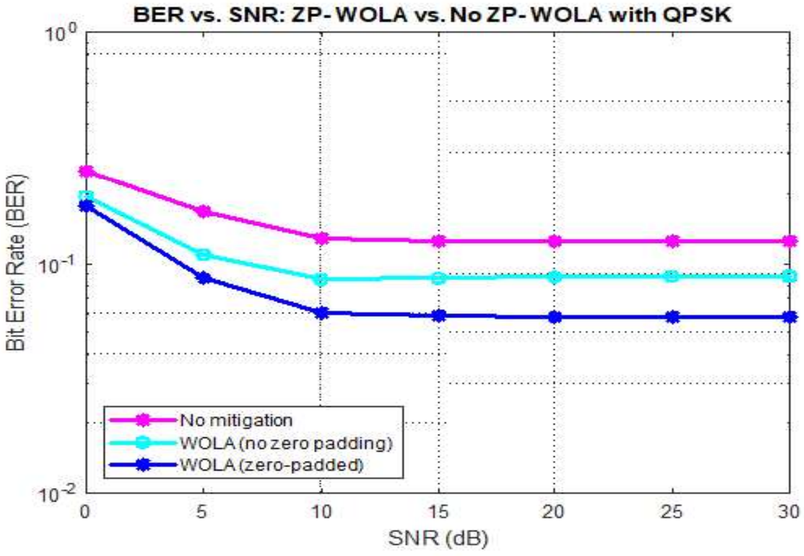

(a)

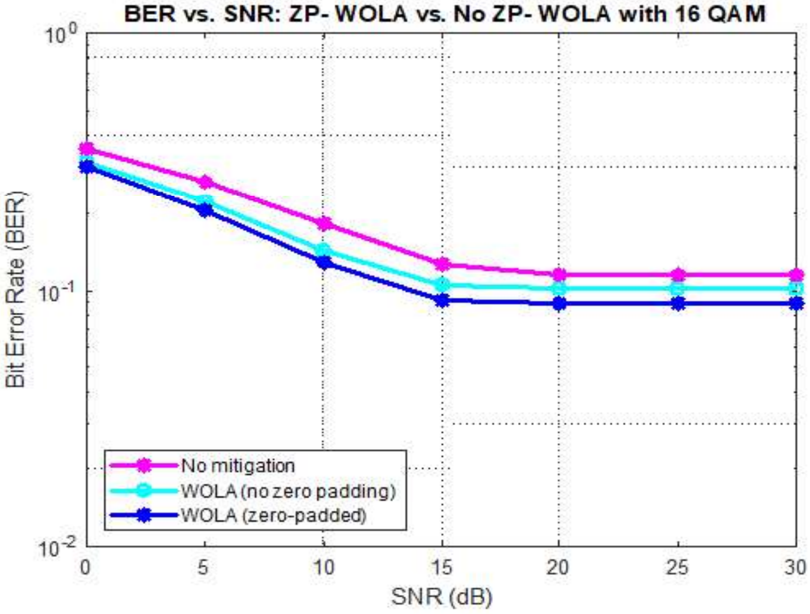

(b)

Figure 3. BER of ZP-WOLA filtering compared to the no-zero-padding WOLA mitigation method. (a) for QPSK and (b) for 16 QAM

5.3 ZP-Hybrid filtering under AWGN

To reduce the persistent inter-numerology interference (INI) observed in the earlier techniques, our final proposed method integrates zero-padded WOLA filtering and guard band insertion in a hybrid mitigation system. This technique leverages the time-domain smoothing provided by WOLA and frequency-domain isolation achieved using guard bands.

As seen from the previous results, the simple filtering using generic FIR or WOLA without padding could not eliminate INI efficiently, especially at larger values of SNR. Similarly, guard band insertion alone, although useful, was of limited effectiveness due to residual spectral leakage. Knowing that WOLA's effectiveness can be compromised both by spectral misalignment and the absence of transition shaping, we augmented it with zero padding to allow the raised cosine windows to gracefully decay without either truncating useful data or bridging significant subcarrier boundaries.

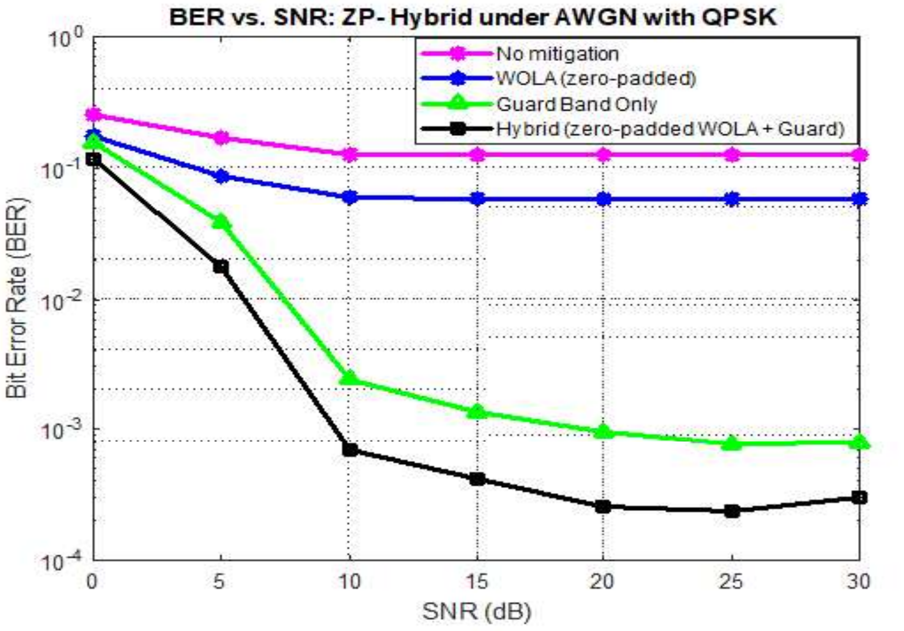

(a)

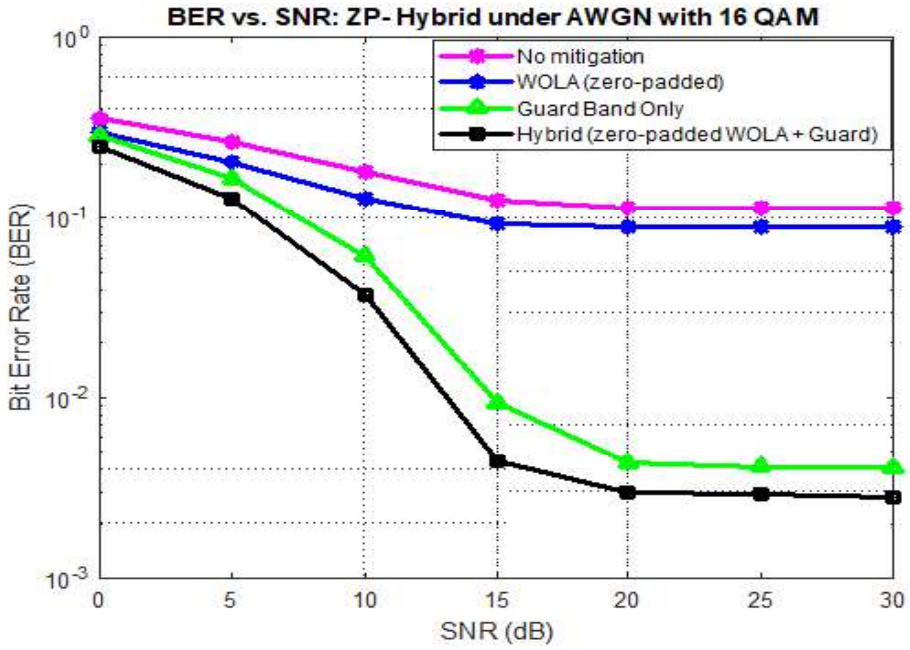

(b)

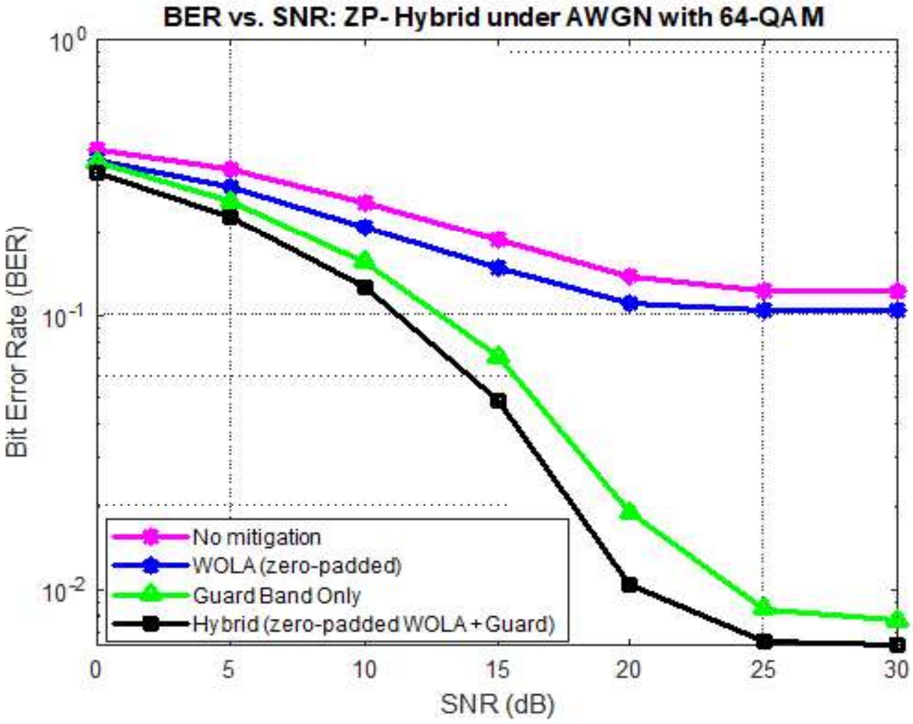

(c)

Figure 4. BER of ZP-WOLA, Gard band, and ZP-Hybrid mitigation. (a) for QPSK, (b) for 16 QAM, and (c) for 64 QAM

Figure 4 shows that WOLA with zero padding outperforms non-padded WOLA, with lower BER at all levels of SNR. Furthermore, in conjunction with guard band insertion, the hybrid padded WOLA solution also performs best, having the lowest BER and steeper downward slope for increasing SNR. This validates that neither single-domain mitigation by itself is sufficient. Instead, cross-domain hybridization-simultaneous optimization of both time and frequency behavior is necessary for effective INI suppression.

5.4 ZP-Hybrid filtering over a Rayleigh fading channel

In this part, the transmission through the wireless channel is defined as frequency flat Rayleigh fading, each sample transmitted is multiplied by an independent complex Gaussian random which creates Rayleigh distributed amplitudes as in multipath, NLOS cases, and then AWGN is added to represent thermal noise and other interfering signals that have a flat spectral density. The receiver employs single-tap equalization, making use of the ‘flat fading’ assumption to fix the distortion in each sample. As a result, the Rayleigh-AWGN channel is useful for testing bit error rates in 5G OFDM, so that different interference management approaches can be directly compared in practical fading and noise conditions.

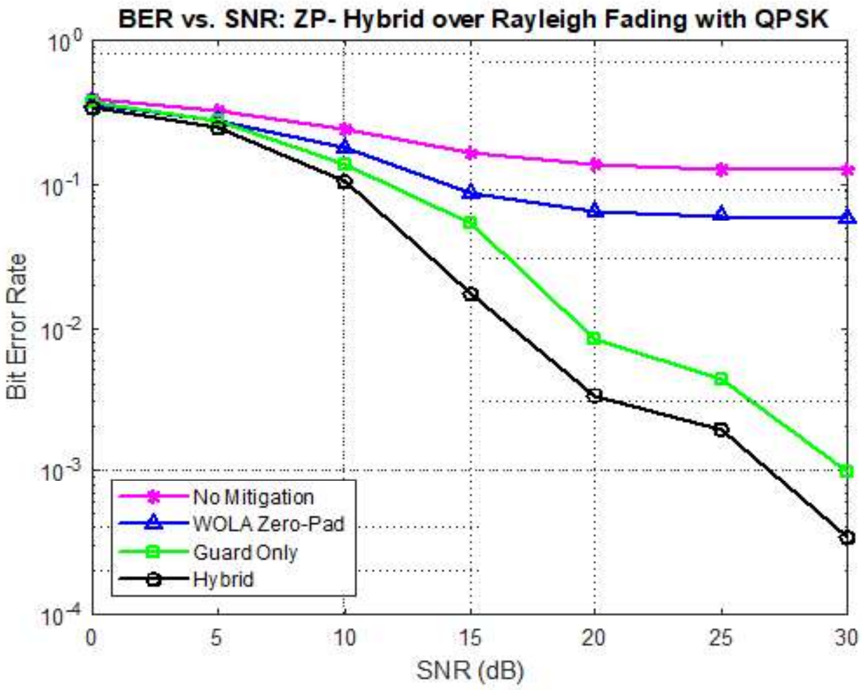

(a)

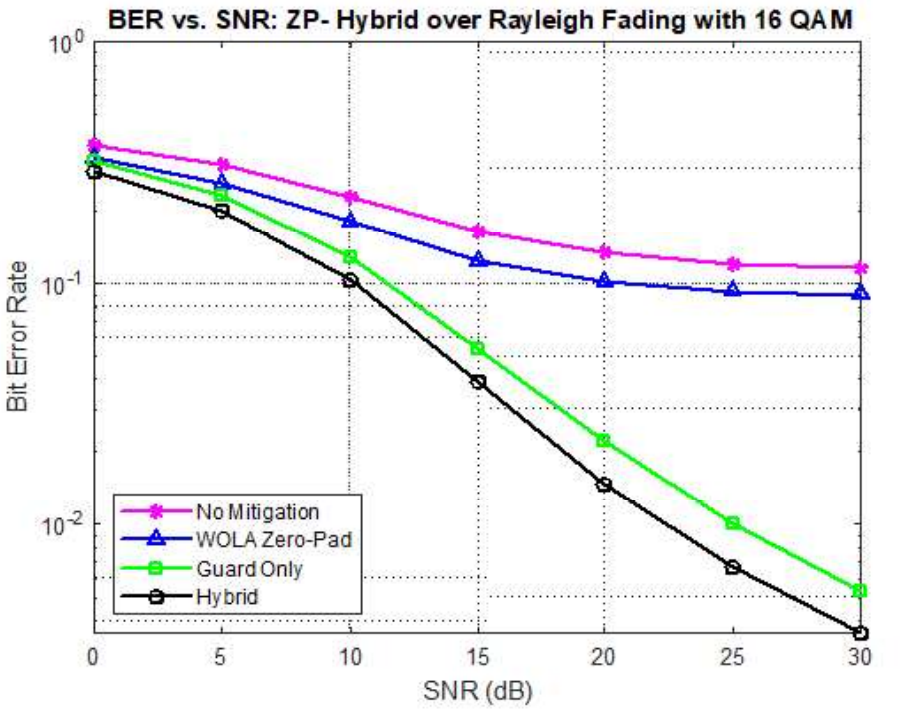

(b)

Figure 5. BER for ZP-WOLA, Gard band, and ZP-Hybrid mitigation over Rayleigh fading. (a) for QPSK and (b) for 16 QAM

As discussed earlier, the ZP Hybrid approach uses zero-padding in time and a WOLA window along with guard subcarriers in the frequency domain to reduce transient artifacts and out-of-band noise at the same time. Over a flat Rayleigh fading channel where every modulated symbol has complex Gaussian amplitude, the padded-hybrid scheme gives good protection against INI and maintains the original spectral efficiency.

The results in Figure 4 illustrate that the hybrid scheme reduced the interference more effectively under fading conditions as compared to WOLA and guard band filtering.

6. Performance comparison

In assessing inter-numerology interference (INI) mitigation for multi-numerology OFDM systems, it is instructive to compare performance under multiple channel models.

In our case, Additive white Gaussian noise (AWGN) and frequency-flat Rayleigh fading in both QPSK and 16-QAM. In AWGN, the channel has only non-correlated white noise, so thermal noise and any influencing INI are the main reasons for the high BER. Alternatively, Rayleigh fading makes the signal's amplitude change in a random way, so random fades can often overshadow the benefits of spectral-leakage suppression.

The effect of a mitigation scheme on the bit-error rate (BER) can be quantified by evaluating the percentage reduction at each signal-to-noise ratio point SNRi, as given by:

$$R_i = \frac{BER_{no\ mitigation}(SNRi) - BER_{mitigation}(SNRi)}{max(BER_{no\ mitigation}(SNRi)\ ,\ \varepsilon)} \times 100\% \qquad \textbf{(6)}$$

Where $BER_{no\ mitigation}$ and $BER_{mitigation}$ denote the baseline and post-mitigation BER curves, respectively, and ε is a small floor to avoid dividing by zero at very high SNR.

The overall percent reduction R is then obtained by averaging Ri across all N SNR samples (0-30 dB):

$$R = \frac{1}{N}\sum_{i=1}^{N} R_i \qquad \textbf{(7)}$$

Table 2 presents the mean BER reduction percentages attained by each mitigation method across two distinct channel models (AWGN and flat Rayleigh fading) for both QPSK and 16-QAM schemes:

Table 2. Average BER reduction percentages for different mitigation methods

Mitigation Method	ZP-WOLA	Guard Band	ZP-Hybrid (ZP-WOLA + Guard Band)
BER Reduction % (over AWGN,QPSK)	49.55%	87.23%	91.68%
BER Reduction % (over AWGN, 16 QAM)	22.90%	72.05%	78.48%
BER Reduction % (over flat Rayleigh, QPSK)	39.38%	65.80%	72.28%
BER Reduction % (over flat Rayleigh, 16 QAM)	13.03%	29.31%	36.74%

The hybrid technique still held a relative advantage over stand-alone ZP-WOLA or guard band approaches. Even under fading-induced symbol losses, which reduce the performance gains. The hybrid approach always produced the lowest error floors, showing its robustness under more realistic propagation models.

7. Conclusion

The proposed approach achieves significant BER reduction across different modulation schemes and channels conditions, demonstrating that the hybrid INI mitigation model, which combines zero-padding WOLA windowing with a spectral guard band, efficiently suppresses inter-numerology interference in both time and frequency domains. The primary trade-off is manifested in the marginal elongation of symbol duration (attributable to zero-padding), which results small amount of time-domain redundancy and the diminution of spectral efficiency (due to the presence of the large guard-band), balanced against the substantial enhancements in error resilience.

Future work will examine broader numerology combinations, FFT size, and symbol duration to improve adaptability, and focus on further optimizing window parameters and evaluating performance complexity trade-offs to enhance scalability for practical 5G and beyond 5G applications.

References

[1] A.Yazar and H.Arslan,“Flexible Multi-Numerology Systems for 5G New Radio,” Journal of Mobile Multimedia, vol. 14, no. 4, pp. 367–394, Sep. 2018.

[2] A. B. Kihero, M. S. J. Solaija, and H. Arslan, "Inter-Numerology Interference for Beyond 5G," *IEEE Access*, 2019.

[3] A. B. Kihero, M. S. J. Solaija, and H. Arslan, "Multi-Numerology Multiplexing and Inter-Numerology Interference Analysis for 5G NR," *arXiv preprint*, 2019.

[4] M. S. Sayed, H. M. Zakaria, A. M. Abdelhady, and A. Zekry, “Interference Mitigation in Mixed-Numerology System Using Hybrid Waveforms,” arXiv preprint, 2024.

[5] J. Mao, L. Zhang, S. McWade, H. Chen, and P. Xiao, "Characterizing Inter-Numerology Interference in Mixed-Numerology OFDM Systems," *arXiv preprint*, 2020.

[6] S. Dogan-Tusha, A. Tusha, E. Basar, S. Althunibat, K. Qaraqe, and H. Arslan, "Inter-Numerology Interference in OFDM-IM Systems," *arXiv preprint*, 2021.

[7] S. Ook eli, T. Levanen, J. Yli-Kaakinen, T. Riihonen, M. Renfors, and M. Valkama, "PAPR Reduction with Mixed-Numerology OFDM," *arXiv preprint*, 2019.

[8] J. Mao, L. Zhang, P. Xiao, and K. Nikitopoulos, "Interference Analysis and Power Allocation in the Presence of Mixed Numerologies," *arXiv preprint,* 2020.

[9] J. Mao, A. Farhang, L. Zhang, Z. Chu, P. Xiao and S. Gu, “Interference Analysis in Multi-Numerology OFDM Systems: A Continuous-Time Approach,” *IEEE International Conference on Communications (ICC) Workshops*, June 2021.

[10] Y. Ouazziz, M. Azni, M. Tounsi, and H. E. Benmadani, "Tackling Inter- Numerology Interference in 5G Multi-Numerology OFDM Systems: A Filtering Approach," *Journal of Electrical Systems*, 2024.

[11] B. A. Cevikgibi, A. M. Demirtas, T. Oirici, and H. Arslan, "Inter- Numerology Interference Pre-Equalization for 5G Mixed-Numerology Communications," *arXiv preprint*, 2022.

[12] A. F. Demir and H. Arslan, "Inter-Numerology Interference Management with Adaptive Guards: A Cross-Layer Approach," *arXiv preprint*, 2020.

[13] A. F. Demir and H. Arslan, “Adaptive guards for mixed numerology systems and associated method of use,” U.S. Patent 11,044,051, June 22, 2021.

[14] Y. Yang, L. Zhang, and P. Xiao, "Mixed Numerology Interference Recognition Approach for 5G NR," 2021.

[15] Michael Aygur, Sithamparanathan Kandeepan, Andrea Giorgetti, Akram Al-Hourani, Edward Arbon, and Mark Bowyer, "Narrowband Interference Mitigation Techniques: A Survey", *IEEE Access,* 2025.

Islamic University Journal of Applied Sciences (IUJAS)
https://journals.iu.edu.sa/jesc
Special Issue, February 2026, Pages 111-126
https://igee.univ-boumerdes.dz/ncaeee25/

Enhancing Quadrotor UAV Trajectory Tracking Using Adaptive Fuzzy PID Control

Hocine LOUBAR [1*], Mohammed Idris ARIF [1], Reda Zakaria BAFFOU[1], Razika Zamoum BOUSHAKI [1]

[1] M'hamed Bougara University (UMBB), Boumerdes, Algeria, h.loubar@univ-boumerdes.dz; dm.arif@ensta.edu.dz; redazakariabaffou@gmail.com; r.boushaki@univ-boumerdes.dz

*Corresponding author: (Hocine LOUBAR), *Email Address*: h.loubar@univ-boumerdes.dz

Abstract

Unmanned aerial vehicles (UAVs) require precise and robust control strategies to ensure safe and efficient flight. This work focuses on the Adaptive Fuzzy PID (AFPID) controller as the main method, which integrates classical Proportional-Integral-Derivative (PID) control with fuzzy logic principles to achieve real-time parameter adaptation. The PID and fuzzy PID controllers are considered as baseline methods for performance comparison with the adaptive fuzzy PID. Simulation was done using MATLAB to evaluate the controllers in terms of trajectory tracking, settling time, Root Mean Square error and robustness under disturbance. Since PID and FPID exhibited similar response shapes to AFPID, only their performance metrics were reported for comparison. The results demonstrate that all controllers successfully stabilize the UAV without steady-state error, while AFPID provides slightly improved settling times and disturbance rejection compared to PID and FPID. These findings confirm the effectiveness of adaptive fuzzy control as a reliable solution for UAV path-tracking tasks.

Keywords: Unmanned Aerial Vehicle (UAV), Trajectory tracking, Quadrotor control, Adaptive Fuzzy PID.

---

https://doi.org/10.63070/jesc.2026.010
Received 20 November 2025; Revised 16 January 2026; Accepted 25 January 2026.

Published by Islamic University of Madinah on behalf of *Islamic University Journal of Applied Sciences*.

1. Introduction

Unmanned aerial vehicles (UAVs) are increasingly employed in diverse applications such as surveillance [1], delivery [2], and Agriculture [3], where precise and robust control strategies are essential to ensure stable flight and accurate trajectory tracking.

In recent quadrotor UAV research, advanced nonlinear based controllers (e.g., backstepping, sliding-mode, and model predictive control) have been widely studied to handle the vehicle's nonlinear dynamics [4]. While these approaches can provide high precision, they often involve complex modeling or heavy computation, making classical proportional–integral–derivative (PID) control attractive for its simplicity and ease of implementation. Quadrotor UAV control has been extensively studied, and PID-based controllers are commonly used but often enhanced with fuzzy logic for greater robustness [5]. For example, Melo et al. (2022) applied a fuzzy gain-scheduling mechanism to adjust PID gains for quadrotor altitude and position control, reporting better trajectory tracking and resilience than a conventional PID [5]. Ye et al. (2024) developed an adaptive fuzzy-PID controller for a quadrotor, finding much lower overshoot and higher disturbance rejection compared to a standard PID [6]. These studies demonstrate that combining a classical PID structure with real-time fuzzy adaptation (AFPID) can significantly enhance UAV flight stability and tracking performance.

In this work, the Adaptive Fuzzy PID (AFPID) controller is presented as the main control approach for trajectory tracking. The AFPID combines the principles of classical proportional–integral–derivative (PID) and fuzzy PID (FPID) control, while introducing adaptive mechanisms that dynamically adjust the control gains in real time to enhance robustness and flexibility. For comparison, PID and FPID are considered as baseline methods. Since their response plots were nearly identical to AFPID, only their performance metrics—such as settling time and root mean square error, and robustness under disturbance —are reported in the results section.

The paper structured as follows. Section II presents the modelling of the quadrotor. Section III details the control methodology, including the baseline controllers and the adaptive fuzzy PID. Section IV describes the simulation setup, while Section V presents and discusses the results. Finally, Section VI provides the conclusion.

2. Dynamic Model of Quadrotor

This section explores the dynamic modelling, which includes forces and torques affecting the quadrotor movement.

As shown in figure 1, two reference frames, also called coordinate system, are usually used to describe the absolute special position and orientation of the quadrotor [7].

The motion of the quadrotor can be classified into two subsystems; rotational subsystem which contains the angles: roll ϕ, pitch θ and yaw ψ. Translational subsystem contains altitude z, and x and y position.

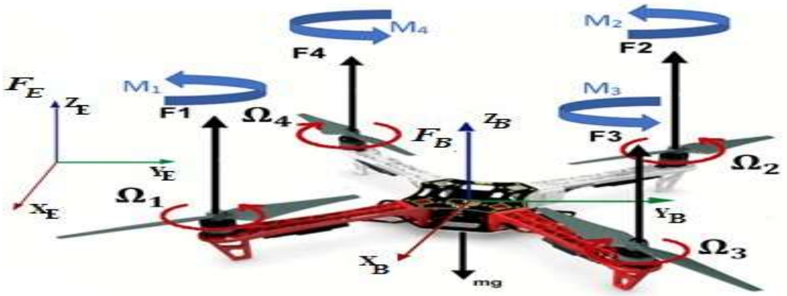

Figure 1. Quadrotor reference frames

2.1 Rotational Subsystem

Using the Newton-Euler method, to deduce the rotational equations of motion which are derived in the body frame [7]:

$$I\dot{\omega} + \omega \times I\omega = M_B \tag{1}$$

Where I is the inertia matrix of the quadrotor and it is a diagonal matrix, ω represents the angular body rate, M_B refers to the moments acting on the quadrotor in the body frame, and $\dot{\omega}$ is the rate of change of angular momentum in the body frame. So, by defining exactly the Inertia matrix and the moment of quadrotor:

- Inertia matrix

The inertia matrix is a diagonal matrix denoted as:

$$I = \begin{bmatrix} I_{xx} & 0 & 0 \\ 0 & I_{yy} & 0 \\ 0 & 0 & I_{zz} \end{bmatrix} \tag{2}$$

The off-diagonal elements, resulting from inertia, are null because of the quadrotor's symmetry. Where I_{xx}, $I_{yy}$and I_{zz} are the area moments of inertia about the principal axes in the body frame.

- Moments of the Quadrotor (MB):

The rotor generates a moment M_i, which has an opposite direction to the directions of the corresponding rotor. It divides into three moments in the body frame's axis, which are: M_x, M_y and M_z.

The moment of quadrotor will be defined as $M_B = [\ M_x\ \ M_y\ \ \ M_z]$

$$M_B = \begin{bmatrix} lK_f(-\Omega_1{}^2 + \Omega_2{}^2 + \Omega_3{}^2 - \Omega_4{}^2) \\ lK_f(\Omega_1{}^2 - \Omega_2{}^2 + \Omega_3{}^2 - \Omega_4{}^2) \\ K_M(\Omega_1{}^2 + \Omega_2{}^2 - \Omega_3{}^2 - \Omega_4{}^2) \end{bmatrix} \tag{3}$$

Where:

l: is the distance between the center of mass of the quadrotor and the axis of rotation of each rotor, $\boldsymbol{K_f}$ and $\boldsymbol{K_M}$ are the aerodynamic force and moment constants, respectively. And $\boldsymbol{\Omega_i}$ is the angular velocity of rotor i.

In addition, by replacing (3) in (1) and around the hover position, small angle assumption is made the equation will be:

$$I \begin{bmatrix} \ddot{\phi} \\ \ddot{\theta} \\ \ddot{\psi} \end{bmatrix} = \begin{bmatrix} lK_f(-\Omega_1{}^2 + \Omega_2{}^2 + \Omega_3{}^2 - \Omega_4{}^2) \\ lK_f(\Omega_1{}^2 - \Omega_2{}^2 + \Omega_3{}^2 - \Omega_4{}^2) \\ K_M(\Omega_1{}^2 + \Omega_2{}^2 - \Omega_3{}^2 - \Omega_4{}^2) \end{bmatrix} - \begin{bmatrix} \dot{\phi} \\ \dot{\theta} \\ \dot{\psi} \end{bmatrix} \times I \begin{bmatrix} \dot{\phi} \\ \dot{\theta} \\ \dot{\psi} \end{bmatrix} \tag{4}$$

After simplifying (4), the state space functions of rotational subsystem will be:

$$\begin{cases} \ddot{\phi} = \dot{\theta}\dot{\psi}\left(\dfrac{I_{yy} - I_{zz}}{I_{xx}}\right) + \dfrac{l}{I_{xx}} K_f(-\Omega_1{}^2 + \Omega_2{}^2 + \Omega_3{}^2 - \Omega_4{}^2) \\ \ddot{\theta} = \dot{\phi}\dot{\psi}\left(\dfrac{I_{zz} - I_{xx}}{I_{yy}}\right) + \dfrac{l}{I_{yy}} K_f(\Omega_1{}^2 - \Omega_2{}^2 + \Omega_3{}^2 - \Omega_4{}^2) \\ \ddot{\psi} = \dot{\phi}\dot{\theta}\left(\dfrac{I_{xx} - I_{yy}}{I_{zz}}\right) + \dfrac{1}{I_{zz}} K_M(\Omega_1{}^2 + \Omega_2{}^2 - \Omega_3{}^2 - \Omega_4{}^2) \end{cases} \tag{5}$$

2.2 Translational Subsystem

The translational subsystem is based on Newton’s second law of motion in the Earth frame [7]:

$$m\ddot{r} = \begin{bmatrix} 0 \\ 0 \\ -mg \end{bmatrix} - F_a + RF_B \tag{6}$$

Where r refers to the distance between the quadrotor and the inertial frame; $r = [x\ y\ z]^{\mathrm{T}}$, m is the mass of the quadrotor,

and g is the gravitational acceleration ($g = 9.81\ m/s^2$), while F_a is represents the drag forces (negligible), R is the rotation matrix, and F_B refers to the nongravitational forces acting on the quadrotor.

The nongravitational forces are multiplied by the rotation matrix to transform the thrust forces from the body frame into the inertial frame.

In this case, we consider only the horizontal orientation without considering the rolling and the pitching, since the only nongravitational force acting of the quadrotor is the thrust produced by the propellers, hence we obtain:

$$\boldsymbol{F_B} = \begin{bmatrix} \boldsymbol{0} \\ \boldsymbol{0} \\ \boldsymbol{K_f(\Omega_1{}^2 + \Omega_2{}^2 + \Omega_3{}^2 + \Omega_4{}^2)} \end{bmatrix} \tag{7}$$

2.3 Rotation matrix

The quadrotor's orientation is defined by the rotation R from the body frame to the inertial frame. This orientation is characterized by roll (ϕ), pitch (θ), and yaw (ψ) angles, which respectively denote rotations about the X, Y, and Z-axes. After simplification it will be:

$$R = \begin{bmatrix} \cos(\theta)\cos(\psi) & \cos(\psi)\sin(\theta)\sin(\phi) - \cos(\phi)\sin(\psi) & \cos(\phi)\sin(\theta)\cos(\psi) + \sin(\phi)\sin(\psi) \\ \cos(\theta)\sin(\psi) & \sin(\phi)\sin(\theta)\sin(\psi) + \cos(\theta)\cos(\psi) & \cos(\phi)\sin(\theta)\sin(\psi) - \sin(\theta)\cos(\psi) \\ -\sin(\theta) & \sin(\phi)\cos(\theta) & cos(\phi)\, cos(\theta) \end{bmatrix} \tag{8}$$

Thus, by putting (7) and (8) in (6), the result will be:

$$m\begin{bmatrix} \ddot{x} \\ \ddot{y} \\ \ddot{z} \end{bmatrix} = \begin{bmatrix} 0 \\ 0 \\ -mg \end{bmatrix} + \begin{bmatrix} (\sin(\phi)\sin(\psi) + \cos(\phi)\cos(\psi)\sin(\theta))(K_f(\Omega_1{}^2 + \Omega_2{}^2 + \Omega_3{}^2 + \Omega_4{}^2)) \\ (\cos(\phi)\sin(\psi)\sin(\theta) - \cos(\psi)\sin(\phi))\left(K_f\left(\Omega_1{}^2 + \Omega_2{}^2 + \Omega_3{}^2 + \Omega_4{}^2\right)\right) \\ \cos(\phi)\cos(\theta)\left(K_f\left(\Omega_1{}^2 + \Omega_2{}^2 + \Omega_3{}^2 + \Omega_4{}^2\right)\right) \end{bmatrix} \tag{9}$$

After simplifying (9), the state space functions of translational subsystem will be:

$$\begin{cases} \ddot{x} = (\cos\phi\sin\theta\cos\psi + \sin\phi\sin\psi)\dfrac{K_f(\Omega_1{}^2+\Omega_2{}^2+\Omega_3{}^2+\Omega_4{}^2)}{m} \\ \ddot{y} = (\cos\phi\sin\theta\sin\psi - \sin\phi\cos\psi)\dfrac{K_f(\Omega_1{}^2+\Omega_2{}^2+\Omega_3{}^2+\Omega_4{}^2)}{m} \\ \ddot{z} = -g + (\cos\phi\cos\theta)\dfrac{K_f(\Omega_1{}^2+\Omega_2{}^2+\Omega_3{}^2+\Omega_4{}^2)}{m} \end{cases} \tag{10}$$

2.4 State Space Representation

Transforming the acquired mathematical model for the quadrotor into a state space model will help make the control problem easier to handle.

In this simulation, we take 12 state variables, i.e., position, velocity, and attitude of an airframe in the inertial frame, and angular rates:

So, X will be represented as a vector.

$$\mathrm{X} = [x_1\ x_2\ x_3\ x_4\ x_5\ x_6\ x_7\ x_8\ x_9\ x_{10}\ x_{11}\ x_{12}]^T \tag{11}$$

Such that:

$$\mathrm{X} = [\phi\ \dot{\phi}\ \theta\ \dot{\theta}\ \psi\ \dot{\psi}\ x\ \dot{x}\ y\ \dot{y}\ z\ \dot{z}]^T \tag{12}$$

The control input is described by the vector [7]:

$$U = [\, U_1 \; U_2 \; U_3 \; U_4] \tag{13}$$

where:

$$U_1 = K_f\left({\Omega_1}^2 + {\Omega_2}^2 + {\Omega_3}^2 + {\Omega_4}^2\right) \tag{14}$$
$$U_2 = K_f(-{\Omega_1}^2 + {\Omega_2}^2 + {\Omega_3}^2 - {\Omega_4}^2 \tag{15}$$
$$U_3 = K_f\left({\Omega_1}^2 - {\Omega_2}^2 + {\Omega_3}^2 - {\Omega_4}^2\right) \tag{16}$$
$$U_4 = K_M({\Omega_1}^2 + {\Omega_2}^2 - {\Omega_3}^2 - {\Omega_4}^2) \tag{17}$$

U_1: It is responsible for the altitude and its rate of change $(z, \dot{z})$.

U_2: It is responsible for the roll rotation and its rate of change $(\phi, \dot{\phi})$.

U_3: It is responsible for the pitch rotation and its rate of change $(\theta, \dot{\theta})$.

U_4: It is responsible for the yaw rotation and its rate of change $(\psi, \dot{\psi})$.

Using (14) to (17) and replace them into the Rotational and Translational subsystems (5) and (10), respectively.

The final mathematical model, which defines the position of the quadrotor in space and its angular and linear velocities, will be as follows:

$$\begin{cases}
\dot{x}_1 = \dot{\phi} = x_2 \\
\dot{x}_2 = \ddot{\phi} = x_4 x_6 a_1 + b_1 U_2 \\
\dot{x}_3 = \dot{\theta} = x_4 \\
\dot{x}_4 = \ddot{\theta} = x_2 x_6 a_2 + b_2 U_3 \\
\dot{x}_5 = \dot{\psi} = x_6 \\
\dot{x}_6 = \ddot{\psi} = x_2 x_4 a_3 + b_3 U_4 \\
\dot{x}_7 = \dot{x} = x_8 \\
\dot{x}_8 = \ddot{x} = \dfrac{U_1}{m}(\cos x_1 \sin x_3 \cos x_5 + \sin x_1 \sin x_5) \\
\dot{x}_9 = \dot{y} = x_{10} \\
\dot{x}_{10} = \ddot{y} = \dfrac{U_1}{m}(\cos x_1 \sin x_3 \sin x_5 - \sin x_1 \cos x_5) \\
\dot{x}_{11} = \dot{z} = x_{12} \\
\dot{x}_{12} = \ddot{z} = -g + \dfrac{U_1}{m} \cos(x_1) \cos(x_3)
\end{cases} \tag{18}$$

Where:

$$a_1 = \frac{I_{yy} - I_{zz}}{I_{xx}} \;;\; a_2 = \frac{I_{zz} - I_{xx}}{I_{yy}} \;;\; a_3 = \frac{I_{xx} - I_{yy}}{I_{zz}}$$

$$b_1 = \frac{l}{I_{xx}} \;;\; b_2 = \frac{l}{I_{yy}} \;;\; b_3 = \frac{1}{I_{zz}}$$

Since the quadrotor is rotating around its hover point, the roll and pitch angles, represented by the values of ϕ and θ, are small enough to support the hypotheses that: $cos(\phi) = cos(\theta) = 1$ and $sin(\phi) = \phi$, and $sin(\theta) = \theta$. Thus:

$$\begin{cases} \ddot{x} = (\theta \cos\psi + \phi \sin\psi)\dfrac{U_1}{m} \\ \ddot{y} = (\theta \sin\psi - \phi \cos\psi)\dfrac{U_1}{m} \end{cases} \tag{19}$$

Hence, the angles ϕ_d and θ_d can be obtained from the following matrix form:

$$\begin{bmatrix} \theta_d \\ \phi_d \end{bmatrix} = \frac{m}{U_1}\begin{bmatrix} cos(\psi_d) & \sin(\psi_d) \\ sin(\psi_d) & -\cos(\psi_d) \end{bmatrix}\begin{bmatrix} \ddot{x} \\ \ddot{y} \end{bmatrix} \tag{20}$$

$$\begin{bmatrix} \ddot{x} \\ \ddot{y} \end{bmatrix} = \frac{U_1}{m}\begin{bmatrix} U_{\mathrm{x}} \\ U_{\mathrm{y}} \end{bmatrix} \tag{21}$$

The vector in (21) represents a virtual input control from which we calculate the desired roll and pitch angles. In order to simplify the design approach, in this work the desired yaw angle ψ_d is considered to be equal to zero. Therefore, by replacing (21) in (20) and putting $\psi_d = 0$, the final equation will be as follows:

$$\begin{cases} \theta_d = U_{\mathrm{x}} \\ \phi_d = -U_{\mathrm{y}} \end{cases} \tag{22}$$

3. Methodology

Precise control methods are needed for the efficient and safe navigation of unmanned aerial vehicles (UAVs). Fuzzy logic control works with approximate or uncertain information, in contrast to standard control techniques that depend on exact mathematical models and crisp values. This makes it especially well-suited and effective for systems with ill-defined or unknown properties [8].

In this work, the Adaptive Fuzzy PID (AFPID) controller is presented as the main method, combining the principles of two baseline approaches: classical PID and Fuzzy PID (FPID) to enhance flexibility, robustness, and overall tracking performance.

3.1 Baseline Controllers (PID & Fuzzy PID)

As baseline controllers for UAV path tracking, we consider the classical PID controller and a Fuzzy-PID (FPID) regulator. These serve as fundamental methods and points of comparison before introducing the main approach, the Adaptive Fuzzy PID (AFPID) controller.

PID controllers are widely used in robotics applications, including path trajectory tracking. The key advantages of using PID controllers for these tasks are their ability to continuously minimize the error between the desired path/trajectory and the robot's actual position and orientation.

The PID controller can be presented as a mathematical equation given by:

$$u(t) = K_p e + K_i \int_0^t e \; dt + K_d \frac{d}{dt} e \tag{23}$$

K_P, K_D and K_I are the proportional, derivative and integral gains, respectively. However, in this work it required manual tuning of the gains by trial and error to achieve acceptable tracking performance. The Fuzzy PID (FPID) controller improves upon the classical PID by using a Mamdani fuzzy inference system (FIS) [9,10] to regulate the control action, which reduces the need for constant manual adjustment. figure 2 illustrates the key components of a fuzzy logic system [11].

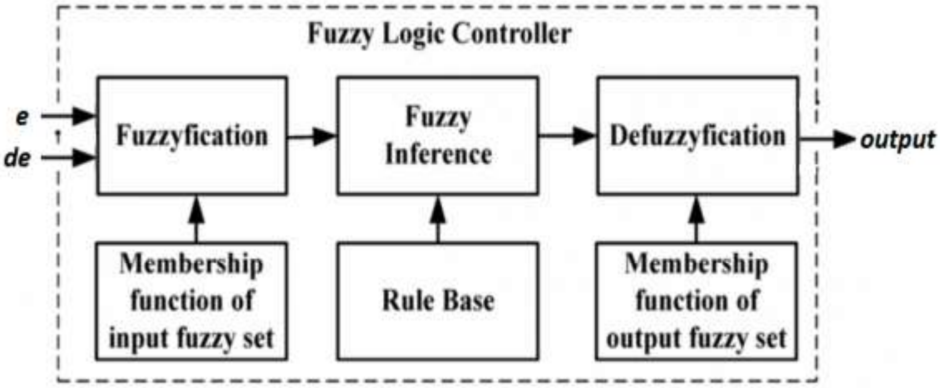

Figure 2. Block diagram of Fuzzy logic controller system

The FPID controller can be presented as a mathematical equation given by:

$$u(t) = K_p e + K_i \int_0^t e \, dt + K_d \frac{d}{dt} e + FIS(e, de) \tag{24}$$

Where FIS is the Mamdani fuzzy inference output. In MATLAB, this term is obtained using evalfis instruction. Nevertheless, the FPID still operates with fixed PID gains and its performance depends on the design of the fuzzy rule base and membership functions, so it cannot adjust parameters in real time.

3.2 Adaptive Fuzzy PID control (AFPID)

Adaptive control is a method used to allow the real-time system to self-correct its configuration to handle any external issue. As the name suggests, the Adaptive Fuzzy PID methodology combines both PID control methods with adaptive fuzzy logic [12].

The main objective is to tune the gains of the PID controller (proportional, derivative and integral) using fuzzy logic, allowing the system to adapt to any changes or issues that could occur. The fuzzy logic controller uses the error and rate of change of error to adaptably regulate the proportional K_p, integral K_I, and derivative K_D gain as illustrated in figure 3 [13].

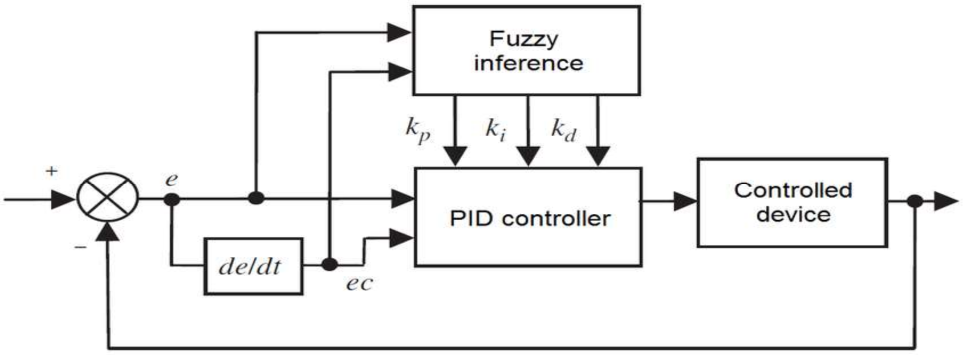

Figure 3. The design of Adaptive Fuzzy PID

For the control of UAV. figure 4 shows the design of the system controllers and the below sub-sections describe the work of each controller.

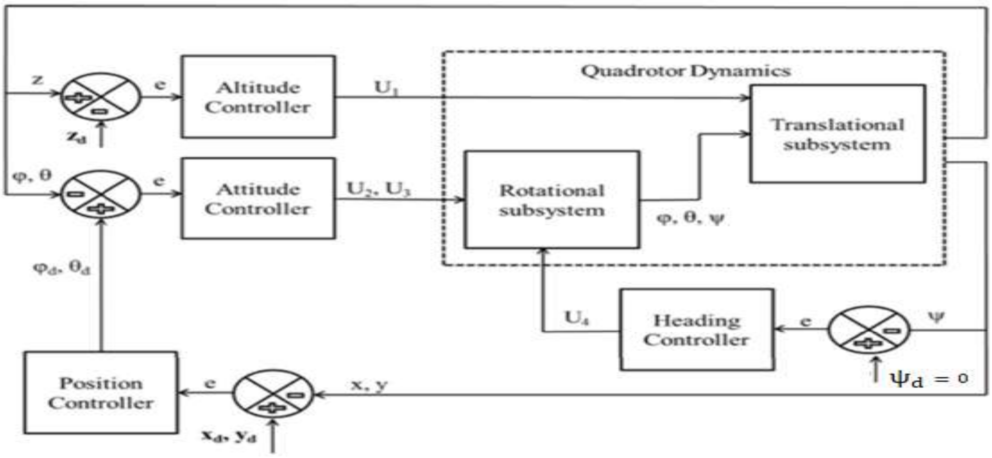

Figure 4. Block diagram of all system controllers.

- **Altitude Controller**

The feedback signal from the quadrotor dynamics subsystem will be compared with the desired z-position and this error signal e_z will be input to the altitude controller.

$$U_1(k) = K_{Pz_{FIC}} e_z(k) + K_{Dz_{FIC}}[e_z(k) - e_z(k-1)] + K_{Iz_{FIC}}\left[\sum_{i=0}^{k} e_z(i)\right] \tag{25}$$
$$+\, evalfis\big(U_{z_{FIS}}, [\, e_z(k), e_z(k) - e_z(k-1)]\big)$$

Where $U_{z_{FIS}}$ is the fuzzy inference system that contains two inputs: error of the altitude "**z**" and its derivative and provides the output value.

- **Position Controller**

The quadrotor subsystem provides feedback on x and y positions. When these positions are not in line with the desired positions, an error signal is sent to the position controller, which modifies the error to ensure that the quadrotor is moving in the correct direction. The outputs of x and y position controllers are U_{x} and U_{y}, respectively.

$$U_x(k) = K_{Px_{FIC}} e_x(k) + K_{Dx_{FIC}}[e_x(k) - e_x(k-1)] + K_{Ix_{FIC}}\left[\textstyle\sum_{i=0}^{k} e_x(i)\right] + evalfis\left(U_{x_{FIS}}, [\, e_x(k), e_x(k) - e_x(k-1)]\right) \qquad (26)$$

$U_{x_{FIS}}$ is the fuzzy inference system that contains two inputs: error of "x" and its derivative and provides the output value.

$$U_y(k) = K_{Py_{FIC}} e_y(k) + K_{Dy_{FIC}}[e_y(k) - e_y(k-1)] + K_{Iy_{FIC}}\left[\textstyle\sum_{i=0}^{k} e_y(i)\right] + evalfis\left(U_{y_{FIS}}, [\, e_y(k), e_y(k) - e_y(k-1)]\right) \qquad (27)$$

$U_{y_{FIS}}$ is the fuzzy inference system that contains two inputs: error of "y" and its derivative and provides the output value.

- **Attitude Controllers**

The attitude controller receives the roll and pitch angles as feedback from the dynamic subsystem, which compares to the desired roll and pitch, coming from the position controller. The roll and pitch controller are as follows:

$$U_2(k) = K_{P\phi_{FIC}} e_\phi(k) + K_{D\phi_{FIC}}[e_\phi(k) - e_\phi(k-1)] + K_{I\phi_{FIC}}\left[\textstyle\sum_{i=0}^{k} e_\phi(i)\right] + evalfis\left(U_{2_{FIS}}, [\, e_\phi(k), e_\phi(k - e_\phi(k-1)]\right) \qquad (28)$$

$U_{2_{FIS}}$ is the fuzzy inference system that contains two inputs: error of "roll" and its derivative and provides the output value.

$$U_3(k) = K_{P\theta_{FIC}} e_\theta(k) + K_{D\theta_{FIC}}[e_\theta(k) - e_\theta(k-1)] + K_{I\theta_{FIC}}\left[\textstyle\sum_{i=0}^{k} e_\theta(i)\right] + evalfis(U_{3_{FIS}}, [\, e_\theta(k), e_\theta(k) - e_\theta(k-1)]) \qquad (29)$$

$U_{3_{FIS}}$ is the fuzzy inference system that contains two inputs: error of "pitch" and its derivative and provides the output value.

- **Yaw controller**

The control input for the yaw angle is defined by this equation:

$$U_4(k) = K_{P\psi} e_\psi(k) + K_{D\psi}[e_\psi(k) - e_\psi(k-1)] + K_{I\psi}\left[\sum_{i=0}^{k} e_\psi(i)\right] + evalfis(U_{4_{FIS}}, [\, e_\psi(k), e_\psi(k) - e_\psi(k-1)]) \qquad (30)$$

$U_{4_{FIS}}$ is the fuzzy inference system that contains two inputs: error of **"yaw"** and its derivative and provides the output value.

In the previous control inputs, $\mathrm{e}(k)$ represents the error between the z-reference and z-position $\mathrm{e}(k) = ref\ (k) - \mathrm{pos}(k)$, U_{FIS} is the fuzzy inference system that contains two inputs: error and its derivative and provides the output value and $K_{P_{FIC}}, K_{D_{FIC}}, K_{I_{FIC}}$ are the adaptable outputs gains (proportional, derivative and integral) of the PID controller.

4. Simulation Setup

The simulation is done utilizing Matlab. The PID controller was designed based on the equations (25) to (29). The quadrotor is simulated using the model described in the second section and the parameters of the model are listed in table 1 [14].

Table 1. The parameters of quadrotor model

m	0.486(Kg)
l	0.25(m)
g	9.81(m/s^2)
I_x	$3.82 \times 10^{-3}(\mathrm{Kg} \times m^2)$
I_y	$3.82 \times 10^{-3}(\mathrm{Kg} \times m^2)$
I_z	$7.65 \times 10^{-3}(\mathrm{Kg} \times m^2)$

In the first time, the values of PID parameters are manually tuned through trial-and-error; by taking values and see if they satisfy the desired result with minimizing the error.

In fuzzy system inference, Three linguistic values: negative (N), zero (Z), and positive (P) are used for two inputs (error and rate of error) and one output with five linguistic values: great negative (GN), negative (N), zero (Z), positive (P) and great positive (GP). So, after accurate observation, rule base is defined as shown in table 2 [15].

Table 2. UAV controllers rule table.

de e	N	Z	P
N	GN	N	Z
Z	N	Z	P
P	Z	P	GP

Mamdani-type Fuzzy inference system with triangular and trapezoidal membership functions is used in our simulation, where the input range for both error and error's rate is defined from [-5, 5]. Whereas, there exist four controllers outputs for each Fuzzy logic system $\boldsymbol{U_1}, \boldsymbol{U_2}, \boldsymbol{U_3}$ and $\boldsymbol{U_4}$ with two virtual controllers $\boldsymbol{U_x}$ and $\boldsymbol{U_y}$; each one of them has its own output range: [-12, 12] for $\boldsymbol{U_1}$, [-3.05, 3.05] for $\boldsymbol{U_2}$ and $\boldsymbol{U_3}$, [-0.06, 0.06] for $\boldsymbol{U_4}$, and [-1, 1] for $\boldsymbol{U_x}$ and $\boldsymbol{U_y}$.

Therefore, in order to see the performance of the AFPID controller compared to well-tuned PID and FPID, we will take example path of quadrotor in 3D environment, and compare them in terms of the settling time, the steady state error and the total Root Mean Square error (RMSe) defined by (30).

$$RMSe = \sqrt{\frac{1}{\mathrm{n}}\sum_{i=1}^{\mathrm{n}} \left((e_x(\mathrm{i}))^2 + (e_y(\mathrm{i}))^2 + (e_z(\mathrm{i}))^2\right)} \qquad (30)$$

5. Results and Discussion

In the result part, we got the outcomes of the Adaptive Fuzzy PID response concerning the Y position, X position, roll, pitch, yaw (considered as zero in this context), and altitude Z in figure 5. The control inputs results are shown in figure 6 and the final simulated 3D UAV path in figure 7.

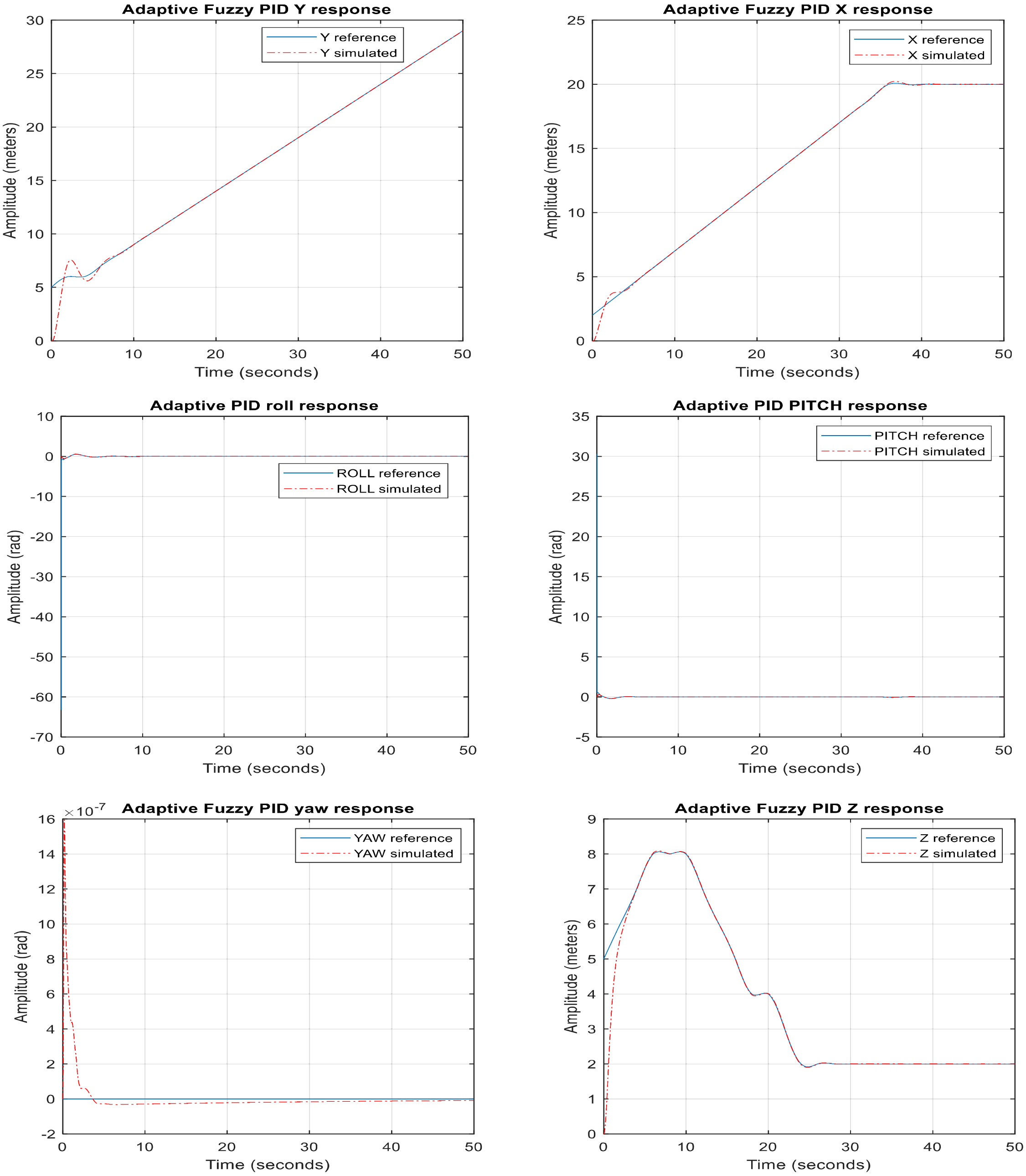

Figure 5. Adaptive Fuzzy PID Response for the First Path: Y-X Positions, Roll, Pitch, Yaw, and Altitude Z

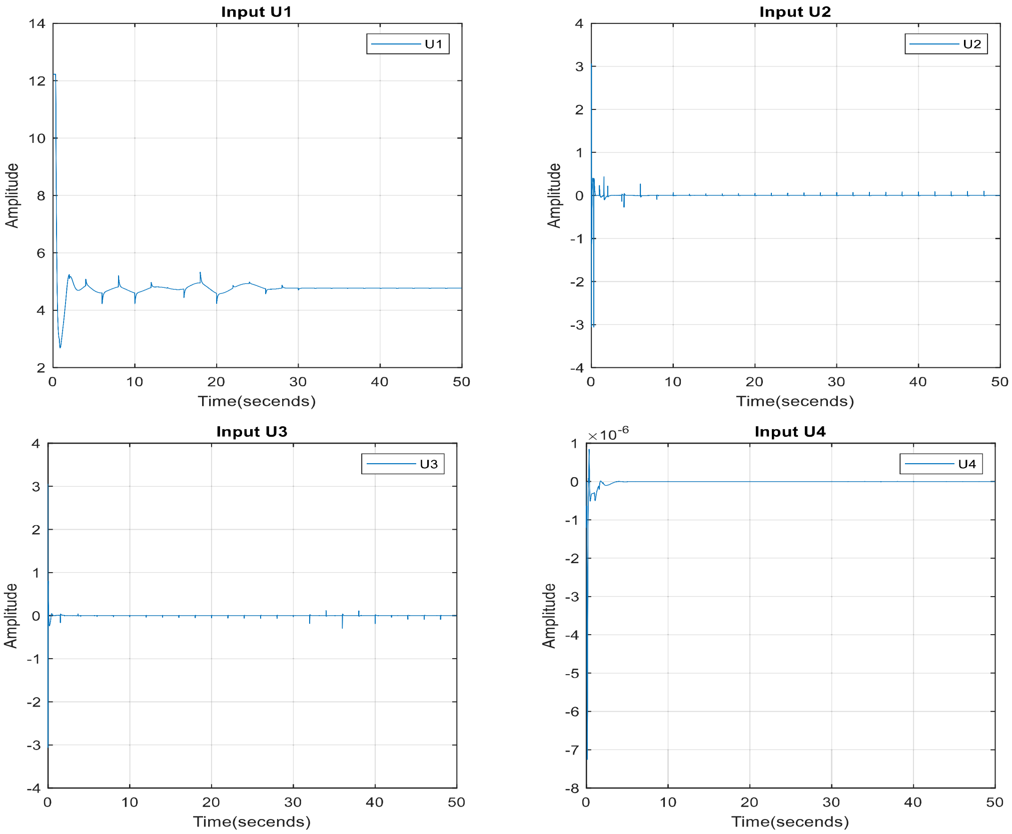

Figure 6. Control inputs Adaptive Fuzzy PID response.

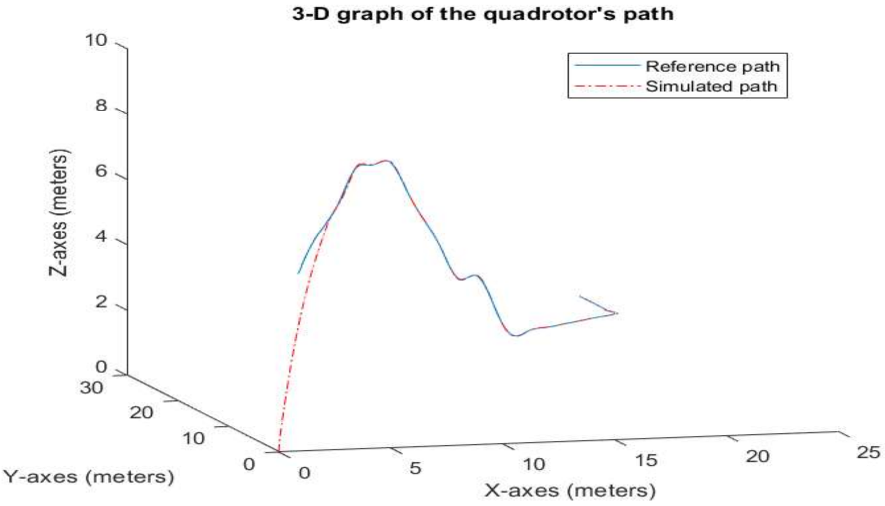

Figure 7. Adaptive Fuzzy PID Control Simulation of a 3D UAV's Trajectory.

From figure 5, we can notice that the X and Y response, both have a small overshoot from 0s to 5s and from 0s to 8s, respectively. For the altitude-Z, roll and pitch response, we can see that the controller follows directly the desired path with no overshoot.

Concerning the controller's outputs in figure 6, $\boldsymbol{U_1}$ has a fluctuation due to the sudden changes in the altitude Z. For $\boldsymbol{U_2}$,$\boldsymbol{U_3}$ and $\boldsymbol{U_4}$, we can notice that they were unstable a bit in the beginning but after that they maintain in the value of '0'.

Table 3 shows the performance of three controller methods: PID, FPID, and AFPID, across three positions X, Y, and Z. All controllers successfully drive the UAV to the desired setpoint without steady-state error. The comparison of settling times and RMSe shows that AFPID achieves slightly better performance than both FPID and PID.

Table 3. PID, FPID and AFPID Response for Trajectory Tracking: Settling Time and RMSe.

Controller Type	Settling Time (X-pos)	Settling Time (Y-pos)	Settling Time (Z-pos)	RMSe
PID	5s	6.2s	3.5s	1.0185
FPID	4.5s	5.75s	3.5s	0.9064
AFPID	3.5s	5.7s	3s	0.9063

All simulated plots demonstrate convergence to the reference one without any steady state error in all three control types.

The closeness of the results could be explained by the well-tuned parameters of the PID. The manual tuning method is an easy way for PID controllers to obtain a reasonable result. However, it may take a long time to obtain the gains that generate a reasonable result, and it is difficult to determine if the final settings are optimal. Due to their little knowledge of the process plant, PID controllers are unable to adjust themselves automatically when the system faces a certain change. Hence, other approaches such us the Fuzzy logic technique, could be integrated into the PID controller to ensure the output is obtained as desired and the parameters are tuned automatically when changes are applied to the system.

To obtain a better comparison of the control methods' adaptability in the presence of Gaussian disturbance over time from 10 seconds until 20 seconds. The effects of the disturbances are shown in figure 8. AFPID was the best, followed by FPID, with PID controller performing the least effectively.

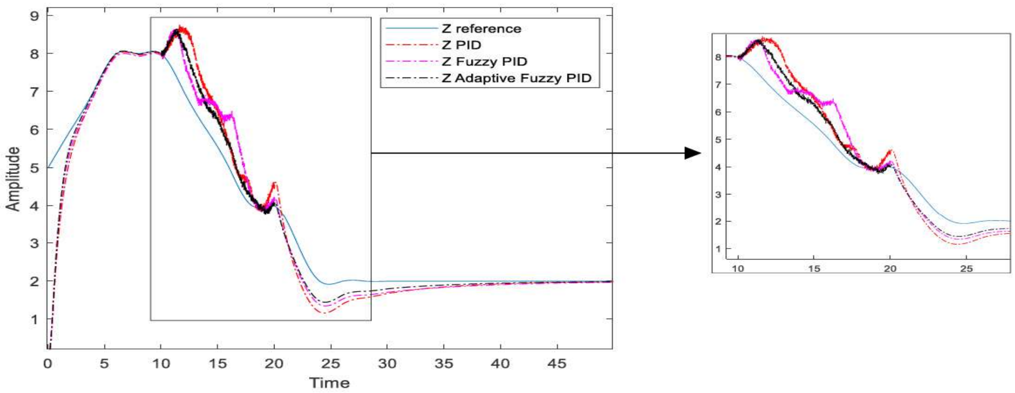

Figure 8. The response of PID, Fuzzy PID and Adaptive Fuzzy PID with Gaussian disturbance.

In overall, the Adaptive fuzzy PID, fuzzy PID and PID controllers proved that they are adapted to the quadrotor when flying. However, the adaptive fuzzy PID controller includes the adaptive mechanism that continuously adjusts the parameters of the controller in real-time. Instead of tuning the parameters manually, this is the main difference that makes AFPID better than FPID and PID.

6. Conclusion

In this paper, we investigated the Adaptive Fuzzy PID (AFPID) control strategy for quadrotor UAVs, with classical PID and fuzzy PID (FPID) used as baseline controllers. The results showed that all controllers achieved stable trajectory tracking without steady-state error and performed approximately the same due to well-tuned PID parameters. However, AFPID demonstrated superior performance, providing faster settling times and greater robustness against disturbances thanks to its ability to adjust parameters in real time. These improvements confirm the effectiveness of integrating adaptiveness with fuzzy reasoning in UAV control. For future work, we will focus on extending the AFPID approach to more complex flight scenarios and validating its performance in real-world experiments.

References

[1] T. Ahmad, A. E. Morel, N. Cheng, K. Palaniappan, P. Calyam, K. Sun, and J. Pan, Future UAV/Drone systems for intelligent active surveillance and monitoring, ACM Comput. Surv., Aug. 2025. doi: 10.1145/3760389.

[2] S. Simon, Drones for automated parcel delivery: Use case analysis, Transp. Res. Interdiscip. Perspect., vol. 40, 2024, Art. no. 100931. doi: 10.1016/j.trip.2024.100931.

[3] Nandini and S. R. Singh, Application of drones technology in agriculture: A modern approach, J. Sci. Res. Rep., vol. 30, no. 7, pp. 142–152, 2024. doi: 10.9734/jsrr/2024/v30i72131.

[4] A. Noordin, M. A. A. Basri, and Z. Mohamed, Adaptive PID control via sliding mode for position tracking of quadrotor MAV: Simulation and real-time experiment evaluation, Aerospace, vol. 10, no. 6, Art. no. 512, May 2023. doi: 10.3390/aerospace10060512.

[5] A. G. Melo et al., Fuzzy gain-scheduling PID for UAV position and altitude controllers, Sensors, vol. 22, no. 6, Art. no. 2173, Mar. 2022. doi: 10.3390/s22062173.

[6] Y. Ye, Homeostasis of a quadrotor UAV based on fuzzy adaptive PID controller, in Proc. 2024 Int. Conf. Intell. Auto. and Adv. AI (ICIAAI), Atlantis Press, 2024. doi: 10.2991/978-94-6463-540-9_53.

[7] F. Fahmizal, Altitude control of quadrotor using fuzzy self-tuning PID controller, in Proc. IEEE Int. Conf. Control, Robot. Integr. Syst. (ICCRIS), 2017. doi: 10.1109/ICCRIS.2017.8068415.

[8] H. Hagras, General Type-2 Fuzzy Logic Systems to Enable Better Uncertainty Handling for Real World Application, The Computational Intelligence Center. Lecture presented at the The computational intelligence center.

[9] E. H. Mamdani, S. Assilian. "An Experiment in Linguistic Synthesis with a Fuzzy Logic Controller". International Journal of Man-Machine Studies 7,January 1975

[10] Mathwork, Mamdani and Sugeno Fuzzy Inference System, https://www.mathworks.com/help/fuzzy/types-of-fuzzy-inference-systems.html.

[11] M. Makhtoumi, Active Vibration Control of Launch Vehicle on Satellite Using Piezoelectric Stack Actuator, arXiv [Physics.Space-Ph], 2023. arXiv. http://arxiv.org/abs/1903.07396.

[12] M. A. Sattar, Adaptive Fuzzy Control of Quadrotor, M.S. thesis, Rochester Institute of Technology, Dubai, 2017. [Online]. Available: https://repository.rit.edu/theses/9618/

[13] M. A. Chancán León, S. Leal Braga, and J. C. Cuisano Egúsquiza, Combustion air temperature and humidity control for engine testing, in Proc. VII Congresso Nacional de Engenharia Mecânica (CONEM), São Luís, Maranhão, Brazil, Jul.–Aug. 2012, pp. 1–7.

[14] H. Boudjedir, Dual Neural Network for Adaptive Sliding Mode Control of Quadrotor Helicopter Stabilization, International Journal of Information Sciences and Techniques 2, no. 4 (July 31, 2012). https://doi.org/10.5121/ijist.2012.2401.

[15] A. Eltayeb, M. F. Rahmat, M. A. M. Eltoum, M. H. S. Ibrahim and M. A. M. Basri, Trajectory Tracking for the Quadcopter UAV utilizing Fuzzy PID Control Approach, 2020 International Conference on Computer, Control, Electrical, and Electronics Engineering (ICCCEEE), Khartoum, Sudan, 2021.

Islamic University Journal of Applied Sciences (IUJAS)
https://journals.iu.edu.sa/jesc
Special Issue, February 2026, Pages 127-135
https://igee.univ-boumerdes.dz/ncaeee25/

Modeling of Grounding Grids under Lightning Currents Using a Nonuniform Transmission Line Approach

Boutadjine Ahmed [1,*]

[1] Departement of Electrical Engineering-University of Jijel, Algeria, boutadjine92@gmail.com

*Corresponding author: (Boutadjine Ahmed), *Email Address*: boutadjine92@gmail.com

Abstract

Modeling a grounding system in the time domain makes it possible to account for the nonlinear phenomenon of soil ionization, which occurs following the injection of a very high-intensity lightning current. Several numerical studies using the Finite-Difference Time-Domain (FDTD) method have focused on modeling grounding systems while considering soil ionization. These works, which have produced excellent agreement with experimental measurements, directly solve Maxwell's equations in three dimensions (3D), but they remain computationally intensive and numerically complex. In this paper, we propose a model for a grounding grid that offers a simplified implementation while accounting for the various electromagnetic couplings that arise after spatial discretization of the grid, as well as for soil ionization caused by the injection of a high-intensity lightning pulse. This new formulation is developed based on the equations of nonuniform Transmission Lines (nuTL) combined with the Finite-Difference Time-Domain (FDTD) method.

Keywords: Modeling; Grounding Grid; FDTD; Ionization; nuTL.

---

https://doi.org/10.63070/jesc.2026.011
Received 24 November 2025; Revised 18 January 2026; Accepted 26 January 2026.

Published by Islamic University of Madinah on behalf of *Islamic University Journal of Applied Sciences*.

1. Introduction

Lightning strikes are among the main causes of overvoltages and equipment failures in power transmission networks. When a direct lightning stroke impacts a transmission tower, the associated transient current propagates toward the grounding system. If the grounding is properly designed, it can effectively limit the Ground Potential Rise (GPR) and thereby prevent back-flashover phenomena [1]. To minimize such incidents, engineers must give particular attention to the correct dimensioning and configuration of grounding systems.

The design of an effective grounding system can be approached through three complementary methods : experimental, analytical, and numerical. Although experimental tests are indispensable [2], they are often insufficient to ensure reliable and reproducible results due to the heterogeneous nature of soils-characterized by stratification and large variations in resistivity. To complement experimental investigations, researchers increasingly rely on simulation methods based on [1] circuit theory, transmission line modeling and numerical resolution of Maxwell's equations. During the injection of a very high-intensity lightning current, the soil may experience significant heating, sometimes leading to ionization phenomenon [3]. To model this nonlinear behavior, several studies have been conducted. Among these different works, Liew's dynamic model is the one that comes closest to reality [4].

In this work, we aim to simplify the simulation of the transient behavior of a grounding grid while incorporating the effects of soil ionization. We propose a new numerical modeling approach developed in the time domain, based on the resolution of nonuniform transmission line equations using the Finite-Difference Time-Domain (FDTD) method [5]. This approach offers the advantage of being both very low computational time and straightforward to implement, while maintaining good accuracy in reproducing the electromagnetic coupling and ionization phenomena observed during high-intensity lightning strikes.

2. New formalism based on non-uniform transmission line theory

The use of numerical method FDTD requires the spatial discretization of the thin-wire conductor in element of size Δx. If the thin-wire conductor is considered as a transmission line and its discretization is achieved by neglect the propagation, then each element (cell) of size Δx is represented by the π electrical (Figure 1) circuit and the general equations for a cell ¨i¨ are given by telegrapher’s equations as follows [6] :

$$\frac{\partial V(x_i,t)}{\partial x} + R_{ii} I(x_i,t) + M_{ii} \frac{\partial I(x_i,t)}{\partial t} = 0 \qquad (1)$$

$$\frac{\partial I(x_i,t)}{\partial x} + G_{ii}\, V(x_i,t) + C_{ii}\frac{\partial V(x_i,t)}{\partial t} = 0 \qquad (2)$$

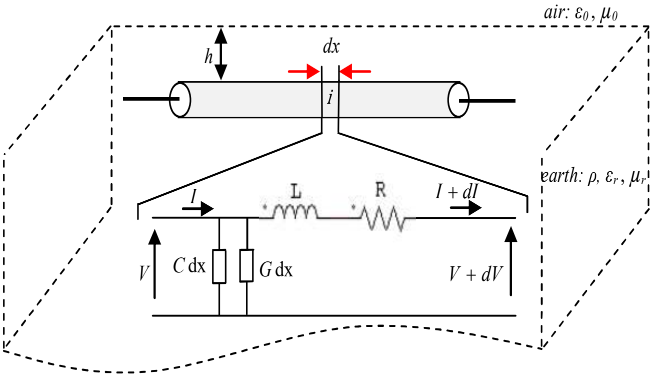

Figure 1. Equivalent electrical circuit of a cell.

These two partial differential equations describe the evolution of voltage $\boldsymbol{V(x_i,t)}$ and current $\boldsymbol{I(x_i,t)}$ as a function of distance ¨*x*¨ and time ¨*t*¨. In which appear $\boldsymbol{R_{ii}}$, $\boldsymbol{M_{ii}}$, $\boldsymbol{G_{ii}}$ and $\boldsymbol{C_{ii}}$ are respectively, the per unit length longitudinal resistance, longitudinal inductance, conductance to ground and capacitance to ground of a cell ¨*i*¨.

Classically, if we model an electrical device as thin-wire by adopting the transmission line approach, after subdivision of the conductor into several π-cells, equations (1) and (2) do not allow to take into account the electromagnetic interactions between two different cells (¨*i*¨ and ¨*j*¨) (Figure 2).

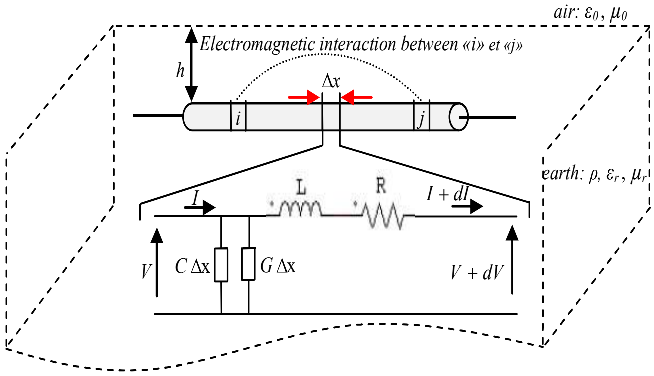

Figure 2. Electromagnetic interactions between cells ¨*i*¨ and ¨*j*¨.

So in our work, to take into account the electromagnetic interactions between two different cells ¨*i*¨ and ¨*j*¨ we complete the general and classical equations of transmission line (1) an d (2) as follow [5]:

$$\frac{\partial V(x_i,t)}{\partial x} + R_{ii} I(x_i,t) + \sum_{j=1}^{k_{max}} M_{ii}\frac{\partial I(x_i,t)}{\partial t} = 0 \qquad (3)$$

$$\frac{\partial I(x_i,t)}{\partial x} + G_{ii}\, V(x_i,t) + \sum_{j=1,j\neq i}^{k_{max}} G_{ij}\big[V(x_j,t) - V(x_i,t)\big] + C_{ii}\frac{\partial V(x_i,t)}{\partial t} + \sum_{j=1,j\neq i}^{k_{max}} C_{ij}\frac{\partial[V(x_j,t)-V(x_i,t)]}{\partial t} = 0 \qquad (4)$$

We calculate the self and mutual per-unit length parameters in (3) and (4) according to the geometrical position of the elements (cells) [7]. We therefore use in this paper rather the term nonuniform Transmission Line (nuTL) [5]. Note that, after subdividing the electrode into k_{max} cells of size Δx, the per unit length parameters matrix ([R], [L], and [G]) are calculated using the model proposed by Y. Liu [7]. Also, when the line is discretized into elementary segments (cells), we note the presence of a set of elementary electrical charges and the calculation of the matrix of the capacitance coefficients [CN] must be done by inverting the matrix of susceptance coefficient [P] [7].

$$[CN] = [P]^{-1} \qquad (5)$$

The elements of the capacity matrix $[C]$ are then calculated as follows : $C_{ii} = CN_{ii}$, $C_{ij} = -CN_{ij}$ and $C_{ij} = C_{ji}$.

To apply the numerical method called FDTD [6] for solving the equations (3) and (4) along the line, we subdivide the grounding electrode into cells of length Δx and we place nodal voltages at its two ends and at its middle point (node) a branch (node) current (Figure 3). In the time domain, two adjacent current and voltage nodes are separated by $\Delta x/2$ in space and shifted by $\Delta t/2$ in time. Spatio-temporal discretization obeys a stability criterion [8].

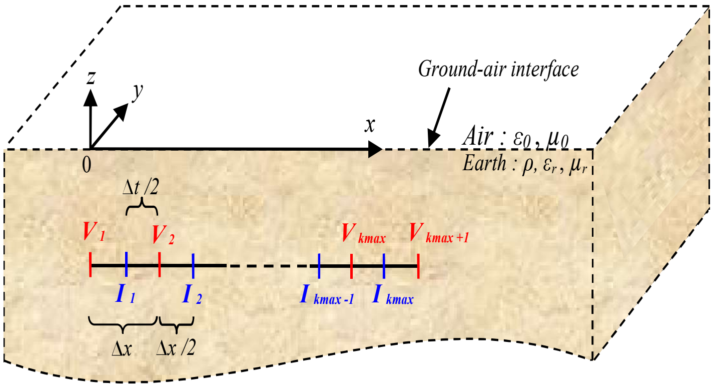

Figure 3. Presentation of nodal voltages and currents after spatial discretization of the buried conductor.

$$\frac{V_{i+1}^n - V_i^n}{\Delta x} + R_{ii}\frac{I_i^{n+1/2} + I_i^{n-1/2}}{2} + \sum_{j=1}^{k_{max}} M_{ij}\frac{I_j^{n+1/2} - I_j^{n-1/2}}{\Delta t} = 0 \qquad (6)$$

$$\frac{I_i^{n-1/2} - I_{i-1}^{n-1/2}}{\Delta x} + G_{ii}\frac{V_k^n + V_k^{n-1}}{2} + \sum_{j=1, j\neq i}^{k_{max}} G_{ij}\frac{\left[\left(V_j^n - V_i^n\right) + \left(V_j^{n-1} - V_i^{n-1}\right)\right]}{2} + C_{ii}\frac{V_k^n - V_k^{n-1}}{\Delta t} + \sum_{j=1, j\neq i}^{k_{max}} C_{ij}\frac{\left[\left(V_j^n - V_i^n\right) - \left(V_j^{n-1} - V_i^{n-1}\right)\right]}{\Delta t} = 0 \qquad (7)$$

Where ¨*n*¨ indicating time and ¨*i*¨ and ¨*j*¨ the space.

The objective of our work is to propose a new numerical model for studying the transient behavior of grounding grid.

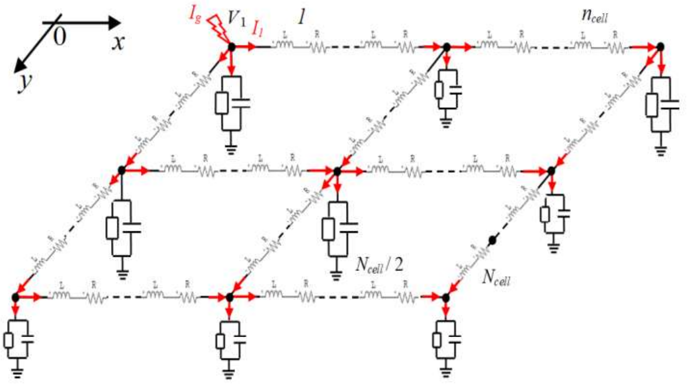

Figure 4. Electrical circuit equivalent of grounding grid.

For the grounding grid (Figure 4), the grid is subdivided into several π-shaped cells, each with a length Δx along the x-direction and a length Δy along the y-direction, assuming $\Delta x = \Delta y$.

- The intersections between the conductors represent the nodal tensions (physical nodes);
- The nodes located between two physical nodes represent a succession of branch currents and node voltages (fictitious nodes);

This new topological electromagnetic modeling consists on using the equations (6) and (7) to deduce a matrix system :

$$[A][X] = [B] \tag{8}$$

The unknown vector [X] represents the nodal voltages in each node of the grounding grid and the currents of branches between two successive nodes after its subdivision. To generate the matrix system (8) in time, firstly we define the unknown vector as follows :

$$[X(t)] = \left[V_1(t), V_2(t), \ldots, V_i(t), \ldots, V_{k_{max}+1}(t), I_1(t), I_2(t), \ldots, I_i(t), \ldots, I_{k_{max}}(t)\right]^t \tag{9}$$

Note that, the number of nodes ¨$k_{max} + 1$¨ for the voltages and the number of nodes ¨ k_{max} ¨ for the currents is given just for a single electrode. Also for the computer implementation, we shift the currents backwards by half a time step. Once the unknown vector is defined, to build the matrix [A] we apply the equation (6) on all voltages nodes and equation (7) on each of the current node.

[A] is a topological matrix defined from the per unit length parameters, the step Δx and the step Δt and [B] is source vector (contains the current source located at the injection point, and the known prior values of current and voltage). The matrix [A] is full and contains the couplings between cells which appear following the effects of mutual inductances, mutual capacitances and mutual conductances. This new writing (equations (6) and (7)) allows us to get as close as possible to full wave modeling using method of moment [1]. A certain advantage, compared to other purely numerical modeling, is to allow access to the currents and voltages at each time step.

3. Dynamic model of soil ionization in our modeling

Measurement results clearly show that under the effect of a strong discharge, a phenomenon of non-linearity appears in the soil [3]. In fact, when the leakage current intensity in soil is very high (ie $E \geq E_C, E$: the local electric field in the soil and E_C : the critical electric field of the soil), the zones around the grounding grid are going through an ionization and discharge. A dynamic model for taking into account the heating of the ground and the non-linearity of its resistivity in the presence of very intense currents was introduced by Liew [4] and compared to the measured results [9]. The dynamic model of Liew [4] is described by a closed cycle of three phases. During the first phase (phase 1), the resistivity of the soil remains constant, then the ionization phase (phase 2) occurs when the electric field in the soil is greater than its critical field ($E \geq E_C$), and finally the deionization phase (phase 3) when the electric field E in the region of the ionized soil drops below critical field E_c (Figure 5).

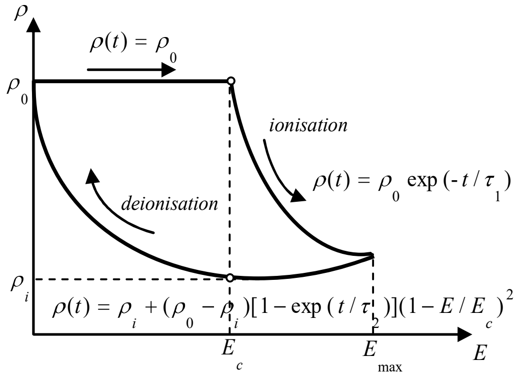

Figure 5. Resistivity profile in the dynamic model proposed by A. C. Liew [4].

For phases 2 and 3 of the dynamic cycle Liew [4] proposes analytical expressions to describe the variation of soil resistivity over time. Knowing that our temporal modeling allows us to calculate simultaneously at each time step both voltages, currents along the grounding grid and the leakage current in soil, in our work we easily apply the Liew model [4].

Indeed, we can introduce into our modeling the dynamic model of Liew [4] knowing that we can know the electric field (E) in the near of the grounding grid by applying Ohm's law (10) :

$$J_l = \sigma E = \frac{1}{\rho} E \tag{10}$$

With : $J_l = \frac{I_l}{S}$ and $S = 2r\pi\Delta l$

Where J_l is the surface density of the leakage current in the soil, I_l is the leakage current in the soil (transversal current drained to earth), S is the lateral surface of a cell, Δl is the length of cell after spatial discretization of the buried grid and r is the radius of the buried electrodes composing the grounding grid.

4. Simulation results

Firstly, we validate our proposed modeling approach; we precede by a comparison of our calculation results with those obtained by the measurement carried out by N. Harid [2]. For this application, we consider the case of square grounding grid ($3m \times 3m$) buried at a depth $d = 0.3\ m$ in a soil with two horizontal layers. The first layer has a depth of 8 meters and has electrical resistivity $\rho_1 = 200\ \Omega.m$. The second layer with infinite depth and has electrical resistivity $\rho_2 = 50\ \Omega.m$. For our calculations we use the notion of apparent electrical resistivity [10] for taking into account the two-layer soil.

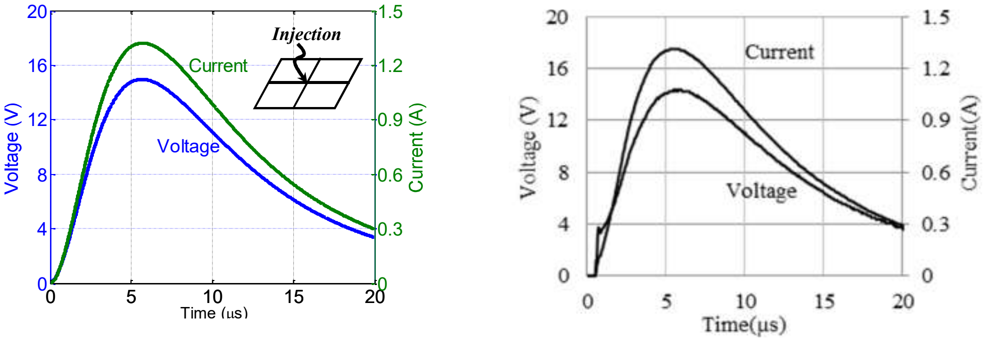

(a) Our calculations results (b) Measured results [2]

Figure 6. GPR at the injection point current of the grounding grid.

Figure 6 shows the variation of the Ground Potential Rise (GPR) at the injection point current. We note a perfect agreement between our calculations (Figure 6 (a)) and those measured (Figure 6 (b)) [2]. To complete the study of the effect of soil ionization on the transient response of grounding systems with complex geometries, we consider the case illustrated in Figure 7. It consists of a square-shaped grounding grid buried in a homogeneous soil characterized by an electrical resistivity of $\rho = 200\ \Omega.m$, a relative permittivity of $\varepsilon_r = 10$, and a critical electric field value of $E_C = 200\ kV/m$.

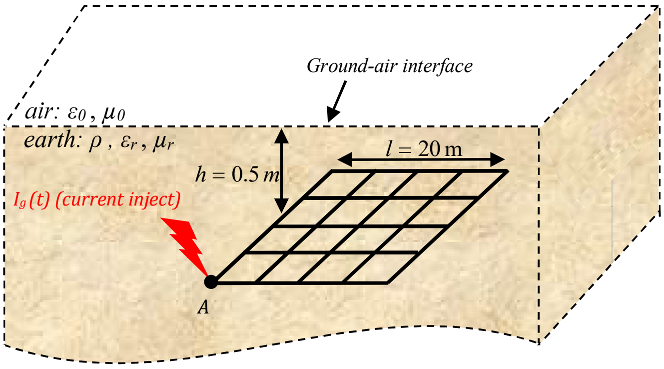

Figure 7. Grounding grid with corner injection (point A).

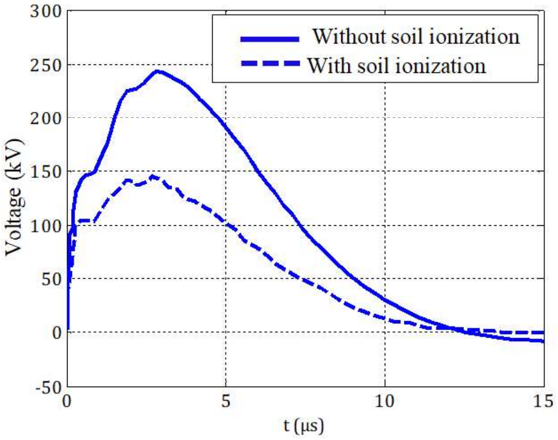

Figure 8. Voltage at point A of grounding grid.

The results presented in Figure 8 clearly show that the occurrence of the ionization phenomenon (ie $E \geq E_C$) leads to a decrease in the Ground Potential Rise (GPR) (with a reduction of the peak voltage by nearly 40%) since the electrical resistivity of the soil in the vicinity of the grounding conductors decreases up to the maximum value of the electric field (E_{max}) in the soil (see Figure 5). We then observe a reverse phenomenon, in which the soil begins to recover its initial electrical resistivity (de-ionization phase), and the GPR subsequently follows the same process. The adopted modeling approach makes it possible to identify the region of the soil, in the vicinity of the conductors, that is affected by ionization. The computation times for this application (for a transient of 15 μs) are low and are given in Table 1 (using a processor : Intel® Core™ i7 - 4600U CPU at 2.10 GHz).

Table 1. CPU time consumed.

	Without soil ionzation	With soil ionization
CPU time (sec)	312.044	345.15

5. Conclusion

The good results obtained when considering soil ionization confirm that the proposed model, developed from the nonuniform transmission line equations and the FDTD numerical method, is well suited for taking into account the dynamic behavior of soil resistivity during the injection of very high current amplitudes. Since the computation times are quite reasonable and the quality of the results is satisfactory, the proposed

References

[1] Ametani Akihiro, and al., Guideline for Numerical Electromagnetic Analysis Method, CIGRE Technical Brochure 543, pp. 1-106. 2013.

[2] N. Harid and al., On the Analysis of Impulse Test Results on Grounding Systems, EEE Transactions on Industry Applications, 2015.

[3] A. Mousa, The soil ionization gradient associated with discharge of high currents into concentrated electrodes, IEEE Transactions on Power Delivery, Volume: 9, Issue: 3. 1994.

[4] A. C. Liew and al., Dynamic model of impulse characteristic of concentrated earths, Proc. IEE, 121, (2), pp. 123–135. 1974.

[5] A. Boutadjine, B. Nekhoul and al., Realistic modeling of the grounding system transient behavior with frequency dependence, Electric Power Systems Research, volume 203, February 2022, 107644.

[6] C. R. Paul, Analysis of Multiconductor Transmission Lines, John Wiley & Sons, Inc., New York, 1994.

[7] Y. Liu, N. Theethayi, and R. Thottappillil, An Engineering Model for Transient Analysis of Groundig system Under Lightning Strikes: Nonuniform Transmission-Line Approach. IEEE Trans. on Power Delivery. Vol. 20. N° 2. April 2005.

[8] D. M. Sullivan, Electromagnetic Simulation Using the FDTD Method, by Wiley edition. 2013.

[9] K. Otani and al., FDTD Simulation of Grounding Electrodes Considering Soil Ionization, International Conference on Lightning Protection (ICLP), Vienna, Austria. 2012.

[10] IEEE Guide for Measuring Earth Resistivity, Ground Impedance, and Earth Surface Potentials of a Grounding System. Revision of IEEE Std 81-1983.

Islamic University Journal of Applied Sciences (IUJAS)
https://journals.iu.edu.sa/jesc
Special Issue, February 2026, Pages 136-148
https://igee.univ-boumerdes.dz/ncaeee25/

Design of Monopole Antenna Integrated with an CSRR-SIW band-pass Filter using a Cascaded Approach

Fatma Zohra Hamrioui [1*], Rachida Touhami [1,2], Mustapha C.E. Yagoub [3]

[1] Laboratoire des Dispositifs de Communication et de Conversion Photovoltaïque (LDCCP), Département d'Electronique, Ecole Nationale Polytechnique, 10 Rue des Frères OUDEK, El Harrach 16200, Algiers, Algeria, fatma_zohra.hamrioui@g.enp.edu.dz

[2] Instrumentation laboratory, Electronics and Informatics faculty, USTHB university, Bp32,El Alia ,Bab Ezzouar, Algiers, Algeria, rachida.touhami@g.enp.edu.dz

[3] ELEMENT laboratory, School of Electrical Engineering and Computer Science, University of Ottawa, Ottawa, Canada, myagoub@uottawa.ca

*Corresponding author: (Fatma Zohra Hamrioui), *Email Address*: fatma_zohra.hamrioui@g.enp.edu.dz

Abstract

In this paper, a butterfly-shaped monopole antenna is integrated with a CSRR-SIW band-pass filter using a cascaded approach. Initially, the design of the monopole antenna was suggested and studied. The bandwidth of this monopole antenna was extended by inserting a L-Shaped DGS into the partial ground plane, where the extended bandwidth ranges from 2.49 to 6.53 GHz . The design of an SIW band-pass filter based on extended split rectangular CSRRs is suggested to operate within the Wi-Fi 5 GHz band. The proposed band-pass filter operates at 5.47 GHz with -3dB fractional bandwidth of 13.52% (i.e., 5.07 GHz -5.81 GHz). The observed insertion loss is around 0.24 dB and the return loss is 32.23 dB. To validate the SIW-CSRR filter performance, it was cascaded with the previous wideband monopole antenna to cover the 5 GHz WI-Fi band. The resulting filtenna successfully achieves the primary goal of sharply defining the operating frequency band while maintaining good impedance matching within that band. Moreover, the suggested filtenna provides an omnidirectional radiation pattern over the desired band with a realized gain of 2.93 dB_i.

Keywords: Antenna; Filter; SIW; Filtenna.

---

https://doi.org/10.63070/jesc.2026.012
Received 25 November 2025; Revised 20 January 2026; Accepted 25 January 2026.

Published by Islamic University of Madinah on behalf of *Islamic University Journal of Applied Sciences*.

1. Introduction

Band pass filters and antennas are essential components in most RF front-ends, and their performance is critical to the overall system operation [1]. Compact size, low cost, light weight, robustness, and excellent filtering and radiating characteristics are the key properties driving an exponential surge in research focused on RF front-end system development [2]. In this context, Substrate Integrated Waveguides (SIW) have piqued the interest of researchers in microwave circuits due to their inherent benefits such as a higher quality factor, low radiation losses, compact size, and high power handling capacity [3]. Substrate integrated waveguide is a popular guided-wave configuration, intermediate between regular bulky waveguides and planar structures. It is synthesized on a planar dielectric substrate using linear, periodic arrays of metalized vias to form the sidewalls. This arrangement creates a discontinuity of the metal sidewall, which prevent the propagation of transverse magnetic TM mode wave [4].

Different technological approaches have been employed to realize high-performance filtennas. In [2], the integration utilized a synthesis approach where an inverted L-shaped monopole antenna replaced the second resonator of the band-pass filter. The antenna was integrated into the filter structure via a coupled line admittance inverter, resulting in a compact module that exhibits near-zero insertion loss within the operating frequency band. In [1], a compact integrated filtering antenna was proposed. This design utilized a microstrip structure combining a square ring resonator and a capacitor-loaded microstrip line filter, which was connected to the feeding line of a conventional patch antenna without adding extra space. In [5], a compact, wideband circularly polarized planar filtenna based on filter synthesis methodology was proposed for 5 GHz WLAN applications. The design integrates a third-order hairpin line resonator filter with a circularly polarized hexagonal radiating element. The high level of integration resulted in a wide impedance bandwidth, good stop-band gain rejection, and high selectivity at the band edges.

In this paper, a butterfly-shaped monopole antenna is integrated with a CSRR-SIW band-pass filter using a cascaded approach. The objective of this work is to demonstrate the ability of SIW structures to integrate with other microwave components by designing a band-pass filter based on this technology. The first component is a wideband monopole antenna that covers N77,N78 and N79 5G bands, and WIFI bands with large bandwidth more than 4 GHz. and the second component is a SIW-CSRR band-pass filter that operates at WIFI 5GHz band with minimum insertion loss.

The result of this cascading is a successful filtenna that achieves a sharply defined operating frequency band while maintaining good impedance matching within that band and provides an omnidirectional radiation pattern over the desired band with a realized gain of 2.93 dB_i. Therefore, this approach demonstrates the ability to utilize a single, high-performance wideband antenna for diverse applications, either in its unfiltered state for wideband capability or in its filtered state for narrow-band communication, with the latter being the primary focus and core contribution of this paper. To thoroughly cover the methodology, implementation, and performance of the proposed design, the paper is organized into several sections: Section 2 details the methodology used to design the wideband antenna with L-shaped defected ground structure (DGS). Section 3 focuses on the design of the SIW band-pass filter by loaded extended Complementary split Ring Resonators (CSRRs), including its S-parameters and current distribution. Section 4 describes the final cascaded implementation, presenting the resulting simulated performance, such as the sharp input reflection coefficient response and omnidirectional radiation pattern. Finally, Section 5 provides the conclusion of the paper.

2. Design and analysis of the proposed monopole antenna

One category of antenna used in wireless technology is the monopole antenna due to their wide bandwidth, light weight and small size. In this section, a butterfly-shaped monopole antenna is designed. This proposed antenna is printed on Rogers RT/Duroid 5880 substrate having a thickness of 0.79 mm , permittivity of 2.2 and dielectric loss tangent of 0.0009. The proposed structure is illustrated in figure 1 and the geometric dimensions are given in table 1. Note that the partial ground plane is etched with an L-shaped defected ground structure (DGS) to extend the operating band. To illustrate the effect of the DGS on the input reflection coefficient, the design evolution of the proposed antenna, evolving from prototype 1 to prototype 2, is depicted in figure 2. The input reflection coefficients of these antennas are shown in figure 3.

The design of the proposed antenna starts with a butterfly-shaped patch antenna with a partial ground plane (Prototype I, Figure 2). The antenna resonates at 5.28 GHz with -10 dB bandwidth spanning from 3.71 GHz to 5.83 GHz. To enhance bandwidth performance, two L-shaped DGS elements are etched onto the partial ground plane (Prototype 2, Figure 2). Consequently, the bandwidth expands from 2.49 to 6.53 GHz with maximum return loss of 29.12 dB.

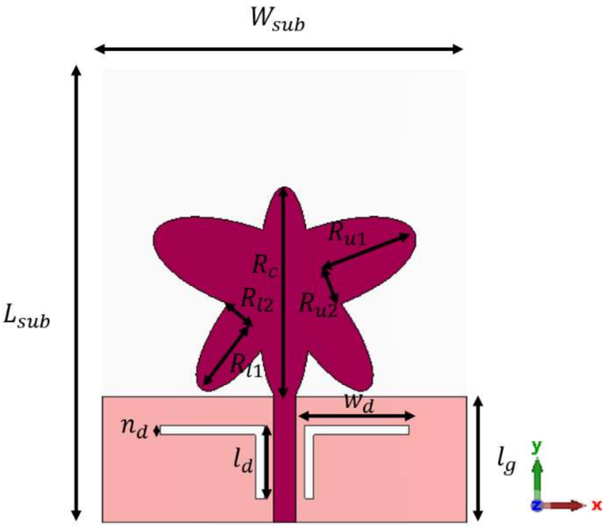

Figure 1. Geometric structure of the proposed butterfly monopole antenna.

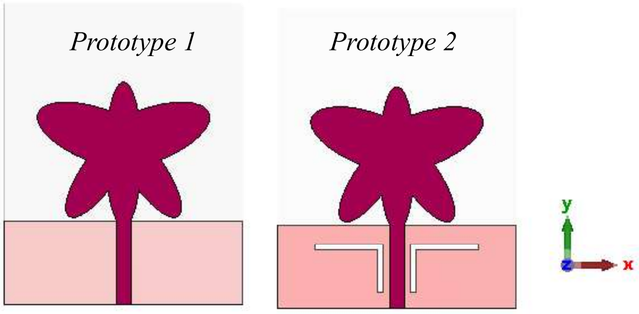

Figure 2. The design evolution of the suggested monopole antenna.

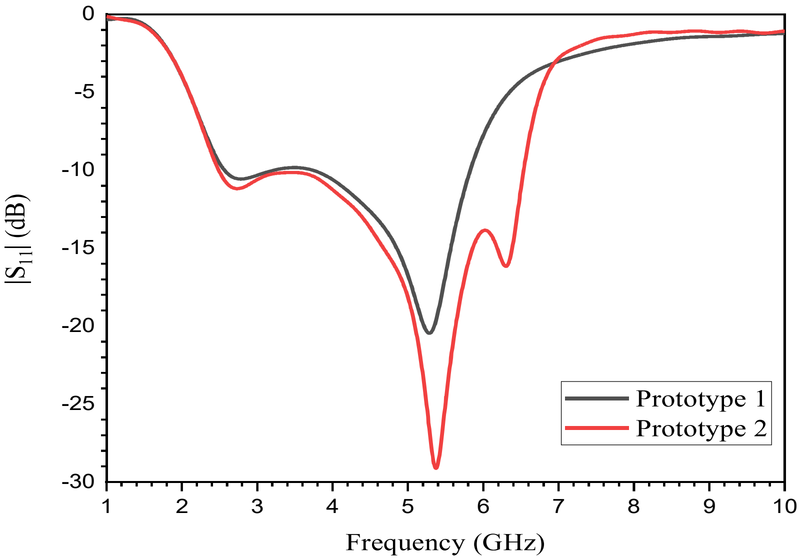

Figure 3. the input reflection coefficient for each prototype.

Table 1. Detailed dimensions of the proposed monopole antenna.

W_{sub}	**L_{sub}**	**W_d**	**L_d**	**L_g**
50.00 mm	40.00 mm	11.50 mm	8.00 mm	13.80 mm
n_d	**R_{u1}**	**R_{l1}**	**R_c**	**h**
1.00 mm	11.00 mm	9.00 mm	24.00 mm	0.79 mm
R_{u2}	**R_{l2}**	**Θ_1**	**Θ_2**	
4.50 mm	3.00 mm	-70°	-35°	

Next, the effect of the parameters Θ_1 and Θ_2 on the upper and lower wings are shown in figures 4 and 5, respectively. As Θ_1 is increased, the return loss is reduced and the primary resonant frequency is moved toward a higher frequency .Whereas, as Θ_2 is increased from 15° to 45°, the primary resonant frequency shifts to a higher frequency and the bandwidth is extended except that as Θ_2 exceeds 45° ,the bandwidth is reduced. Therefore, Θ_2 is a sensitive tuning parameter for the antenna's operating frequency. Changing Θ_2 effectively changes the antenna's geometry, which directly dictates its resonant frequency and the operating bandwidth . These results suggest that $\Theta_2 = 35°$ is the optimal design point for this antenna within the tested range, as it provides the best and the widest impedance bandwidth.

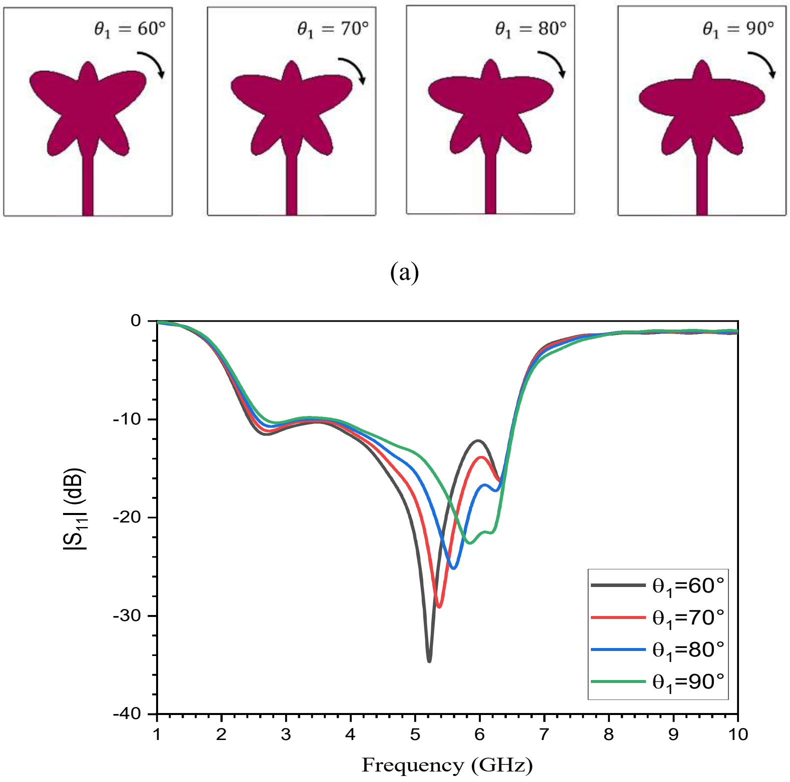

(a)

(b)

Figure 4. Input reflection coefficient of the proposed monopole antenna by varying Θ_1, (a) Varying Θ_1 (b) the input reflection coefficient for each Θ_1.

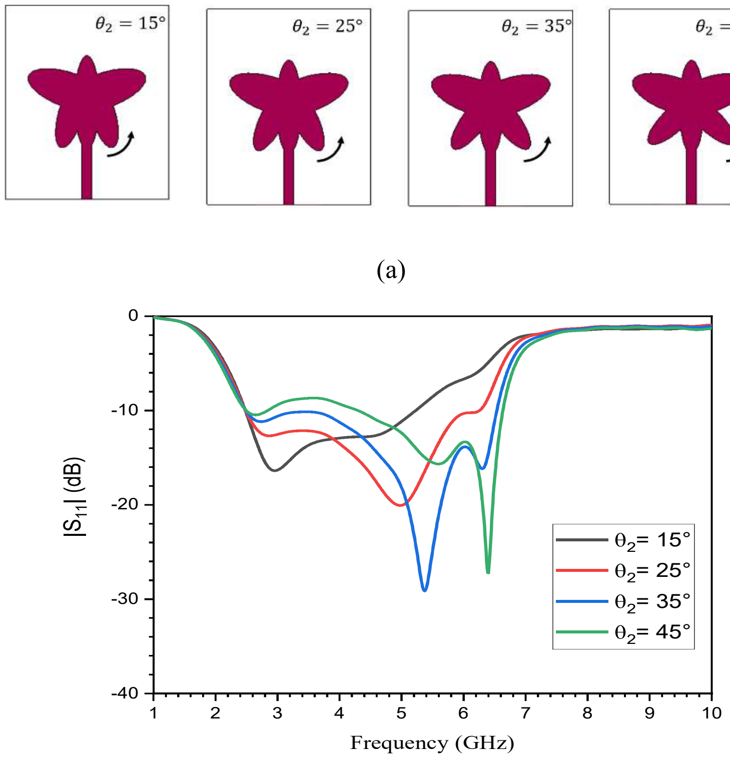

(a)

(b)

Figure 5. Input reflection coefficient of the proposed monopole antenna by varying Θ_2, (a) Varying Θ_2 (b) the input reflection coefficient for each Θ_2 .

The simulated 3D radiation patterns of the proposed monopole antenna at 5.37 GHz is shown in figure 6. From this figure, we can see that the antenna exhibits almost broadside omnidirectional radiation pattern at this operating frequency with maximum realized gain of 2.92 dB_i and directivity of 3.01 dB_i.

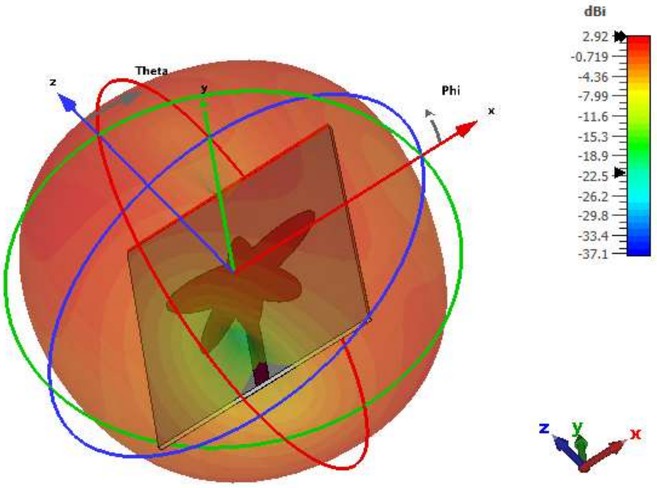

Figure 6. Simulated 3D radiation patterns of the proposed filtenna at 5.37 GHz.

3. Design of the proposed CSRR-SIW band-pass filter

The design structure of the suggested SIW band-pass filter based on CSRRs is shown in Figure 7. Two rows of metallic via holes are inserted on the waveguide's two long sides, to form the waveguide's metal walls. The diameter d of the via is fixed to 0.60 mm and pitch s of via holes is fixed to 1.10 mm. a face-to-face extended split rectangular resonators are etched on the top of the metal plane of the SIW cavity to provide a pass-band below the waveguide cutoff in accordance with the theory of evanescent-mode propagation[6].

The 50Ω microstrip lines are directly connected to the cavity at input/output ports. This suggested filter is designed using 0.79mm thick Rogers RT/Duroid 5880 substrate having a permittivity of 2.22 and dielectric loss tangent f 0.0009.The geometric dimension are : l_p=4.40 mm and w_p=10.00 mm.

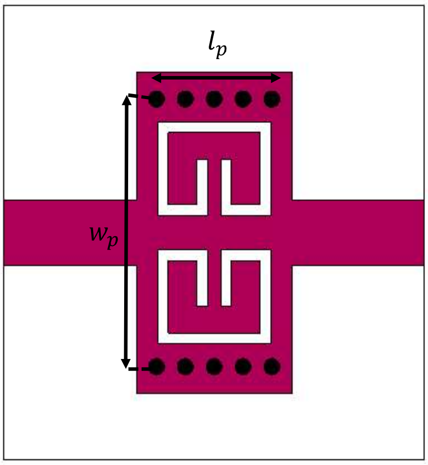

Figure 7. Geometric structure of the proposed SIW-CSRR band-pass filter

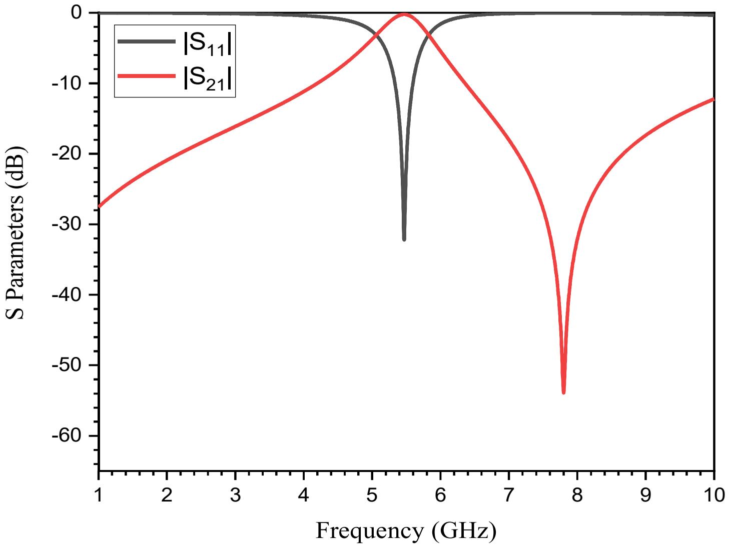

Figure 8. Simulated S-Parameters of the suggested SIW-CSRR band-pass filter.

The simulated results of the proposed band-pass filter are shown in figure 8. It is seen that the proposed filter operates at 5.47 GHz with -3dB fractional bandwidth of 13.52 % (i.e., 5.07 GHz-5.81 GHz) covering the 5 GHz Wi-Fi band. The observed insertion loss is around 0.24 dB and the return loss is 32.23 dB. One transmission zero around 7.80 GHz is detected at upper stop-band with high attenuation of 53.91 dB.

The electric field distribution of the proposed SIW-CSRR band-pass filter is shown in figure 9. The electric field distribution is concentrated around the CSRRs as indicated by the color ramps, demonstrating that the pass-band created below the waveguide cutoff frequency is caused by loading the CSRRs into the SIW.

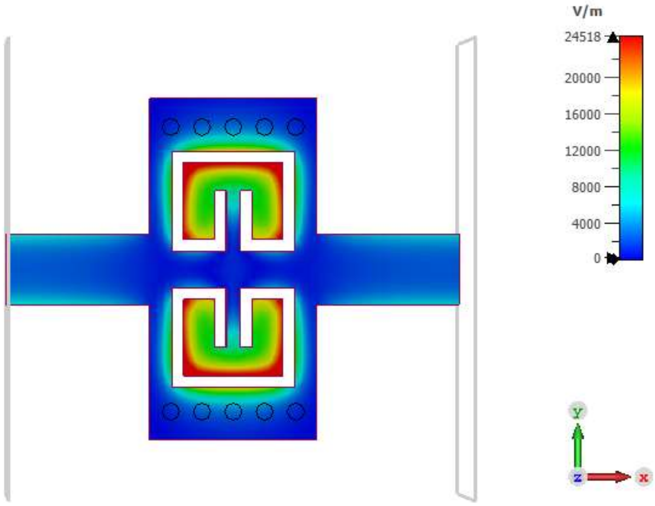

Figure 9. Simulated E field distribution of the proposed SIW-CSRR band-pass filter.

4. Design and analysis of the proposed filtenna

To achieve a filtering response, the proposed butterfly monopole antenna is cascaded with the suggested SIW-CSRR band-pass filter. The resulting filtenna from this cascaded structure is shown in figure 10. The geometric dimensions are: $W_{sub}= 40\ mm$ and $L_{sub}= 66\ mm$.

The input reflection coefficient versus frequency is depicted in figure 11. It can be seen that the suggested design successfully achieves the primary goal of a filtenna: sharply defining the operating frequency band while maintaining good impedance matching within that band. The suggested filtenna resonates at frequency of 5.41 GHz with a minimum input reflection coefficient of -25.38 dB, indicating a near-perfect impedance match where virtually all power is delivered to the antenna .A$-10\ dB$ impedance bandwidth from 5.27GHz to 5.54 GHz is obtained around the resonant frequency. Outside the desired band, the return loss rises sharply and approaches 0 dB.

This value in the stop-band confirms the functionality of the suggested filter, which effectively rejects unwanted signals and interference.

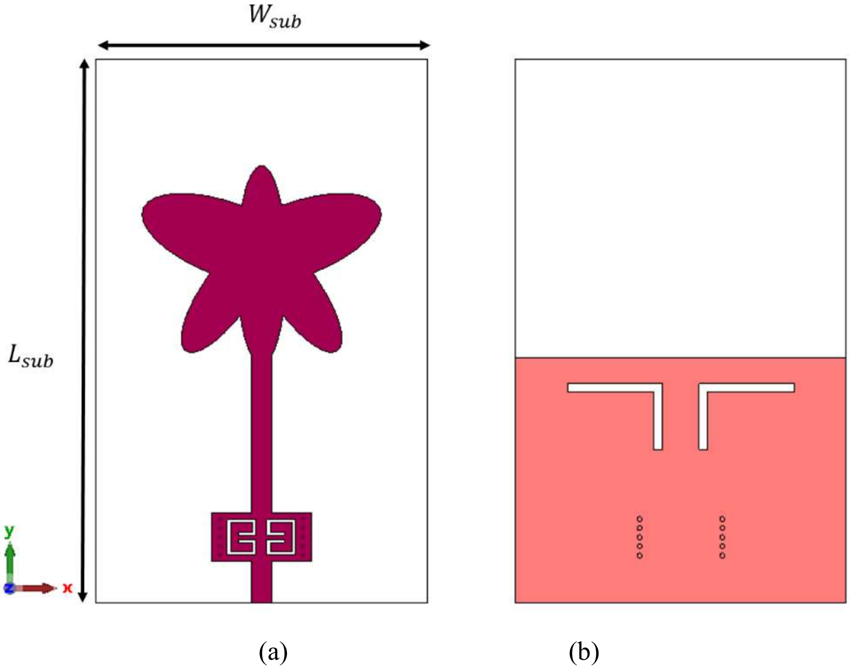

Figure 10. Geometric structure of the proposed filtenna, (a) Top view, (b) back view.

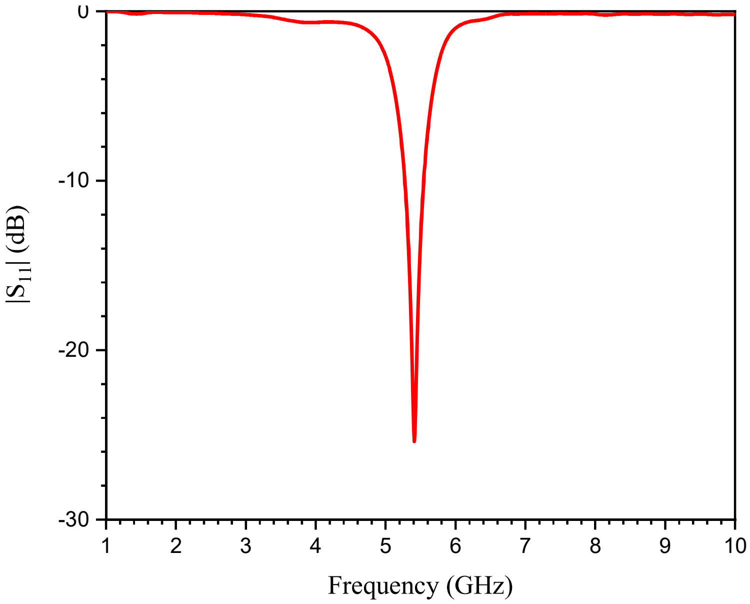

Figure 11. Input reflection coefficient of the proposed filtenna.

The E plane (φ = 90°) and H plane (φ = 0°) radiation patterns at 5.41 GHz of the proposed filtenna are illustrated in figure 12. It can be seen that this filtenna exhibits broadside ,omnidirectional pattern similar to radiation pattern of the monopole antenna at the same operating band .The realized gain is around 2.93 dB_i and the directivity of 3.23 dB_i.

Therefore, the suggested filter does not change the physical structure of the radiator itself, thus the pattern is preserved. The 3D radiation pattern is illustrated in figure 13.

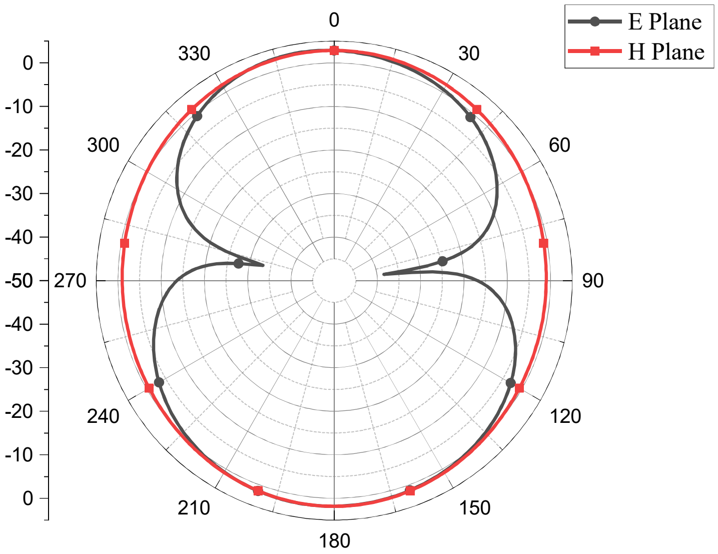

Figure 12. Simulated radiation patterns of the proposed filtenna at 5.41 GHz.

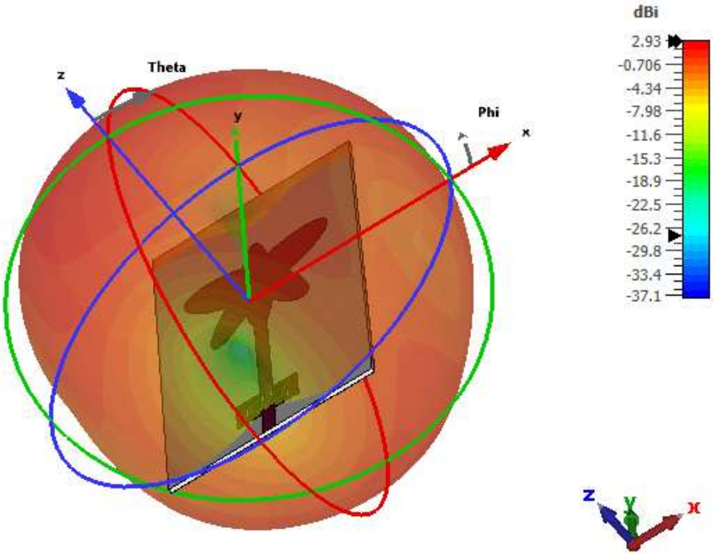

Figure 13. Simulated 3D radiation pattern of the proposed filtenna at 5.41 GHz.

To demonstrate the impact of the filter on the antenna's realized gain, figure 14 compares the realized gain of the standalone antenna and the proposed filtenna across the 1–10 GHz frequency range. The realized gain of the suggested antenna varied from 1.63 dB_i to 3 dB_i across the frequency band from 2.47 GHz to 5.45 GHz. Specifically, the gain reached a maximum of 5.17 dB_i at 6.28 GHz before decreasing to -1.70 dB_i at 10 GHz.

Whereas, the filtenna exhibits a selective gain response where the gain varies from 2.46 dB_i to 2.52 dB_i across the operating band, achieving a peak gain of 2.92 dB_i at the center frequency. Outside this band, the realized gain drops significantly, decreasing to -21.90 dB_i at 1.80 GHz on the lower side ,and further decreasing by -13.10 dB_i at 7.10 GHz on the higher side, before increasing again to -9.23 dB_i at 10 GHz.

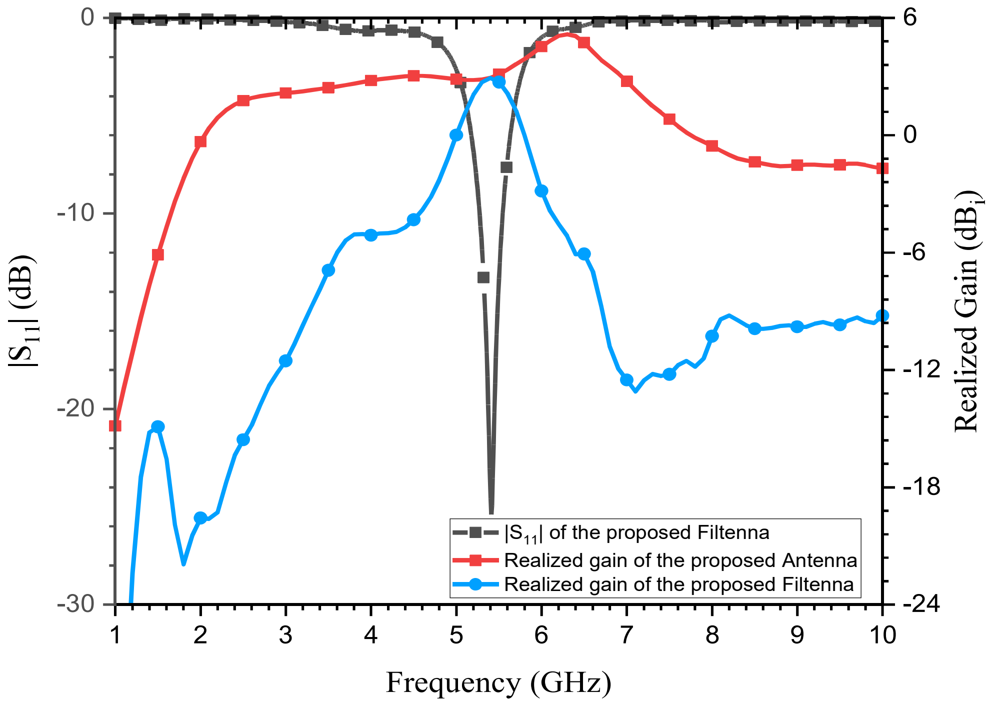

Figure 14. Simulated realized gain versus frequency.

The performance of the suggested filtenna compared to similar works is illustrated in table 2. The proposed filtenna achieves a maximum gain of 2.93 dB_i, which is the highest value compared to the cited works. This value is consistent with the gain of the standalone wideband antenna before integration. Therefore, this high gain is attributed to the effective integration of the low-loss SIW-CSRR band-pass filter. However, this high performance comes at the expense of footprint where the size of the proposed design is larger than the cited works.

Table 2. Performance comparison of the suggested filtenna with existing works (*: Simulated, **: Measured)

Works	f_r (GHz)	10 dB FBW (%)	RL (dB)	Gain (dB_i)	Size (mm^2)
[1] (**)	2.40	3.00	-	2.61	-
[2] (**)	2.40	7.50	-	0.74	$0.28\lambda_0 \times 0.24\lambda_0$
[7] (**)	2.45	10.00	-	0.65	$0.49\lambda_0 \times 0.49\lambda_0$
[8] (**)	2.45	-	-	1.20	$0.41\lambda_0 \times 0.41\lambda_0$
This work (*)	5.41	5.00	25.38	2.93	$0.72\lambda_0 \times 1.19\lambda_0$

5. Conclusion

This paper presents the cascaded integration of a butterfly-shaped monopole antenna and a CSRR-SIW band-pass filter. The proposed monopole antenna covers the (2.49 - 6.53 GHz). Its wide bandwidth is attributed to the L-shaped DGS etched into the partial ground plane. On the other hand, the design of a compact SIW CSRRs band-pass filter is suggested. The proposed filter covers the 5 GHz WI-Fi band with -3dB fractional bandwidth of 13.52 % (i.e., 5.07 GHz -5.81 GHz). To verify the functionality of the proposed filter, it is cascaded with the previous monopole antenna. The suggested filtenna resonates at frequency of 5.41 GHz with a minimum input reflection coefficient of -25.38 dB, indicating a near-perfect impedance match and $-10\ dB$ impedance bandwidth from $5.27 GHz$ to 5.54 GHz is obtained around the resonant frequency. In addition, the suggested filtenna provides an omnidirectional radiation pattern over the desired band with a realized gain of 2.93 dB_i. These results prove that the suggested SIW-CSRR band-pass filter does not change the physical structure of the radiator and the monopole antenna's omnidirectional radiation pattern is preserved. Furthermore, because the antenna and filter are well-matched in the pass-band, the power delivered to the antenna is maximized. Consequently, the realized gain and the pattern form of the filtenna system is nearly the same as the original wideband monopole antenna's peak gain and pattern.

References

[1] Z. A. Nasser, Z. Zakaria, N. A. Shairi, S. N. Zabri, and A. M. Zobilah, “Design of compact filtenna based on capacitor loaded square ring resonator for wireless applications,” *Progress in Electromagnetics Research M*, vol. 96, pp. 21–31, 2020.

[2] P. Pal, R. Sinha, and S. K. Mahto, “Synthesis approach to design a compact printed monopole filtenna for 2.4 GHz Wi-Fi application,” *International Journal of RF and Microwave Computer-Aided Engineering*, vol. 31, no. 5, Mar. 2021

[3] M. Bozzi, A. Georgiadis, and K. Wu, “Review of substrate-integrated waveguide circuits and antennas,” *IET Microwaves Antennas & Propagation*, vol. 5, no. 8, pp. 909–920, Jun. 2011

[4] Q. Tan, Y. Guo, L. Zhang, F. Lu, H. Dong, and J. Xiong, “Substrate Integrated Waveguide (SIW)-Based wireless temperature sensor for harsh environments,” *Sensors*, vol. 18, no. 5, p. 1406, May 2018

[5] P. Pal, R. Sinha, and S. K. Mahto, “A compact wideband circularly polarized Planar filtenna using synthesis technique for 5 GHz WLAN application,” *AEU - International Journal of Electronics and Communications,* vol. 148, p. 154180, Mar. 2022.

[6] N. Y. D. Dong, N. T. Yang, and T. Itoh, "Substrate integrated waveguide loaded by complementary Split-Ring resonators and its applications to miniaturized waveguide filters," *IEEE Transactions on Microwave Theory and Techniques*, vol. 57, no. 9, pp. 2211–2223, Aug. 2009.

[7] C.-T. Chuang and S.-J. Chung, "Synthesis and design of a new printed filtering antenna," *IEEE Transactions on Antennas and Propagation,* vol. 59, no. 3, pp. 1036–1042, 2011.

[8] C.-T. Chuang and S.-J. Chung, "A compact printed filtering antenna using a Ground-Intruded coupled line resonator," *IEEE Transactions on Antennas and Propagation*, vol. 59, no. 10, pp. 3630–3637, 2011.

Islamic University Journal of Applied Sciences (IUJAS)

https://journals.iu.edu.sa/jesc
Special Issue, February 2026, Pages 149-161
https://igee.univ-boumerdes.dz/ncaeee25/

Enhancing Phased-Array Radiation Pattern Synthesis with a Hybrid Complex-Valued Deep Learning

Mansour Djassem BENDREF[1, *], Mouloud CHALLAL[1], Ghillasse BENTAYEB[1], Abdelaziz ZERMOUT[1]

[1] Signals and System Laboratory, Institute of Electrical and Electronic Engineering, University M'Hamed BOUGARA- Boumerdes, Boumerdes, Algeria, m.bendref@univ-boumerdes.dz, mchallal@univ-boumerdes.dz, G.bentayeb@univ-boumerdes.dz, az.zermout@univ-boumerdes.dz

*Corresponding author: (Mansour Djassem BENDREF), *Email Address*: m.bendref@univ-boumerdes.dz

Abstract

Phased antenna arrays are essential for millimeter-wave (mmWave) communications in 5G/6G systems, enabling adaptive beamforming and precise radiation pattern control. Traditional array synthesis methods rely on analytical techniques or iterative optimization algorithms that are computationally intensive and often too slow for real-time applications. This paper presents a novel hybrid deep neural network (DNN) architecture that incorporates complex-valued neural network (CVNN) processing for rapid synthesis of phased array radiation patterns. Unlike conventional real-valued DNNs that treat amplitude and phase as separate outputs, our approach employs a CVNN output layer to directly predict complex excitations, naturally capturing the coupled amplitude-phase relationships inherent in electromagnetic wave phenomena. We trained and validated the model on an 8-element uniform linear array operating at 28 GHz, using 8000 electromagnetic simulations generated in CST Microwave Studio.

---

https://doi.org/10.63070/jesc.2026.013
Received 24 November 2025; Revised 18 January 2026; Accepted 25 January 2026.

Published by Islamic University of Madinah on behalf of *Islamic University Journal of Applied Sciences*.

The network accepts a desired radiation pattern (181 angular samples covering 0°–180°) as input and outputs the complex excitations for seven array elements (with one reference element fixed). Experimental results across three challenging beamforming scenarios—main-beam steering with shaped sidelobes, aggressive sidelobe suppression (target: -30 dB), and broad beam shaping—demonstrate that the DNN-CVNN consistently outperforms a baseline real-valued DNN. The hybrid model achieves sidelobe levels 15-20 dB better than the baseline, maintains sub-degree beam-pointing accuracy, and produces smooth, physically realizable excitation distributions. CST-validated patterns confirm that the learned weights directly correspond to accurate far-field radiation, with the DNN-CVNN achieving pattern synthesis in milliseconds compared to hours required by traditional optimization methods. These results establish complex-valued neural networks as a powerful and practical tool for real-time adaptive beamforming in next-generation wireless communication systems.

Keywords: Phased array synthesis, Complex-valued neural networks, Deep learning, Millimeter-wave beamforming, 5G/6G communications, Antenna pattern synthesis.

1. Introduction

Phased antenna arrays are key to modern mmWave communications (e.g. 5G/6G systems around 28 GHz) because they enable highly directive beamforming and adaptive radiation patterns [1]-[4]. In an 8-element linear array, controlling the amplitude and phase of each element lets us steer the main beam and shape sidelobes to achieve a desired pattern. Traditionally, array pattern synthesis relies on analytical methods (like Dolph–Chebyshev tapers) or numerical optimizers (e.g. iterative Fourier techniques, genetic algorithms) [5]-[8]. These methods can be robust but often require substantial computation and many EM simulations, making them slow for real-time adaptation [8] Machine learning, especially deep neural networks (DNNs), offers a data-driven alternative [9] once trained, a DNN can quickly map a target radiation pattern to the needed element excitations (amplitudes and phases). Recent studies show that neural networks can learn this inverse mapping efficiently, reducing synthesis time and handling complex patterns that traditional methods struggle with [10]-[12].

In this work, we develop a DNN–CVNN model for pattern synthesis of an 8-element array (with one reference element fixed at amplitude = 1 and phase = 0). We feed the network with a sampled desired pattern (181 angular points covering 0–180°) and train it to output the complex excitations for the other elements. Unlike a conventional DNN that outputs real amplitudes and phases separately, our approach uses a complex-valued neural network (CVNN) for the output layer to directly predict complex weights. This can better capture the amplitude–phase relationships in a compact form.

We will compare this DNN–CVNN model to a purely real-valued DNN baseline (with separate outputs for amplitude and phase as in prior work). All predictions are validated by EM simulations in CST Microwave Studio to ensure the learned excitations produce the intended beam.

Beam pattern synthesis means choosing element weights to form a beam in a given direction with controlled sidelobes [13]. Classical approaches include Fourier-based methods and global optimizers. However, these can be slow for large arrays or complex beam specifications. In practice, designers often exploit symmetries (e.g. symmetric amplitude tapers) to reduce variables. For an 8-element array, one common scheme fixes one element as a reference (amplitude 1, phase 0) so only the remaining 7 complex excitations must be found; symmetry can further cut down unknowns [14].

Early ML work showed feasibility of training ANNs to learn array weights from target patterns [15]. For example, a deep CNN was used to predict phase shifts for a 2D reflect array from a desired 2D pattern[15][16], and another CNN was trained to infer phase values for an 8×8 planar array given its 2D pattern[15]. In linear-array contexts, Kim and Choi (2020) introduced a DNN that inputs sampled gain patterns (e.g. 19 points per side) and outputs element phases for beamforming [15]. More recently, Zaib *et al.* (2024) proposed a DNN for an 8-element linear array: they feed 181 pattern samples into a network and extract the 7 element phases (fixing one reference) as outputs [17]. Their work also discusses reducing training data by exploiting the array's constant phase-shift symmetry. Similarly, Abdullah *et al.* (ACES 2025) trained a fully-connected DNN with 181 inputs and 10 outputs (3 amplitudes + 7 phases) for an 8-element array, demonstrating that a single DNN can control both beam steering and sidelobe levels simultaneously. In these examples, after training on many simulated patterns, the DNN can "instantly" predict the complex excitations needed to realize a new target pattern.

Various network architectures have been explored. Convolutional networks (CNNs) help when pattern inputs have spatial structure (as in 2D aperture problems) [15]. Recurrent networks (RNNs/LSTMs) have also been tested: Arce *et al.* (2025) used an LSTM-based model that learned from GA-optimized patterns and found it outperformed fully-connected DNNs [13]. All these works share a similar training paradigm: generate a large dataset of (pattern, weight) pairs via simulation or optimization, train the network to regress from pattern to weights, and then validate on new patterns. In practice, 1×8 arrays commonly use 181 samples (1° resolution) as input features, though other works have used finer grids or two-channel representations (linear/gain) for more complex scenarios.

Most cited approaches use real-valued DNNs that output real numbers for amplitudes and phases separately [171]. By contrast, complex-valued neural networks (CVNNs) natively handle complex weights and can model rotations and phase relationships inherently [18]. In the beamforming literature, CVNNs have been shown to converge faster and suppress interference better than conventional real-valued algorithms [18]. Although CVNNs are common in communications tasks (e.g. modulation classification), they have seen less use in antenna synthesis. Our work leverages a hybrid DNN–CVNN: real-valued layers process the real pattern input, while the output layer uses complex weights and activation to produce the complex excitations. We expect this to better capture the amplitude–phase coupling and compare its performance to a standard real-DNN approach.

The choice of 28 GHz places this work firmly in the mmWave regime, which is important for 5G/6G applications (massive MIMO, fixed wireless access, etc.). At such high frequencies, even small phase errors can dramatically distort the beam, so precise synthesis is critical. In this band, real-time pattern reconfiguration (for beam steering or sidelobe control) is valuable, motivating fast ML-based solutions. We will validate our learned weights via CST simulations at 28 GHz to ensure real-world fidelity.

In summary, recent literature confirms that DNNs can learn to synthesize array patterns from example data [14]. Our approach extends this by using a complex-valued output network and by benchmarking against a conventional DNN. The novelty lies in the DNN–CVNN hybrid and its application to 28 GHz array design, building on the state-of-the-art methods cited above.

2. Methodology

2.1 Data Preparation

An 8-element linear array at 28 GHz was modeled in CST Microwave Studio. The array elements were assumed uniformly spaced 0.5λ apart on a typical substrate, and one element was chosen as a fixed reference (amplitude = 1, phase = 0). To build the dataset, the excitation of the other 7 elements was varied (amplitude and phase) and the corresponding far-field pattern was simulated in CST for each case. Each radiation pattern was sampled in the 0°–180° angular range at 1° resolution (resulting in 181 sample points). The pattern values (linear gain or magnitude) were normalized (to the peak value) so that they form a consistent input range. The input to the model is thus a vector of ~180 real values (gain at each angle). The output target for each sample is the set of 7 complex excitations (one per non-reference element). In practice, these complex targets can be represented directly (as a CVNN output) or split into real and imaginary (or magnitude/phase) components. In this work, we keep the reference element fixed and train the network to predict the complex amplitudes of the remaining 7 elements. A total of 8000 CST simulations were generated in this way, yielding 8000 input–output pairs (pattern → excitations). (All inputs and outputs were assembled into training and validation sets after generation).

2.2 Model Architecture

The hybrid neural network consists of a real-valued deep feedforward DNN to process the input pattern and a complex-valued output layer to predict the excitations. The input layer has one neuron per angle (180 inputs for 0°–180°). The hidden part of the network comprises 3 fully connected layers (experimentally chosen, with widths like 128→64→32) using ReLU activations. These layers learn nonlinear features of the radiation pattern. The output layer is a complex-valued fully connected layer with 7 neurons (one for each of the 7 predicted elements). This Complex Dense/CVNN layer produces 7 complex outputs directly (each as a complex weight), naturally encoding both amplitude and phase. Using a CVNN output is motivated by the fact that antenna excitations are inherently complex-valued (amplitude and phase) and CVNNs can model the necessary complex multiplication/rotation operations more compactly [19].

In practice, this layer is implemented using a CVNN library (PyTorch complex layer) so that the network learns complex weights via Wirtinger backpropagation. (No nonlinearity is applied at the output – it is a linear complex layer.

- **Input layer:** 180 real nodes (gain at each 1° from 0–180°).
- **Hidden layers:** 3–5 dense layers (widths 128, 64, 32) with ReLU activations.
- **Output layer:** 7 complex neurons (Complex Dense)

This hybrid architecture leverages the DNN to extract features from the real-valued pattern, and the CVNN layer to naturally output complex phasors. Using complex weights avoids splitting the problem into separate real/imaginary regressions and exploits the amplitude-phase structure of wave phenomena [19].

2.3 Training Setup

The network was trained as a regression model. The loss function was the mean squared error (MSE) between the predicted complex outputs and the true excitations.

$$L_{MSE} = \frac{1}{N}\sum_{i=1}^{N}\sum_{j=1}^{M}(\emptyset_{pred}^{(i)} - \emptyset_{true}^{(i)})^2 \qquad (1)$$

Where N = Number of training samples (batch size)

M = Number of active elements requiring phase prediction

Equivalent to sum of squared errors on real and imaginary parts. We used the Adam optimizer (a gradient-based method) with a typical learning rate (10^{-3}). Training was done in minibatches (batch size 32) for up to several hundred epochs, with early stopping on a validation set to prevent overfitting. An 80/20 split of the data was used for training vs. validation. Standard regularization such as weight decay or dropout could also be applied to the DNN layers if needed.

- **Loss:** MSE on complex outputs.
- **Optimizer:** Adam (. lr = 0.001).
- **Data split:** ~80% training, 20% validation; early stopping on validation loss.
- **Regularization:** dropout to avoid overfitting.
- **Framework:** Implemented in a deep learning library that supports complex numbers (PyTorch with a complex extension). The cvnn Complex Dense layer can be used for the final layer, allowing end-to-end complex-valued backpropagation.

Throughout training, we monitor both training and validation loss (MSE) on the excitations. When training converges (or early stopping is triggered), the model weights are saved for use in validation.

2.4 Simulation-Based Validation

After training, the learned mapping is tested by "closing the loop" in simulation. Given a new desired pattern, the network predicts a set of excitations (complex weights) for the 7 elements. These predicted excitations are then applied to the array (via CST or a custom array-factor calculation) to compute the resulting far-field pattern. We then compare the simulated pattern to the target.

The plot below (Figure 1) illustrates the training and validation loss curves for our model. As shown, the training loss decreases steadily, reaching approximately -25 dB, while the validation loss achieves its minimum at about -23 dB at epoch 114. This epoch marks the point of best validation performance, and beyond it, the validation loss begins to increase, indicating potential overfitting.

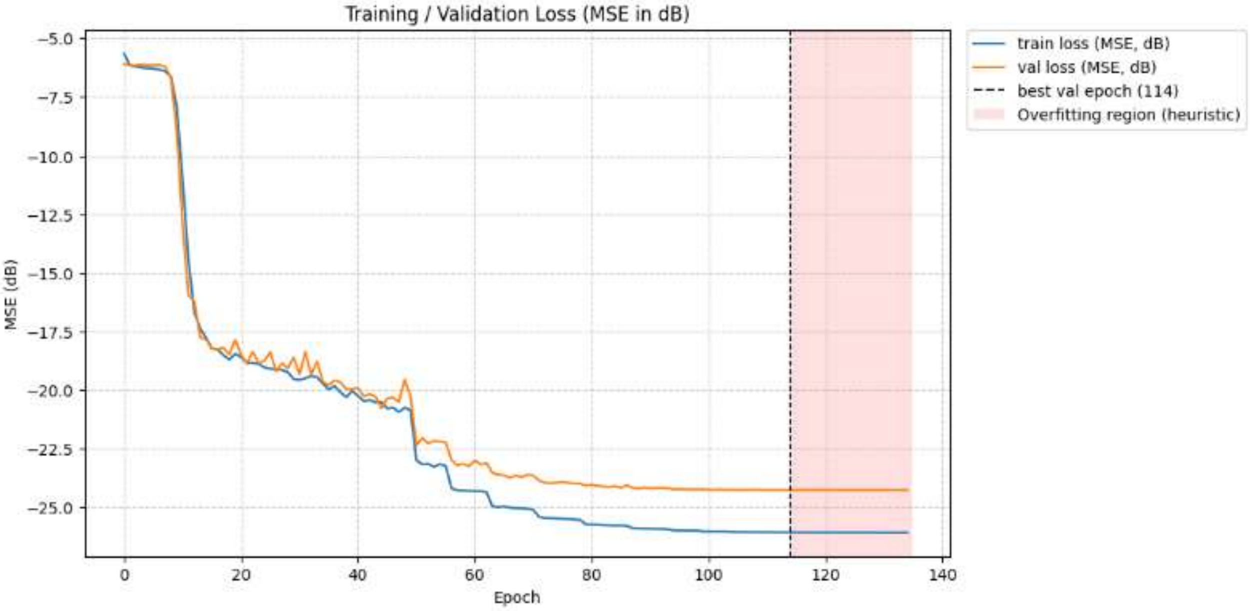

Figure 1 The training and validation plot

A successful synthesis produces a pattern whose main lobe and sidelobe structure closely match the desired specification. By iterating over multiple test cases (beam directions, shapes, etc.), we assess the generalization of the model. Quantitative results (angle error, SLL difference, HPBW error, etc.) are reported to validate the accuracy of the model in practical beamforming tasks.

3. Result and Discussion

The proposed hybrid DNN–CVNN model was evaluated on three beamforming tasks (main-beam steering, sidelobe reduction, and multi-beam generation) and compared to the baseline real-valued DNN. In each case, the networks were used to predict antenna element weights (amplitude and phase) for a uniform linear array at 28 GHz, and the resulting beams were simulated in CST.

Figure 2 represents the main-beam steering. In this beam-steering scenario with shaped sidelobe constraints, both methods attempt to synthesize a directive beam at approximately -17° with selective sidelobe suppression.

The DNN–CVNN demonstrates remarkable pattern accuracy: it generates a well-defined main lobe peaking at 0 dB near the target angle with smooth, controlled transitions into the adjacent sectors. Critically, the hybrid model maintains sidelobe suppression close to the -30 dB specification across the critical back-lobe and far-sidelobe regions (beyond ±60°), achieving levels between -24 and -30 dB. The forward-quadrant sidelobes (+20° to +60°) are contained at -22 to -23 dB, representing minor deviations of 7-8 dB from the ideal mask but still maintaining pattern integrity. Conversely, the real-valued DNN produces severe pattern degradation: while it captures the approximate main beam location, massive sidelobe intrusions plague the positive angular hemisphere. Specifically, the +10° to +30° sector exhibits catastrophic sidelobe elevation to -7 to -11 dB—more than 20 dB above specification—creating unacceptable spillover radiation. Even the negative-angle sidelobes deteriorate to -13 to -17 dB, falling 13-17 dB short of requirements. The error comparison starkly illustrates this gap: the DNN–CVNN maintains deviations predominantly within ±10 dB, whereas the baseline accumulates errors exceeding +20-25 dB throughout the positive hemisphere. Examining the complex excitations, the DNN–CVNN weights exhibit a well-ordered phase progression (approximately 300° span across elements) characteristic of a steered beam, coupled with amplitude tapering that enforces the asymmetric sidelobe constraints. The real-valued DNN's excitations display fragmented phase structure and imbalanced amplitudes that fail to generate the required null placement. This shaped-beam task underscores the critical advantage of complex-valued learning: the DNN–CVNN directly encodes the precise phase relationships necessary for both accurate beam steering and asymmetric null placement, while the real-valued network's indirect phase representation cannot simultaneously satisfy pointing and sidelobe specifications, resulting in a pattern with correct beam direction but uncontrolled radiation elsewhere.

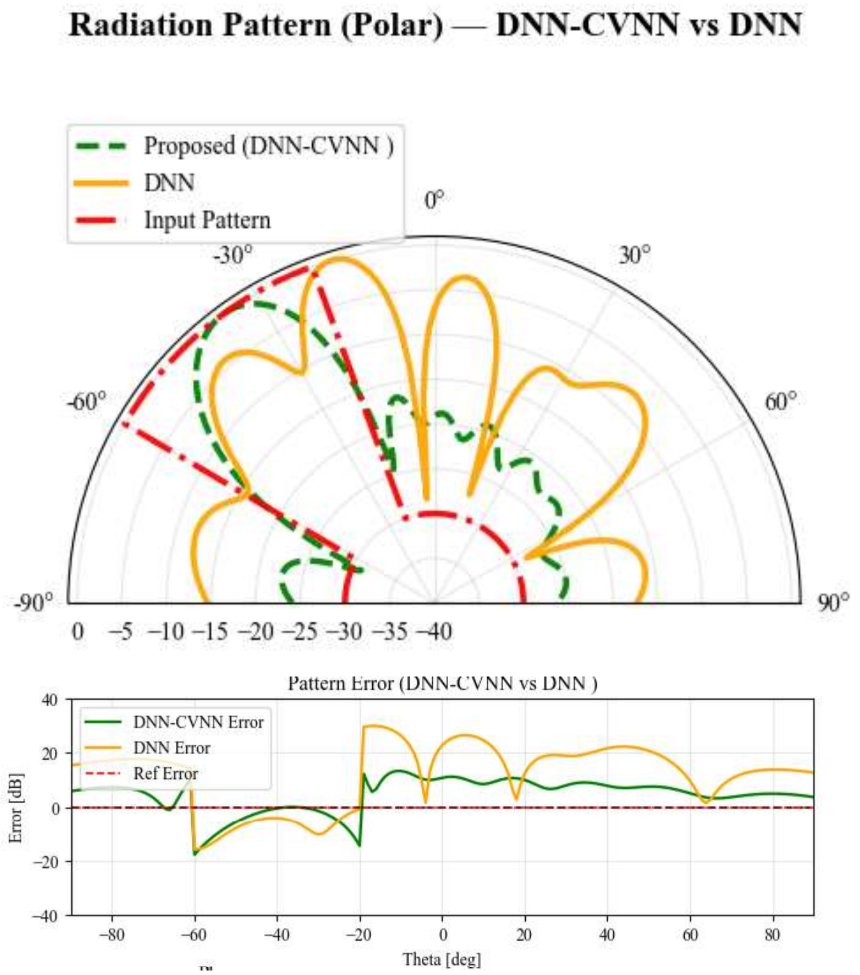

Figure 2 Radiation Pattern Synthesis: Beam Steering

Figure 3 (sidelobe-level reduction) In this sidelobe suppression scenario, both methods aim to synthesize a pencil beam centered near broadside (0°) with stringent sidelobe level requirements of -30 dB. The polar plots reveal that the DNN–CVNN achieves exceptional sidelobe control: its pattern maintains suppression levels consistently below -29 dB throughout the far sidelobe regions (beyond ±30°), with performance reaching -30 to -31 dB at the extreme angles (±90°). The main beam peaks cleanly at 0 dB near -7° with smooth roll-off into the transition zones. In stark contrast, the real-valued DNN exhibits dramatically elevated sidelobes—particularly in the ±25° to ±60° angular sectors where levels deteriorate to only -14 to -8 dB, representing a catastrophic 15-20 dB degradation from the target specification. The pattern-error analysis confirms this disparity: the DNN–CVNN maintains errors within ±5 dB across most of the pattern space, while the baseline's error explodes to +15-20 dB throughout the near-sidelobe region. Quantitatively, the hybrid network achieves a worst-case SLL better than -26 dB, whereas the real-valued DNN's worst sidelobes exceed -8 dB—an 18 dB performance gap. Examining the element excitations, the DNN–CVNN weights display a coherent phase taper (spanning approximately 220° to 280° across elements) coupled with amplitude shading that naturally produces the required destructive interference at sidelobe angles. The baseline DNN's excitations show erratic phase variations and unbalanced amplitudes that fail to establish the necessary null-steering conditions.

This low-SLL design task starkly illustrates the CVNN advantage: complex-valued processing allows direct manipulation of the array's phase front to place deep nulls at specific angles through controlled interference, while the real-valued architecture's decoupled handling of amplitude and phase prevents it from achieving the precise cancellation patterns essential for aggressive sidelobe suppression.

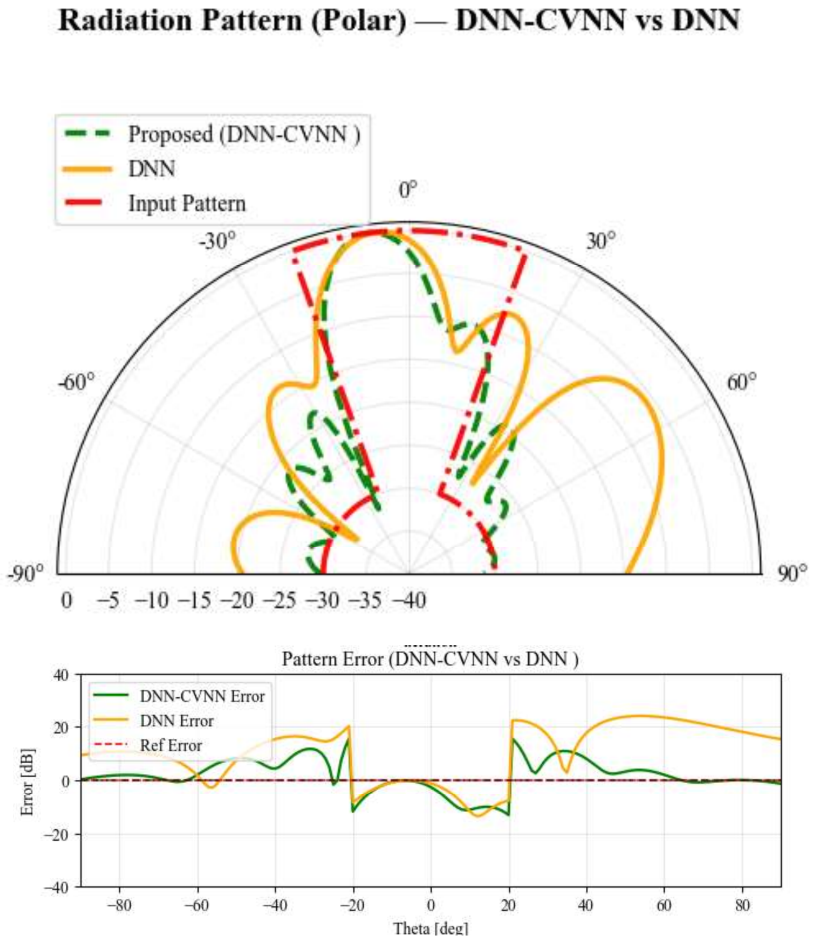

Figure 3 Radiation Pattern Synthesis: Sidelobe Level Suppression

In Figure 4 (multi-beam generation), In this beam shaping scenario, both methods attempt to synthesize a broadside pattern with a wide main lobe spanning approximately ±70° and sidelobes suppressed to -30 dB beyond those angles. The DNN–CVNN demonstrates superior pattern fidelity: it maintains sidelobe levels consistently between -22 and -27 dB across the ±71° to ±90° regions, achieving much closer adherence to the -30 dB target than the baseline DNN. More critically, the hybrid model produces a relatively smooth main lobe that peaks near 0 dB around 44°, with gradual roll-off toward the edges of the beam. In contrast, the real-valued DNN exhibits significant pattern distortion—most notably, severe nulls appear at -18° and +20° where the pattern unexpectedly plunges to nearly -28 dB, creating unintended deep notches within what should be a uniform main beam. Additionally, the baseline DNN's sidelobes are considerably worse, reaching only -17 to -25 dB in regions where -30 dB suppression is required. The error comparison reveals that the DNN–CVNN maintains low deviation throughout the main lobe (typically within 1-2 dB of target), whereas the baseline's spurious nulls represent errors exceeding 25 dB at certain angles.

Examining the excitation amplitudes and phases, the DNN–CVNN weights exhibit a coherent phase progression and smooth amplitude taper characteristic of a well-formed broadside array, effectively synthesizing the desired aperture distribution. The real-valued DNN's weights, however, show irregular phase discontinuities and amplitude fluctuations that manifest as the observed pattern distortions. This beam-shaping task highlights the fundamental advantage of complex-valued processing: the DNN–CVNN directly manipulates the phase and amplitude of array elements in a unified complex framework, enabling it to enforce the precise constructive and destructive interference required for clean pattern synthesis, while the real-valued network struggles to coordinate these coupled parameters through separate real and imaginary channels, resulting in corrupted radiation characteristics.

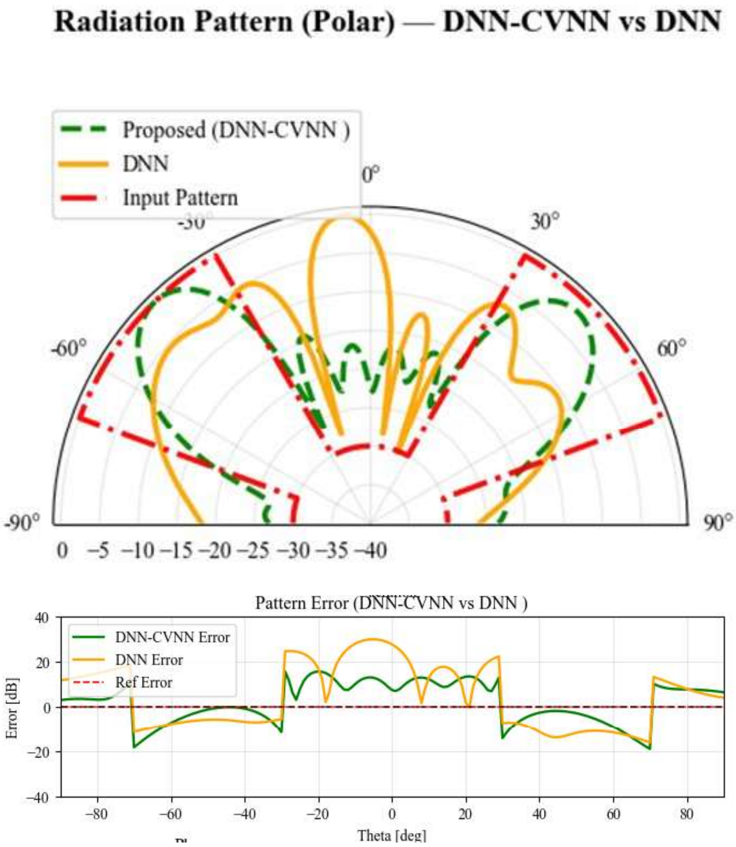

Figure 4 Radiation Pattern Synthesis: Dual-Beam Synthesis

Across all scenarios, the aggregate performance metrics favor the hybrid model. On average, the DNN–CVNN reduced sidelobe levels by several dB compared to the real-valued DNN, and it steered the main beams with sub-degree accuracy. The learning curves show that both networks eventually converge to stable solutions, but the CVNN's training is more stable and reaches a lower final error more rapidly, as expected from its physics-aware design [19]. We also note that the amplitudes predicted by the DNN–CVNN tend to follow a smooth taper (often raised-cosine or Gaussian-like), and the phases progress monotonically, making the outputs immediately usable for practical phased-array hardware. By contrast, the real-valued DNN occasionally outputs weight distributions that would require additional processing to interpret as valid antenna settings.

In this sense, the hybrid model learns "realistic" excitation vectors: when these weights are applied in CST Microwave Studio, the simulated beams match the network's predictions almost perfectly, verifying that the learned weights correspond to implementable antenna excitations (this is in line with other studies showing DL can generate valid complex excitations from desired patterns).

In summary, the proposed DNN–CVNN approach consistently outperforms the baseline real-valued DNN in our experiments. Its ability to natively handle phase information leads to better pattern conformity (main-lobe shape and direction), stronger sidelobe suppression, and more accurate multi-beam shaping across the tested cases. The CST-validated patterns demonstrate that the learned complex weights are both physically plausible and effective. These results confirm that incorporating complex-valued processing into the neural network is an effective strategy for phase-sensitive beamforming problems [20-21].

4. Conclusion

This work shows that a hybrid DNN–CVNN model can accurately learn the inverse mapping from target radiation patterns to complex excitations for an 8-element phased array at 28 GHz. By integrating complex-valued processing in the output layer, the model naturally captures amplitude–phase coupling, achieving better performance than conventional real-valued DNNs.

Across beam steering, sidelobe suppression, and broad-beam shaping, the DNN–CVNN consistently outperforms the baseline, improving sidelobe levels by 15–20 dB, maintaining sub-degree pointing accuracy, and generating smooth, physically realizable excitations. CST validation confirms that the predicted weights produce accurate far-field patterns, demonstrating practical viability for mmWave systems.

The complex-valued formulation enables direct manipulation of phase fronts and interference conditions, leading to faster convergence, more stable training, and better generalization. This makes the approach well suited for real-time adaptive beamforming in 5G/6G systems, where the trained model generates weights in milliseconds—far faster than iterative optimization methods. The framework can be extended to larger arrays, planar architectures, and multi-band applications.

Future work includes incorporating physics-informed constraints, supporting multi-objective pattern control, quantifying prediction uncertainty, and deploying the model on edge hardware for real-time operation.

In summary, complex-valued neural networks provide an efficient and accurate solution for phased-array synthesis, bridging machine learning and electromagnetic design for next-generation wireless communication systems.

References

[1] L. Godara, “Applications of antenna arrays to mobile communications. I. Performance improvement, feasibility, and system considerations,” *Proc. IEEE*, vol. 85, pp. 1031–1060, 1997.

[2] T. S. Rappaport, *Wireless Communications: Principles and Practice*, 2nd ed. Upper Saddle River, NJ, USA: Prentice Hall, 2002.

[3] S. Kumar, “6G Mobile Communication Networks: Key Services and Enabling Technologies,” *J. ICT Stand.*, vol. 10, pp. 1–10, 2022.

[4] M. Dehmas, M. Challal, A. Arous and H. Haif, “A Novel Design of a Microstrip Antenna Array for Wireless Power Transfer Applications,” Wireless Personal Communication, 134, pp. 581–596, March 2024.

[5] M. Li, Y. Liu, Z. Bao, L. Chen, J. Hu, and Y. J. Guo, “Efficient phase-only dual- and multi-beam pattern synthesis with accurate beam direction and power control employing partitioned iterative FFT,” *IEEE Trans. Antennas Propag.*, vol. 71, pp. 3719–3724, 2023.

[6] D. R. Prado, “The generalized intersection approach for electromagnetic array antenna beam-shaping synthesis: A review,” *IEEE Access*, vol. 10, pp. 87053–87068, 2022.

[7] A. Vié, “Qualities, challenges and future of genetic algorithms,” *SSRN Electron. J.*, 2020.

[8] A. G. Gad, “Particle swarm optimization algorithm and its applications: A systematic review,” *Arch. Comput. Methods Eng.*, vol. 29, pp. 2531–2561, 2022.

[9] M. Challal, A. Mekircha, M. D. Bendref, “Antenna Design and Optimization using AI-based Techniques,” International Conference on Computational Engineering, Artificial Intelligence and Smart Systems (IC2EAIS2), 29-31 October 2025, Djanet, Algeria.

[10] L. Alzubaidi *et al.*, “Review of deep learning: Concepts, CNN architectures, challenges, applications, future directions,” *J. Big Data*, vol. 8, p. 53, 2021.

[11] Y. Wang, L. Liu, and C. Wang, “Trends in using deep learning algorithms in biomedical prediction systems,” *Front. Neurosci.*, vol. 17, p. 1256351, 2023.

[12] M. M. Taye, “Understanding of machine learning with deep learning: Architectures, workflow, applications and future directions,” *Computers*, vol. 12, p. 91, 2023.

[13] *Recurrent Deep Learning for Beam Pattern Synthesis in Optimized Antenna Arrays*, unpublished.

[14] M. A. Abdullah *et al.*, “Antenna array pattern with sidelobe level control using deep learning,” *Appl. Comput. Electromagn. Soc. J. (ACES)*, pp. 427–435, 2025.

[15] M. R. Ghaderi and N. Amiri, “Application of machine learning techniques in phased array antenna synthesis: A comprehensive mini review,” *J. Commun.*, vol. 18, no. 10, pp. 629–642, 2023.

[16] M. D. Bendref, M. Challal**,** A. Mekircha, “AI-Driven Real-Time Adaptive Beam Steering for 5G Fixed Wireless Access Antenna Systems,” 9th International Conference on Artificial Intelligence in Renewable Energetic Systems (ICAIRES), 28-30 October 2025, Mostaganem, Algeria.

[17] Z. A. I. B. Alam *et al.*, “AESA antennas using machine learning with reduced dataset,” *Radioengineering*, vol. 33, no. 3, p. 397, 2024.

[18] A. B. Suksmono and A. Hirose, “Performance of adaptive beamforming by using complex-valued neural network,” in *Proc. Int. Conf. Knowledge-Based Intell. Inf. Eng. Syst.*, Berlin, Germany: Springer, 2003.

[19] R. Abdalla, “Complex-valued neural networks—Theory and analysis,” *arXiv preprint* arXiv:2312.06087, 2023.

[20] S. Oh, S. Pyo, and H. Jang, “PhaseNet: A deep learning framework for reflectarray antenna gain prediction by integrating 2D phase maps and angular embeddings,” *Mathematics*, vol. 13, no. 21, p. 3509, 2025.

[21] J. Bassey, L. Qian, and X. Li, “A survey of complex-valued neural networks,” *arXiv preprint* arXiv:2101.12249, 2021.

الفهرس

Editorial Secertary

	**Mussa. A. Said** Professor, Chemistry, Islamic University of Madinah, Saudi Arabia. **Orcid:** https://orcid.org/0000-0003-3073-5449
	**Fazal Noor** Professor, Computer science and engineering, Islamic University of Madinah. Saudi Arabia **Orcid:** https://orcid.org/0000-0002-0096-3435
	**Basem Rashid Alamri** Associate Professor, Electrical Engineering, Taif University, Saudi Arabia https://orcid.org/0000-0002-8667-0042
	**Saad Talal Alharbi** Professor in Computer Science, � Human Computer Interaction, Faculty of Computers, Taibah University, Saudi Arabia https://orcid.org/0000-0003-0913-8631
	**Yazed Alsaawy** Associate Professor, Computer and information systems, Islamic University of Madinah. Saudi Arabia **Orcid:** https://orcid.org/0000-0001-5031-3388

Editorial Board

Editorial Board Members

قواعد النشر في المجلة

- ➢ أن يكون البحث جديدا، ولم يسبق نشره
- ➢ أن يتسم بالأصالة والجدة والابتكار والاضافة للمعرفة
- ➢ أن لا يكون مستلا من بحوث سبق نشرها للباحث/للباحثين
- ➢ أن تراعى فيه قواعد البحث العلمي الاصيل، ومنهجيته.
- ➢ أن يشتمل البحث على:
    - ✓ صفحة عنوان البحث باللغة الانجليزية.
    - ✓ مستخلص البحث باللغة الانجليزية.
    - ✓ صفحة عنوان البحث باللغة الانجليزية.
    - ✓ مستخلص البحث باللغة العربية.
    - ✓ مقدمة.
    - ✓ صلب البحث.
    - ✓ خاتمة تتضمن نتائج وتوصيات.
    - ✓ ثبت المصادر والمراجع.
    - ✓ الملاحق الملازمة(إن وجدت.)
- ➢ في حال (نشر البحث ورقا)يمنح الباحث نفسه نسخة من عدد المجلة الذي نشر بحثه بها و10 نسخ من بحثة بشكل مستقل
- ➢ في حال اعتماد نشر البحث تؤول حقوق نشره كافة للمجلة، ولها ان تعيد نشره ورقيا أو إلكترونيا، ويحق لها
- ➢ إدراجه في قواعد البيانات المحلية والعالمية- بمقابل أو بدون مقابل -وذلك دون حاجة للإذن الباحث.
- ➢ لا يحق للباحث إعادة نشر بحثه المقبول للنشر في المجلة- في أي وعاء من أوعية النشر -إلا بعد إذن
- ➢ كتابي من رئيس هيئة تحرير المجلة
- ➢ نمط التوثيق المعتمد في المجلة هو نمط IEEE

معلومات الإيداع

النسخة الورقية :

تم الإيداع في مكتبة الملك فهد الوطنية برقم 1439/8742 وتاريخ 1439/09/17 هـ

الرقم التسلسلي الدولي للدوريات **(ردمد)** 7936 – 1658

النسخة الإلكترونية:

تم الإيداع في مكتبة الملك فهد الوطنية برقم 4287 /1439 تاريخ 1439/9/17 هـ

الرقم التسلسلي الدولي للدوريات **(ردمد)** 7944- 1658

الموقع الإلكتروني للمجلة:

https://jesc.iu.edu.sa

ترسل البحوث باسم رئيس تحرير المجلة إلى البريد الإلكتروني

jesc@iu.edu.sa

Islamic University Journal of Applied Sciences (IUJAS)

مجلة الجامعة الإسلامية للعلوم التطبيقية

(IUJAS)

صادر عن

الجامعة الإسلامية بالمدينة المنورة

إصدار خاص

The 1st National Conference of Advanced Electrical and Electronics Engineering

NCAEEE'25

held at the Institute of Electrical and Electronic Engineering, University M'Hamed Bougara of Boumerdes, Algeria, November 30th, 2025.

بسم الله الرحمن الرحيم

الجامعة الإسلامية بالمدينة المنورة
ISLAMIC UNIVERSITY OF MADINAH

مجلة الجامعة الإسلامية للعلوم التطبيقية

مجلة علمية دورية محكمة

مجلة ذات وصول مفتوح

Print ISSN: 1658-7936
Online ISSN: 1658-7944

إصدار خاص فبراير ٢٠٢٦